DETERMINATION OF ENERGY SPECTRA OF PROTON THERAPY BEAMS

M.R. NCHODU

Thesis presented for the degree of
Doctor of Philosophy
in the Department of Physics
Faculty of Science
University of Cape Town

August 2002

Abstract

A technique has been developed for measuring the energy spectra of high-energy proton therapy beams *in situ* under conditions similar to those used for radiotherapy at the South African National Accelerator Centre. The method is based on proton elastic scattering, H(p,p)H, in a thin polyethylene radiator and uses two ΔE-E detector telescopes to detect coincident proton pairs. Measurements have been made to investigate the effect of standard beam modification elements on the energy spectra of proton therapy beams produced by a passive scattering system. Monte Carlo simulations of the spectra were computed with the MCNPX 2.1.5 Monte Carlo code to compare with experimental measurements.

Tlotlisong le sehopotsong sa mme motswadi waka

Sekobi Mitta Nchodu

I declare that, except where acknowledged, the work contained in this thesis to be my own original work, carried out with the guidance and advice from my supervisors. I also acknowledge the assistance of my supervisors, colleagues and fellow students during the periods when experimental measurements were made, this not being possible to execute except by way of a team.

M.R. Nchodu

ACKNOWLEDGEMENTS

I wish to express my appreciation and gratitude to my supervisor Professor F.D. Brooks, for his assistance, encouragement and support.

In addition, I wish to express my gratitude to the following people:

Drs. A. Buffler and D.T.L. Jones for their supervision and support

Professor M.S. Allie for his support and encouragement

Drs. K. Langen and J.V. Siebers for helping me with the Monte Carlo simulations

Dr. P. Binns and Messrs J.E. Symons and M. Herbert for their contribution in the running of the experiments

The staff of National Accelerator Centre for their co-operation and use of their facility

My colleagues in the Physics department at the University of the Western Cape, in particular Professors C.J. Linder and D. Marshall, for their friendship and support.

The students and staff of the University of Cape Town for their support and encouragement

My wife Martha and my daughters Dimakatso and Keabetsoe for putting up with far more than could be reasonably expected during the completion of this work

My family and friends for support and encouragement

The University of the Western Cape and the South African Institute for Race Relations for financial assistance

Contents

List of Figures

List of Tables

Chapter 1

Introduction

Radiation therapy plays an important role in cancer treatment, and is involved in about half of cancer treatments in industrialised societies [Ko97, Kh98, Jo01b], and is often used in conjunction with other treatment techniques such as surgery and chemotherapy. All of these treatment methods strive to halt or restrict the growth of tumours or lesions that are produced by malignant disease. Surgery may involve traumatic physical intervention but can sometimes remove tumours precisely. Chemotherapy, which is based on the use of drugs to destroy tumours or to inhibit tumour growth, can be very successful. However, it may also have adverse side effects since it is difficult to restrict the effects of the drug application to the tumour alone.

Radiation therapy uses the radiobiological effects of ionizing radiation (charged particles, neutrons, gamma rays or x-rays) to destroy lesions or to halt their growth. The success of radiotherapy depends on the ability of the therapy system to concentrate the radiation on the target region i.e. lesion or tumour. Ideally, a lethal quantity (dose) of radiation should be delivered to the lesion while simultaneously minimizing the irradiation of healthy adjacent tissues. This can be achieved by irradiating the lesions from different directions. The irradiation is usually repeated up to 36 times, depending on the type of lesion, over a period of several weeks (fractionated). Such fractionation allows the less irradiated healthy tissues to repair themselves since their repair rate is usually faster than that of the lesion cells, which receive a higher dose. The restriction of the high dose region to the lesion reduces the frequency and severity of treatment-related complications

[Su74, Sh79, Su92, Su90, Su97]. Consequently, a higher dose may be administered to the target tissues, resulting in an increase in the probability to control the tumour [Su74, Ok95, Su80, Su92a, Ve82, Jo01b] and therefore, higher cure rates and an improved quality of life [Su74, Su92a, Ko97, Jo01b]. Proton therapy is a relatively young form of radiotherapy which is presently attracting much interest and attention [Ve82, Bo93, Ra95, Si95, Kh98, Wa99, Jo01b] as it promises to come close to achieving this ideal.

The dominant constituent of human tissue is water. For the purpose of discussing or modelling the interaction of radiation with the human body, water forms a suitable first approximation to human tissue. Consider the interactions of different radiations with water in a cylinder with a diameter of about 400 mm (see figure 1.1) containing a region marked R to represent a target volume, located at a depth of about 240 mm along the direction of the beam. Protons from a 200 MeV proton beam, entering the cylinder with an energy of 191 MeV after interacting with the beam modification elements travel in a relatively straight path have a well-defined range of about 240 mm in water, and therefore *stop* in the target region R. The radiation dose, that is the energy deposited in the water (material) per unit mass, delivered to any region in the cylinder can be determined by measurements with ionization chambers. Figure 1.2 shows the dose delivered by different types of radiation in water as a function of penetration distance (depth) in water. High-energy photons and neutrons have a dose distribution that diminishes exponentially with depth, and therefore the dose distribution delivered by photons and neutrons in water will be concentrated within region A in figure 1.1. In contrast to neutrons and photons, the dose distribution delivered by a proton beam in water is characterized by a flat distribution in the entrance region, a sharp Bragg peak at the end of the protons' path and negligible dose beyond the Bragg peak (see section 1.1). The dose distribution of a beam of 200 MeV protons is therefore relatively "small" and uniform between the entrance point and the region marked R, increases about threefold at the end of the proton range at some point within region R, for example the cross-hatched region in figure 1.1, and drops significantly beyond this region. The concentration of high dose near the end of the proton range and the negligible dose beyond this region make proton beams advantageous for the treatment of lesions adjacent to sensitive structures [Sh79, Ve82, Bo93, Su92, Jo95b].

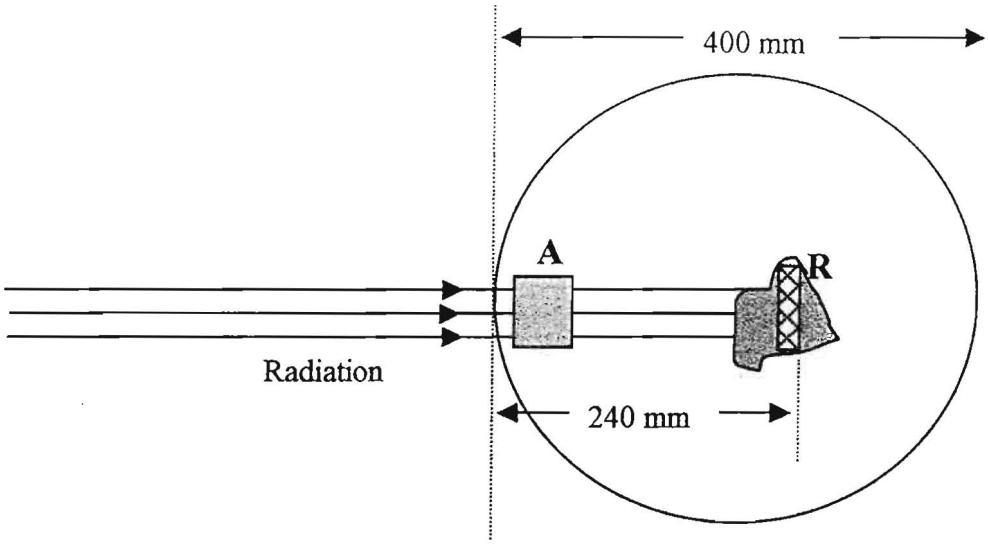

Figure 1.1: *A schematic illustration of radiation beams irradiating water in a cylinder with a diameter of 400 mm. The dose delivered by protons will be concentrated within region R, for example in the cross-hatched region, and the dose delivered by neutrons and high-energy photons will be concentrated within region A. See text for details.*

The cross sectional area of a monoenergetic beam and the width of the Bragg peak are usually too small for irradiating large lesions but can be useful for irradiating small lesions. The energy of the proton beam must also be controlled to attain the desired penetration (range) in the body. The two approaches used to deal with this problem are characterized as either passive or dynamic. In a dynamic beam scanning system, magnets move the beam across the target cross-section and a range shifter dynamically changes the penetration depth of the beam in the tissue [Ch93, Pe95, Kh98, Bo93, ICRU59, Jo01b]. In a passive beam delivery system, beam modification elements such as energy degraders and scatterers are used to reduce the range of the proton beam from the accelerator and to increase the diameter of the beam through multiple scattering, respectively, to conform the high dose region to the target volume [Ch93, Kh98, Bo93, ICRU59] (see figure 1.3). A suitable combination of beam modification elements can thus be used to produce a proton beam that will result in a relatively low dose at the entrance, high and homogenous dose on the lesion, and low dose to structures surrounding the lesion. Thus, it is important to understand the effects of the beam modification elements on the characteristics of the beam, such as its energy distribution and size in order to choose a suitable combination of beam modification elements to optimise the beam for radiation therapy. Knowledge

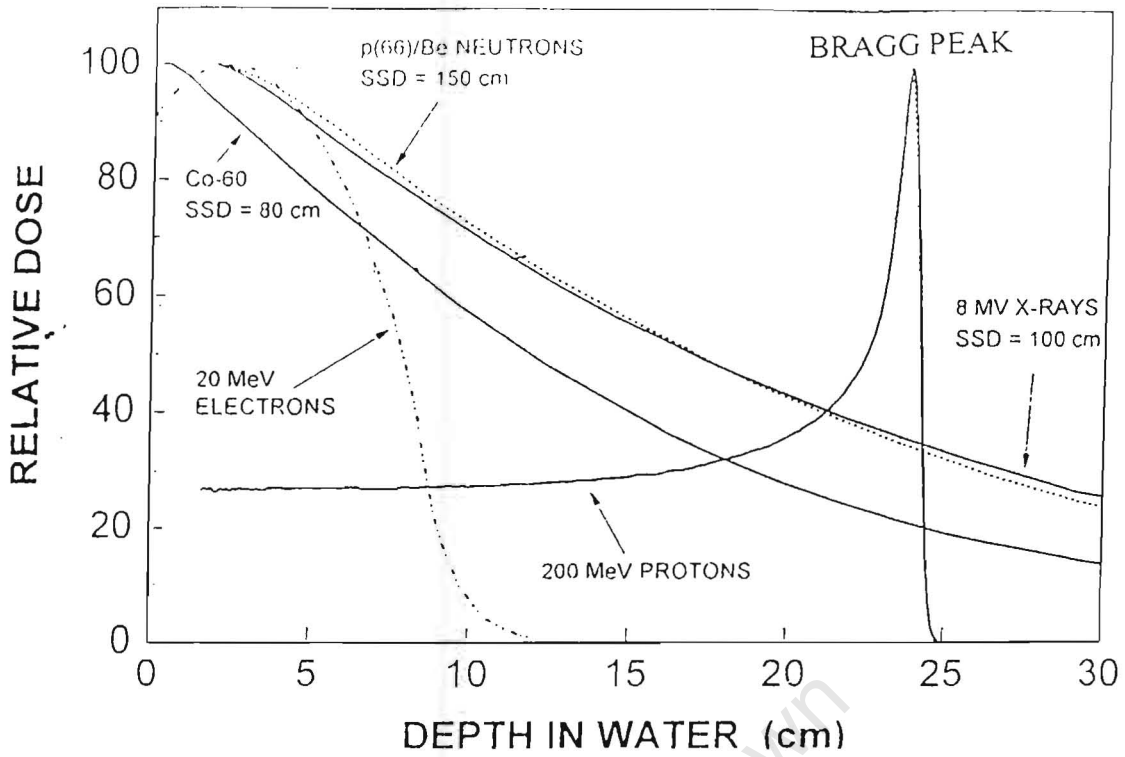

Figure 1.2: *Relative dose as a function of depth for a 191 MeV proton therapy beam compared with a p(66)/Be neutron source (66 MeV protons on a beryllium target), a 8 MV X-ray beam from a linear accelerator, photons from a ^{60}Co source, and a 20 MeV electron beam [Jo94, Jo95b]. Each curve is normalised to a maximum dose of 100 J/kg.*

of the characteristics of the proton therapy beam is also vital for treatment planning programs, shielding designs in the therapy room, and for comparison of clinical, radiobiological and dosimetric data between various proton therapy centres.

A passive beam delivery system is used to tailor proton therapy beams at the South African National Accelerator Centre[1] (NAC). Protons are accelerated by a separated sector cyclotron and exit the vacuum system with an energy ranging from about 200.0 to 202.5 MeV [NA94]. A beam-flattening device comprising lead scatterers and brass occluding rings [Ko77] is used at the NAC to enlarge the diameter of the beam and to maintain a uniform dose distribution over a diameter of about 100 mm at the treatment position (isocentre) [Jo94, Jo95b, Sc95]. The energy of the beam and hence its penetrating distance in tissue is varied by introducing graphite wedges and polyethylene plates [Ko72, Sc95] in the beam. Modulator propellers are used to spread the high dose region over the lesion by placing material of varying thickness in the beam that increasingly degrade the beam energy, resulting in a series of Bragg peaks which superimpose to produce a

[1] Now called iThemba Laboratory for Accelerator Based Sciences since October 2001.

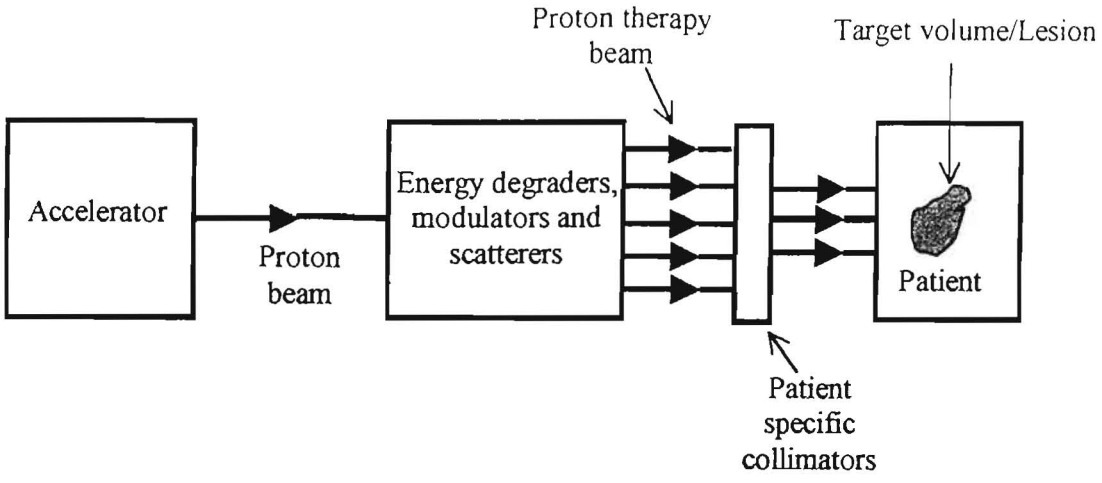

Figure 1.3: *An illustration of a passive beam delivery system. Energy degraders, modulator propellers and scatterers are used to achieve the required dose distribution in the lesion.*

dose distribution with a "spread out Bragg peak" (SOBP) [Ko72]. The layout of the proton therapy facility of the NAC and the operation of the beam line will be discussed in Chapter 2.

Monte Carlo transport codes [Be93, Fe95, Me97, SA97, Si97] and theoretical [Go90, Bo96, Ca97] calculations may be made to predict the effects of beam modification elements on the characteristics of the proton therapy beam in a passive beam delivery system. Experimental measurements of, for example energy spectra, made under conditions that are similar to therapy conditions [Br97b] are essential to test the validity of these calculations. In the present work energy spectra of typical proton therapy beams at the South African National Accelerator Centre have been measured and compared with the MCNPX [Hu97, Wa99] Monte Carlo calculations.

1.1 Monte Carlo simulations for radiotherapy treatment planning

The absorbed dose delivered by proton beams in body tissue is normally determined indirectly from measurements made with ionization chambers in tissue-like materials such as water phantoms [Mo81, Bl83, ICRU59, Ha98]. The absorbed dose in the patient is inferred from the measurements taken in the tissue-like material after correcting for beam shape, tissue geometry and the variation in density and composition from one type of body tissue to another [Mo81, Bl83]. Such empirical methods of dose calculation are accurate for situations where the patient and beam conditions are similar to measurement conditions [Ha98]. In most cases, however, the tissue geometry is complex and dose calculations from empirical methods are inadequate to predict the resultant dose distribution in the patient from the planned irradiation. Monte Carlo calculations can be used to predict the dose distribution in the tissue delivered by the planned irradiation [Ha95a, Ha95b, Ha98, ICRU59] by simulating the path of the particles through the beam delivery system and the patient. The dose deposited by each of the tracked particles is recorded and a detailed map of the dose distribution is developed [Bo99, De98, Ha95a, Ha95b, Ha98, Pa98, Wa98]. The Monte Carlo method is in principle the most complete and rigorous method presently available for calculating dose distributions, since it can accurately take account of the material density and composition variations within the patient. Densities and compositions of materials in the beam line and tissues must be known, ideally to 1% or better to make the Monte Carlo results useful.

Fast Monte Carlo calculations would be ideal for treatment planning, due to the accuracy of the results expected from such calculations. The calculation of the dose distribution in the patient must be completed in a relatively short time for routine use in radiotherapy centres. Due to the statistical nature of the Monte Carlo calculations, a large number of particle histories must be simulated to obtain reliable results. This will normally require long computation times. Existing Monte Carlo programs, such as MCNPX [Hu97, Wa99] for example, running on a Linux platform on an Intel Pentium IV processor with 256 Megabytes of RAM, typically takes several hours to complete a simulation of protons in a passive beam delivery system. The program then takes many more hours tracking the particles through

the patient to calculate the dose distribution in the target volume. The lengthy computing time needed for simulations limits the present use of Monte Carlo calculations in treatment planning programs.

One way of shortening the simulation time is to divide the calculation into two parts. The first part of the simulation will be the calculation of the effects of beam modification elements on the energy spectrum. In the second part of the simulation the calculated spectrum obtained in the first part of the simulation can then be used as the input source (pre-calculated source) in the simulation of the particles through the patient up to the target volume. This reduces the simulation period of the treatment plans, as the simulation of the beam line does not have to be repeated in every treatment plan. Routine Monte Carlo treatment planning calculations for that beam line could therefore use this pre-calculated radiation source as an input source and save computing time [Ha98, Bo99]. Patient specific beam modifying elements such as energy degraders and modulator propellers are interspersed throughout the proton therapy beam lines in passive beam delivery systems. A single pre-calculated source is therefore not possible for passive beam delivery systems such as the one at the NAC. A library of pre-calculated sources will have to be generated for different combinations of the energy degraders and modulator propellers. Energy spectrum measurements are needed for comparison with Monte Carlo calculations to test the reliability of the pre-calculated sources.

1.2 Measurements of energy spectra of proton therapy beams

The beam modification elements used to tailor the proton beam for therapeutic purposes, as illustrated in figure 1.3, may introduce low-energy components in the proton beam. Furthermore, high beam currents (20-100 nA) are used during therapy at the NAC in order to deliver lethal radiation doses to the target lesion. It is therefore important that the experimental system used to measure spectra should be capable of monitoring the energy spectrum over a wide range of energies and also a wide range of intensity. These requirements are difficult to meet with

standard proton spectroscopy methods, such as detector telescopes with detection volumes large enough to stop 200 MeV protons. Large beam fluxes lead to pulse pile-up in the detection system and consequently distort the pulse height spectrum. The reduction in the beam current may alleviate this problem. However, the beam control system at the NAC causes problems with the control and focusing of the beam at low beam currents. The pulsed nature of the proton therapy beams at the NAC may also contribute to pulse pile up problems in the detection system and the summation effect whereby a combination of pulses produced in a detector by protons in the same bunch, in a cyclotron "burst", "appear" similar to a pulse produced by a proton with a higher energy. At energies used for proton therapy (50-250 MeV), inelastic nuclear reactions of protons on any high-Z material in the detector are significant and produce a so-called "reaction tail" which distorts the observed spectrum by enhancing the low energy component [Go59, Bu59, Go60, Gi64, Me65, Me66, Ma68, Me69, Pa69].

When a beam of monoenergetic protons is incident upon a detector whose volume is large enough to stop the incident protons, the observed pulse height spectrum is characterized by a peak at the maximum pulse height corresponding to the incident beam energy, and a low pulse height tail [Bu59, Jo58, Ei63, Ma68, Pa69]. Figure 1.4 shows the pulse height spectrum measured by the NaI crystals in the detection system shown in figure 1.6, for a monoenergetic incident proton beam of 160 ± 1 MeV from the Harvard Cyclotron Laboratory [Pa69]. There are two main components in this spectrum: firstly a sharp peak at the upper limit of the spectrum, which has been used to calibrate the pulse height scale to proton energy; and secondly a broad continuum stretching downwards from the peak to about 10 MeV, corresponding to the detector threshold. The counts within the peak can be ascribed to protons in which the proton kinetic energy was lost entirely and exclusively by excitation or ionization of electrons in the detector material. The counts in the continuum region, the so-called "reaction tail" can be attributed to events in which only a fraction of the initial proton energy is converted to excitation and ionization, usually because the proton has undergone a nuclear reaction within the detector material. Three types of mechanism that lead to the reaction tail can be identified.

i. nuclear reactions with the detector material resulting in the production of

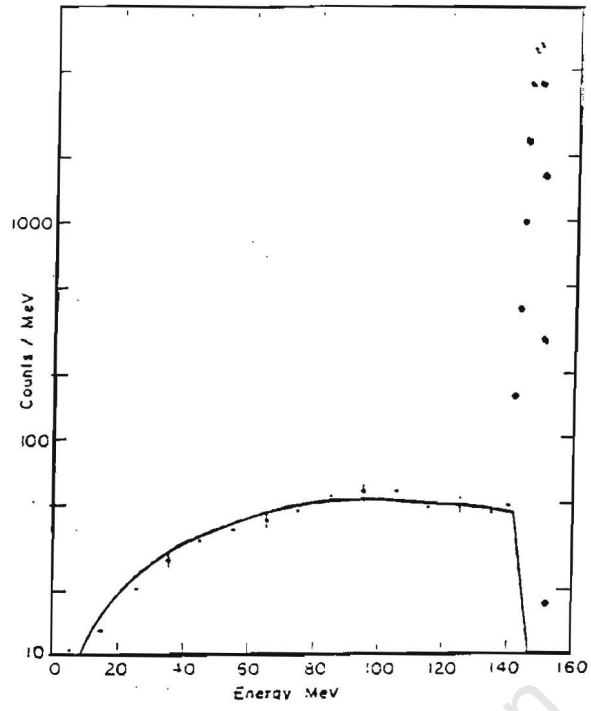

Figure 1.4: *Pulse height spectrum of a high-energy proton beam measured by a Sodium Iodide scintillator. Events in the peak at pulse height are attributed to protons that lost energy through ionization or excitation of the electrons in the detector until coming to rest in the detector. The events in the low energy tail are attributed to protons that deposited energy in the scintillator through ionization or excitation and underwent inelastic nuclear interactions with the sodium and iodine nuclei in the scintillator. Reproduced from [Pa69].*

uncharged particles such as neutrons and gamma rays which do not deposit all their energy in the detector [Me65, Me66, Ma68, Pa69];

ii. the proton is scattered and escapes from the detector medium before it loses all its kinetic energy; or

iii. nuclear reactions with the detector material resulting in the production of heavier secondary charged particles. Proton reactions with negative Q-values produce secondary particles with lower energies than the incident proton energy [Go59, Bu59, Go60, Gi64, Me65, Ma68, Pa69].

The fraction of protons contributing to this "reaction tail" increases with increasing incident proton energy, rising to about 27% for 200 MeV protons in an organic scintillator such as anthracene, as shown in figure 1.5 [Ja82]. The effects of the inelastic nuclear interactions on the measured pulse height spectrum can be corrected by measuring [Ba69, Re72, Pa69] or calculating [Jo58, Me65, Me66, Ma68, Me69] the reaction tail contribution in the measured pulse height spectrum. This method of correcting for reaction tail requires knowledge of the distribution of pulse

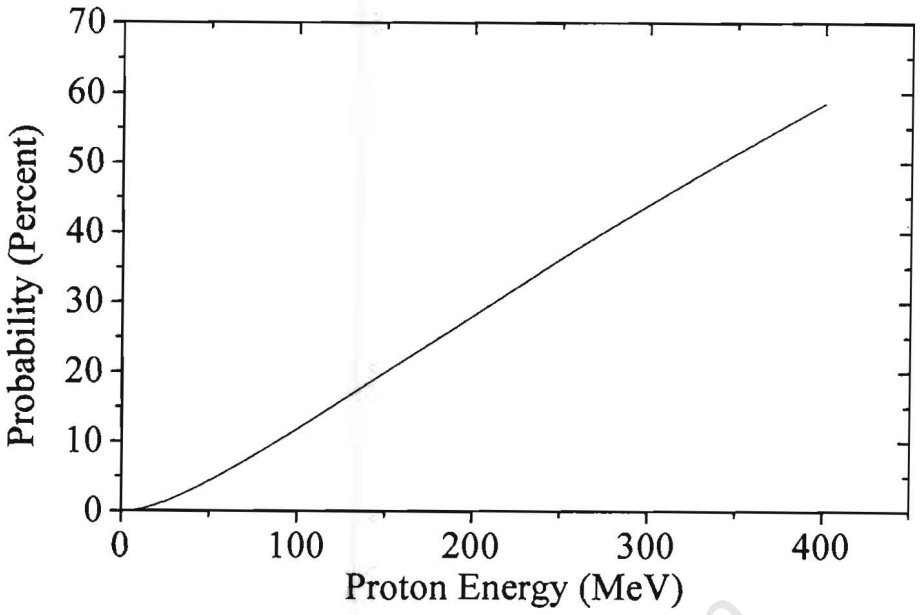

Figure 1.5: *Calculated inelastic nuclear interaction probabilities of protons in anthracene as a function of incident proton energy based on the data from "proton range-energy tables" [Ja82].*

height events from monoenergetic incident particles in the region of interest, and a correction for particles escaping through the sides of the detectors.

A detection system based on proton elastic scattering H(p,p)H in a thin polyethylene radiator was used to investigate the influence of inelastic nuclear scattering in the measurement of the energy spectrum of a 160 MeV proton beam with NaI crystals at the Harvard University Cyclotron Laboratory (HCL) [Pa69]. The detection system used at HCL, shown in figure 1.6, comprised of a detector telescope consisting of three Pilot-B scintillators followed by a (76.2 mm diameter $\times$ 76.2 mm thick) sodium iodide crystal and a (76.2 mm $\times$ 127.0 mm $\times$ 3.2 mm) plastic scintillator. A carbon target was used to measure background and accidental coincidences. The thicknesses of the polyethylene and carbon radiators are not mentioned in the published paper [Pa69]. Coincident proton pairs were detected by the two telescopes. An aluminum absorber was placed in front of the recoil detector so that only protons of about 130 MeV or more could satisfy detection conditions. This was done to discriminate against low-energy protons in the beam [Pa69], which implies that the tail in the pulse height spectrum measured with the NaI can be

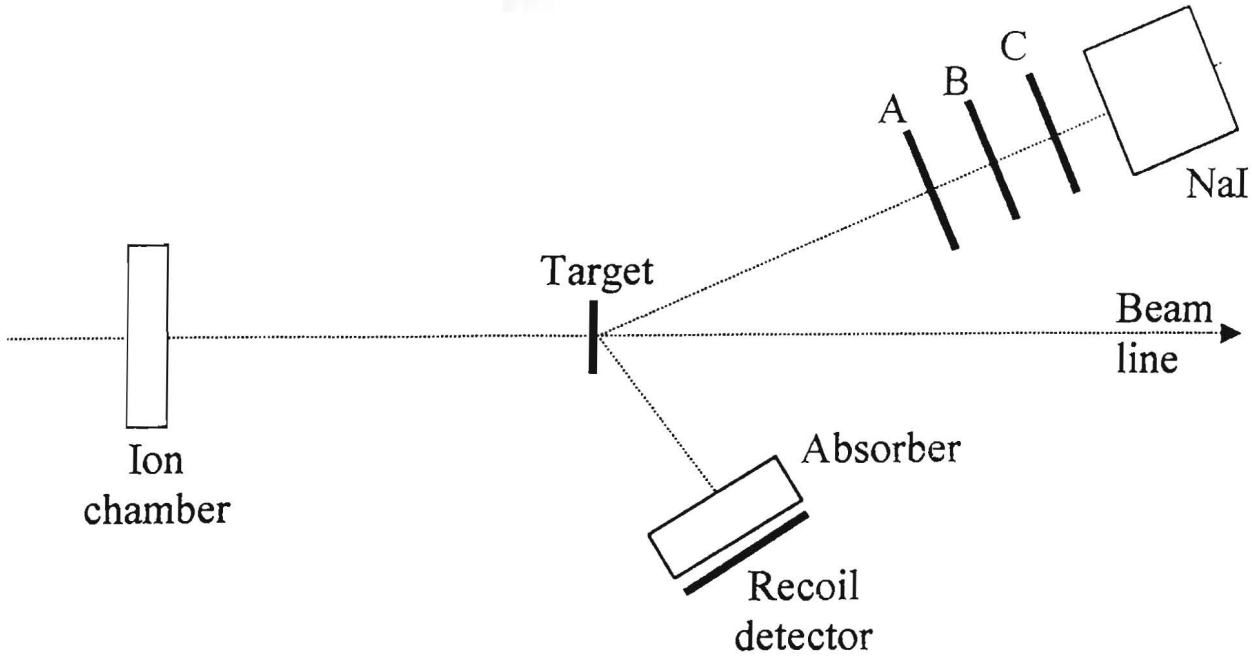

Figure 1.6: *A schematic layout of the detection system used to measure the proton energy spectra at the Harvard Cyclotron Laboratory [Pa69]. A detector telescope consisting of three Pilot-B scintillators (A, B and C) followed by a sodium iodide crystal and a plastic scintillator were used to detect coincident proton pairs from elastic scattering on a polyethylene radiator. See text for details. Adapted from [Pa69].*

attributed to reaction tail events. The detection system, therefore, had a high detection threshold of 130 MeV, rendering the system incapable of measuring low energy protons in the beam. The pulse height spectra measured at the HCL were corrected for reaction tail effects by measuring the tail to peak ratio in the pulse height spectrum of the scattered protons. This ratio was used in the fitting of the tail in the energy spectrum (see figure 1.4) by a quadratic function [Pa69]. A cut-off point at 5 MeV below the average peak energy in the pulse height spectrum was chosen to separate events from inelastic nuclear interactions from events resulting from the interaction of protons with electrons in the detector [Pa69]. This method of discriminating against inelastic nuclear interactions can only be used when there is also a method to discriminate against low-energy protons in the beam. The low-energy tail in the spectrum such as the one shown in figure 1.4 will therefore be solely due to reaction tail.

A coincidence detection system based on proton elastic scattering H(p,p)H in a thin polyethylene radiator was also used to measure energy spectra of proton therapy beams at the South African National Accelerator Centre [Br97b]. The spectrometer used at the NAC consisted of two ΔE-E detector telescopes to

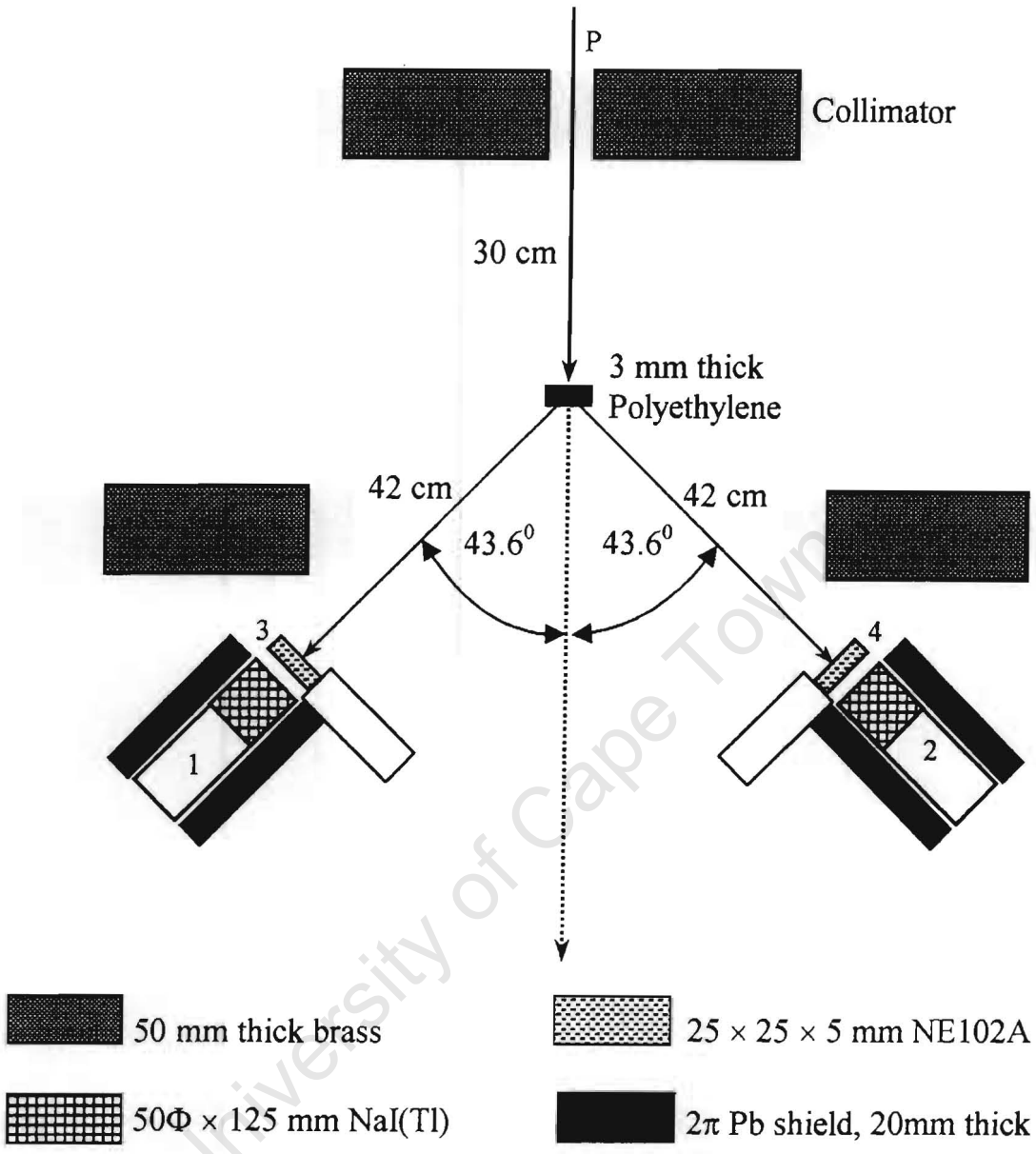

Figure 1.7: *A schematic layout of the coincident detection system used to measure the proton energy spectra at the NAC [Br97]. The detection system consisted of two detector telescopes placed at an angle (θ) of 44° relative to the beam axis. Each telescope consisted of an NE102 (ΔE) detector and a NaI(Tl) (E) detector. Incident protons were scattered by protons in the polyethylene radiator. The scattered protons and the associated recoil protons were detected by the two detector telescopes.*

detect scattered and recoil protons in coincidence (figure 1.7). Each detector telescope consisted of a (50 mm diameter × 125 mm thick) NaI(Tl) crystal and a (25 mm × 25 mm × 5 mm thick) NE102 plastic scintillator. The NaI(Tl) crystals had thin entrance windows (7 μm Havar) and were enclosed in annular lead shields. The distance between the radiator and the entrance window of each NaI(Tl) crystal was 420 mm. The kinematics of non-relativistic ($E < 30$ MeV) p-p elastic scattering (see figure 1.8) dictates that the paths of the incident and outgoing protons be coplanar and that $\theta_1 + \theta_2 = 90°$. However, as the incident proton energy increases, the laboratory angle between the two outgoing protons ($\theta_1 + \theta_2$) becomes smaller in accordance with relativistic kinematics. If we assume that the collision is between an incident proton of energy E and a target proton at rest in the laboratory frame, and that $\theta_1 \approx \theta_2$, then according to the kinematics of relativistic p-p elastic scattering, the angle (θ_1 or θ_2 in figure 1.8) between the scattered protons and the incident proton direction is given by the equation [Ma69]

$$tan^2\theta = \frac{2}{\frac{E}{E_o} + 1} \tag{1.1}$$

where E_o is the rest energy of the proton and E is the relativistic énergy of the incident proton, that is $E = E_{kinetic} + E_o$. Figure 1.9 shows a plot of the laboratory angle between the scattered and recoil protons ($\theta_1 + \theta_2$) as a function of incident proton energy, calculated using equation 1.1. As the incident proton energy increases from 0 to 200 MeV, $\theta_1 + \theta_2$ decreases from 90° to 87.1° as shown in figure 1.9.

The telescopes in figure 1.7 were symmetrically aligned with their axes subtending equal laboratory angles of 44° with the beam axis. The finite angular resolution of the detectors (3° FWHM) [Br97b] allowed coincidences to be registered at proton energies up to 200 MeV with $\theta = 44°$. The data analysis, which was carried out off-line, consisted of applying appropriate windows on the pulse height parameters of the ΔE and E detectors and the coincidence time delay parameter to select coincidence proton events. These windows excluded a large fraction of reaction tail events, which occurred in the scintillators. The pulse height of the NaI and NE102 scintillators were calibrated to proton energies E_1, E_2, E_3 and E_4, where the subscripts 1 to 4 refer to the detector numbers indicated in figure 1.7. The energy

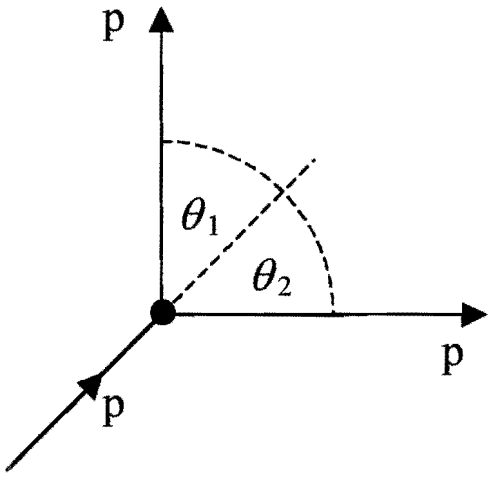

Figure 1.8: *A schematic diagram of p-p elastic scattering in the radiator. θ_1 and θ_2 are laboratory angles between the outgoing protons and the incident proton direction. The paths of the incident and outgoing protons are coplanar. The angle between the two outgoing protons (θ_1 + θ_2) varies with incident proton energy (see figure 1.9 below). Below 30 MeV relativistic effects are negligible.*

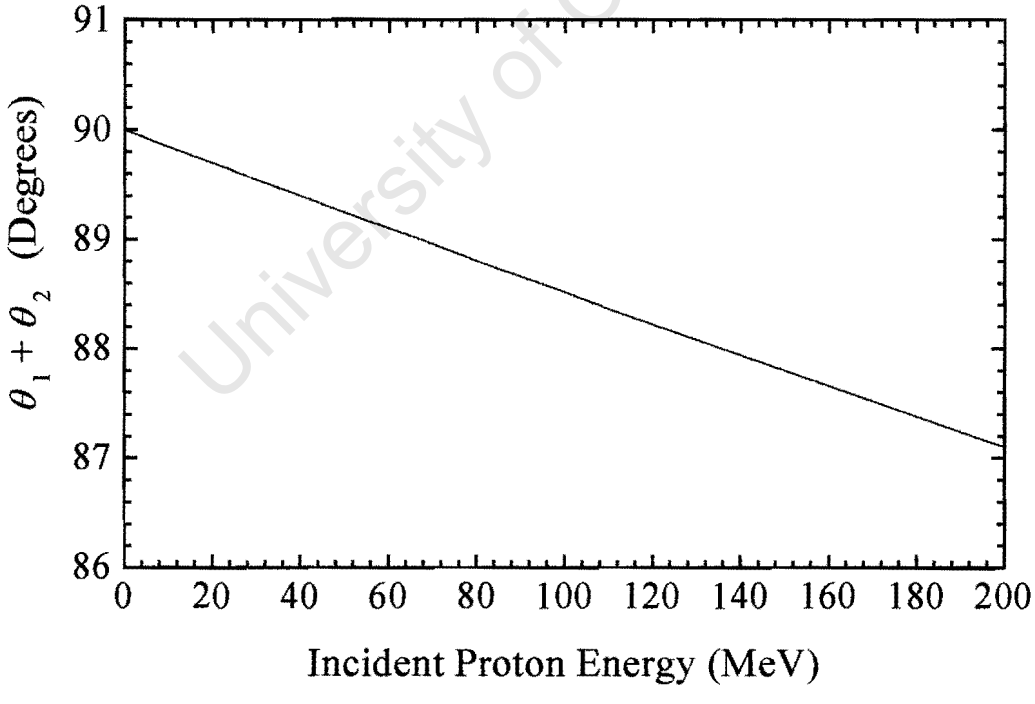

Figure 1.9: *Variation of the laboratory angle (θ_1 + θ_2 in figure 1.8) between the scattered and recoiling protons from p-p scattering as a function of the incident proton energy. θ_1 + θ_2 decreases as the incident proton increases due to relativistic effects. The data are calculated using equation 1.1.*

of the incident proton beam E was therefore obtained from

$$E = E_1 + E_2 + E_3 + E_4 \tag{1.2}$$

The variation in the angle between the two outgoing protons $(\theta_1 + \theta_2)$ with energy, due to relativistic effects, introduced an energy dependent geometrical efficiency factor $\Phi(E)$ in the detection efficiency of the spectrometer. $\Phi(E)$ was calculated and included in the efficiency correction of the measured energy spectra. The efficiency of the detection system $\epsilon(E)$, was assumed to be proportional to the geometrical efficiency factor $\Phi(E)$ and to the Rutherford cross section for p-p elastic scattering which varies as E^{-2} in the laboratory frame [Br97b] that is

$$\epsilon(E) = k\Phi(E)E^{-2} \tag{1.3}$$

The constant k was adjusted so as to normalize the peak intensity of each spectrum to the arbitrary value of 1000 counts per energy bin [Br97b]. Some of the energy spectra measured with this spectrometer are shown in chapter 2 to illustrate the effect of the beam modification elements on the energy spectra of proton therapy beams.

A multilayer Faraday cup (MLFC) such as the one used at the HCL to measure the distribution of charged deposited by a 160 MeV proton beam [Go99b] can be used to determine the proton energy spectrum in a proton therapy facility. A MLFC consists of a stack of metal sheets (e.g. copper plates) separated by an insulator. The sheet thickness should be thick enough so that the proton beam stops near the end of the stack. The charge deposited by protons in each plate can be measured by connecting the MLFC to a multichannel charge meter [Go99b]. Uncertainties in the MLFC measurements are mainly from the uncertainties in the determination of the stopping power data. The spectrum from the MLFC also has contributions from secondary charged particles in the beam. The spectrometer used in this work provides an alternative method of measuring the energy spectrum of proton therapy beams and the method can also discriminate against secondary charged particles and the associated neutrons and gamma rays.

1.3 The present work

Some of the challenges of making measurements of energy spectra of proton therapy beams were explained in the previous section. The spectrometer shown in figure 1.7 was used to study the energy spectrum of proton therapy beams at the NAC [Br97b]. The gain stability in the NaI(Tl) detectors detection system was monitored by incorporating an LED pulser system in the electronics used for data acquisition. The NaI(Tl) crystals used in the previous work [Br97b] were longer (125 mm thick) than the maximum range (about 37 mm) of the scattered/recoiling protons, satisfying the detection conditions in the scintillator for $\theta_1 \approx \theta_2$. Thus the back section of these scintillators (about 88 mm long) contributed mainly to the detection of background radiation in the room and high energy protons scattered by the carbon nuclei in the radiator, which increased the probability of accidental coincidences and pulse pile-up problems in the detection system.

A spectrometer such as the one shown in figure 1.6 can be used to measure the proton energy fluence of a proton therapy beam at the isocentre. Such fluence measurements can be used to determine the number of protons in the beam irradiating the patient at the isocentre and consequently the dose delivered to the patient. An ionization chamber is used at the NAC to monitor the beam exiting from the beam line vacuum pipe (figure 2.1). This ionization chamber is designed to monitor the beam at the high currents (20-100 nA) used for therapy. This monitor was, however, not sensitive enough to monitor the beam when these measurements were made because the beam current was kept low (~0.5 nA) in order to minimize pulse pile-up in the detection system (see section 1.2). It was therefore not possible to normalize different runs to the same number of protons entering the beam modification system. The spectrometer measurements could therefore not be used to compare spectra on a common intensity scale. However it was still possible to compare the shapes of different spectra. Energy spectra of measurements made under different conditions were compared to check for variations in the energy spectra. The absolute fluence could be determined if the efficiency of the detection system was determined, but this was not done as the information obtained from the energy spectra was sufficient to achieve the aim of this work.

The aim of this project was to measure the energy spectra of proton therapy beams at the South African National Accelerator Centre using a proton pair spectrometer, which is a modified version of the p-p coincidence detection system (see figure 1.7), previously used at the NAC [Br97b]. The detection system shown in figure 1.7 was modified to address some of the issues raised above. The modifications made to the detection system included (i) modifying the geometry of the detection system to eliminate the need to correct for the energy dependent geometrical efficiency factor in the calculation of the detection efficiency of the spectrometer, caused by the variation in the angle between the two outgoing protons ($\theta_1 + \theta_2$ in figure 1.8) with energy (relativistic effects), (ii) replacing NaI(Tl) scintillators with NE213 liquid scintillators and (iii) replacing the NE102 plastic scintillators with surface barrier detectors. Pulse shape discrimination was used in the NE213 scintillators for the identification and rejection of the inelastic nuclear reaction events (reaction tail component) and background gamma radiation. NE213 scintillators also have a faster timing response compared to NaI(Tl) scintillators which reduces pulse pile-up problems in the detection system. Furthermore NE213 scintillators have low-Z values compared NaI(Tl) scintillators and will therefore reduce accidental coincidences with the background gamma radiation. The coincidence condition between the ΔE and E detectors in each telescope and the coincidence condition between the two telescopes discriminates against neutrons and the associated gamma ray events detected by the NE213 scintillators (see section 3.2).

The modified proton pair spectrometer was used to measure the energy spectra of proton therapy beams at the radiotherapy facility of the NAC *in situ* under conditions similar to treatment conditions. Measurements were made at the treatment position (isocentre), to investigate spectrum variations associated with changes in beam modification elements, such as energy degraders, modulator propellers, and collimator sizes. Measurements were also made at positions displaced upstream from the isocentre, towards the accelerator, and lateral to the isocentre to investigate the variation in the energy spectra, across the plane perpendicular to the beam axis. Monte Carlo simulations of the proton therapy facility of the NAC were computed using the Monte Carlo code, MCNPX 2.1.5 [Hu97, Wa99], developed at the Los Alamos National Laboratory. Measured proton spectra were compared with the Monte Carlo results, and these results provide a test of the reliability of the MCNPX code to simulate proton therapy beam lines. This work is

important as it provides a direct method of measuring the proton energy spectrum *in situ* under conditions that are similar to treatment conditions. The results of this work will contribute to the existing knowledge about the effects of the beam modification elements on the energy spectrum on proton therapy beams, which is crucial for proton therapy. This will help to confirm the results from other experiments such as fluence measurements made with multilayer Faraday cups and dose measurements with ionisation chambers in the water phantoms, and to check for any unexpected results which may impact on the ability of protons to deliver doses in patient that are concentrated in specified regions. This information will be useful for further modifications of the existing proton therapy beam line and in the development of other proton therapy beam lines at the NAC. The measurements will also be useful for validating Monte Carlo calculations.

Chapter 2

The NAC proton therapy facility

The cyclotron facility of the NAC is used for both neutron and proton radiation therapy treatment during weekdays, isotope production during weeknights, and physics experiments over weekends that is from Friday evening (18:00) to Monday morning (06:00). Physics experiments carried out over a period of several days in the treatment vault have to the moved out of the vault during treatment times and reassembled and tested again to continue with the measurements in the following weekend.

Proton beams are tailored for therapeutic purposes at the South African National Accelerator Centre using the passive scattering system shown in figure 2.1. Protons are accelerated by a separated sector cyclotron and exit the vacuum system with an energy of approximately 200 MeV. The energy spread of the proton beam depends on the settings of the cyclotron such as the flat-top accelerating system [Co92]. The energy spread of a 200 MeV proton beam from the cyclotron is approximately 200 keV FWHM at a beam current of 500 nA [NA94]. Most of the beam line components are mounted on an optical bench and their positions can be easily changed when required. Some of the components can be retracted or inserted remotely [NA94, Jo94, Sc95]. The proton beam, of energy ~200 MeV, exits the vacuum system through a 0.025 mm Havar window, and loses about 9 MeV through electronic scattering with the beam line elements before reaching the isocentre, 7.00 m downstream, when all the standard beam modification elements are in place, and the energy degraders and modulator propellers are not included. The patient is positioned so that the location of the lesion coincides with the isocentre position

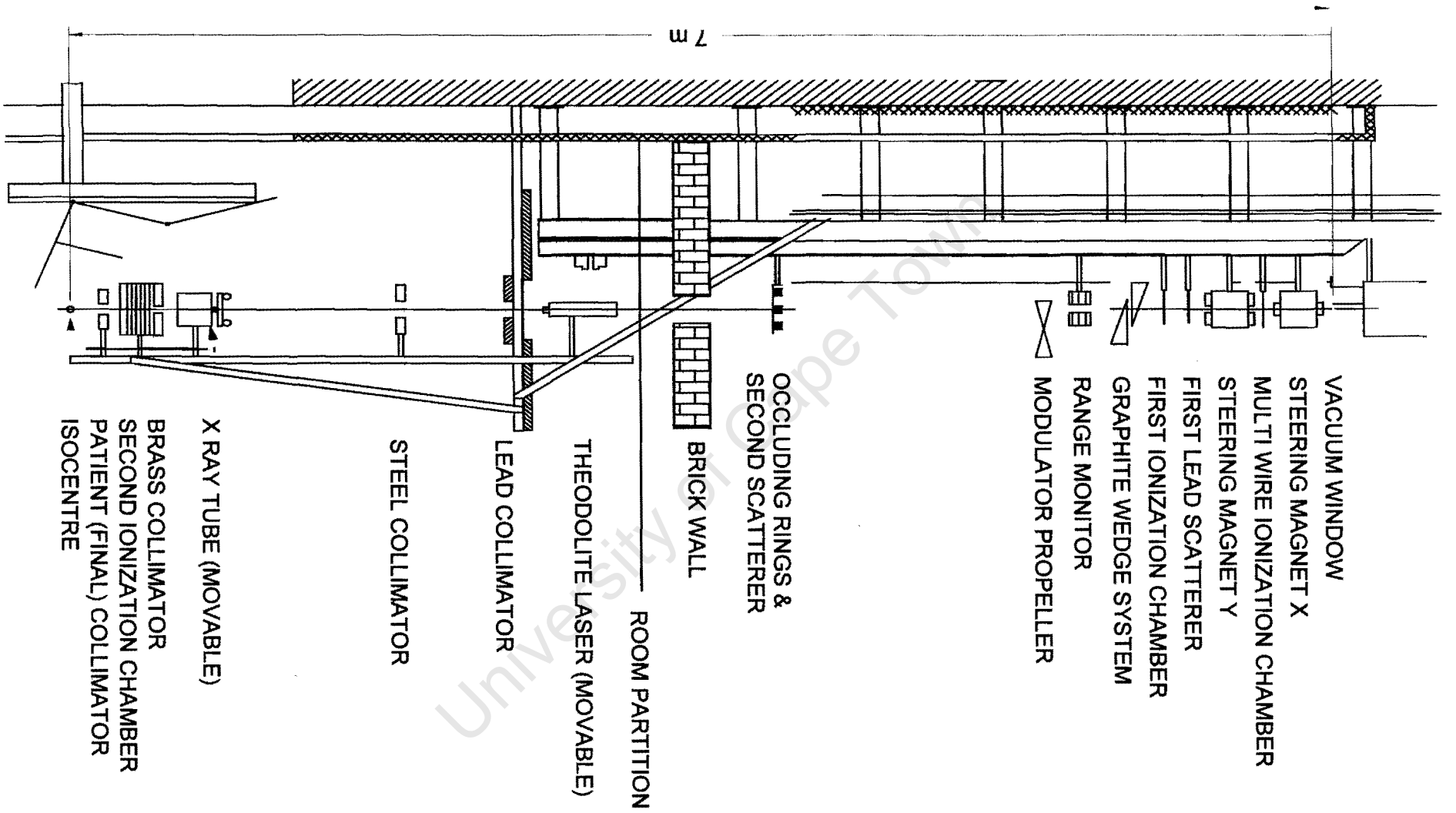

Figure 2.1: *A schematic layout of the NAC proton therapy beam line. The beam exits the vacuum system through a Havar vacuum window and travels through the beam modification elements to deliver the desired dose distribution in the target volume, which is located at the isocentre. See table 2.1 and text for details.*

during therapy. Front and back-pointer lasers used to indicate the beam axis and lateral lasers are used to indicate the position of the isocentre. The locations of all the beam line elements are measured relative to the Havar (exit) window, (see table 2.1). The beam delivery system is designed to deliver a beam with an approximately uniform intensity over an area with a diameter of 100 mm in a plane perpendicular to the beam axis at the isocentre [NA94, Jo94, Jo95b, Sc95]. Double scatterers and an occluding ring system [Ko77] is used to spread the proton beam at the NAC. A graphite wedge system [NA98] is now used, instead of acrylic degraders, to reduce the energy of the beam and consequently the range of the protons in tissue to conform to the treatment requirements. Modulator propellers [Ko75] made up of different thicknesses of acrylic [NA94, Jo94, Jo95b, Sc95] are rotated in the beam to superimpose a series of Bragg curves of different ranges in order to produce a dose distribution (in a patient) with a spread out Bragg peak that covers the length of the lesion. Multiwire ionization chambers are used to monitor the position of the beam and parallel plate ionization chambers monitor the dose delivered at the treatment isocentre. Steering magnets are used in a feedback system with signals from the ionization chambers (beam monitors) to align the beam and to ensure that the beam is symmetric at the isocentre [NA94, Jo94, Jo95b, Sc95]. Collimators are used to reduce the lateral penumbra of the beam and shape the beam to conform to the shape of the lesion. These beam modification elements are used in different combinations to tailor the proton therapy beam to specific therapy requirements.

2.1 Beam Flatteners

The small (~3 mm radius) beam exiting the vacuum pipe is broadened through multiple scattering effects [Be53a, Be53b, Bi82, Ca73, Go93, Go99a, Bu86, Ma69], by a beam flattening system comprised of lead scatterers and brass occluding rings [Ko77] and then collimated to a radius of 100 mm at the isocentre [NA94, Jo94, Jo95b, Sc95]. The action of the beam flattener is based on Molière's theory of multiple Coulomb scattering [Be53a, Be53b, Go93] of charged particle beams in matter. According to Molière's theory, the angular distribution of charged particles, which have experienced multiple Coulomb scattering can be approximated by an

Table 2.1: *The NAC proton therapy beam line components. The beam modification components listed in this table are shown in figure 2.1 and their functions are explained in the text.*

Beam line Component	**Distance from Havar (exit) Window (m)**	**Material**	**Thickness (mm)**
Vaccum Window	0.000	Havar	0.025
X-Steering Magnet	0.090	Iron	200.0 (see text)
MWIC	0.340	see text	see text
Y-Steering Magnet	0.470	Iron	200.0 (see text)
Trimmer Plates	0.710	Plastic	see text
First Lead Scatterer	0.745	Lead	1.00
Ionization Chamber 1	0.770	Aluminized Mylar	0.01
Second Lead Scatterer	0.785	Lead	1.00
Graphite Degrader	0.925	Carbon	see text
Modulator Propeller	1.155	Acrylic	see text
Range Monitor	2.920	Brass	see text
Occluding Rings	3.025	Brass	50.00
Brass Scatterer	3.075	Brass	1.00
Concrete Collimator	3.445	Concrete	195.00
Lead Collimator	4.525	Lead	49.00
Iron Collimator	5.135	Iron	52.00
Brass Collimator	6.444	Brass	50.00
Ionization Chamber 2	6.510	see text	see text
Patient Collimator	6.635	see text	see text
Isocentre	7.000		

exponential function [Be53b, Ca73]

$$P(\theta) = \frac{1}{\pi \langle\theta^2\rangle} \exp\left(-\frac{\theta^2}{\langle\theta^2\rangle}\right) \tag{2.1}$$

where θ is the scattering angle and $\langle\theta^2\rangle$ is the mean square angle of deflection. The amount of scattering material in the beam required to produce a desired scattering angle θ is given by Highland's formula [Hi75, Hi79, Go99a]

$$\theta = \frac{14.1}{pv}\sqrt{\frac{t}{L_R}} \times \left[1 + \frac{1}{9}\log\left(\frac{t}{L_R}\right)\right] \tag{2.2}$$

where t is the scatterer thickness, L_R is the radiation length of the scatterer, p is the momentum of the charged particle, and v is the velocity of the particle. From equation 2.1, the angular distribution of charged particles scattered by a material of finite thickness has a Gaussian shape for small scattering angles. Carlson and Rosander [Ca73] used Molière's theory in their analysis of multiple scattering of light ion beams at various depths in a medium. Gottschalk *et al.* [Go93] also used Molière's theory in the analysis of their measurements, to calculate scattering angles of protons on a wide range of materials. Their results showed the angular distribution to be Gaussian at small scattering angles [Ca73, Go93].

The energy loss of a beam of charged particles traversing an absorbing material consists of a large number of inelastic collisions between the incident ion and the electrons of the absorbing material. The collisions are discrete and random in nature. Thus, a monoenergetic beam of charged particles will have a distribution of energies after travelling through an absorbing material [Sk67, Bi70, Wi76]. This effect is referred to as the Landau-Symon effect. The broadening of the energy distribution of the beam due to the statistical process can be described by an energy dependent probability function [Ko68, Ma68a, Ts68a, Ts68b, Go75, Wi76] known as energy loss straggling. This energy distribution function depends on the thickness of the absorber, x [Ts68a, Ts68b, Wi76]. The probability of energy loss in a single collision with an electron is proportional to ε^{-2} (where ε is the energy transferred to an electron in a single collision); consequently collisions resulting in a large energy transfer to an electron are relatively infrequent in comparison with collisions resulting in small energy transfer [Sk67]. When the number of collisions with mean energy loss (ζ) is much greater than ε_{max} (the maximum energy which can be transferred to an electron in a single collision), that is $\zeta/\varepsilon_{max} \geq 10.0$, the

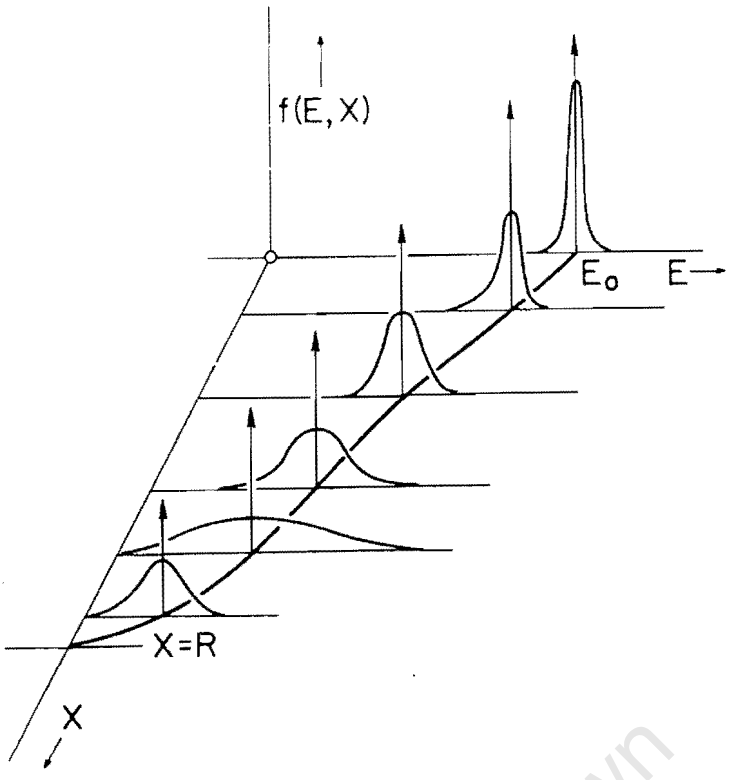

Figure 2.2: *Energy distribution of a monoenergetic beam of charged particles at various penetration depths in an absorbing material. E is the particle energy and X is the distance along the track. Reproduced from [Wi76].*

the distribution function is Gaussian in shape [Sk67, Ko68, Go75, Wi76]. This occurs when the absorber is thick and/or the energy of the incident charged particles is low, resulting in larger values of ζ [Sk67]. In the opposite extreme where the absorber is very thin or/and the energy is very high, the number of collisions is very small and the mean energy loss is much less than ε_{max} ($\zeta/\varepsilon_{max} \leq 0.01$) [Sk67]. The number of collisions may be so small that the random statistical variations in this numbers are relatively large, resulting in significant fluctuations in the energy lost in this mode. The distribution function in this case is asymmetric with a high energy tail corresponding to higher energy losses [Sk67, Ko68, Ma68a]. The intermediate region is explained by the Vavilov theory [Ko68, Ma68a]. Figure 2.2 shows the variation of the distribution function as a function of incident particle energy and absorber thickness. The energy spread of proton therapy beams at the NAC is dominated by the contribution from the beam flattening system (double scatterer and occluding ring system) and was determined from the energy spectrum measurement using the spectrometer described in section 1.2 to be about 3 MeV (see figure 2.4).

The first scatterer and occluding rings of the NAC proton therapy beam line are located 0.745 m and 3.02 m downstream of the Havar vacuum window, respectively,

to produce, after collimation, a 100 mm diameter circular beam with a uniform dose distribution at the isocentre. The first scatterer is a 1 mm thick lead plate, and the occluding rings are made up of 50 mm thick concentric brass rings (see figure 2.3 (a)). The central stopper of the occluding rings has a radius of 13.4 mm, while the inner and outer radii of the concentric rings are 24.2 and 36.1 mm respectively [NA94, Jo94, Sc95]. The occluding rings are mounted on a 1.0 mm thick brass plate (second scatterer). Lead and brass are suitable for beam flattening because high Z materials give the most scatter and least energy loss [Go99a]. Figure 2.3 (b) shows a schematic illustration of the proton beam traversing the components of the flattener, and part (c) of the figure 2.3 illustrates the dose profiles of the proton beam after each component of the flattener. The double scatterer and occluding ring system operates in the following way [Ko77]. The first scatterer spreads the beam into a Gaussian shaped distribution as shown in part (i) of figure 2.3 (c). The central stopper of the occluding rings blocks the central portion of the beam as shown in part (ii) of figure 2.3 (c), part of the portion of the beam passing around the central stopper is scattered by the outer ring and the other part passes through the gap unchanged. The effect of the outer ring is to scatter protons on the periphery of the beam into the beam thereby filling up the gap produced by the central stopper. The second scatterer further scatters the beam to produce a uniform distribution at the isocentre as shown in part (iii) of figure 2.3 (c). Figure 2.4 shows the proton energy spectrum measured at the isocentre by Brooks *et al.* [Br95, Br97b], with the coincidence detection system developed at the NAC and discussed in chapter 1, with the flattener (double scatterer plus occluding rings system) in (triangles) and out (histogram) of the beam. The spectrum was measured for a proton beam of energy 200 MeV at the exit (Havar) window (see figure 2.1), without energy degraders in the beam and using the final (patient) brass collimator of 100 mm diameter. The flattener reduces (degrades) the energy of the beam by about 6 MeV. The proton beam incident at the isocentre has the most probable energy (E_{iso}) of 190.8 MeV when the flattener and other standard beam modification elements are in place, and the graphite wedges and modulator propeller are not in the beam. The energy spectrum measured with the flattener in place (triangles in figure 2.4) has a peak with a centroid at 190.8 MeV. E_{iso} is therefore 190.8 MeV when all the standard beam modification elements are in place and can be adjusted to the required value by inserting the graphite wedges in the beam. The width (FWHM) of the peak in the spectrum measured with the flattener out of the beam (histograms in figure 2.4

is about 5 MeV [Br97b]. This FWHM is caused by the energy spread of the beam from the cyclotron, the broadening of the energy of the beam due to scattering in the air and the remaining beam modification elements, and the detection system (see section 4.3.3).

2.2 Energy Degraders

Three types of energy degraders are now used at the NAC; plastic trimmer plates and graphite wedges for energy degradation and modulator propellers for widening of the Bragg peak. Range trimmers made of plastic, 0.6 g cm^{-2} thick, are used to correct for the slight changes in the proton energy from the cyclotron from day to day, and are manually inserted in the beam line to trim the range of the beam to 240.0 $\pm$ 00.3 mm in water [NA94, Jo94, Jo95b, Sc95]. This range corresponds to proton energy of 190.8 MeV at the isocentre.

The range of the protons is adjusted to conform to the position of the lesion by inserting energy degraders, which are slabs of material introduced in the beam path before the beam reaches the isocentre [Ko72, NA94, Jo94, Jo95b, Sc95]. Figure 2.5 shows the proton energy spectrum when the energy of the beam was degraded by acrylic plates of various thickness [Br97b], to illustrate the effect of energy degraders on the energy spectrum. The FWHM of the peaks in the measured energy spectra increases with the increase in the degrader thickness. A graphite wedge system is now used at the NAC, instead of acrylic degraders, to modify the proton range. The present system consists of two identical parallel-opposed graphite wedges, each 400 mm long, with a wedge angle of 11.9°. A computer-controlled stepper motor drives the wedges, and their positions are verified by a V-binary position encoder as they move in opposite directions across the beam axis. The design of the wedges ensures that the total thickness of carbon at any setting is uniform across the beam [NA98]. The graphite wedges are calibrated to proton range in water by measuring the range of the proton beam in a water phantom (see figures 1.1 and 1.2) as a function of wedge (graphite) thickness. The range of the proton beam in water is determined by scanning along the beam axis with an air-filled thimble ionization chamber with an ionization volume of 7.3 mm^3 [Sc95] in a water

(a)

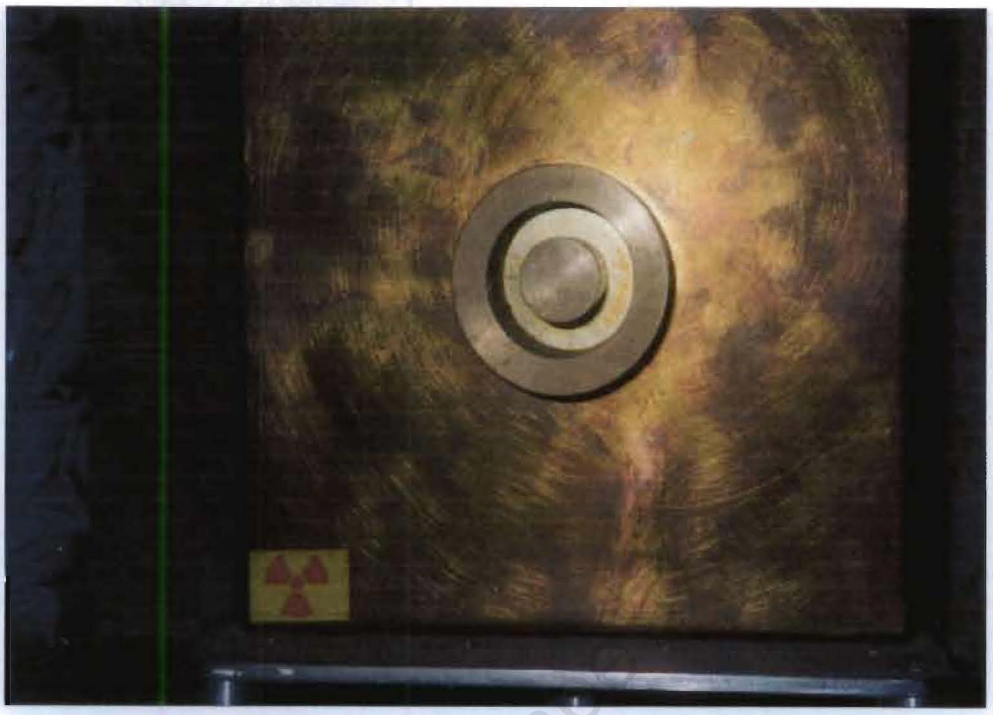

(b)

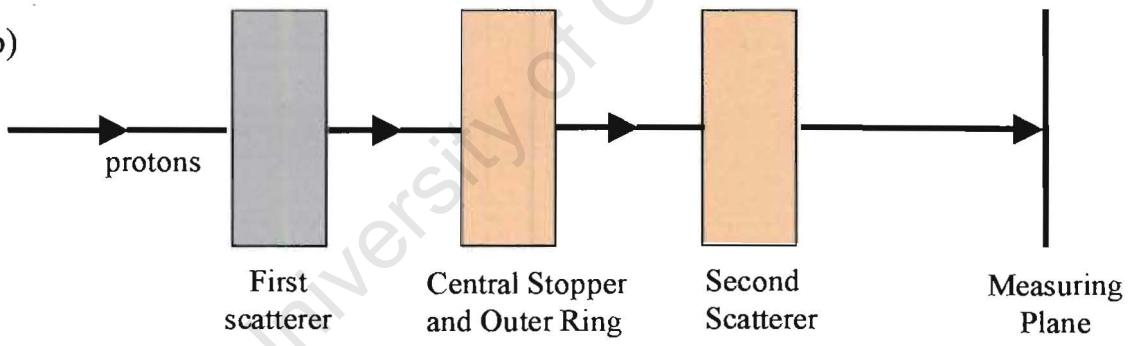

(c)

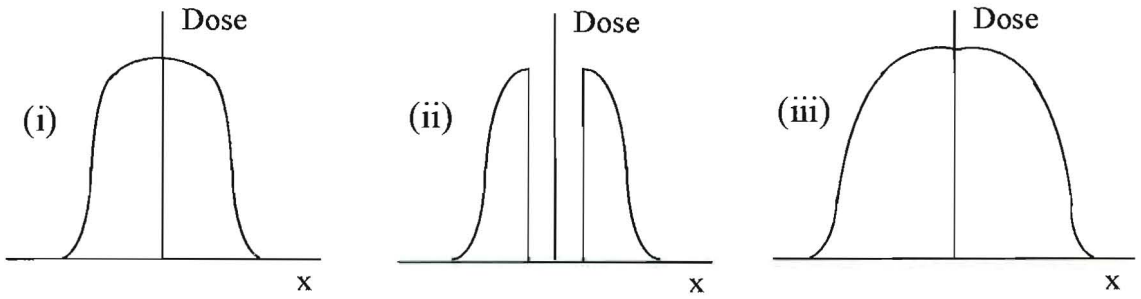

Figure 2.3: *(a) A picture of the occluding rings and (b) a schematic illustration of the path of the proton beam through the components of the flattener. (c) Schematic illustration of the dose profiles of the proton beam traversing the components of the flattener as shown in (b) (i) after the first scatterer, (ii) after the central beam stopper and outer ring of the occluding rings, and (iii) after the second brass scatterer of the occluding rings.*

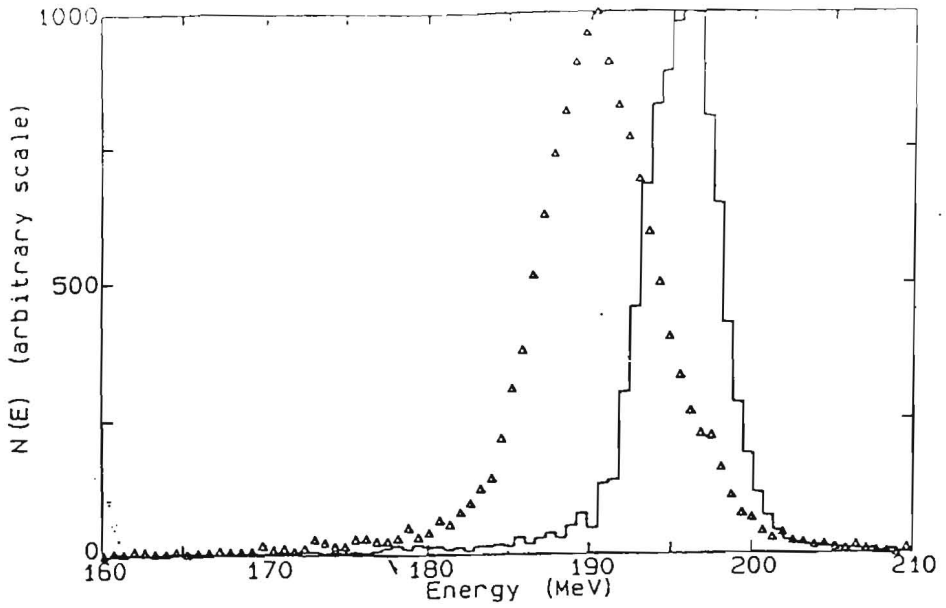

Figure 2.4: *Proton energy spectra measured at the NAC with the coincidence technique for an incident proton beam with E_{iso} of 190.8 MeV, with the flattener (double scatter plus occluding rings) in (triangles) and out (histogram) of the beam, using a 100 mm diameter final brass collimator. The flattener degrades the energy of the beam and increases the width (FWHM) of the peak at the highest energy [Br95].*

phantom to locate the position of the Bragg peak. This ionization chamber has an equivalent accuracy to the Markus type parallel plate ionization chamber for range measurements and better than the Markus chamber for beam profile measurements due to the geometry of the Markus chamber [Sc95]. The range-energy conversion is calculated using available range and stopping power data [IC49]. Since the range measurements can be determined accurately to less than 1 mm, the uncertainty in determining E_{iso} is therefore dominated by the uncertainties in the stopping power data which ranges from 0.5 to 2 percent [IC49]. The uncertainties in values for E_{iso} were taken to be 1 percent in this work.

A uniform dose distribution over the length of the lesion can be achieved by spreading out the Bragg peak [Wi46], using modulator propellers [Ko75] (see figure 2.6). A modulator propeller is made up of a series of acrylic slabs, of varying thicknesses, stacked up in a pyramid shape, on opposite sides of a common shaft (see figure 2.7). The propeller is rotated in the beam, progressively placing different thicknesses of acrylic slab (blade) in the beam. Each slab degrades the energy of the beam, in proportion to its thickness, resulting in a series of Bragg peaks, at different depths in the material [Ko72]. The Bragg peaks are superimposed to produce a broad dose distribution referred to as the spread out Bragg peak (SOBP)

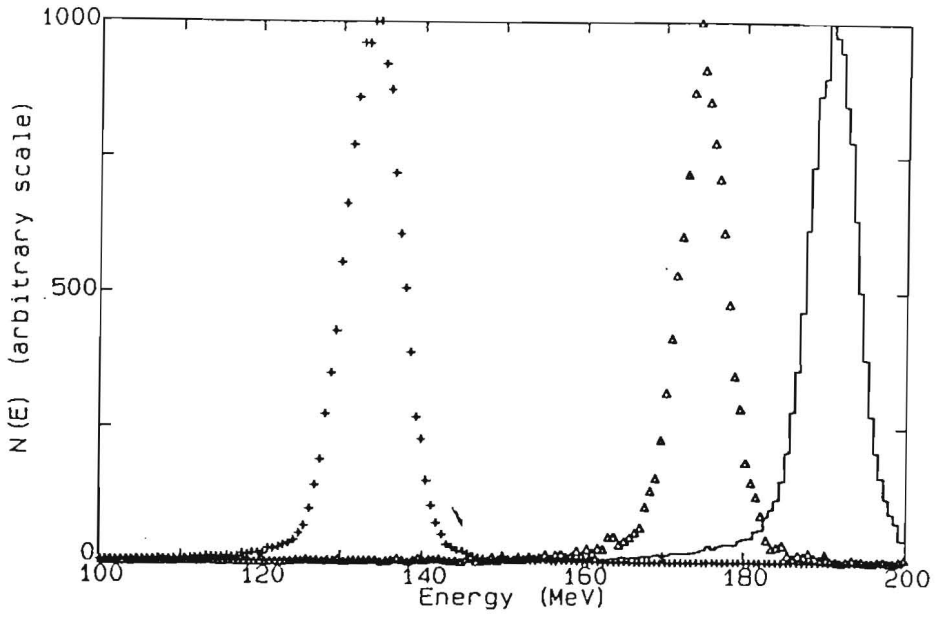

Figure 2.5: *Proton energy spectra measured with no degrader in the beam (histogram) and acrylic degraders of thickness 31 mm (triangle) and 93 mm (crosses) in the beam. All the spectra were measured with a flattener in the beam using a 10 mm diameter final Brass collimator [Br97].*

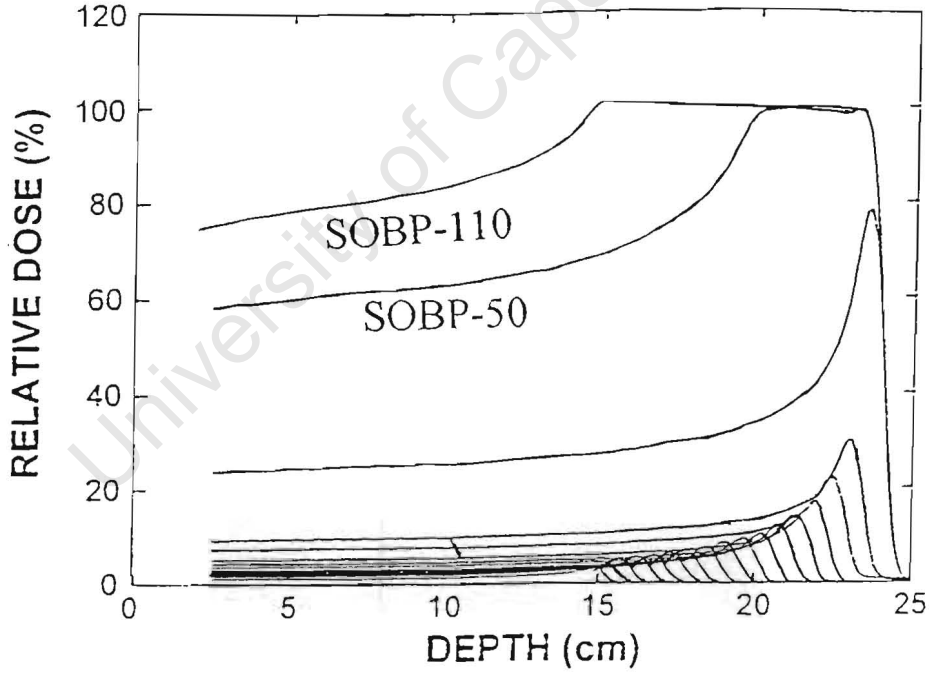

Figure 2.6: *Dose curves measured in water for a proton beam with E_{iso} of 190.8 MeV with modulator propellers in the beam. The spread out Bragg peaks are formed by the superposition of individual dose curves of the 50 (SOBP-50) and 110 mm (SOBP-110) modulator propellers [NA94, Jo94, Jo95b, SC95]. See text for details.*

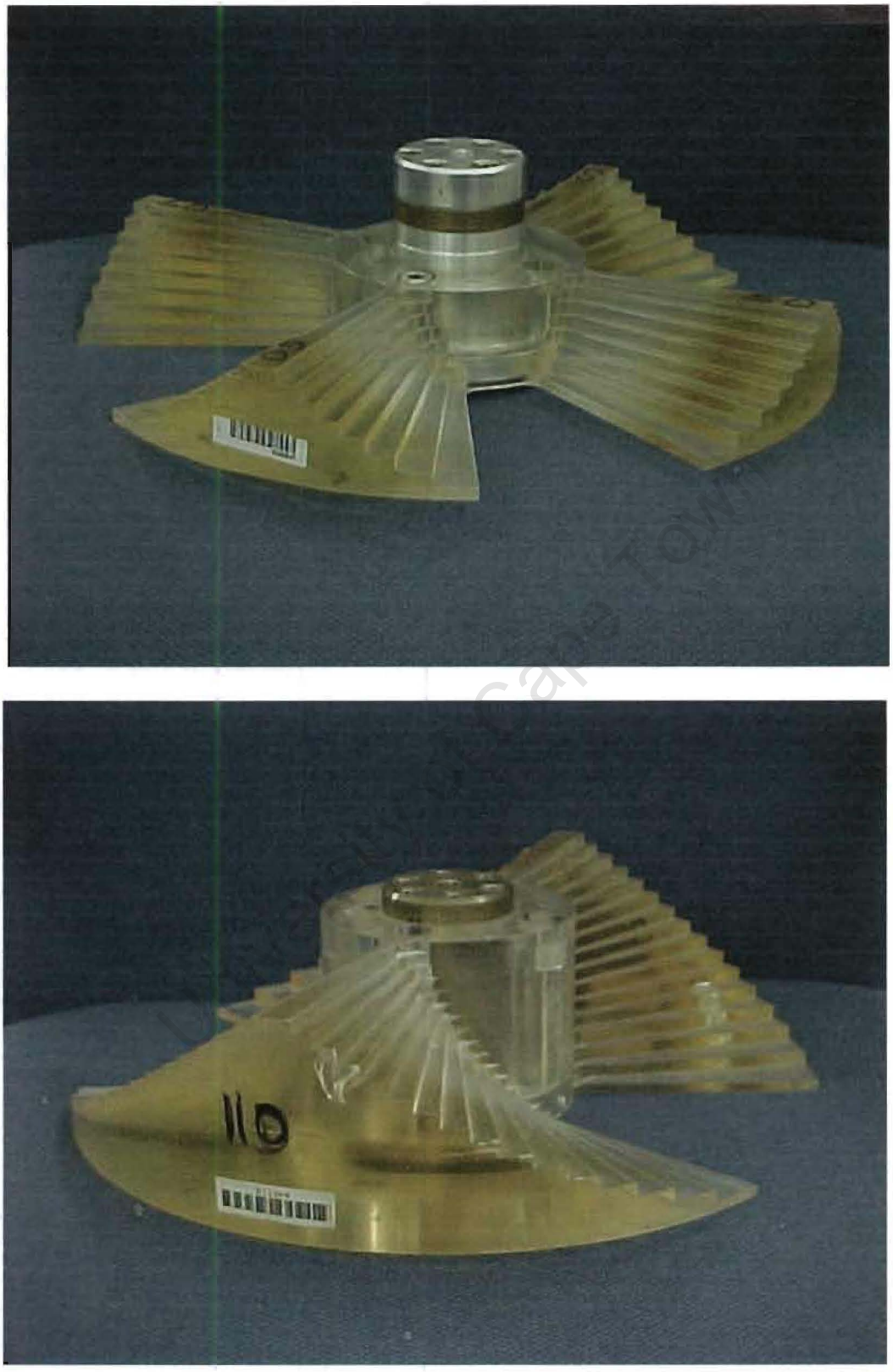

Figure 2.7: *Pictures of modulator propellers used to spread out the Bragg peak of the proton beam*

as shown in figure 2.6. Propellers are usually made up of relatively low-Z material to minimize multiple scattering [Pe94]. Table 2.2 shows the thickness of the slabs constituting the 50 mm and 110 mm modulator propellers used at the NAC with the corresponding weighting factors. The individual dose curves corresponding to the dose of the energy-degraded beam due to the different blades of the 50 and 110 mm propellers are shown in figure 2.6. The dose curves have been weighted to take into account the thickness of the blades and the time they spend in the beam. Also shown in the figure are dose curves formed by the superposition of the individual range-shifted curves produced by the 50 mm (SOBP-50) and 110 mm (SOBP-110) modulator propellers. Although proton beam modulation has the advantage of spreading out the Bragg peak to cover the length of the lesion, it also raises the dose delivered to the skin and the tissues between the skin and the lesion lying on the path of the proton beam [Ko75, Pe90] (see figure 2.6). The ratios of entrance dose to that at the position of the middle of the SOBP is 0.33:1, 0.6:1 and 0.77:1 for no modulator propeller in the beam, 50 mm and 110 mm modulator propellers in the beam, respectively. Figure 2.8 show energy spectra measured with a 110 mm modulator propeller and without a modulator propeller in the beam [Br95]. The effect of the modulator is to broaden the spectrum by increasing the number of protons in the energy range $E_0 - E_m$, where E_0 is the energy of the beam without the modulator in the beam and E_m is the energy of the beam when the beam is degraded by the full thickness of the modulator propeller. Due to the proportionally higher weighting factors in the open section and the thinnest blades of the propeller blades, as shown in table 2.2 and figure 2.6, the modulated proton beam spectrum has a skewed shape with the peak at E_0.

2.3 Beam Monitors

The characteristics of the beam must be monitored at all times to ensure that optimum treatment conditions are maintained throughout the treatment. Ionization chambers and range monitors are used to monitor the range of the beam and the dose delivered to the patient at the isocentre. The double scattering system used at the NAC is extremely sensitive to the position of the proton beam, hence the beam is automatically controlled by two computerized feedback systems [Jo94, Jo95b, Sc95]. The feedback systems act on two sets of XY-steering magnets

Table 2.2: The acrylic slab thickness and the corresponding weighting factors for the 50 mm (SOBP–50) and 110 mm (SOBP–110) modulator propellers See text for details.

Component	Thickness (mm)	Weighting factor for SOBP–50	Weighting factor for SOBP–110
Open	-	0.363	0.278
Blade 1	5.0	0.138	0.100
Blade 2	10.0	0.108	0.0833
Blade 3	15.0	0.084	0.0617
Blade 4	20.0	0.075	0.0571
Blade 5	25.0	0.064	0.0494
Blade 6	30.0	0.059	0.0450
Blade 7	35.0	0.055	0.0411
Blade 8	40.0	0.054	0.0392
Blade 9	45.0	-	0.0366
Blade 10	50.0	-	0.0347
Blade 11	55.0	-	0.0322
Blade 12	60.0	-	0.0322
Blade 13	65.0	-	0.0303
Blade 14	70.0	-	0.0287
Blade 15	74.4	-	0.0252
Blade 16	78.8	-	0.0243

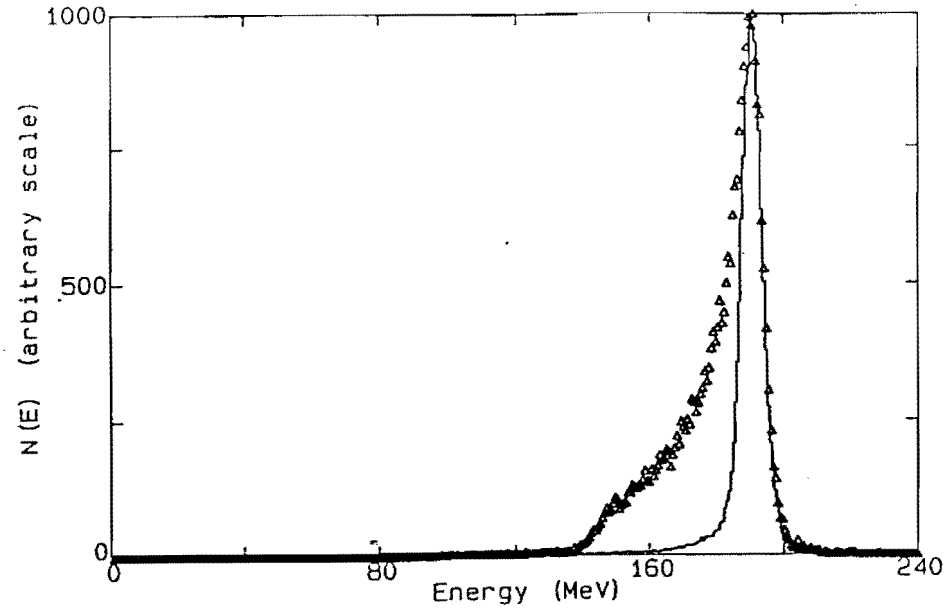

Figure 2.8: *Measured proton energy spectra for a proton beam with E_{iso} of 190.8 MeV with a flattener in the beam and a 50 mm diameter collimator without (histogram) and with (triangles) a 110 mm modulator propeller in the beam [Br95].*

shown in figure 2.1 [NA94, Jo94, Sc95]. In the first feedback system, multiwire ionization chambers (MWIC) are used to monitor the position of the beam and the steering magnets use the positional information of the beam from the MWICs to align the central axis of the beam. The MWICs monitor the position of the beam in a plane perpendicular to the beam axis. The MWICs are mounted in such a way that the central wires in both planes align with the beam axis. In the second feedback system a segmented (quadrant) transmission ionization chamber (Lawrence Berkeley Laboratory) monitors the symmetry of the beam. Positional information from this chamber is fed back into the steering magnet feedback control system.

A range monitor, shown in figure 2.9, was used to determine the energy of the incident protons by measuring the range of the proton beam in brass. The monitor is made up of 12 transmission parallel plate ionization chambers made from PC board material, sandwiched between brass plates [Sc95]. The ionization chambers and brass plates had 100 mm diameter aperture in the centre, which allowed the central portion of the beam to pass uninterrupted and utilized protons on the periphery of the beam for range measurements (see figures 2.9 and 2.10). The ionization chambers located after each brass plate measured the dose deposited by the beam at that point, the ionization currents in each of the 12 ionization

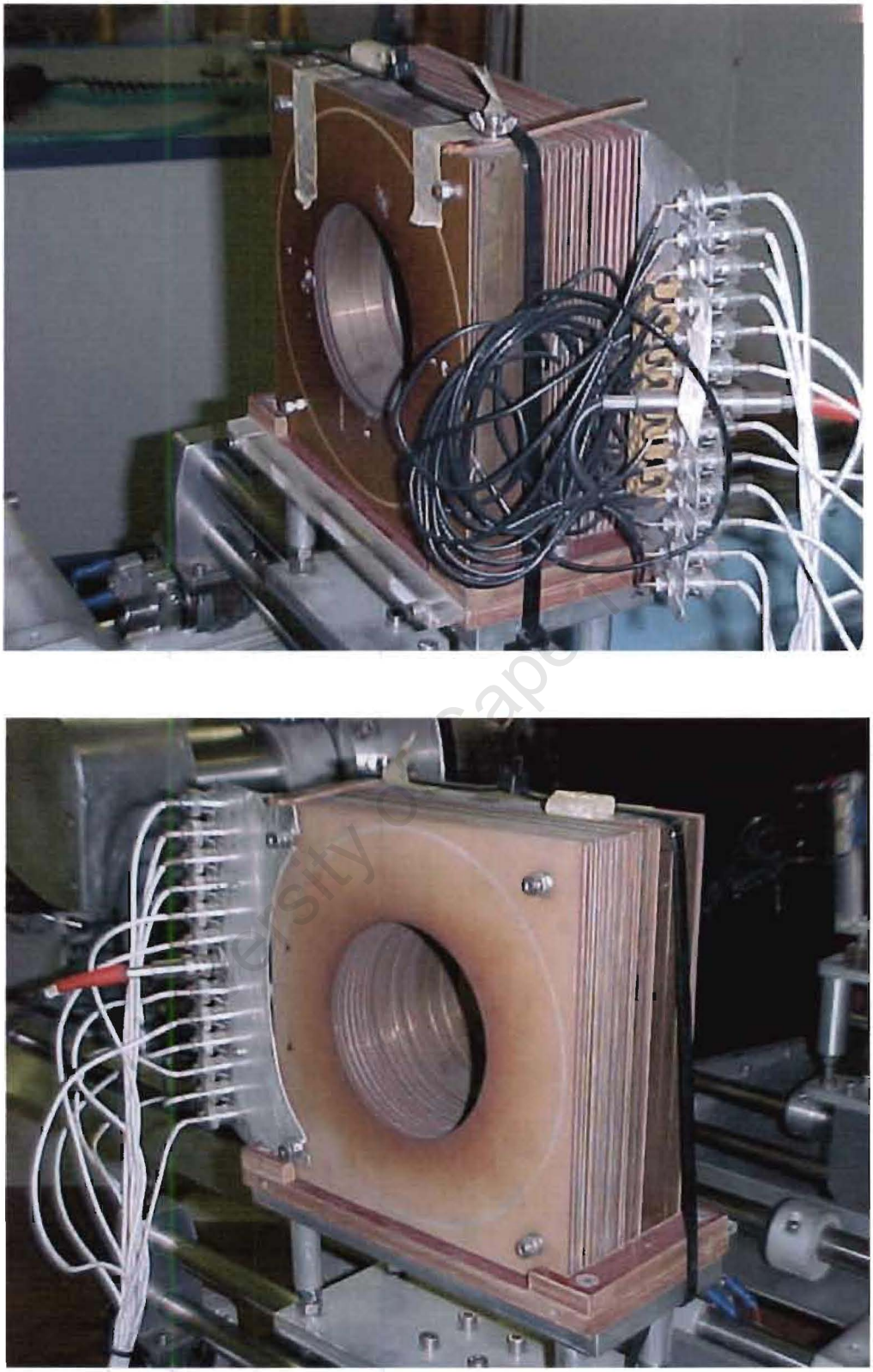

Figure 2.9: *Pictures of the range monitor that was used at the NAC to determine the energy of the beam in real time, by measuring the range of the protons in the brass plates.*

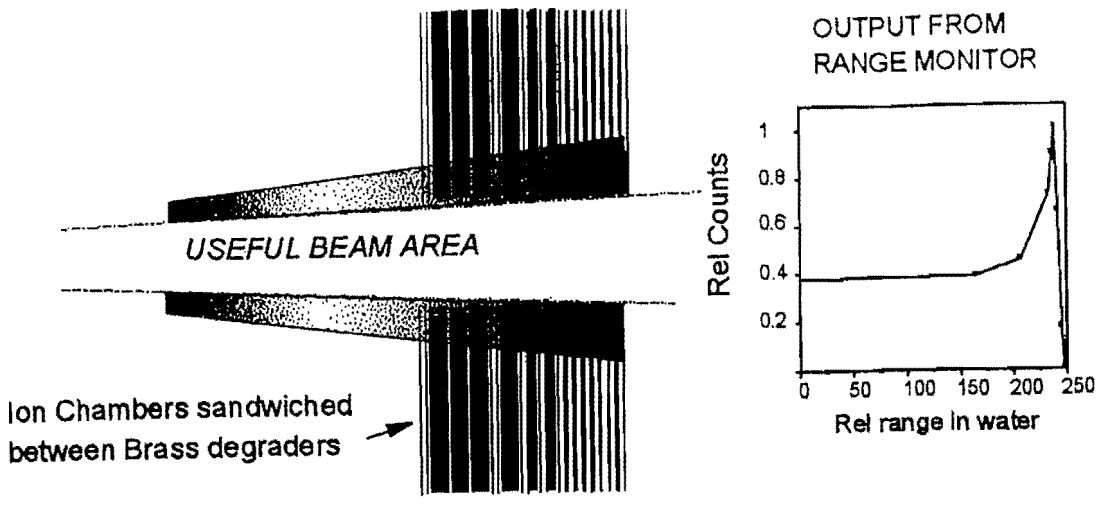

Figure 2.10: *A schematic illustration of the range monitor. The central part of the beam pass through the aperture in the monitor unaltered and the protons on the periphery of the beam travel through the brass plates and the parallel plate ionisation chambers behind the each brass plate measures the dose at that point. Reproduced from [Sc95].*

chambers characterized the depth dose curve in the monitor, when plotted as a function of the absorber (brass) thickness. The thicknesses of the brass plates were carefully selected to obtain more data points at the Bragg peak (see figure 2.10). The reading obtained with the monitor was calibrated against the range of the protons that pass uninterrupted through the aperture of the range monitor in water. The resolution of the range monitor from this calibration in water is about 0.4 mm [Jo01c].

A single transmission ionization chamber located immediately downstream of the first lead scatterer is used for experimental purposes and to provide the reference signal for dose distribution measurements [NA94, Sc95]. A dual transmission ionization chamber located immediately upstream of the patient collimator is used to monitor the dose delivered to the patient. In addition to the dual transmission ionization chambers, segmented ionization chambers located next to the dual transmission ionization chamber are also used to monitor beam symmetry as mentioned above [NA94].

2.4 Collimators

The proton beam experiences multiple Coulomb scattering as it traverses the air and various beam modification elements. Most of the scattering occurs in the flattener (double scatter plus occluding ring system) and energy degraders such as trimmer plates and graphite wedges when inserted in the beam. Collimators are used to stop the particles that are scattered out of the beam and the protons on the periphery of the beam, allowing only the protons in the central part of the beam to pass through unaltered. The area around the isocentre is shielded from the scattered protons and secondary particles by a concrete wall located 1.6 m upstream of the isocentre. The beam passes undisturbed through a square aperture, of sides 200 mm, in the 195 mm thick concrete wall. Three more layers of shielding material, consisting of 49.0 mm thick lead, 52.0 mm iron and 50.0 mm brass slabs, are placed between the concrete wall and the isocentre to optimise the shielding around the isocentre. Each slab has a circular aperture centred on the beam axis. The central part of the beam passes through the apertures undisturbed and the particles (mainly protons) on the periphery of the beam stop in the shielding material. The final (patient) collimator situated just upstream of the patient, can be varied in size and shape to conform the field shape to the lesion shape. These shaped inserts, fit into the final collimator assembly, which can rotate around the beam axis in order to align non-circular collimators with the required treatment field. These inserts are made of brass and low-melting point alloy (cerrobend) [NA94, Sc95]. The distance between the patient collimator and the isocentre is kept small (31.5 mm) to reduce multiple scattering in the air between the collimator and the patient and consequently reduce the lateral beam penumbra [Ur86, Lu01]. Figure 2.11 shows the proton energy spectra measured at the isocentre, for a proton beam of 190.8 MeV at the isocentre with the flattener (double scatterer plus occluding rings) in place and circular collimators with diameters of 10, 50 and 100 mm [Br95]. The effect of the collimator diameter on the FWHM of the peak in the measured energy spectra is not clearly established. The collimator diameter may affect the low-energy tail of the spectrum (see section 4.1.3).

Results shown in this chapter from studies of proton energy spectra indicate that a

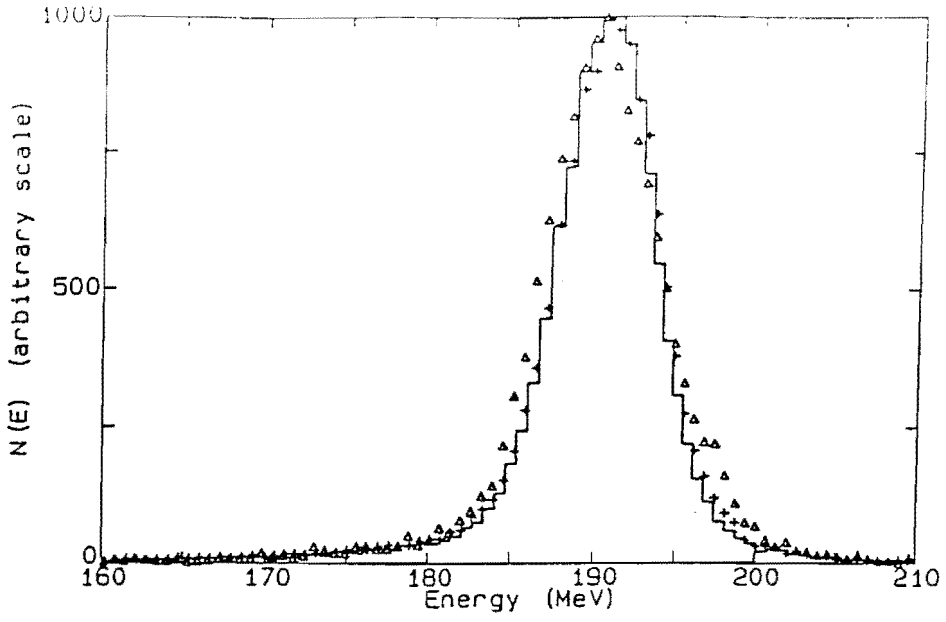

Figure 2.11: *Proton energy spectrum measured with the flattener in the beam using collimator diameters of 10 mm (histogram), 50 mm (triangles) or 100 mm (crosses) [Br95].*

spectrometer such as the one shown in figure 1.6 can provide valuable information about the effects of the beam modification elements. The results from this work are expected to enhance the understanding of the performance of beam modification elements in tailoring the proton beam for therapeutic purposes at the NAC.

Chapter 3

Experiments and data reduction

The aim of the project was to measure proton spectra at and near the isocentre for a representative set of proton therapy beams and to compare the measured spectra with Monte Carlo simulated spectra. Measurements were made using the modified proton pair spectrometer, which is described below followed by description of the experiments and data reduction procedures used to derive the spectra. Experimental results and Monte Carlo simulations are presented in chapters 4 and 5 respectively. The experience gained in the development of the spectrometer used for the previous measurements [Br97b], with the spectrometer shown in figure 1.7, was invaluable for the measurements made in this work and provided the basis for the modified spectrometer. Prior to this run series a series of three one weekend long runs, spread over a period of three years, were made where measurements were made with detector telescopes consisting of (50 mm diameter $\times$ 125 mm thick) NaI(Tl) scintillators (E detectors) and surface barrier detectors (ΔE detectors) of different thickness (500, 1000 and 1500 μm) to optimise the proton pair spectrometer. The experiments conducted for this project were completed over a period of two weekends. The first weekend was dedicated to set up and test the spectrometer. The spectrometer was therefore partially dismantled after the first weekend and had to be reassembled again and tested in the second weekend. Spectra were measured during the second weekend over a single continuous period of 60 hours. The beam time was divided to make measurements for a suitable range of combinations of beam modification elements and to have runs that were long enough to gather sufficient statistics for spectral analysis. Table 3.1 shows a summary of measurements completed during the second weekend. The spectra studied can be classified as follows. Run numbers for the

Table 3.1: *Summary of experimental measurements completed in this work to investigate spectral variations of the proton therapy beams at the NAC. The coincidence runs were approximately 1.5 hours long per run, with the exception of the runs 376 and 378, which were 0.5 and 1 hour long, respectively. The singles runs (run 367 and 369) were approximately 4 minutes long per run.*

Run number	E_{iso} (MeV)	Run category	Objective
365	190.8	Standard proton therapy beam	Measurements to investigate gain drifts
380	190.8		
403	190.8		
366	91.9	Energy degrading material in the beam	Measurements to investigate the effects of beam modification elements
373	174.1		
399	134.6		
374	59.3		
384	190.8	Modulator propeller in the beam	
385	190.8		
386	91.9	Modulator propeller and graphite energy degrader in the beam	
387	190.8	Diameter of final (patient) collimator varied	
388	190.8		
389	190.8		
390	190.8	Upstream (close to final collimator)	Measurements at positions away from the treatment isocentre
391	190.8	Upstream and off the beam's central axis	
392	190.8		
393	190.8		
394	190.8		
395	190.8	Off the beam's central axis, at the treatment isocentre	
396	190.8		
397	190.8		
376	190.8	No radiator	Measurements to investigate background and instrumental effects
378	190.8	Graphite radiator	
398	--	Blocked beam	
400	91.9	Thin radiator, wedges in	
401	190.8	Size of polyethylene radiator varied	
402	190.8		
404	190.8		

corresponding measurements are given in brackets.

1. the standard beam (365), which is the proton beam used for calibration purposes and quality control measurements at the NAC. It was a proton beam with E_{iso} of 190.8 MeV with standard beam modification elements (BME) and a 40 mm diameter final (patient) collimator in place and no energy degraders (wedges) and modulator propellers in the beam. The energy spectrum of this beam was measured at different times during the run series to monitor the stability of the detection system (365, 380 and 403).

2. spectra of beams with standard BME but with different thicknesses of degrader (graphite wedge) in the beam (366, 373, 399, and 374).

3. spectra of beams with standard BME and modulator propellers with energy degraders in the beam (386) and without energy degraders (384 and 385)

4. spectra at off-isocentre positions (390, 391, 392, 393, 394, 395, 396, and 397) that is measurements made with the radiator placed at positions away from the isocentre

5. spectra for different final collimators (387, 388 and 389) that is measurements of spectra of beams with standard BME and final collimators of different diameters

6. singles measurements (367 and 369) that is measurements of spectra of beams with standard BME made with coincidence condition between the two detector telescopes "switched" off.

7. miscellaneous other spectra to investigate backgrounds instrumental effects such as radiator size.

The singles measurements were used for setting of windows on event parameters to select p-p coincidence events. All other measurements were made in the coincidence mode to discriminate in favour of the coincident proton pairs. The measurements were made with a polyethylene radiator (3 mm thick $\times$ 10 mm diameter polyethylene disc) mounted at the isocentre. The choice of the radiator size was based on the preliminary measurements made in the development of the spectrometer shown in figure 1.7. Results of measurements made with the 3 mm thick polyethylene radiator had the optimum signal to background ratio

compared to those of measurements using thinner (1 and 2 mm) and thicker (4 to 10 mm) radiators. This radiator was changed for some runs in order to investigate background, contribution of the accidental coincidences from the carbon nuclei in the polyethylene and instrumental effects (runs 376, 378, 400, 401, 402 and 404). The energy of the protons at the isocentre (E_{iso}) for the proton beam with standard BME and no wedges in the beam was 190.8 MeV. E_{iso} was adjusted by inserting graphite wedges in the beam as discussed in section 2.2. E_{iso} was therefore 190.8 MeV for all the measurements made in this run series, except for runs 382, 398 and runs with energy degraders in the beam. In order to carry out measurements at positions displaced from the isocentre (runs 390 to 397), the entire detection system, that is the radiator and detector telescopes (see figure 3.1), was mounted on a table, which could be moved both along and at right angles to the beam axis without changing the geometry of the detection system.

The energy calibration of the detectors in the telescopes was performed by investigating the variation in the position of the peaks in the pulse height spectra of coincident proton pairs measured by the NE213 scintillator and surface barrier detector as a function of proton energy. There were no separate calibration runs for pulse height to energy calibrations, but the standard proton therapy beam run (run 365) and runs with standard BME and wedges in the beam (366, 373, 374 and 399) were used for the calibration of the pulse heights measured by the NE213 scintillators (D_{213}) and surface barrier detectors (C_{SBD}) to proton energy. These runs were utilized for this purpose because E_{iso} is accurately known for protons from these beam line configurations and the runs cover the energy range of interest (E_{th} to 190.8 MeV) for this study.

The energy spectrum of the so-called "virgin" beam, i.e. the beam without modification by the energy degraders and the beam-flattening device (double scatterer plus occluding rings system), was also measured in the present work (run 382). This measurement was meant to be used to determine the overall resolution of the detection system. However, this run was unfortunately subject to technical difficulties and the results were deemed not to be reliable for use.

3.1 The proton pair spectrometer

Studies of the energy spectra of proton therapy beams were made at the NAC using the proton pair spectrometer based on a design used in previous studies for measuring the proton energy spectra of the NAC proton therapy beams (see figure 1.6) [Br97b]. The following changes were, however, made to the present system;

i. the geometry of the detection system was modified to eliminate the need for correcting for the contribution of the energy dependent geometrical efficiency caused by the relativistic effects (see sections 1.2 and 1.3), on the calculation of the detection efficiency of the system,

ii. the NaI(Tl) scintillators were replaced with NE213 liquid scintillators as E detectors to enhance the efficiency of particle identification and selection in the scintillators,

iii. the NE102 plastic scintillators were replaced with surface barrier detectors as ΔE detectors to improve the efficiency of particle identification and selection in the detector telescopes,

iv. active collimators (NE102 scintillators with apertures) were included in the telescopes to define the detection solid angle in telescope A.

The proton pair spectrometer used in this project consists of a pair of ΔE-E detector telescopes arranged as shown in figure 3.1, to detect the coincident proton pairs. Each of the two detector telescopes in figure 3.1 consisted of a surface barrier detector (20 mm diameter $\times$ 1000 μm thick) as the ΔE detector, followed by an NE213 liquid scintillator (45 mm diameter $\times$ 105 mm long), as the E detector (see figure 3.2). The NE213 detectors were designed and constructed at the University of Cape Town. Each NE213 liquid scintillator was enclosed in a cylindrical aluminium cell with a thin (0.01 mm) aluminium window at the front face. A glass window on the back face was optically coupled to a photomultiplier tube (RCA8850) using a diverging perspex light guide. In the original design it was intended that fibre optics, to accommodate LED pulses (for gain stabilization), would be attached to these light pipes. Unfortunately it proved impossible to complete this component of the system in time for the experimental runs.

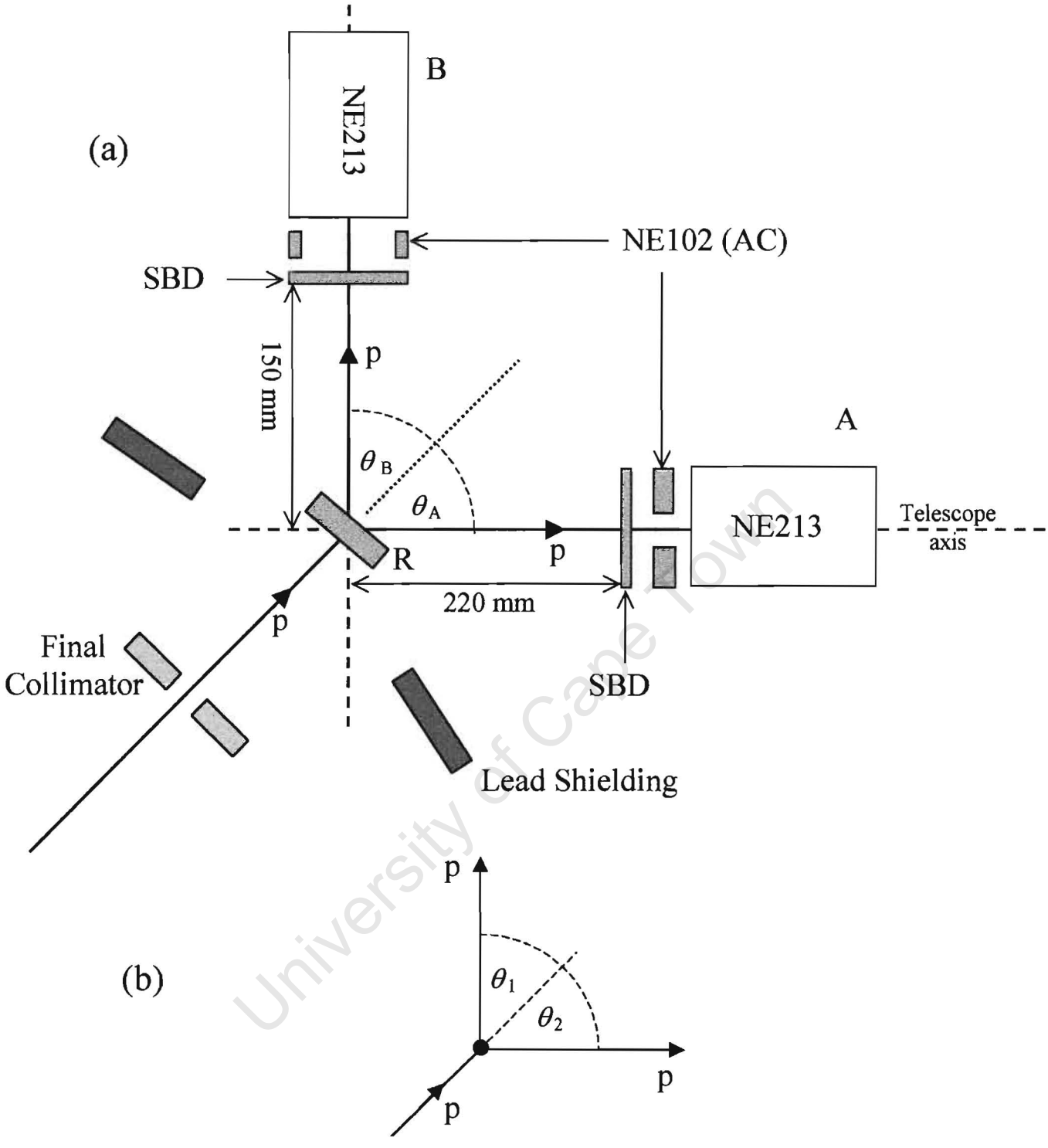

Figure 3.1: *(a) A schematic representation of the proton pair spectrometer used for measurements of energy spectra of the NAC proton therapy beams. The radiator (R) was placed at the treatment isocentre to scatter incident protons in the beam. Detector telescopes, A and B, with axes at laboratory angles $\theta_A = \theta_B = 44.3°$ to the incident proton direction, detect the coincident proton pair. Lead blocks were used to shield the telescopes from background radiation from the beam line components. (b) Schematic diagram (as in figure 1.7) of p-p elastic scattering in the radiator. θ_1 and θ_2 are the laboratory angles between the incident proton and the scattered and recoil protons respectively.*

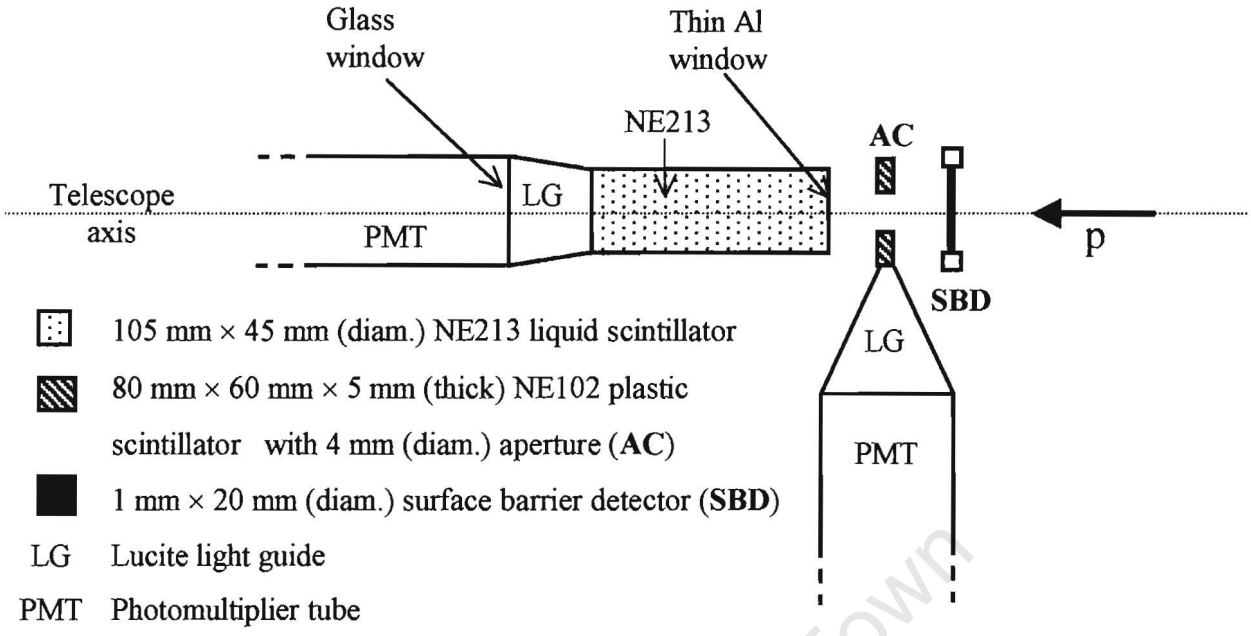

Figure 3.2: *A schematic representation of detector telescope A used in the experiments. Events corresponding to protons detected by the surface barrier detector (SBD) and the NE213 scintillator in coincidence were accepted only if they passed through the aperture of the NE102 scintillator that acts as an active collimator (AC).*

NE102 scintillators (80 mm × 60 mm × 5mm thick) with circular apertures of 4 mm and 10 mm diameters, were placed between the ΔE and E detectors, of telescopes A and B, respectively (see figures 3.1 and 3.2). The plastic scintillators were used as active collimators. The scintillator with the smaller aperture diameter (4 mm) defined the solid angle for the selection of p-p coincidence events. The detection thresholds of the active collimators were set by placing a ^{137}Cs gamma ray source close to the aperture of the collimator and observing the Compton distribution (edge at $\sim$ 0.5 MeV) in the resulting pulse height spectrum. The detector threshold was then set at a level corresponding to about 20% of the Compton edge, in other words a pulse height corresponding to about 100 keVee (100 keVee electron-equivalent). Since 200 MeV protons will produce pulse heights of about 100 keVee when traversing the full thickness (5 mm) of the active collimator this setting should be close to 100% effective in vetoing events due to protons that do not pass through the collimator aperture. Lead blocks were used to shield the detectors from protons scattered from beam modification elements upstream of the radiator.

3.1.1 Detector geometry

The two detector telescopes, A and B, were positioned with axes at laboratory angles $\theta_A = \theta_B = 44.3^o$ to the incident proton direction, to detect coincident proton pairs. The front faces of the surface barrier detectors in telescopes A (SBD A) and B (SBD B) were placed 220 mm and 150 mm from the treatment isocentre, respectively (see figure 3.1). The ranges of acceptance of the two telescopes were therefore $\theta_A = 44.3^o \pm 0.5^o$ and $\theta_B = 44.3^o \pm 1.9^o$. The range of angles between the coincident proton pairs ($\theta_1 + \theta_2$ in figure 3.1 (b)) was calculated using equation 1.1 and found to be $87.1^0 < \theta_1 + \theta_2 < 90^0$ for incident proton energies in the range 0 - 200 MeV (see figure 1.8). The acceptance angles of the active collimators (AC) in telescopes A and B for θ_1 and θ_2 in the non-relativistic ($E \leq 30$ MeV) limit and for 200 MeV incident protons are shown in figure 3.3 and listed in table 3.2.

Figure 3.3 shows a schematic illustration of the trajectories of coincident proton pairs that will be accepted by the active collimators of the spectrometer, for an "ideal" geometry, that is a "pencil" proton beam of negligible radius incident on

an infinitesimally small point radiator and no straggling or multiple scattering of protons in the radiator. The situations corresponding to non-relativistic limit ($E \leq 30$ MeV) and for $E = 200$ MeV are shown. In the non-relativistic limit, for every proton scattered at a laboratory angle of $\theta_1 = 44.8°$ the associated coincident proton will recoil at an angle of $\theta_2 = 45.2°$, that is $\theta_1 + \theta_2 \approx 90°$ (see figure 1.8). These protons will travel along trajectories (i) and (v) in figure 3.3, pass through the apertures of active collimators (AC) in telescopes A and B at points **a** and **e**, respectively, and be detected by the NE213 scintillators. Similarly, for every proton scattered at a laboratory angle of $\theta_1 = 43.8°$ the associated coincident proton will recoil an angle of $\theta_2 = 46.2°$. These protons will travel along trajectories (ii) and (vi) in figure 3.3, pass through the apertures of active collimators (AC) in telescopes A and B at points **b** and **f**, respectively, and be detected by the NE213 scintillators, as illustrated by the dotted lines in figure 3.3. Therefore in the non-relativistic limit and for an "ideal" proton beam incident on a point size radiator, for every proton passing through the aperture of the active collimator in telescope A (i.e. with θ_1 in the range 43.8° to 44.8°), the associated coincident proton will have θ_2 in the range 45.2° to 46.2° (from **e** to **f** in figure 3.3) and will therefore pass through the aperture of the active collimator of telescope B and be detected by the NE213 scintillator.

In the high-energy (relativistic) limit, we will consider 200 MeV protons incident at the radiator located at the isocentre. For every proton scattered at a laboratory angle of $\theta_1 = 44.8°$ the associated coincident proton will recoil at an angle of $\theta_2 = 42.4°$, that is $\theta_1 + \theta_2 \approx 87.2°$ (see figure 1.8). These protons will travel along trajectories (i) and (iii) in figure 3.3, pass through the apertures of active collimators in telescopes A and B at points **a** and **c**, respectively, and be detected by the NE213 scintillators. Similarly, for every proton scattered at a laboratory angle of $\theta_1 = 43.8°$ the associated coincident proton will recoil at an angle of $\theta_2 = 43.4°$. These protons will travel along trajectories (ii) and (iv) in figure 3.3, pass through the apertures of active collimators in telescopes A and B at points **b** and **d**, respectively, and be detected by the NE213 scintillators as illustrated by the dashed lines in figure 3.3. Therefore when an "ideal" 200 MeV proton beam undergo elastic scattering in a point size radiator, for every scattered proton with $E = 100$ MeV passing through the aperture of the active collimator in telescope A (i.e. with θ_1 in the range 43.8° to 44.8°), the associated coincident proton will have θ_2 in the range 42.4°

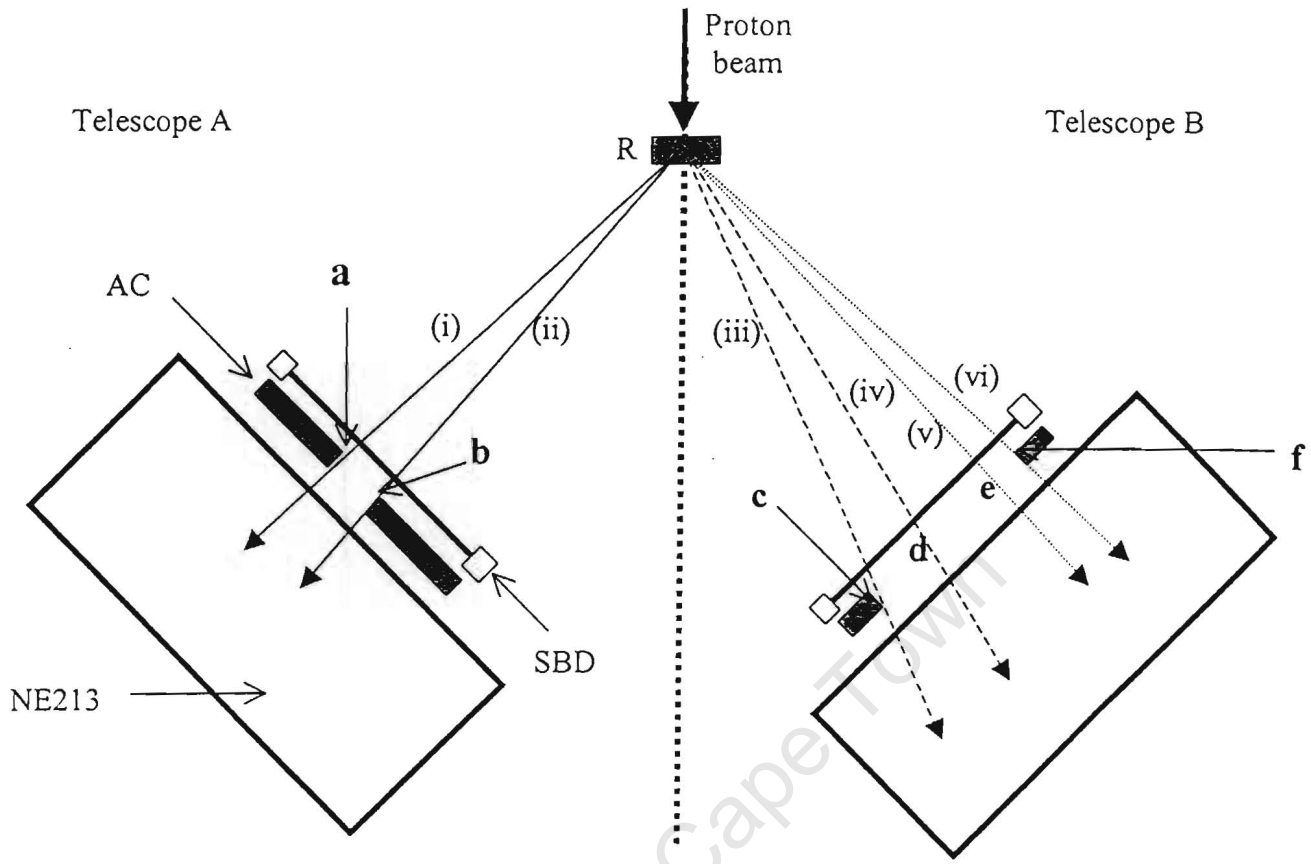

Figure 3.3: Schematic d*iagram illustrating the acceptance ranges of the active collimators in telescopes A and B, for non-relativistic (E ≤ 30 MeV) incident proton energies and 200 MeV incident protons. Non-relativistic coincident proton pairs accepted by the active collimator in telescope A will enter telescope B between points* **e** *and* **f** *(dotted lines) and 200 MeV protons will enter between points* **c** *and* **d** *(dashed lines). The angle between a coincident proton pair is about* 90^{o} *for protons with E ≤ 30 MeV and* 87.2^{o} *for 200 MeV protons, as shown in figure 1.8. See text for details.*

Table 3.2: *Table showing the acceptance angles of the active collimators in telescopes A and B, for non-relativistic ($E \leq 30$ MeV) incident proton energies and 200 MeV incident protons, illustrated in figure 3.3.*

	$E \leq 30$ MeV		$E = 200$ MeV	
$\theta_1 + \theta_2$	90.0	90.0	87.2	87.2
θ_1	43.8	44.8	43.8	44.8
θ_2	46.2	45.2	43.4	42.4

to 43.4° (i.e. from **c** to **d** in figure 3.3) and will therefore pass through the aperture of the active collimator of telescope B and be detected by the NE213 scintillator.

For protons with energies in the range $30 < E < 200$ MeV undergoing elastic scattering in a point size radiator, if the scattered proton passes through the active collimator of telescope A, then the associated coincident proton will have a laboratory angle in the range 43.4° to 45.2° (from **c** to **f** in figure 3.3) and will therefore pass through the aperture of the active collimator of telescope B and be detected by the NE213 scintillator. Thus in this ideal geometry the variations of $\theta_1 + \theta_2$ with proton energy will not affect the detection efficiency of the detection system. The actual geometry of the spectrometer varies from the ideal geometry considered above due to the finite size of the proton beam and of the radiator. The effects of these differences on the spectrometer detection efficiency can be estimated by making Monte Carlo calculations and/or performing experimental measurements. The latter option was followed in the present work. Measurements were made as follows at proton energies of 100.0 and 190.8 MeV to check the dependence of the detection efficiency on the angle $\theta_1 + \theta_2$. Telescope A was kept at a fixed angle $\theta_A = 44.3°$ and telescope B was moved from $\theta_B = 39°$ to $\theta_B = 49°$ in steps of 1°. The ratio of coincidence events to single events in telescope A was measured at each setting. The open circles and squares in figure 3.4 show the number of coincidence events recorded as a function of θ_B for incident proton energies of 190.8 and 100.0 MeV, respectively, and the curves are for guiding the eye. The curves

show that the data are consistent with the expected behaviour in each case, that is the detection efficiency reaches a maximum which is constant over a limited angular range which depends on the proton energy E_p. This angular range is $42.2^\circ \leq \theta_B \leq 45.3^\circ$ for $E_p = 100.0$ MeV and $43.8^\circ \leq \theta_B \leq 46.6^\circ$ for $E_p = 190.8$ MeV. The "flat" region therefore overlap over $\theta_B = 43.8^\circ$ 45.3° indicated by the dashed lines shown in figure 3.4. This confirms that, with the two telescopes located with $\theta_A = \theta_B = 44.3^\circ$ the finite angles of acceptance defined by the respective active collimators will not introduce a geometry-based energy-dependent detection efficiency over the range 100191 MeV. Since the changes due to relativistic effects are very small when the proton energy is reduced below 100 MeV, this results of experimental test can be assumed to apply for all proton energies 191 MeV.

3.1.2 Electronics

A schematic diagram of the electronic configuration is shown in figure 3.5. The output from each surface barrier detector (SBD) was fed into an Ortec 142 preamplifier, which provided a pulse height output (E_{SBD}) and a timing output (T_S). The E_{SBD} signal from the preamplifier was processed by an Ortec 572 amplifier, a delay amplifier (DA), a linear gate and stretcher (LGS) and finally by an ADC for analog-to-digital conversion. The dynode output from each NE213 scintillation detector was fed into an Ortec 113 preamplifier and then processed by a similar electronics chain. The anode outputs from the NE213 detectors were fed into Link pulse shape discriminators [Ad78], model 5010. A Link module generates an F output pulse [Sm86, Sm87] by integrating the input pulse over a period of about 30 ns, thereby taking only the fast (prompt) component of the scintillation pulse. A Link also generates a pulse height pulse, L, which is generated by integrating the input pulse over a period of about 500 ns, and includes the contributions from both the prompt and the delayed scintillation components. The L and F parameters outputs from each Link were processed through a sum invert (SI), a delay amplifier (DA), a linear gate and stretcher (LGS) and finally by an ADC. The L and the F parameters were used to generate a pulse shape parameter (S) in the offline analysis of the data (see section 3.3.1). The Link also provided a timing output, which was used to set a fast coincidence condition between the surface barrier detector, the NE213 scintillator and the active collimator in the two

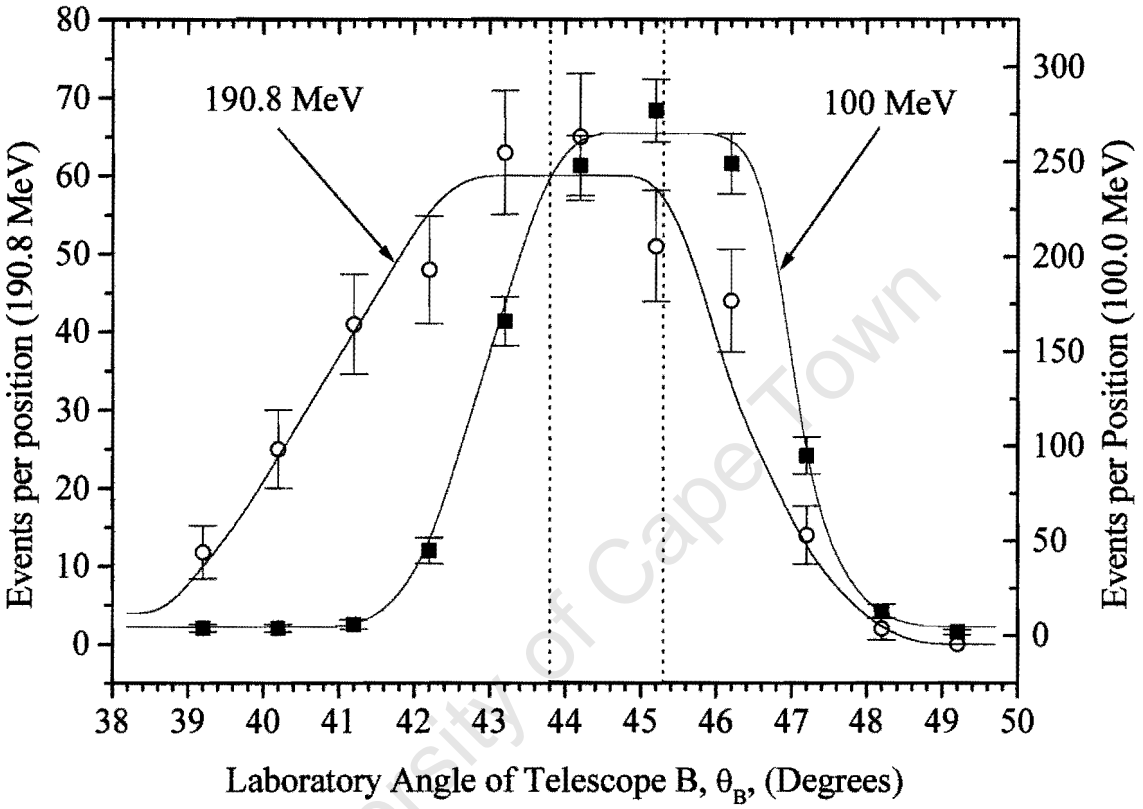

Figure 3.4: *Coincidence events measured by detector telescope B as a function of laboratory angle θ_B when the angle subtended by the axis of detector telescope A was kept fixed at $\theta_A = 44.3^o$, and the angle subtended by the axis of telescope B varied, for an incident proton beam energy of 190.8MeV (open circles and left vertical scale) and 100.0 MeV (squares and right vertical scale) at the isocentre. The curves are for guiding the eye. The region bounded by the dashed vertical lines ($43.8^o \leq \theta_B \leq 45.3^o$) is the range where the plateaus of the curves overlap. See text for details.*

telescopes, as explained below.

Timing signals from the ΔE detector (T_S), and Link module (T_L) together with the signal from the NE102 scintillator were directed into a coincidence (CO) module, to set a fast coincidence condition for each detector telescope. This fast coincidence condition was set to select coincidences between the ΔE and E detectors, and was satisfied when logic pulses from the surface barrier detector (ΔE) and the NE213 scintillator (E) were in coincidence and there was no pulse from the NE102 scintillator (veto detector). The resolving time for this coincidence was set to a few nanoseconds ($\leq$ 5 ns). Logic pulses associated with telescope A coincidence events were used to start the time to amplitude converter (TAC) which was stopped by logic pulses associated with telescope B coincidence events. The TAC output provided a coincidence time delay parameter (T), which was used to monitor the prompt coincidence peak corresponding to the p-p proton pairs detected by the two telescopes in coincidence (see section 3.2.3).

A slow coincidence was set in the universal coincidence (UCO) module to provide the event gate for the experiment. Inputs to the UCO were logic pulses from the PSD output of each Link module, a logic pulse from the TAC and the logic level from the data acquisition system that indicated when it was not busy. The logic pulse from the UCO was used to gate the LGS modules. The UCO was set to four-fold coincidence to select coincidence events.

Nine parameters (L_A, F_A, D_A and C_A, from detector telescope A, L_B, F_B, D_B and C_B from detector telescope B, and the coincidence time T) were recorded event by event. The event signals were directed through a CAMAC interface into a VAX 400 workstation where they were recorded on disk using the data acquisition code *XSYS* [XSYS]. The offline analysis of the data was completed using the multi-parameter code *GNU* which is available [Br01] in the Physics Department, University of Cape Town.

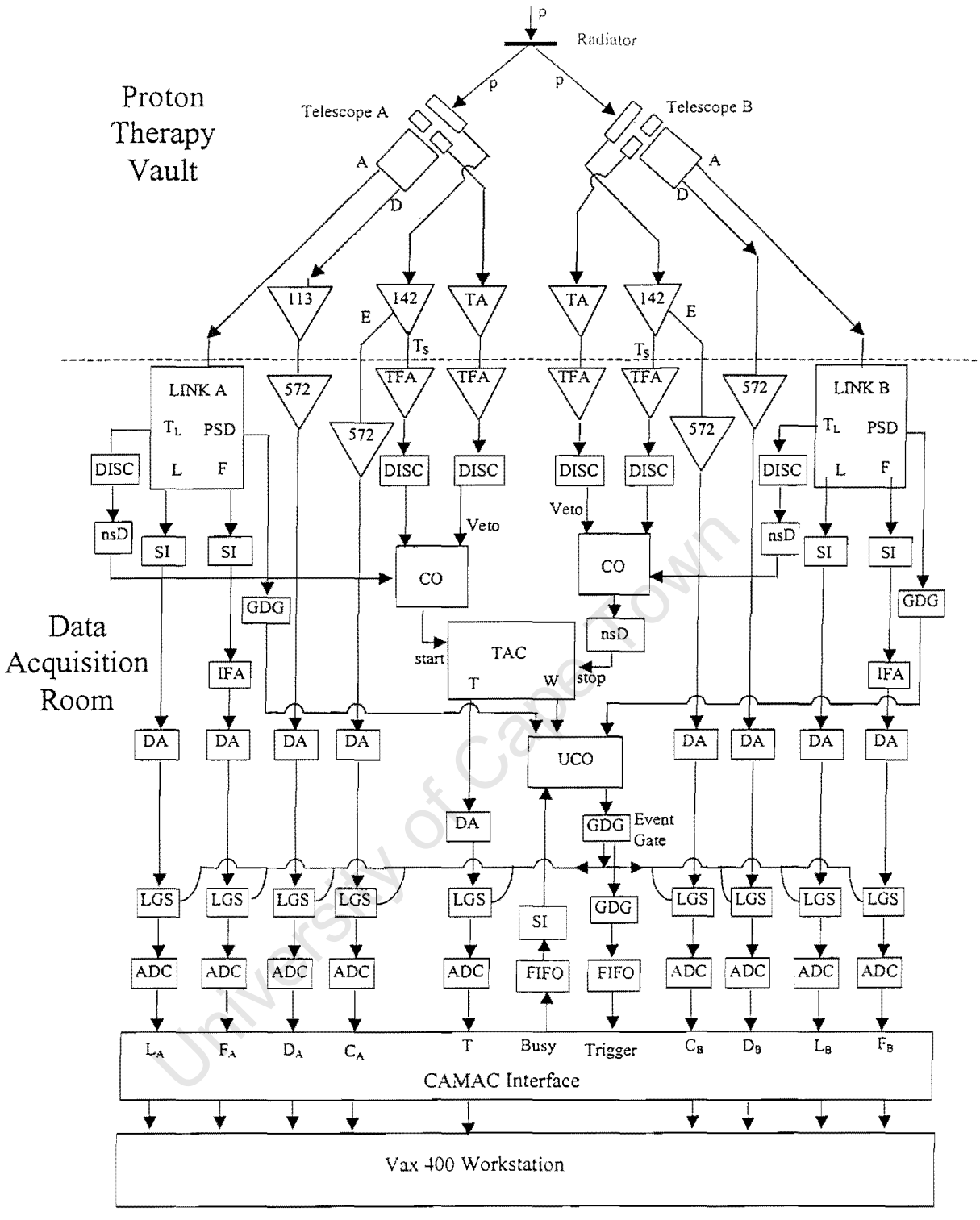

Figure 3.5: *A schematic diagram showing the electronic system used for these experiment. The modules are as follows: 113: Ortec 113 preamplifier; 142: Ortec 142 preamplifier; TA: timing amplifier; TFA: timing filter amplifier; 572: Ortec 572 amplifier; DISC: quad discriminator; LINK: Link pulse shape discrimination module; SI: sum invert; GDG: gate and delay generator; nsD: nanosecond delay box; DA: delay amplifier; TAC: time to amplitude converter; LGS: linear gate and stretcher; FIFO: fan-in fan-out; UCO: universal coincidence; IFA: interface amplifier; CO: Camberra fast/slow coincidence module; ADC: analog-to-digital converter*

3.2 Offline event selection

3.2.1 Particle identification by PSD

The scintillation decay of certain organic scintillators such as NE213 may be used to identify different charged particles detected by the scintillator [Br79, Pe79, Br88]. A pulse shape parameter S was computed for each event using the L and F outputs from the Link modules using the relation [Sm87]

$$S = L - kF + C \tag{3.1}$$

where k and C are arbitrary constants [Sm87]. A plot of counts versus pulse height (L) and pulse shape (S) for events measured by the scintillator make discrete loci on the plane corresponding to the different charged particles detected by the scintillator.

Figure 3.6 shows a perspective plot of counts (vertical) versus pulse height (L) and pulse shape parameter (S) for singles events detected by the NE213 scintillator in telescope A, and figure 3.7 (a) shows the corresponding event density plot. The event signals corresponding to different charged particles detected are seen to lie on well-defined ridges, which are resolved on these two-parameter plots. These ridges correspond to protons that stopped in the scintillator p and protons that escaped from the NE213 detection volume and hence did not deposit all their energy in the detector *ep*. The proton events on the *ep* locus includes events corresponding to protons that were scattered out of the scintillator volume due to large angle scattering with the nuclei of the scintillator material and protons with ranges in NE213 scintillator that are greater than the length of NE213 scintillators (105 mm) used in this experiment. Protons escaping from the back of the scintillator are mainly incident protons that experienced an elastic collision with the carbon nuclei in the radiator and therefore have energies greater than the maximum energy of the protons constituting the coincident proton pairs, that is energies greater than 100 MeV. These high-energy protons only appear in the singles measurements, as they do not satisfy the coincidence conditions (see below), except for the accidental coincidences. The events lying in the region marked r have higher pulse shape values and smaller pulse heights compared to events associated with protons, and do not form any distinguishable structure on the L-S plane. These events are attributed to secondary particles from (p,C) reactions in the radiator and the NE213 scintillator and (p,Si) reactions in the surface barrier

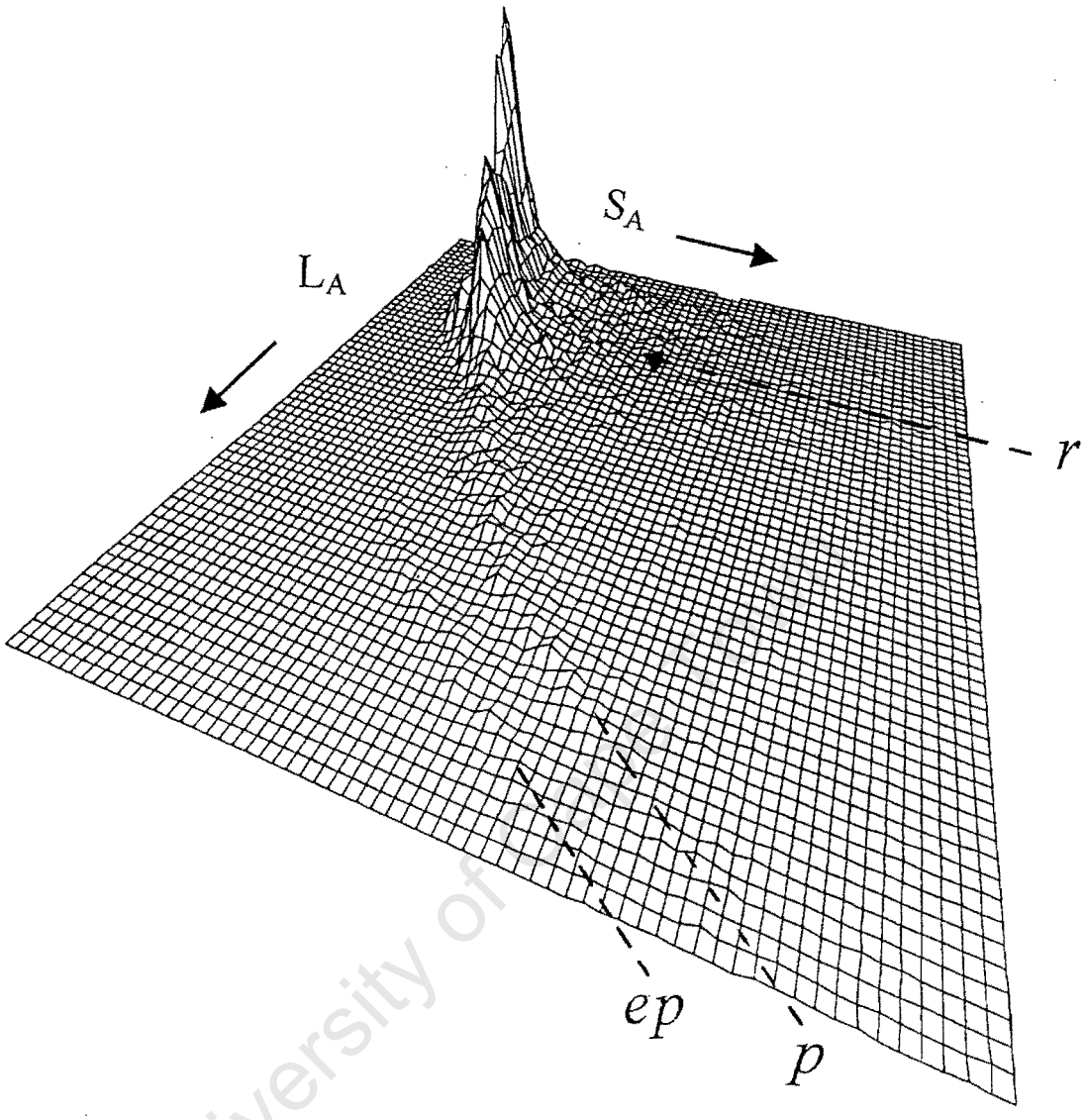

Figure 3.6: *Perspective view of counts (vertical) versus pulse height (L_A) and pulse shape parameter (S_A) for the singles events (run 367) detected by the NE213 scintillator in telescope A. The events in the scintillators form ridges which are associated with protons that stopped in the scintillator (p), protons that escaped from the scintillator either through the sides or back face of the scintillator (ep) and hence did not deposit all their energy in the scintillator. Events in the region marked (r) are attributed to heavy charged particles. See text for details.*

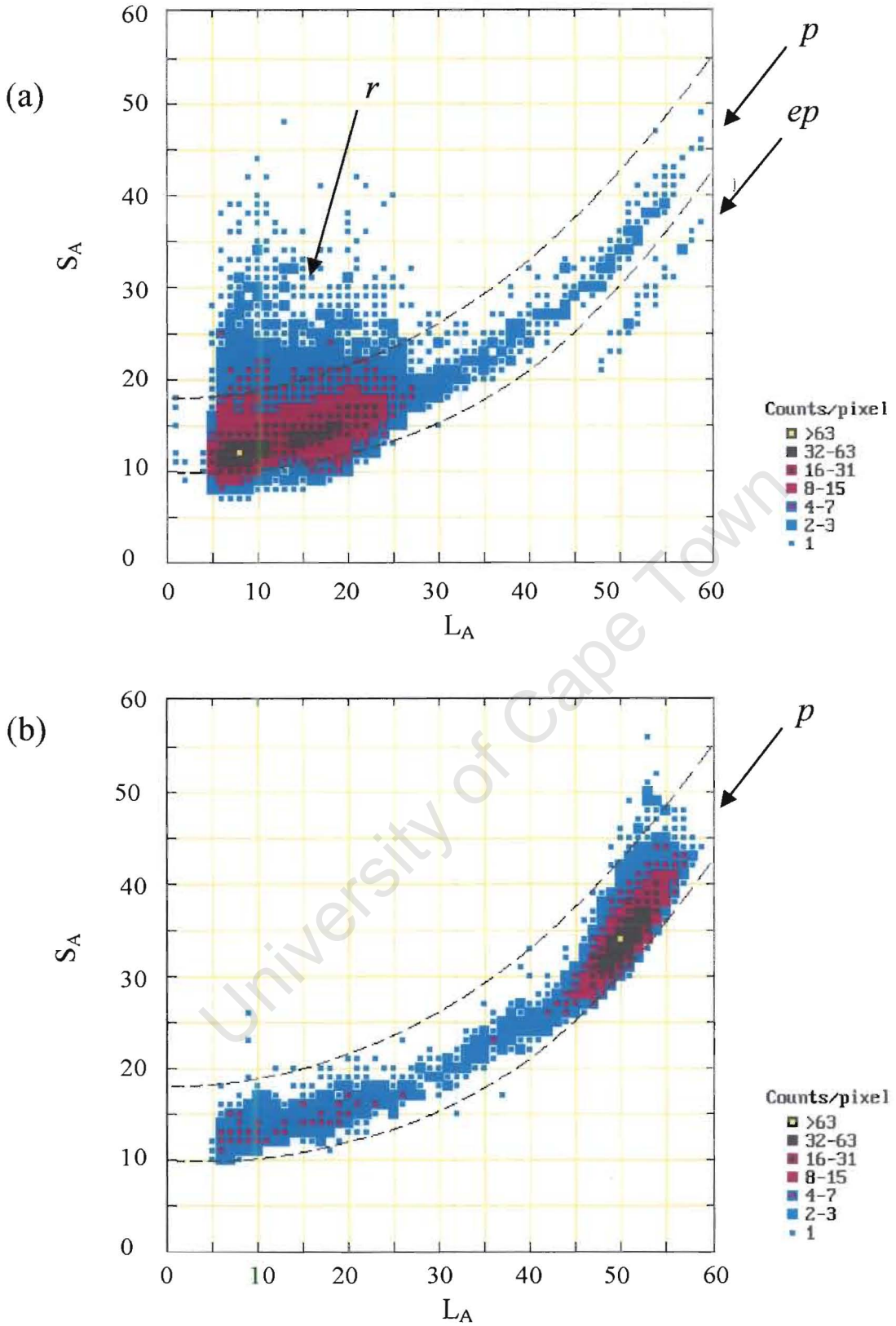

Figure 3.7: *Event density plot of events per pixel as a function of pulse height, L_A, and pulse shape parameter, S_A, for (a) singles (run 367) and (b) coincidence (run 365) events recorded by the NE213 scintillator in telescope A. The events in the scintillators form ridges, which are associated with escaping protons (ep), protons that deposit all their energy in the NE213 scintillator (p), and secondary particles from the* (p,C) *and* (p,Si) *reactions (r). The curves indicate the LS cuts referred to in the text.*

detectors. Figure 3.7 (b) shows an event density plot of events per pixel as a function of pulse height, L_A, and the pulse shape parameter, S_A, for coincidence events (run 365) recorded by the NE213 scintillator in telescope A. Figure 3.7 (b) shows that most of the escaping protons contributing to events in the *ep* locus in figures 3.6 and 3.7 (a), and secondary charged particles contributing to events region marked *r* in figures 3.6 and 3.7 (a) do not satisfy the coincidence condition between the two detector telescopes. Figures 3.8 and 3.9 show the corresponding data and the LS cut for telescope B. A two-parameter cut was imposed on the L-S plane (LS cut) as shown in figures 3.7 and 3.9 in order to select proton events.

3.2.2 Particle Identification by the ΔE-E method

When a beam of different charged particles with the same energy is detected by a ΔE-E detector telescope, the different charged particles deposit different fractions of energy in the ΔE detector [Go64, Pe76], and the residual energy of the particles is usually deposited in the E detector. Figure 3.10 shows a perspective plot of counts (vertical) versus pulse heights D and C from the NE213 scintillator (E detector) and the surface barrier detector (ΔE detector), respectively, of telescope A for singles (run 367) events. Figure 3.11 (a) shows the corresponding event density plot. The events in the prominent locus *p* in figures 3.10 and 3.11 are attributed to protons, and events in the region marked *r* are attributed to heavy charged particle (particles with $m > m_p$, where m_p is the mass of a proton). The events plotted in figures 3.10 and 3.11 satisfied the LS cuts for selecting protons shown in figures 3.7 and 3.9. Figure 3.11 also indicate the two-parameter cut (DC cut) used to select proton events. Figures 3.12 and 3.13 show the corresponding data and the DC cut for telescope B. Figures 3.11 (b) and 3.13 (b) show that the DC cuts should be carefully chosen to select proton events since inappropriate cut selection may result in the inclusion of more background events, which will distort the pulse height spectra by increasing the low pulse height component. On the other hand a tighter cut will result in the rejection of proton events that will result in the distortion of the pulse height spectrum. The cuts were chosen so as to include all the true coincidence events. The event density plot for the coincidence events (run 365) indicates that the contribution of heavy charged particles and accidental coincidences to the coincidence events is negligible (see

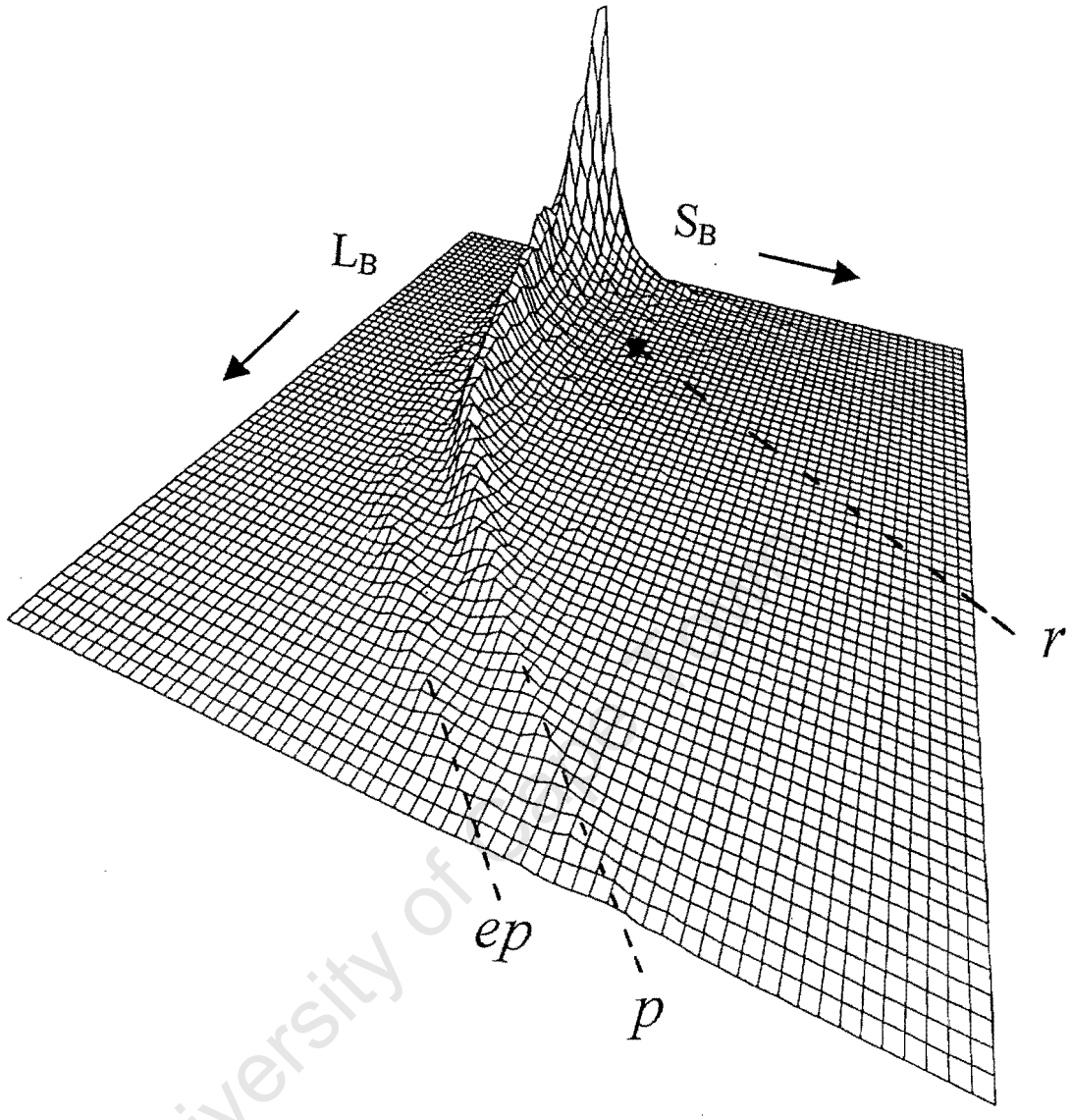

Figure 3.8: *Perspective view of counts (vertical) versus pulse height (L_B) and pulse shape parameter (S_B) for the singles events detected by the NE213 scintillators in telescope B. The events in the scintillators form ridges which are associated with protons that stopped in the scintillator (p), protons that escaped from the scintillator either through the sides or back face of the scintillator (ep) and hence did not deposited all their energy in the scintillator. Events in the region marked (r) are attributed to heavy charged particles. See text for details.*

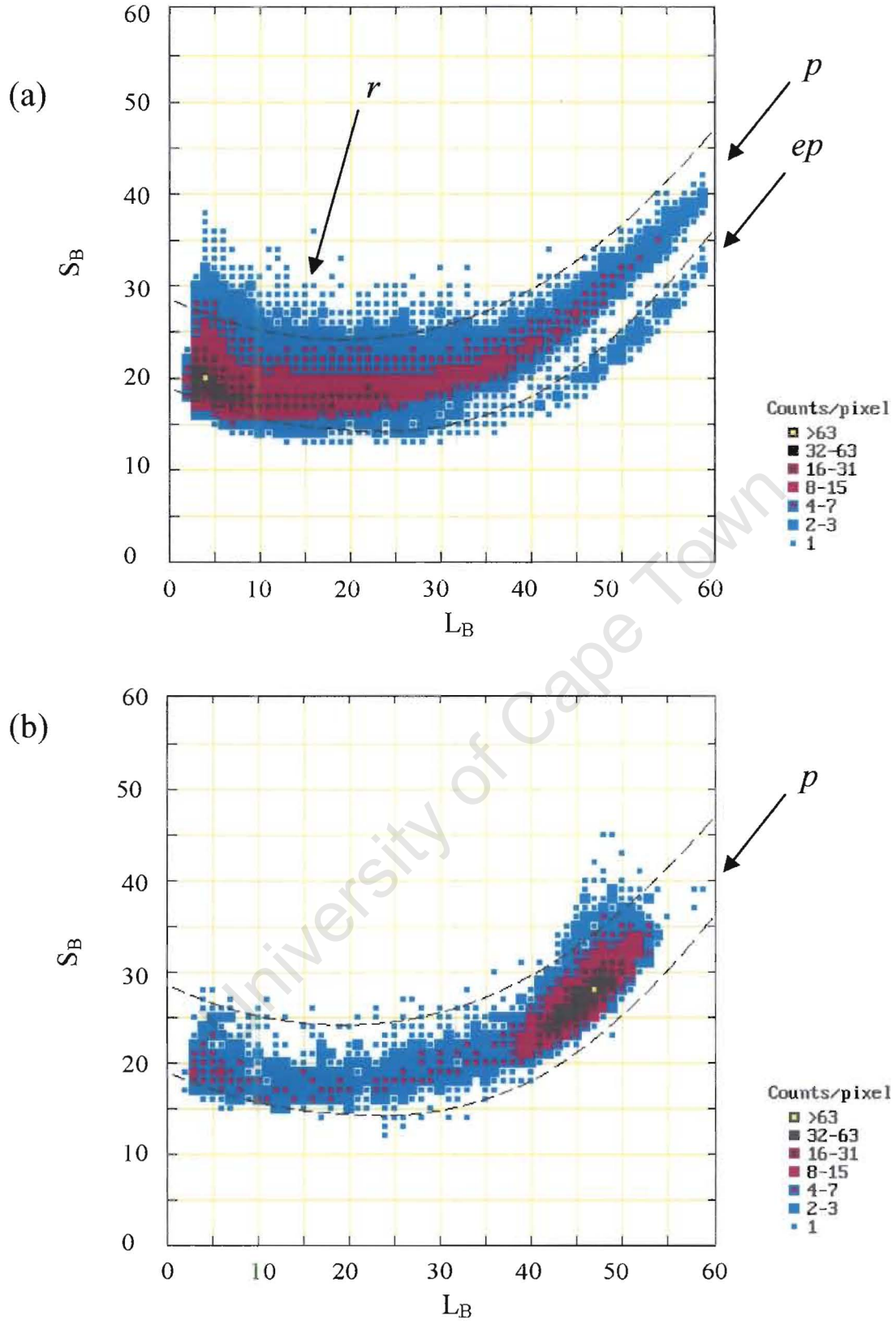

Figure 3.9: *Event density plot of* events per pixel *as a function of pulse height, L_A, and pulse shape parameter, S_B, for (a) singles (run 369) and (b) coincidence (run 365) events recorded by the NE213 scintillator in telescope B. The events in the scintillators form ridges, which are associated with escaping protons (ep), protons that deposit all their energy in the NE213 scintillator (p), and secondary particles from the* (p,C) *and* (p,Si) *reactions (r). The curves indicate the LS cuts referred to in the text.*

figures 3.11 (b) and figures 3.13 (b)). The accidental coincidences (b) in figures 3.12 and 3.13 (a) are more pronounced than in figures 3.10 and 3.11 (a), due to the higher detection threshold in NE213 scintillator in telescope A compared to that of the NE213 scintillator in telescope B. The high threshold of the NE213 scintillator in telescope A compared to that of the NE213 scintillator in telescope B can be seen more clearly in the event density plots (see figures 3.11 and figures 3.13).

3.2.3 Coincidence Time Delay Spectrum

Figures 3.14 (a) and (b) show the coincidence time delay (T) spectra from the time to amplitude converter module (TAC) for the standard proton therapy beam run (run 365), with (b) and without (a) the LS and DC cuts imposed. The time scale was determined from the cyclotron frequency (26.0 MHz). The coincidence time delay measured by the TAC is the time difference between each event satisfying the fast coincidence condition and recorded in detector telescope A and any event satisfying the fast coincidence condition and recorded in telescope B. Events detected in telescope A provided the start signal to the TAC and stop signals were taken from events detected in telescope B (see section 3.1.2). The centroid of the prompt coincidence peak, formed by the coincidence proton pairs detected by the two telescopes, is located at channel number 2000 in the coincidence time delay spectrum. The satellite peaks, seen on each side of the prompt coincidence peak, are attributed to the accidental coincidences of protons from preceding and succeeding cyclotron bursts. Application of the LS and DC cuts reduced these accidental coincidences by a factor of about 10 (dotted lines in figure 3.14 b). A window on the T parameter (T cut) was used in the off-line analysis to select p-p coincidence events (see figure 3.14). The FWHM of the prompt coincidence peak, which is a measure of the timing resolution of the spectrometer, is about 5 ns. The width of the window on the coincidence time delay parameter was set wide enough to accommodate the width of the peak due to uncertainties in the timing electronics and variations in the flight times of coincidence protons producing the start and stop pulses in the TAC. There is a small percentage (about 0.1%) of accidental coincidences in the prompt coincidence peak that are not rejected by the T cut in figure 3.14. The number of these accidental coincidences in the prompt coincidence peak is similar to the number of accidental coincidences that formed

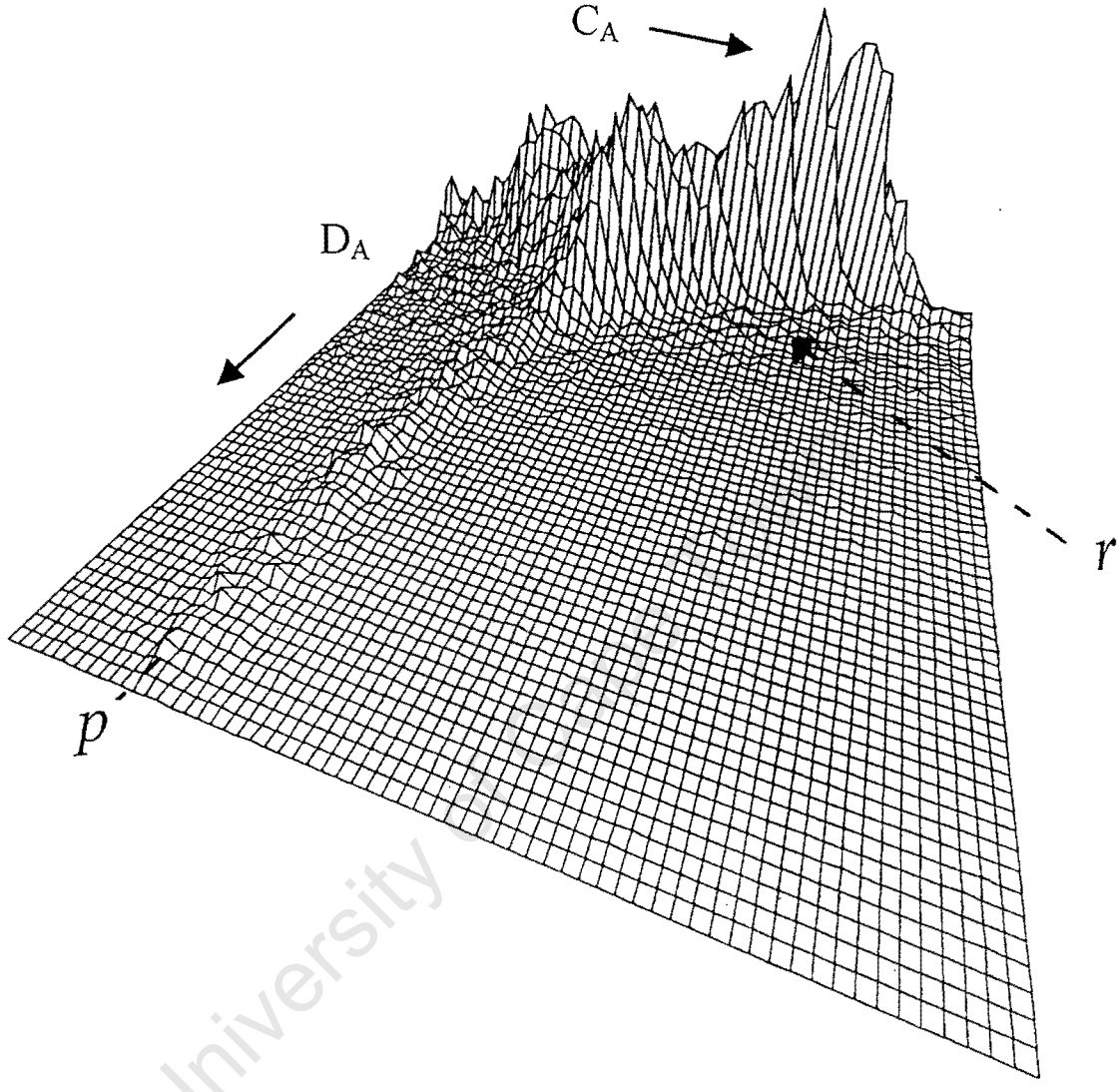

Figure 3.10: *(a) Perspective view of counts (vertical) versus pulse height taken from the dynode output of the NE213 scintillator (D_A) and the pulse height from the surface barrier detector (C_A) for the singles events in telescope A. The events in the locus labelled p are attributed protons that made signals in both the surface barrier detector and the NE213 scintillator.*

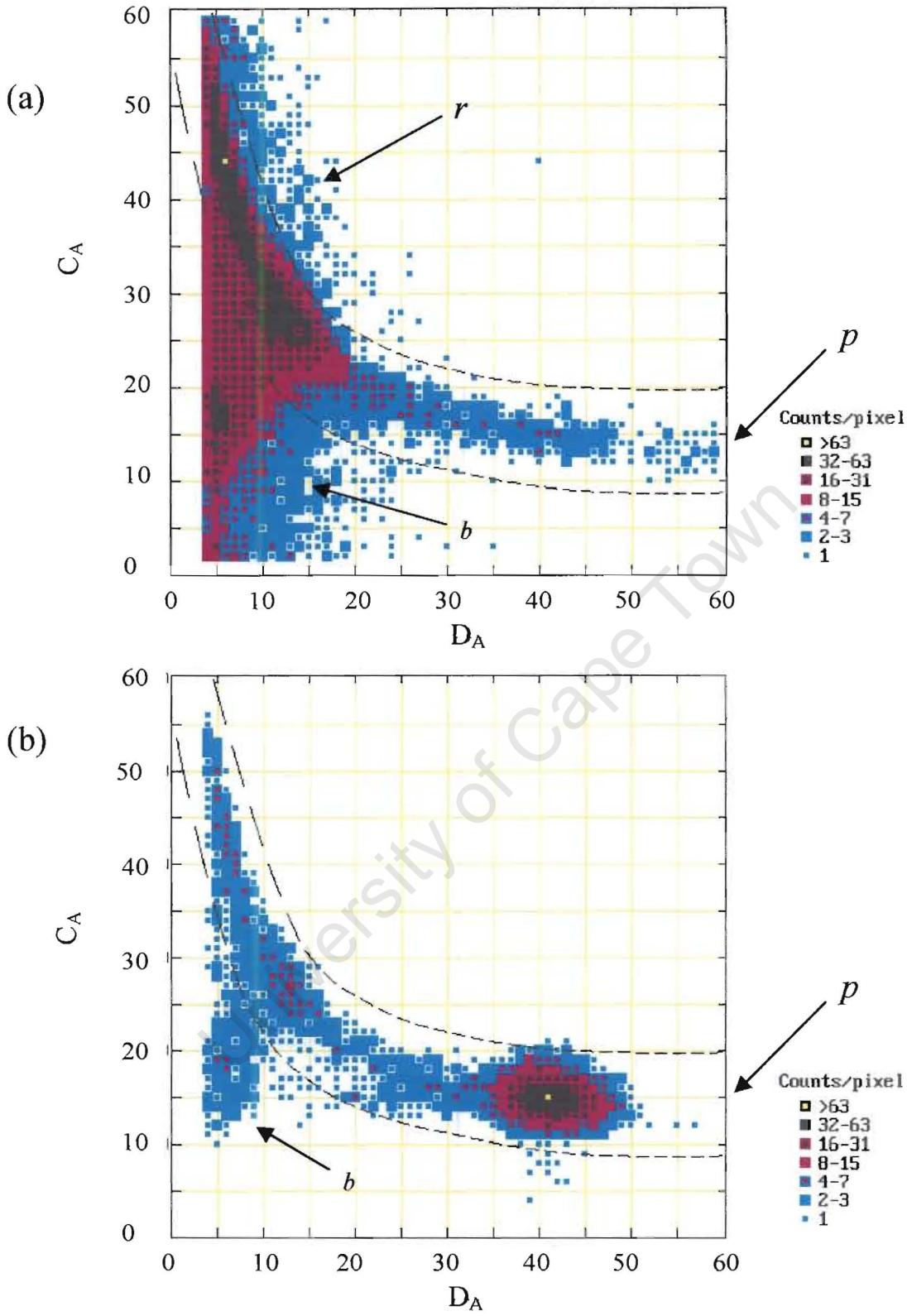

Figure 3.11: *Event density plot of events per pixel as a function of pulse height measured by the NE213 scintillator (D_A) and pulse height measured by the surface barrier detector (C_A) for (a) singles (run 367) and (b) coincidence (run 365) events recorded in telescope A. The events in the locus labelled p are attributed to protons and the events lying in the region labelled r are attributed to secondary particles from the* (p,C) *and* (p,Si) *reactions. Events lying in the region marked b are attributed to accidental coincidences. The curves indicate the DC cuts that are used to select the proton (p) locus.*

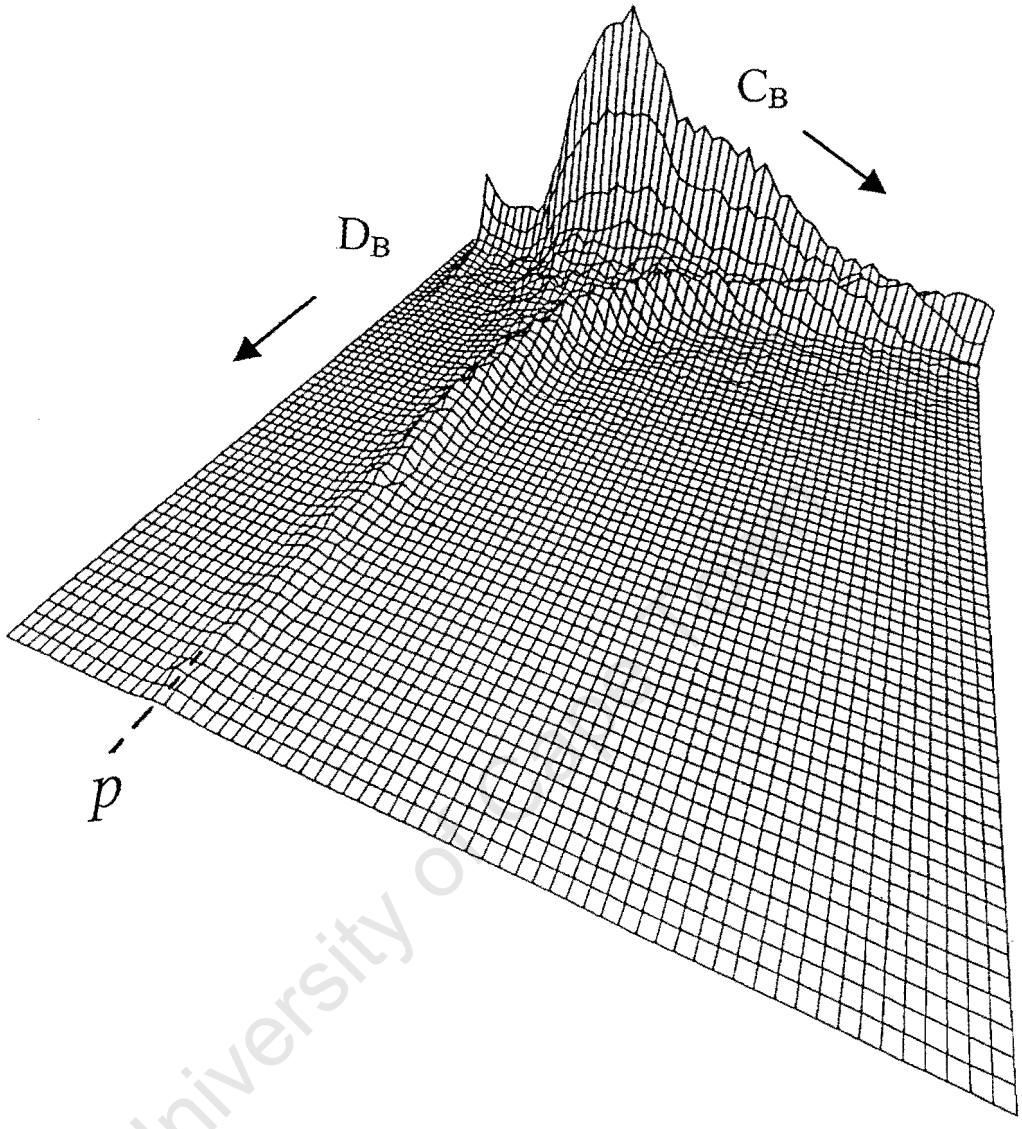

Figure 3.12: *(a) Perspective view of counts (vertical) versus pulse height taken from the dynode output of the NE213 scintillator (D_B) and the pulse height from the surface barrier detector (C_B) for the singles events in telescope B. The events in the locus labelled p are attributed protons that made signals in both the surface barrier detector and the NE213 scintillator.*

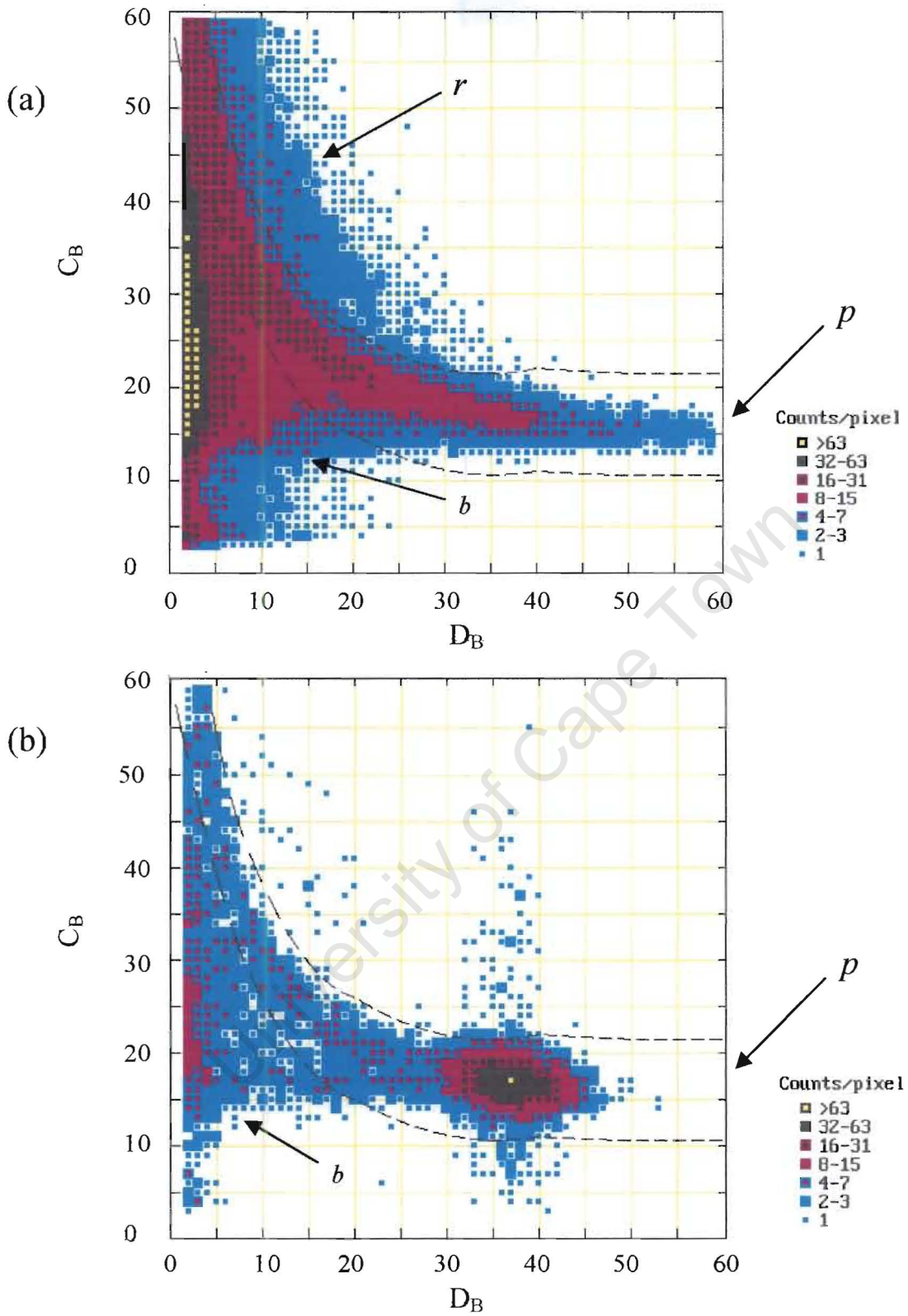

Figure 3.13: *Event density plot of events per pixel as a function of pulse height measured by the NE213 scintillator (D_B) and pulse height measured by the surface barrier detector (C_B) for (a) singles (run 369) and (b) coincidence (run 365) events recorded in telescope B. The events in the locus labelled p are attributed to protons and the events lying in the region labelled r are attributed to secondary particles from the* (p,C) *and* (p,Si) *reactions. Events lying in the region marked b are attributed to accidental coincidences. The curves indicate the DC cuts that are used to select the proton (p) locus.*

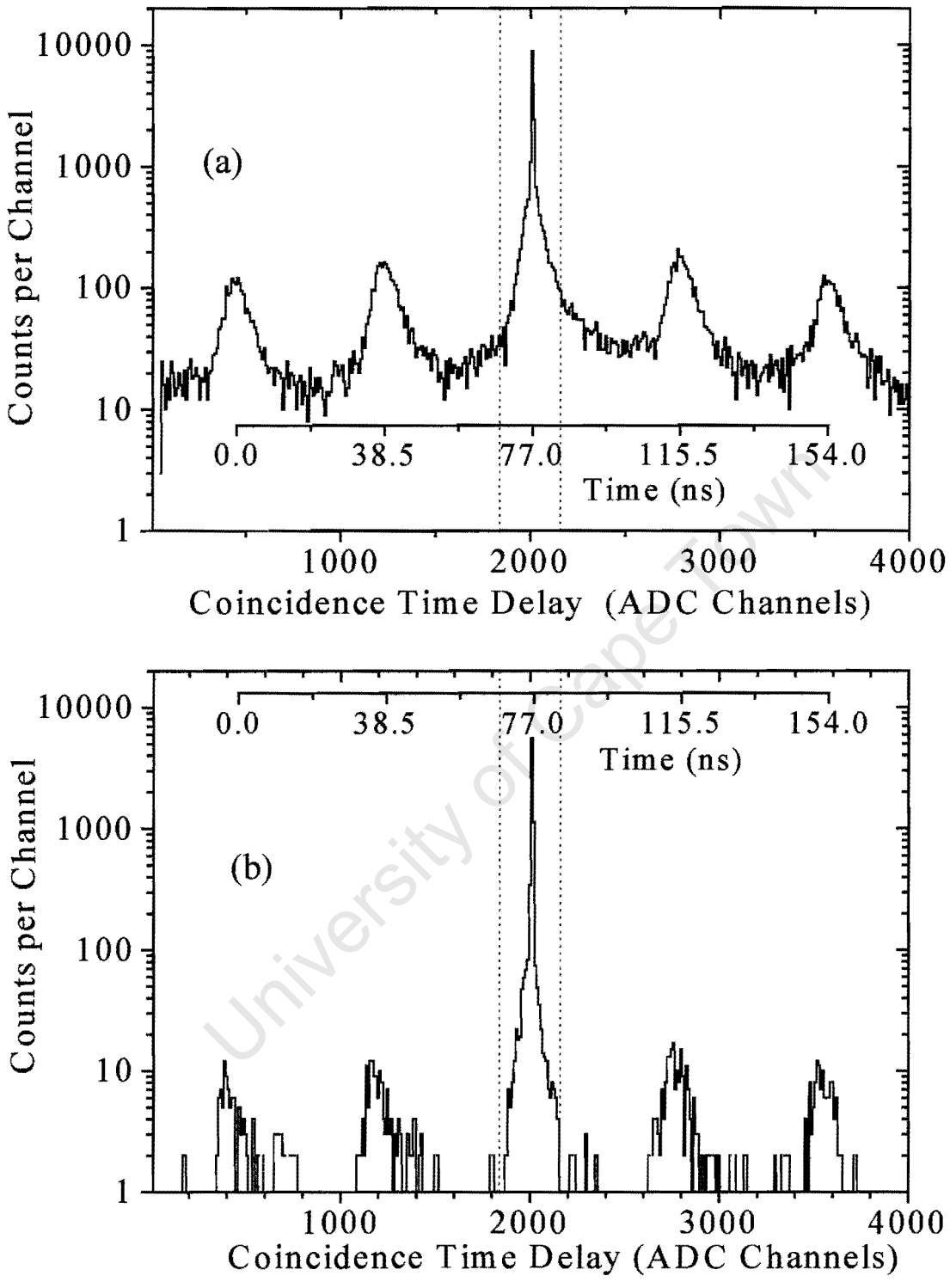

Figure 3.14: *Coincidence time delay spectra recorded by the TAC measured for a proton beam of 190.8 MeV protons incident on the polyethylene radiator at the isocentre for the coincidence condition (a) without and (b) with the LS and DC cuts imposed. The dotted lines show the T cut referred to in the text. The embedded time scale is determined from the cyclotron frequency. The zero of the time scale was arbitrarily chosen to coincide with the centroid of one of the satellite peaks.*

one of the satellite peaks. Therefore the proportion of accidental coincidences that are not rejected by the T cut may be estimated by imposing a T cut that select one of the satellite peaks instead of the prompt coincidence peak (see section 4.3.1).

3.3 Energy Calibrations

Pulse heights measured by the NE213 scintillator (D_{213}) and surface barrier detector (C_{SBD}) in each telescope must be calibrated to proton energy. As in other ΔE-E telescopes using detectors in air and/or with windows or radiators, there are energy losses along the proton paths that must be taken into account. Figure 3.15 shows a schematic illustration of the energy lost by each proton of a coincidence proton pair detected by a detector telescope. The following assumptions were made in the illustration in figure 3.15:

(i) the beam had an infinitesimally small diameter and the detection solid angle is also small,

(ii) the p-p scattering process occurs in the middle of the radiator and the geometry of the detectors is perfectly symmetrical about the beam axis that is $\theta_A = \theta_B$ in figure 3.1) and

(iii) that the scattered and the associated recoiling protons have equal energies E_p which is half the incident proton energy ($E_p = E_0/2$).

The protons lose energy in the radiator (ΔE_R), the air between the radiator and the surface barrier detector (ΔE_{a1}), the surface barrier detector (E_{SBD}) and the aluminium window of the NE213 scintillator (ΔE_w) before coming to rest in the NE213 scintillators (E_{213}). The energy losses ΔE_R, ΔE_{a1}, ΔE_{a2} and ΔE_w shown in figure 3.15 are related to E_p by the following equations:

$$E_p = \Delta E_R + \Delta E_{a1} + E_{SBD} + \Delta E_{a2} + \Delta E_w + E_{213} \quad (3.2)$$

$$= E_{SBD} + E_m \quad (3.3)$$

where

$$E_m = \Delta E_R + \Delta E_{a1} + \Delta E_{a2} + \Delta E_w + E_{213} \quad (3.4)$$

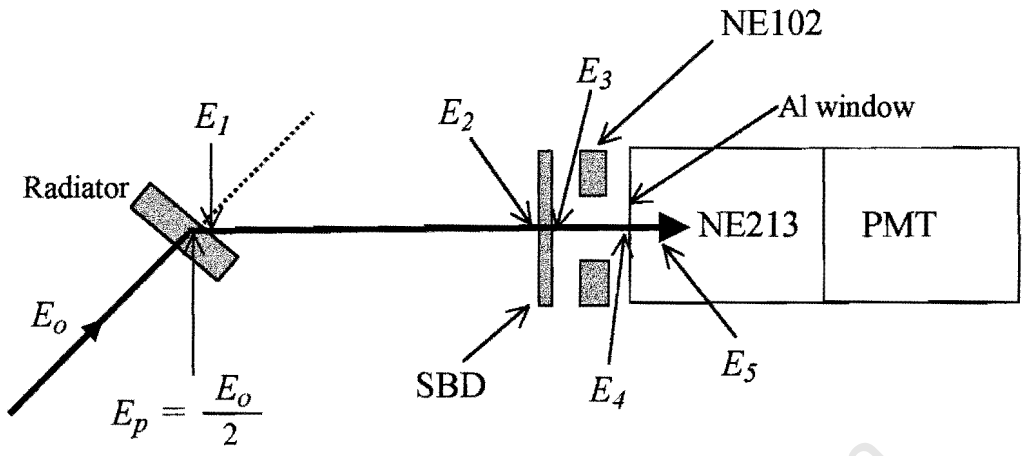

$$E_o = 2E_p \qquad E_p = E_1 + \Delta E_R \qquad E_1 = \Delta E_{a1} + E_2$$

$$E_2 = E_{SBD} + E_3 \qquad E_3 = \Delta E_{a2} + E_4 \qquad E_4 = \Delta E_w + E_5$$

Where:

$\Delta E_R = E_p - E_1$	Energy lost by a scattered/recoil proton in the radiator
$\Delta E_{a1} = E_1 - E_2$	Energy lost by a proton in the air between radiator and SBD
E_{SBD}	Energy deposited by a proton in the SBD
$\Delta E_{a2} = E_3 - E_4$	Energy lost by a proton in air between SBD and Al window of NE213 scintillator
$\Delta E_w = E_4 - E_5$	Energy lost by a proton in the Al window of NE213 scintillator
E_{213}	Energy deposited by a proton in the SBD

Figure 3.15: *A schematic illustration of the energy loss process of a proton in telescope A. See text for details.*

Table 3.3: *Calculated values of energy losses of protons illustrated in figure 3.15, in the radiator (ΔE_R), the air between the radiator and the surface barrier detector (ΔE_{a1}), the surface barrier detector (E_{SBD}), the aluminium window of the NE213 scintillator (ΔE_w) and the NE213 scintillator (E_{213}), and E_m given by equation 3.2. The energy loss of the protons was calculated using stopping power tables [IC49]. All energies are in MeV.*

E_p	ΔE_R	ΔE_{a1}	E_{SBD}	ΔE_w	E_{213}	E_m
95.05	1.6	0.2	1.4	0.2	91.7	93.7
86.65	1.7	0.2	1.5	0.2	83	85.1
66.85	2.1	0.2	1.9	0.2	62.4	64.9
45.4	2.9	0.3	2.6	0.3	39.3	42.8
28.8	4.6	0.5	4.1	0.7	18.7	24.5
22.0	6.0	0.8	6.2	1.0	8.0	15.8

Hence

$$E_m = E_p - E_{SBD} \tag{3.5}$$

For a given incident proton with energy E_0, ΔE_R, ΔE_{a1}, ΔE_{a2}, ΔE_w, E_{213} and E_{SBD} were calculated using the atomic data tables in ICRU report 49 [IC49]. Calculated values of energy losses of protons detected in a telescope, illustrated in figure 3.15, are presented in table 3.3 and figure 3.16. ΔE_R, ΔE_{a1}, ΔE_{a2}, ΔE_w and E_{SBD} decrease when E_p increases and E_{213} is increases when E_p increases. The energy lost by a proton in the air (ΔE_{a1} and ΔE_{a2}) is small (< 0.5 MeV) for $E_p \geq 24$ MeV. Low energy protons with energies up to 13 MeV stop in the polyethylene radiator and contribute to ΔE_R only. Protons with energies up to 20 MeV stop in the material between the radiator and the NE213 and are therefore not detected by the NE213 scintillator (see E_{213} in figure 3.16). This implies that each detector telescope has a detection threshold of 20 MeV due to the energy losses mentioned above (see figure 3.15).

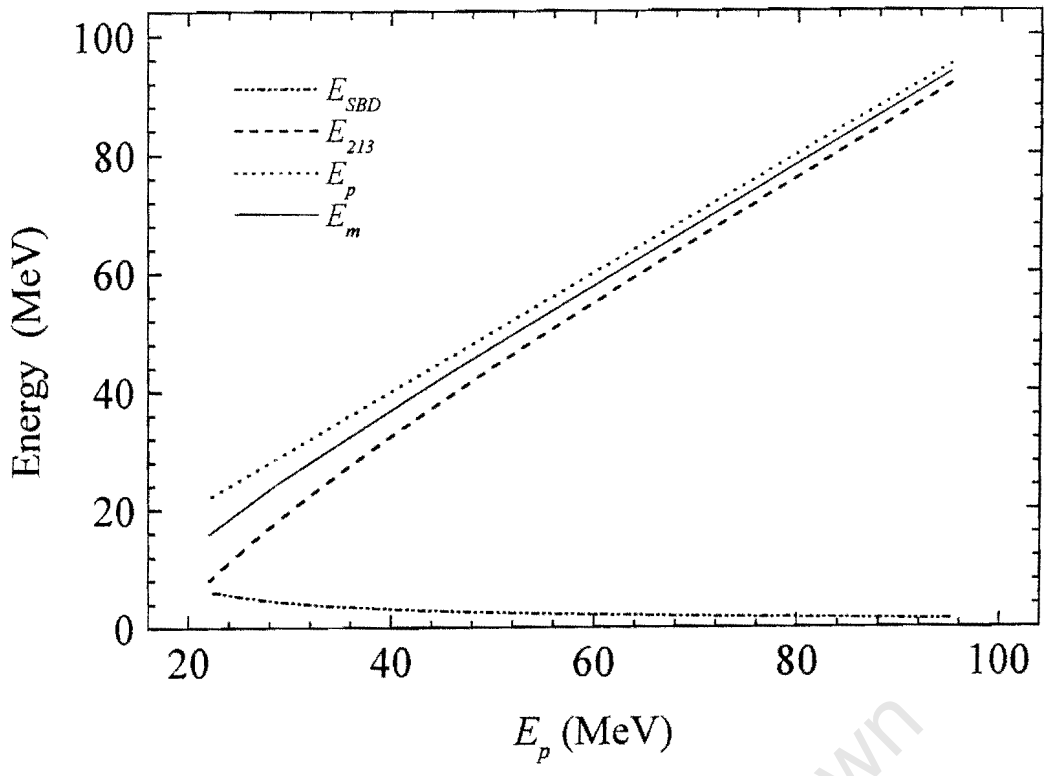

Figure 3.16: *Calculations of the proton energies deposited in the surface barrier detector (E_{SBD}), the NE213 scintillator (E_{213}) and the sum of the two energies (E_d) as functions of E_p (see table 3.3). The energy loss of the protons was calculated using stopping power tables [IC49].*

The pulse heights measured by the surface barrier detectors can be calibrated to energy using alpha sources of known energies such as ^{241}Am. Since the surface barrier detectors respond almost linearly to charged particles, the calibration obtained with alpha particles is similar to the calibration with protons [Kn89]. For a given E_p, E_{SBD}, E_{213} and all the Δ-terms in equation 3.2 have unique values which can be calculated accurately (see table 3.3). We can thus use measurements of C_{SBD} for known E_p to calibrate C_{SBD} to E_{SBD} directly. D_{213} is an unknown function of E_{213}. We could calibrate D_{213} to give E_{213} as for C_{SBD} to E_{SBD}. However, since both E_{213} and the remaining Δ-terms in equation 3.2 are all unique functions of E_p (which can be calculated) so is their sum E_m given by equations 3.4 and 3.5. We can therefore calibrate D_{213} against E_m, which is more convenient in practice. From measurements of D_{213} for different E_p we therefore calibrate D_{213} in terms of E_m, given by equation 3.5. The relationship between E_m and D_{213} is non-linear for various reasons such as quenching in the scintillator due to highly ionizing charged particles [Cr70, Br79, Pe79, Kn89], the non-uniformity in the scintillation light collection efficiency from different points in the detector cell and the attenuation of the scintillation light through absorption by the scintillation material [Fa63, Ku66].

The pulse heights measured by the surface barrier detectors (C_{SBD}) and NE213 scintillator (D_{213}) were calibrated to proton energies E_{SBD} and E_m, respectively, using runs 365, 366, 373, 374 and 399 (see table 3.1) because E_{iso} in each run was accurately known, and the runs covered the energy range of interest (E_{th} to 190.8 MeV) for these experiments. Figures 3.17 and 3.18 show the pulse height spectra of coincidence protons recorded by the surface barrier detectors in detector telescopes A and B, respectively, for proton beams with E_{iso} values of 190.8, 174.1, 134.6, 91.9 and 59.3 MeV. The peak in the pulse height spectrum measured by the surface barrier detector in telescope B for a proton beam with E_{iso} of 59.3 MeV (see figure 3.18) is broader and asymmetric compared to the peak in the spectrum measured by the surface barrier detector in telescope A (see figure 3.17). This could be attributed to the different detection thresholds in the two telescopes which can be clearly seen in figures 3.11 and 3.13. The detection thresholds of the detectors are not sharp thus the "cutoff" in the pulse height spectrum is also not sharp. This leads to a distortion in the shape of the peaks in the pulse height spectrum if these peaks are close to the detection threshold. The peaks in the pulse height spectra measured by the surface barrier detectors in the two telescopes for a proton beam with E_{iso} of 59.3 MeV lie close to the detection thresholds of the telescopes. The detection thresholds of the NE213 scintillators dominate these detection thresholds and affect the pulse height spectra measured by the surface barrier detector because of the coincidence condition between the surface barrier detector and the NE213 scintillator. The peaks in the pulse height spectra measured by the surface barrier detectors in the two telescopes for a proton beam with E_{iso} of 59.3 MeV are distorted by the shift in the centroid of the peaks caused by the detection thresholds. The NE213 scintillator in the telescope A have a higher detection threshold than the NE213 scintillator in telescope B, hence the peak in the pulse height spectrum measured by the surface barrier detector in telescope A have will be more affected by the detection threshold. Consequently the energy spectra measured for a proton beam with E_{iso} of 59.3 MeV cannot be used to provide information about the energy spectrum of the beam because part of the spectrum is below the detection threshold. The main use of these spectra was therefore to show the detection threshold of the spectrometer. The centroids of the peaks in the pulse height spectra in figures 3.17 and 3.18 correspond to the energy deposited by protons (E_{SBD}) in the surface barrier detectors (see figure 3.15 and table 3.3). The pulse height channels corresponding to the peak centroids of

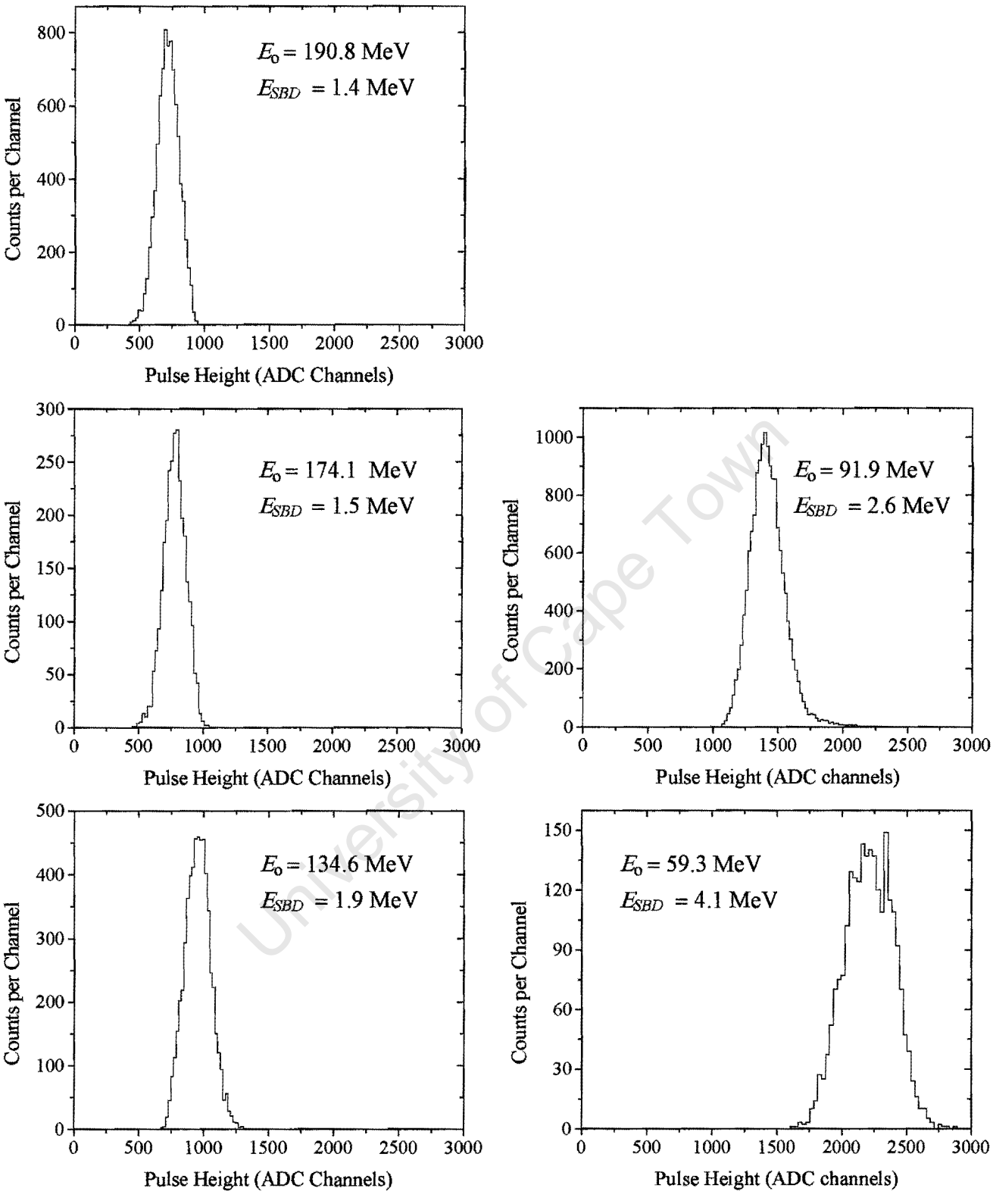

Figure 3.17: *Pulse height spectra recorded by the surface barrier detector in detector telescope A. The data were selected by applying the* ΔE–E, LS *and* T *cuts to select true p-p coincidence events. The energy deposited by the protons in the surface barrier detector* E_{SBD} *is indicated in each spectrum (see figure 3.15 and table 3.3).* E_{SBD} *was calculated using the atomic data tables in ICRU report 49 [IC49].*

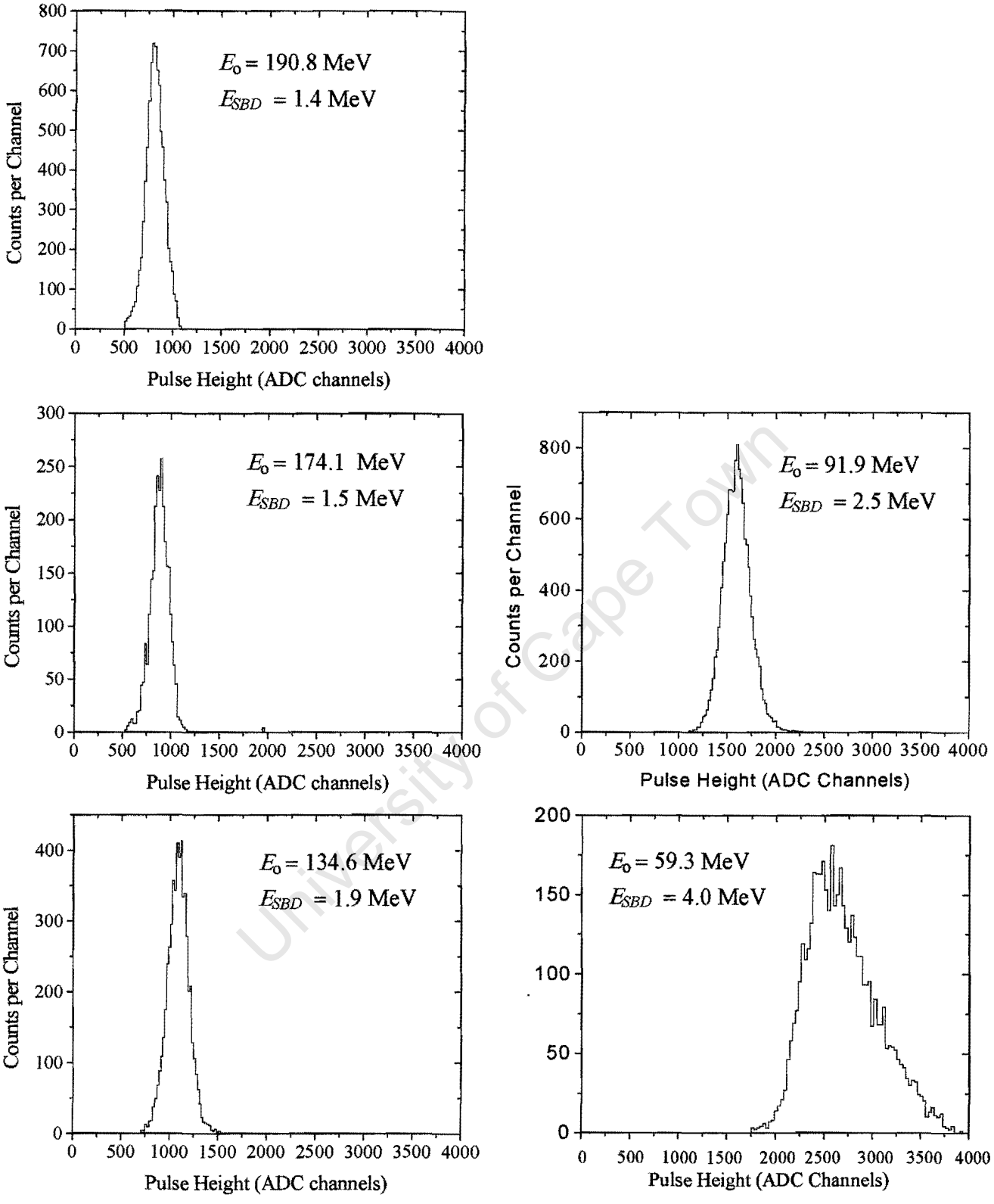

Figure 3.18: *Pulse height spectra recorded by the surface barrier detector in detector telescope B. The data were selected by applying the ΔE–E,* LS *and* T *cuts to select true p-p coincidence events. The energy deposited by the protons in the surface barrier detector E_{SBD} is indicated in each spectrum (see figure 3.15 and table 3.3). E_{SBD} was calculated using the atomic data tables in ICRU report 49 [IC49].*

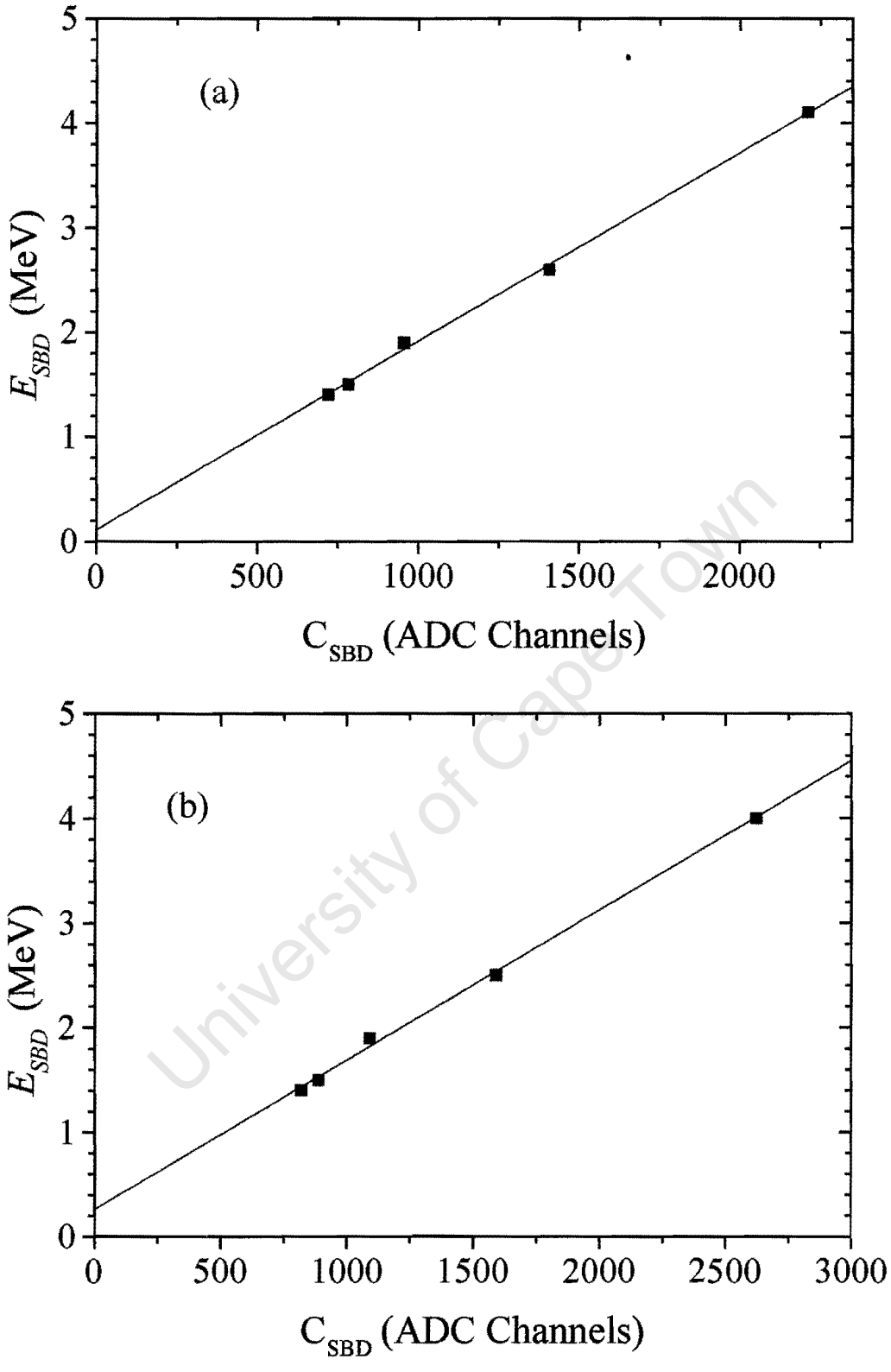

Figure 3.19: *Energy deposited by the protons in the surface barrier detectors versus the corresponding pulse height in these detectors for (a) telescope A and (b) telescope B. The line through the data points is the fit referred to in the text. The error bars are smaller than the data points and are therefore not included in the plot*

the spectra in figures 3.17 and 3.18, were plotted as functions of the calculated proton energies E_{SBD} deposited in the surface barrier detectors of each telescope (see figure 3.19). The experimental data points for the two surface barrier detectors were fitted with straight lines and the slopes of the lines were used to obtain the pulse height to energy calibration. The fits to the data do not go through the origin, because the pulse height scales of the surface barrier detectors were not corrected for any zero offsets, for example in the ADC.

To complete the calibration for determining E_p, the pulse heights of the NE213 scintillators D_{213} were calibrated to proton energy E_m (equation 3.4). Figures 3.20 and 3.21 show pulse height spectra recorded by the NE213 scintillators in telescopes A and B respectively, for proton beams with E_{iso} of 190.8, 174.1, 134.6, 91.9 and 59.3 MeV. Figures 3.22 (a) and (b) show plots of proton energy, E_m, versus the corresponding pulse height for protons detected by the NE213 scintillators in telescopes A and B respectively. The data indicate that pulse height D_{213} is directly proportional to E_m at high proton energies increases exponentially at low energies. The data points in each plot were fitted with a function shown below, that is predominantly exponential at low energies and predominantly linear at high energies,

$$y = p_1 + p_2 x - p_3 \exp(-p_4 x) \tag{3.6}$$

to obtain the pulse height to energy calibration for each NE213 scintillator. The curves in figure 3.22 intercept the energy axes at about 13 Mev, which is the approximately equal to the energy lost by the low energy protons in the radiator, air between the radiator and the surface barrier detector, the surface barrier detector and the aluminium window of the NE213 scintillator (ΔE_R, ΔE_{a1}, E_{SBD} and ΔE_w).

Table 3.4 shows the experimental data used in the energy calibration of the detectors. The residual values in table 3.4 are the differences between the experimental energy data points and the theoretical fits to the data points shown in figures 3.19 and 3.22. The residual values are the differences in the measured and calculated data which give an indication of the goodness of the fit. The residual values for both NE213 scintillators range from 0.01 to 1.3 MeV, and the chi-squared per degree of freedom values of the fits are 0.887 and 0.696 for NE213 scintillators A and B, respectively. Residual values calculated from the experimental and fitted data points

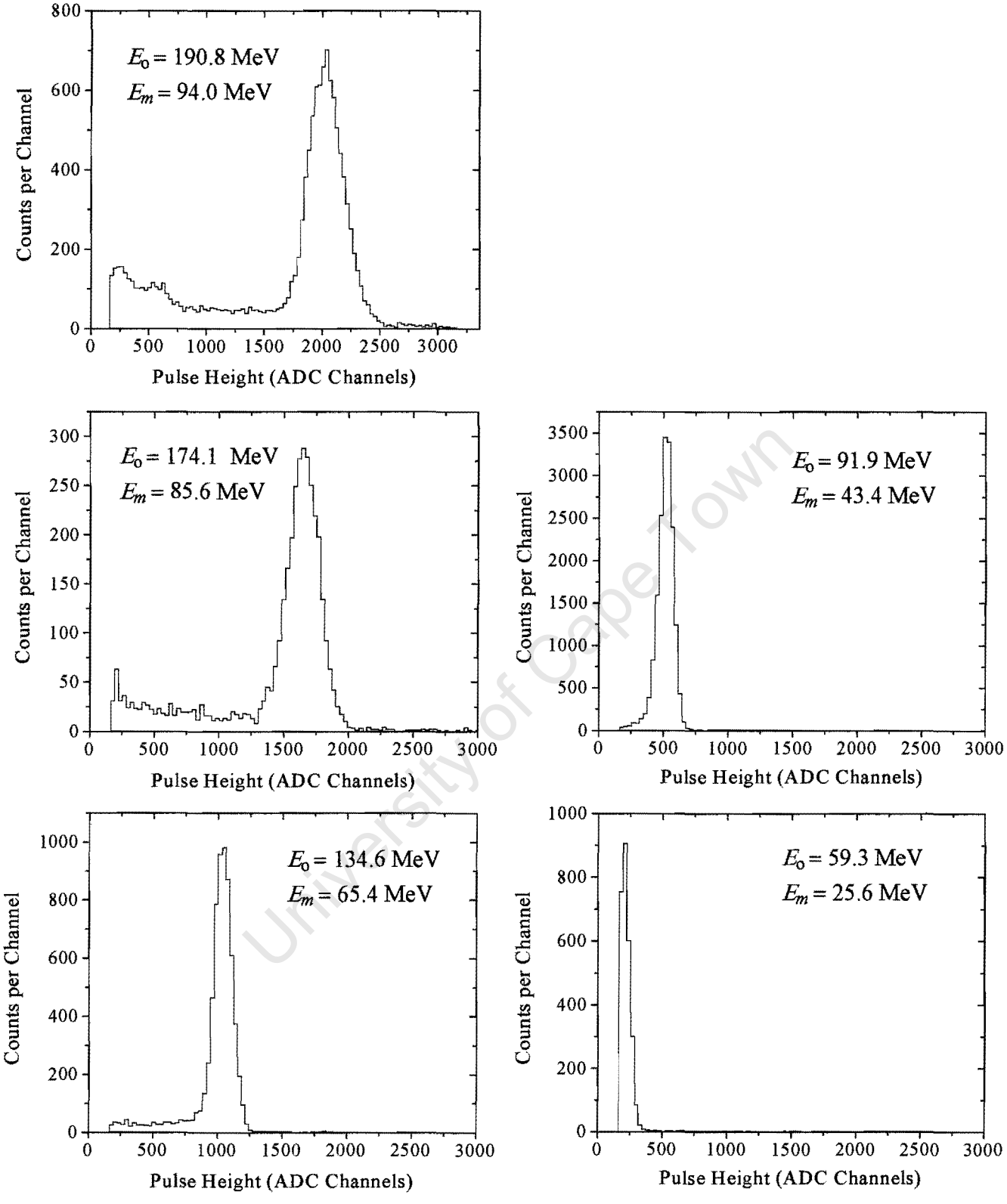

Figure 3.20: *Pulse height spectra recorded by the NE213 scintillator in detector telescope A, for protons satisfying the ΔE–E,* LS *and* T *cuts. The proton energies (E_m) used in the calibration of the detector pulse height to proton energy are indicated on the spectra. See text for details.*

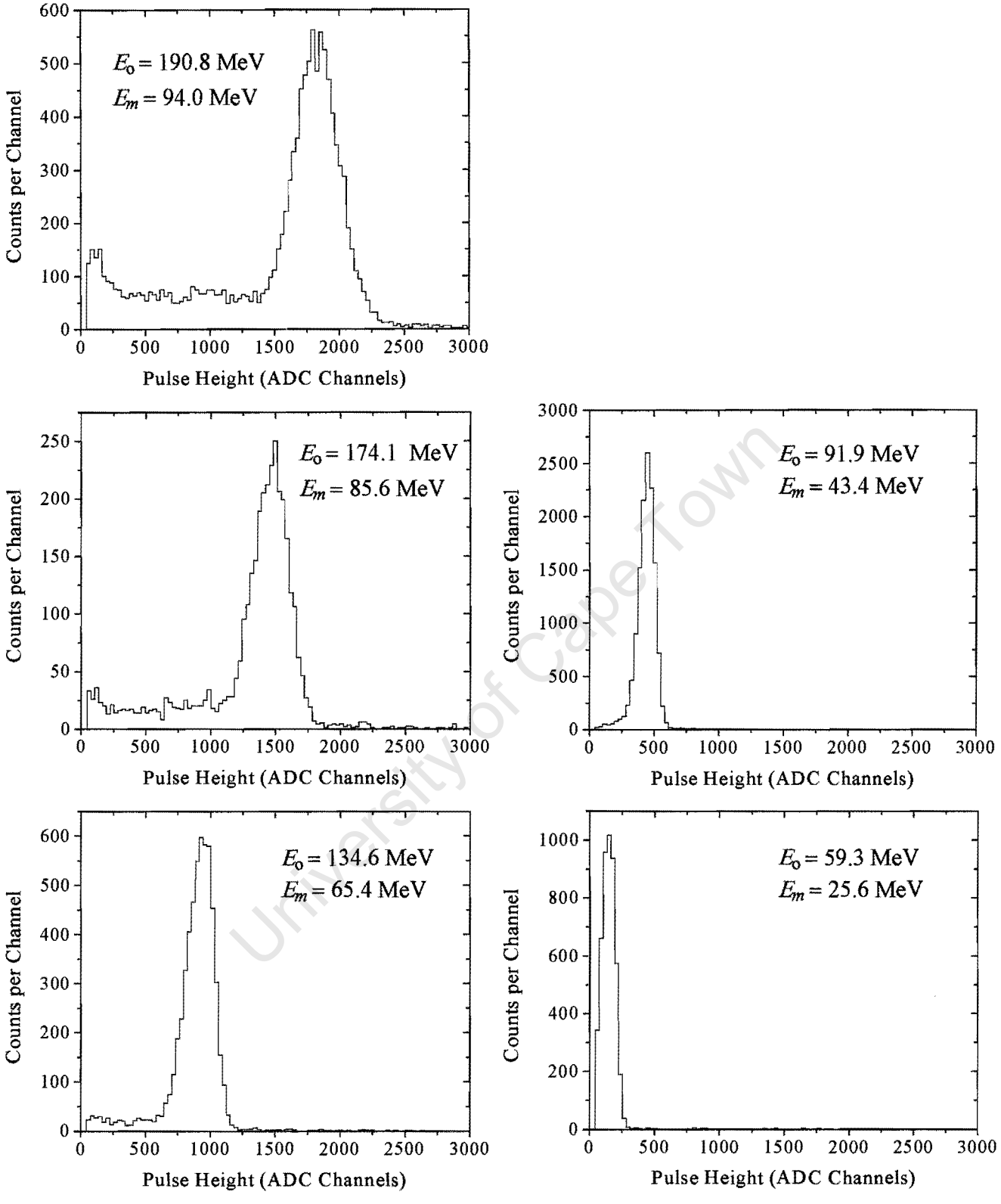

Figure 3.21: *Pulse height spectra recorded by the NE213 scintillator in detector telescope B, for protons satisfying the ΔE–E,* LS *and* T *cuts. The proton energies (E_m) used in the calibration of the detector pulse height to proton energy are indicated on the spectra. See text for details.*

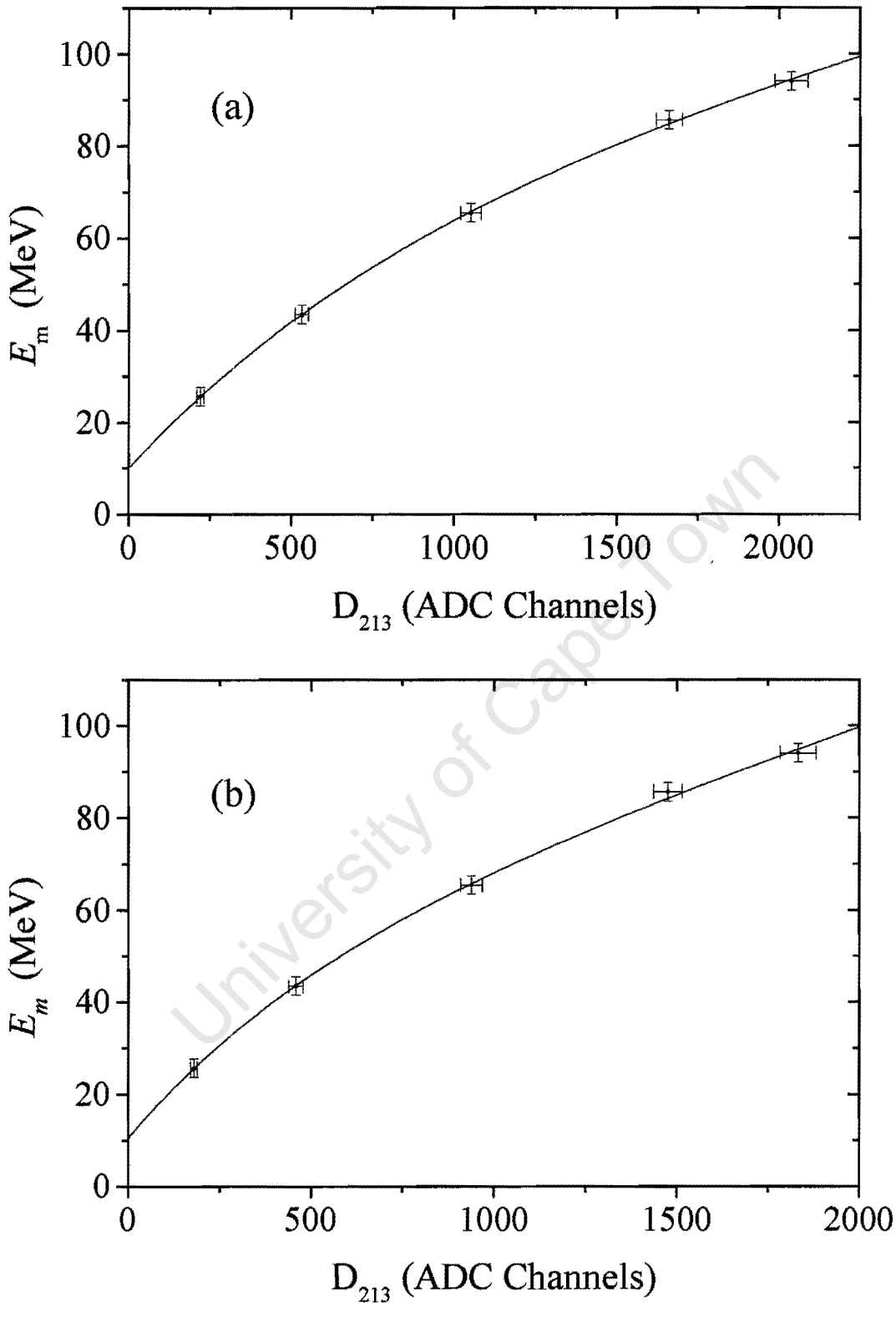

Figure 3.22: *Pulse height to proton energy calibration plots for the NE213 liquid scintillator in (a) telescope A and (b) telescope B. The curve is a nonlinear function fit referred to in the text (equation 3.2).*

Table 3.4 *Experimental data used in the calibration of the detectors in telescopes A and B. The residual values are the differences between the experimental and theoretical fit data. The uncertainties in the pulse heights measured by the surface barrier detectors and the NE213 scintillators are the uncertainties in the position of the centroids of the peaks in the pulse height spectra shown in figures 3.17, 3.18, 3.20 and 3.21, estimated as described in the text.* E_{SBD} *is the energy deposited by the protons in the surface barrier detectors and* E_m *(see equation 3.5) is the energy used to calibrate the NE213 scintillators. See text for details.*

NE213 scintillator A (D_A)			**NE213 scintillator B (D_B)**		
Pulse height (ADC Channels)	**E_m (MeV)**	**Residual (MeV)**	**Pulse height (ADC Channels)**	**E_m (MeV)**	**Residual (MeV)**
2038 ± 51	94.0	−0.4	1833 ± 49	94.0	−0.9
1663 ± 41	85.6	0.8	1476 ± 39	85.6	1.4
1053 ± 31	65.4	−0.3	939 ± 29	65.4	−0.4
533 ± 21	43.4	0.0	459 ± 19	43.4	−0.1
221 ± 11	25.6	0.1	180 ± 9	25.6	0.1
Surface barrier detector A (C_A)			**Surface barrier detector B (C_B)**		
Pulse height (ADC Channels)	**E_{SBD} (MeV)**	**Residual (MeV)**	**Pulse height (ADC Channels)**	**E_{SBD} (MeV)**	**Residual (MeV)**
2212 ± 4.8	4.4	0.1	2622 ± 9.0	4.0	−0.1
1407 ± 0.9	2.6	−0.2	1592 ± 1.2	2.5	0.0
956 ± 0.8	1.9	0.0	1092 ± 1.1	1.9	0.2
783 ± 0.8	1.5	0.0	888 ± 1.3	1.5	0.1
721 ± 0.5	1.4	0.0	820 ± 0.9	1.4	0.1

for the surface barrier detectors range from 0.0 to 0.2. The pulse height spectra measured by the NE213 scintillators for protons with E_{iso} of 59.3 MeV indicate that the peaks in the spectra lie close to the thresholds of the detectors (see figures 3.20 and 3.21). This indicates that the data obtained from this run cannot be utilised in the analysis of the energy spectra or for comparison with Monte Carlo simulations.

The uncertainty in the position of the centroids of the peaks in the pulse height spectra in figures 3.20 and 3.21 can be attributed to statistical effects in the detection process and instrumental effects such as variations in gain of the various active elements in the signal processing chain. The uncertainties in the positions of the centroids of the peaks in figures 3.17, 3.18, 3.20 and 3.21 were used for weighting the data in the fitting process. The pulse height spectrum of the standard proton beam was recorded at different times (runs 365, 380 and 403) during the run series to check for any drifts in the position of the peaks in the recorded spectra.

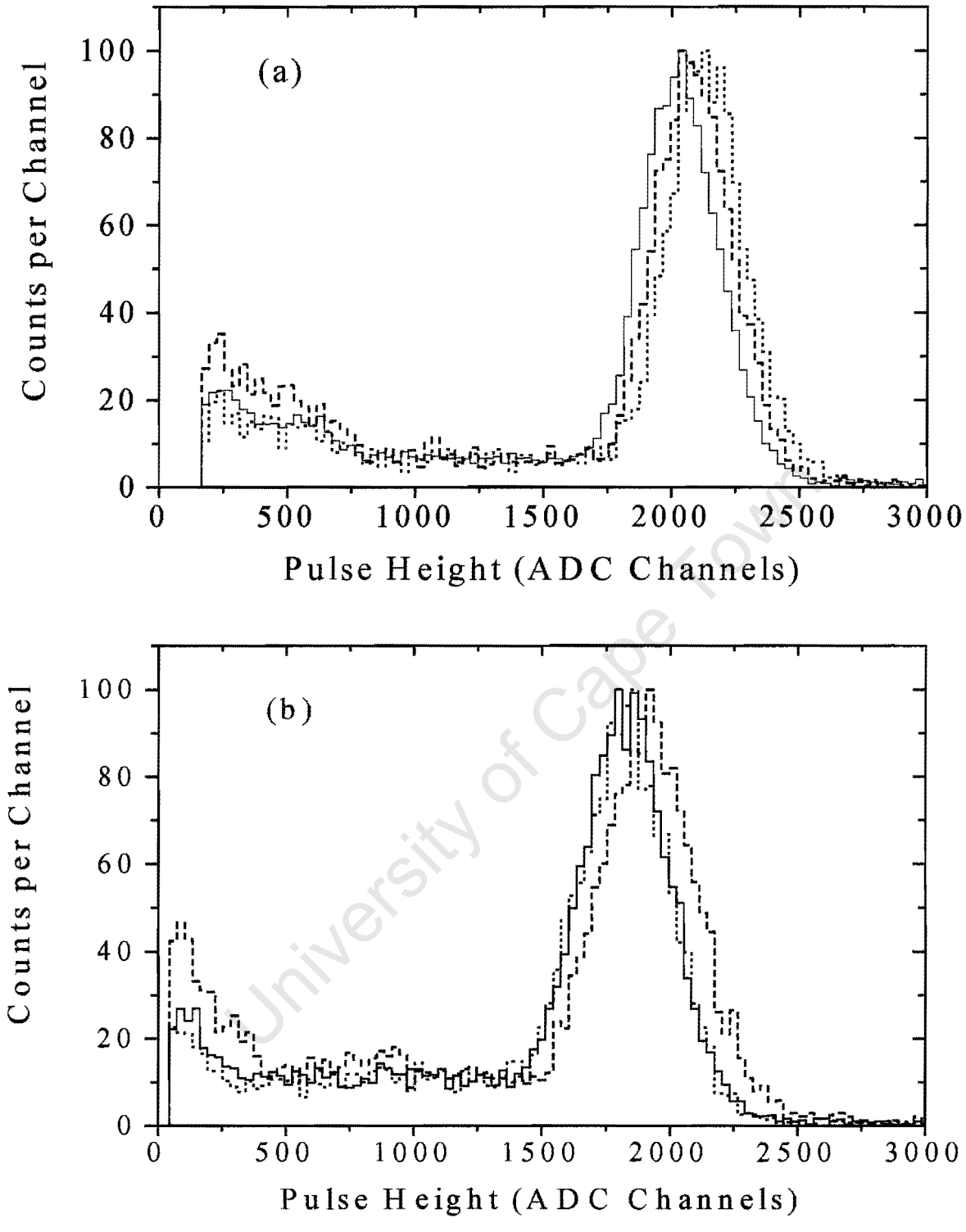

Figure 3.23 *Pulse height spectra measured in (a) telescope A and (b) telescope B for standard proton therapy beam runs. The spectra were measured under identical conditions at different times during the run series. The spectra shown in solid histograms (run 365) were measured at the beginning of the run, the dotted histograms (run 380) in the middle of the run, and the dashed histograms (run 403) at the end of the run.*

Figures 3.23 (a) and (b) show pulse height spectra for proton beams with E_{iso} of 190.8 MeV, measured with NE213 scintillators in telescopes A and B, respectively, at the start of the experimental run series (solid histograms), the middle of the run series (dotted histograms) and at the end of the run series (dashed histograms). The positions of the centroids of the peaks in figure 3.23 are observed to change in time. The maximum drifts in the positions of the centroids of the peaks in the pulse height spectra measured by the NE213 scintillators in telescopes A and B amounted to about 5% of the channel number corresponding to the location of the centroid of the peak in the pulse height spectra. The uncertainty in the position of the centroids due to gain drifts was assumed to increase in proportion to the incident proton energy. The fractional uncertainty of the positions of the centroids of the peaks in the pulse height spectra measured by the NE213 scintillators was assumed to be the same at other energies. The uncertainties in the values of E_m (equation 3.5) is dominated by the uncertainty in E_p ($\sim$1%), which is due to the uncertainties in the stopping power data used in the range-energy conversion in the calibration of the graphite wedges (see section 2.2) [IC49].

3.4 Determination of Proton Energy Spectra

The energies of the proton pairs (E_{A} and E_{B}), after elastic scattering in the radiator, were calculated directly from the pulse heights measured by the detectors using the energy calibration discussed in the previous section. The total energy of the incident proton was obtained from

$$E = E_{\mathrm{A}} + E_{\mathrm{B}} \tag{3.7}$$

and E_{A} and E_{B} were determined from

$$E_{\mathrm{A}} = E_{\mathrm{C_A}} + E_{\mathrm{D_A}} \tag{3.8}$$

and

$$E_{\mathrm{B}} = E_{\mathrm{C_B}} + E_{\mathrm{D_B}} \tag{3.9}$$

where $E_{\mathrm{C_A}}$ and $E_{\mathrm{C_B}}$ are energies determined from the pulse heights measured by the surface barrier detectors in telescopes A and B, respectively, and $E_{\mathrm{D_A}}$ and $E_{\mathrm{D_B}}$

are energies determined from the pulse heights measured by the NE213 scintillators in telescopes A and B, respectively.

Figure 3.24 shows density plots of counts per pixel versus energies E_A and E_B (measured by detector telescopes), with and without the LS and DC T cuts imposed, for measurements with the standard proton therapy beam with a maximum energy of 190.8 MeV at the isocentre (run 365). The reaction tail events at $E_A \approx 95$ MeV, $E_B < 95$ MeV and $E_B \approx 95$ MeV, $E_A < 95$ MeV (figure 3.24 (b)) are suppressed when the LS, DC and T cuts are imposed (figure 3.24 (a)). The symmetry ($\theta_A \approx \theta_B$) of the experimental geometry implies that the condition $E_A \approx E_B \approx 0.5E$ should be valid for detected proton pairs that originate from p-p elastic scattering in the radiator (see figure 3.1). This condition applies for beam protons, that is incident protons moving in a direction parallel to the beam axis at the radiator and undergoing p-p elastic scattering in the radiator resulting in coincident proton pairs with $\theta_1 \approx \theta_2$. Incident protons making an angle with the beam axis at the radiator may undergo p-p elastic scattering resulting in coincident proton pairs that satisfy the detection conditions but with $\theta_1 \neq \theta_2$. These coincident protons with $\theta_1 \neq \theta_2$ and consequently $E_A \neq E_B$ will lie off the region where $E_A \approx E_B \approx 0.5E$. A large fraction of events satisfying the LS, DC and T cuts lie in the region where $E_A \approx E_B \approx 95$ MeV, and are thus consistent with the $E_A \approx E_B \approx 0.5E$ condition. A small number of events trail away from the dominant peak at $E_B \approx 95$ MeV, $E_A < 95$ MeV and $E_A \approx 95$ MeV, $E_B < 95$ MeV. These components are attributed to events that should have contributed to the dominant peak at $E_A \approx E_B \approx 95$ MeV but are displaced because one of the protons in coincident pair underwent a nuclear reactions in the NE213 scintillator of telescope A or B resulting in reaction tail events (see figure 1.4). The reaction tail consists mainly of reaction products from ^{12}C(p,d)^{11}B, ^{12}C(p,pd)^{10}B, ^{12}C(p,α)^{9}Be and ^{12}C(p,p')3α reactions in the NE213 scintillators. Reaction tail events are partially suppressed by applying the two-parameter cut (E_{AB} cut) in the off-line analysis as indicated in figure 3.24 to select proton events satisfying the $E_A \approx E_B$ condition. This cut is effective in rejecting "single" reaction tail events (i.e. nuclear reactions in A or B alone) as can be seen in figure 3.24. Events in which nuclear reactions occur in both detectors ("double" reaction tail) will be distributed over the entire E_A-E_B plane and will therefore be less effectively rejected. Figure 3.24 shows that there is a concentration of events within the E_{AB} cut as expected but the event density outside this cut is

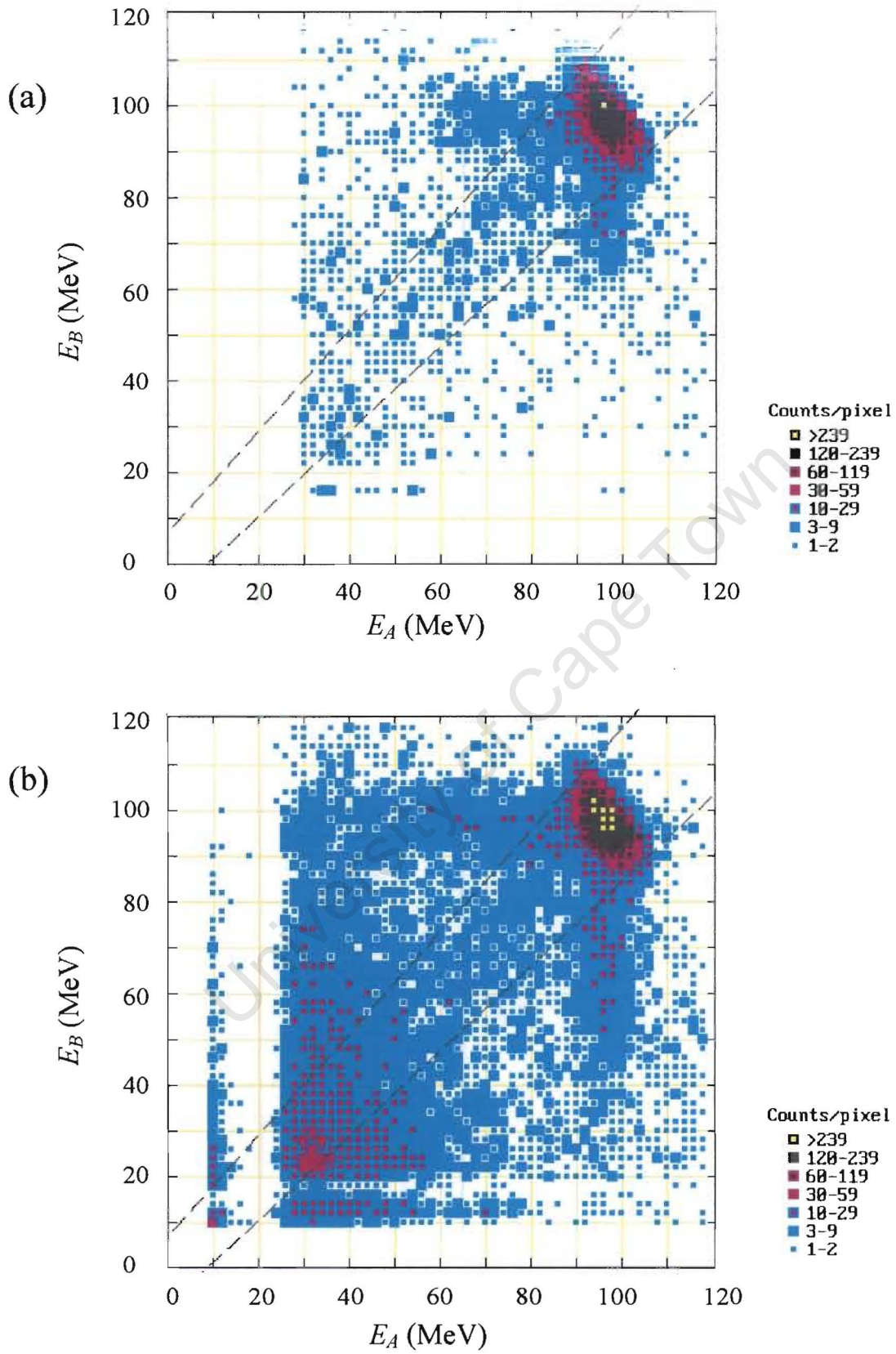

Figure 3.24: *Events per pixel as a function of energies E_A and E_B for the standard proton therapy beam (run 365) measured at the isocentre (a) with and (b) without the LS and DC cuts imposed to select true p-p coincidence events. The dashed lines indicate the E_{AB} cut used in the analysis.*

not negligible. These events can be due to backgrounds (see section 4.3) as well as to "double" reaction tail events.

The energy distribution $N_D(E)$ of detected events that satisfy all the off-line cuts (LS, ΔE-E, T and E_{AB} cuts) mentioned above is related to the proton energy spectrum, $N(E)$, by the equation

$$N_D(E) = \epsilon(E)N(E) \tag{3.10}$$

where $\epsilon(E)$ represents the efficiency for producing and detecting a coincident proton pair from p-p elastic scattering in the radiator (see figure 3.1). Since the proton pair spectrometer is designed so as to ensure that geometrical factors do not contribute to the energy-dependence of $\epsilon(E)$, the variation of $\epsilon(E)$ with E should be only due to the energy-dependence of the Rutherford cross section for p-p elastic scattering which is proportional to $1/E^2$ in the laboratory frame. Thus equation 3.10 may be rewritten as

$$N(E) = kE^2N_D(E) \tag{3.11}$$

where k is a constant. The constant k could not be determined independently, neither could different runs be normalized to the same value of k (same number of incident proton delivered by the accelerator) due to the lack of suitable proton beam monitoring as discussed in section 1.3. The value of k was thus arbitrarily adjusted to normalize the peak intensity of each spectrum to the value of 100 counts per energy bin. Figure 3.25 (a) shows the proton energy spectrum measured in this experiment for the standard proton therapy beam (run 365). The most prominent feature of the spectrum is the peak at high energy, the component that is tailored for proton therapy by the choice of specific beam modification elements. The energy thresholds of approximately 28 MeV for telescope A and approximately 24 MeV for telescope B, are clearly evident in figure 3.24. The E_{A}-E_{B} plots also indicate that peaks lying along the line where $E_{\mathrm{A}} \approx E_{\mathrm{B}}$ corresponding to coincident proton pairs with a combined energy lower than about 70 MeV will be sliced off due to the detection threshold of the spectrometer. This implies that the proton pair spectrometer had a threshold energy that ranges from about 55 to 70 MeV.

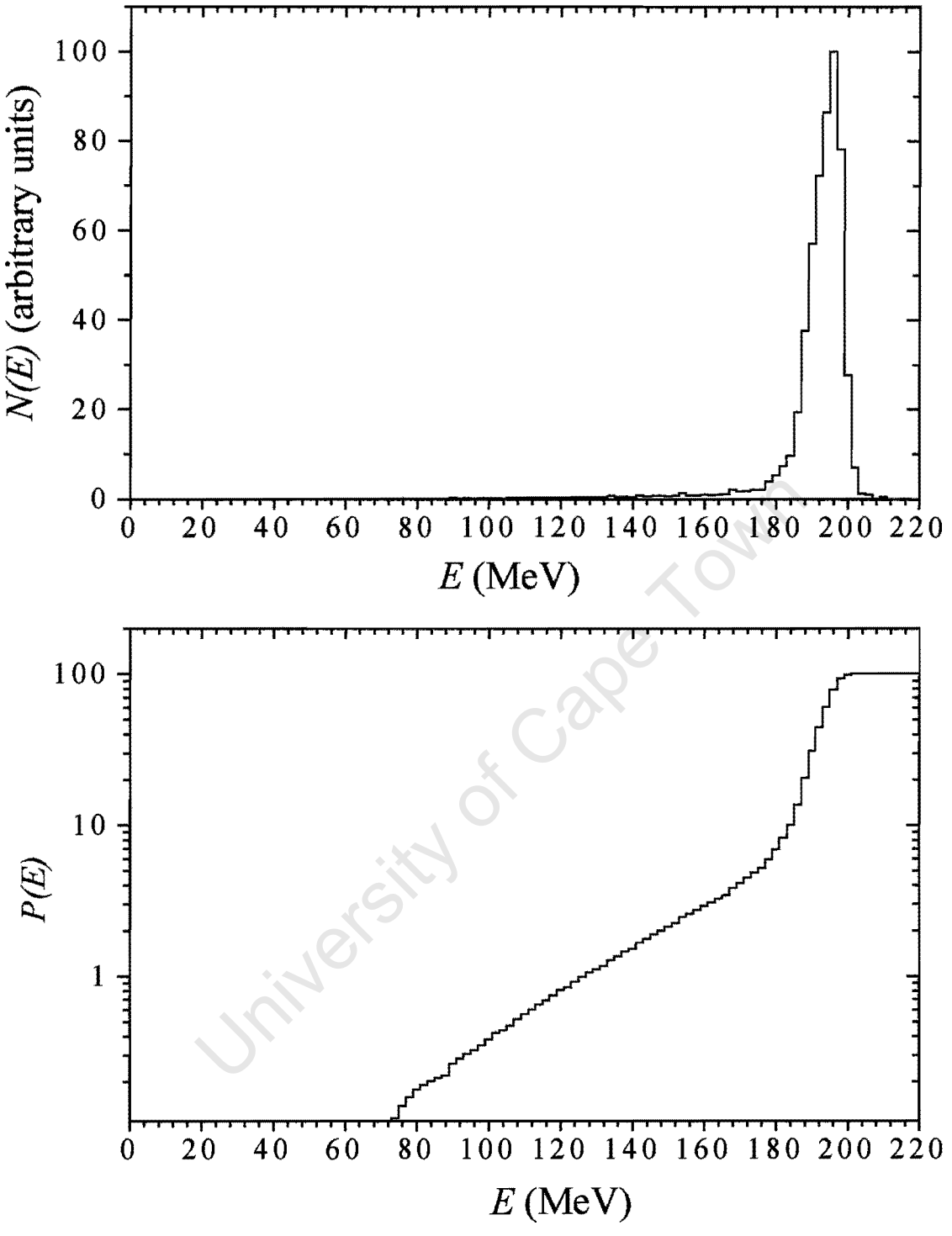

Figure 3.25: *Proton energy spectrum of the standard proton beam (run 365), measured with the proton pair spectrometer using a 3 mm thick polyethylene radiator mounted at the isocentre. (b) Percentage of protons in the spectrum shown in (a) which have energy E_p within the range $E_{th} < E_p < E$ as a function of proton energy (E).*

The fraction of protons with energies lower than E_{iso} may be conveniently displayed by calculating running integrals over the energy spectra, that is integrals P(E) of the number of events at energies between detection threshold energy E_{th} and energy E, as a function of E, from $E = E_{th}$ to an arbitrary upper limit of 200 MeV,

$$P(E) = k' \sum_{E_{th}}^{E} E^2 N_D(E) \tag{3.12}$$

where k' is a constant, which was adjusted to normalize the sum to 100. P(E) therefore gives the percentage of protons in the spectrum which have energy E_p within the range $E_{th} < E_p < E$. Figure 3.25 (b) shows a plot of the integral over the proton energy spectrum of the standard proton therapy beam (run 365), shown in figure 3.25 (a), generated using equation 3.12. The data in figure 3.25 (b) show, for example, that about 6% of the measured spectrum is due to protons of energy less than 176 MeV and more than 76% of the spectrum is due to protons with 180 MeV $< E <$ 200 MeV.

It has been demonstrated that the proton pair spectrometer developed for this work is successful in measuring the energy spectrum of high-energy proton beams. The shape of the measured spectrum gives information about the relative values of $N(E)$ (equation 3.11). The geometry of the detectors made it possible to determine the energy spectrum $N(E)$ without including the energy dependent geometric factor in the detection efficiency calculation spectromter. The spectrometer has an active range of 70 to 200 MeV, which is suitable for measuring energy spectra of proton therapy beams. The distribution of events in figure 3.24 (a) indicates that the background contribution to the measured energy spectrum is small ($< 1\%$), more details on the measurements of background and instrumental effects will be presented in section 4.3. The analysis of the spectra measured under these various irradiation conditions (shown in table 3.1) will be discussed in the following chapter.

Chapter 4

Measurements of proton energy spectra

Energy spectra of proton therapy beams were measured with the proton pair spectrometer shown in figure 3.1. The data reduction process was discussed in chapter 3 and the determination of the energy spectrum was demonstrated with the standard proton therapy beam (run 365). The energy spectrum measured with the standard proton therapy beam indicates that the spectrometer can successfully discriminate against events where one of the protons constituting the coincidence pair underwent a nuclear reactions in the NE213 scintillator as shown in figure 3.24 (a) (see section 3.4).

Studies have also been made of the spectra obtained using different beam line configurations such as including energy degraders and/or modulator propellers in the beam, final collimators of different diameters, and at positions displaced from the isocentre both along and perpendicular to the central axis of the beam. Measurements were also made with different radiators mounted at the isocentre to investigate the contribution of the background and accidental coincidences to the measured energy spectra. Table 4.1 shows a summary of measurements completed during the second weekend, grouped in terms of the objectives of the measurements. The table shows beam modification elements used for varying the properties of the beam, such as energy and spatial distribution, variations in the positioning of the detection system and the different radiators used.

Table 4.1: *Summary of experimental measurements completed in the present work to investigate spectral variations of proton therapy beams at the NAC. The energies are in units of MeV and distances and dimensions are in mm.*

Run number	(E_{iso})	Collimator diameter	Modulator propeller	Radiator size		Displacement from isocentre		Run category
				diam	thick	y	z	
365	190.8	40	0	10	3	0	0	Standard beam runs
380	190.8	40	0	10	3	0	0	
403	190.8	40	0	10	3	0	0	
366	91.9	40	0	10	3	0	0	Energy degraders (graphite wedges) in the beam
373	174.1	40	0	10	3	0	0	
399	134.6	40	0	10	3	0	0	
374	59.3	40	0	10	3	0	0	
384	190.8	40	50	10	3	0	0	SOBP-50
385	190.8	40	110	10	3	0	0	SOBP-110
386	91.9	40	50	10	3	0	0	SOBP-50, Wedges in the beam
387	190.8	5	0	10	3	0	0	Final (patient) collimator diameter changed
388	190.8	10	0	10	3	0	0	
389	190.8	100	0	10	3	0	0	
390	190.8	50	0	10	3	0	–280	Upstream of isocentre
391	190.8	50	0	10	3	25	–280	Off beam axis, upstream of isocentre
392	190.8	50	0	10	3	40	–280	
393	190.8	50	0	10	3	50	–280	
394	190.8	50	0	10	3	60	–280	
395	190.8	50	0	10	3	60	0	Off beam axis
396	190.8	50	0	10	3	50	0	
397	190.8	50	0	10	3	40	0	
376	190.8	40	0	0	0	0	0	No radiator
378	190.8	40	0	10	3	0	0	Graphite radiator
398	--	0	0	10	3	0	0	Blocked beam
400	91.9	40	0	10	1	0	0	Thin radiator, wedges in beam
401	190.8	40	0	10	1	0	0	Thin radiator
402	190.8	40	0	10	10	0	0	Thick radiator
404	190.8	40	0	22	3	0	0	Large diameter radiator
367	190.8	40	0	10	3	0	0	Singles in A
369	190.8	40	0	10	3	0	0	Singles in B
382*	196.0	40	0	10	3	0	0	No beam flattener

* The beam-flattening device (double scatterer and occluding rings) was out of the beam for run 382.

For each measurement shown in table 4.1, the following plots and spectra were generated:

i. an event density plot of events per pixel as a function of energies E_A and E_B measured in telescopes A and B, respectively, for events satisfying the LS, DC and T cuts (E_A-E_B plot). The counts per pixel scale (step sizes) in these plots differ in different figures, so as to suit the range of counts in the figure (from lowest to highest),

ii. the energy spectrum $N(E)$ of the incident proton beam was determined using equation 3.11 and normalized to a peak intensity of $N(E) = 100$,

iii. the integral $P(E)$ (equation 3.12) over the energy spectrum $N(E)$.

4.1 Effects of beam modification elements

4.1.1 Energy degraders

Figures 4.1 and 4.2 show E_A-E_B plots for incident proton energies with E_{iso} of 174.1, 134.6, 91.9 and 59.3 MeV (runs 373, 399, 366 and 374). The E_A-E_B plot for the standard proton therapy beam run was presented in section 3.4 (figure 3.24). A large fraction of events in figures 4.1 and 4.2 lie in the region where $E_A \approx E_B \approx 0.5E$, as required for events corresponding to detected proton pairs that originate from p-p elastic scattering of beam protons in the radiator (see section 3.5). The fraction of events from inelastic nuclear scattering in one of the detectors, that is events that trail away from the dominant peak at $E_A \approx E_B \approx 87$ MeV in figure 4.1 (a), either horizontally ($E_B \approx 87$ MeV, $E_A < 87$ MeV) or vertically ($E_A \approx 87$ MeV, $E_B < 87$ MeV), is observed to decrease with the decrease in the incident proton beam energy as expected (see figure 1.3 [Ja82]). Figure 4.2 shows that the low-energy part of the of the peak is sliced off due to the detection threshold of the system.

Figure 4.2 also shows that there is a small number of events ($< 1\%$) that extend beyond the region $E_A \approx E_B \approx 0.5E$ for the measurements made for proton beams with E_{iso} values of 91.9 and 59.3 MeV at the isocentre. These events are

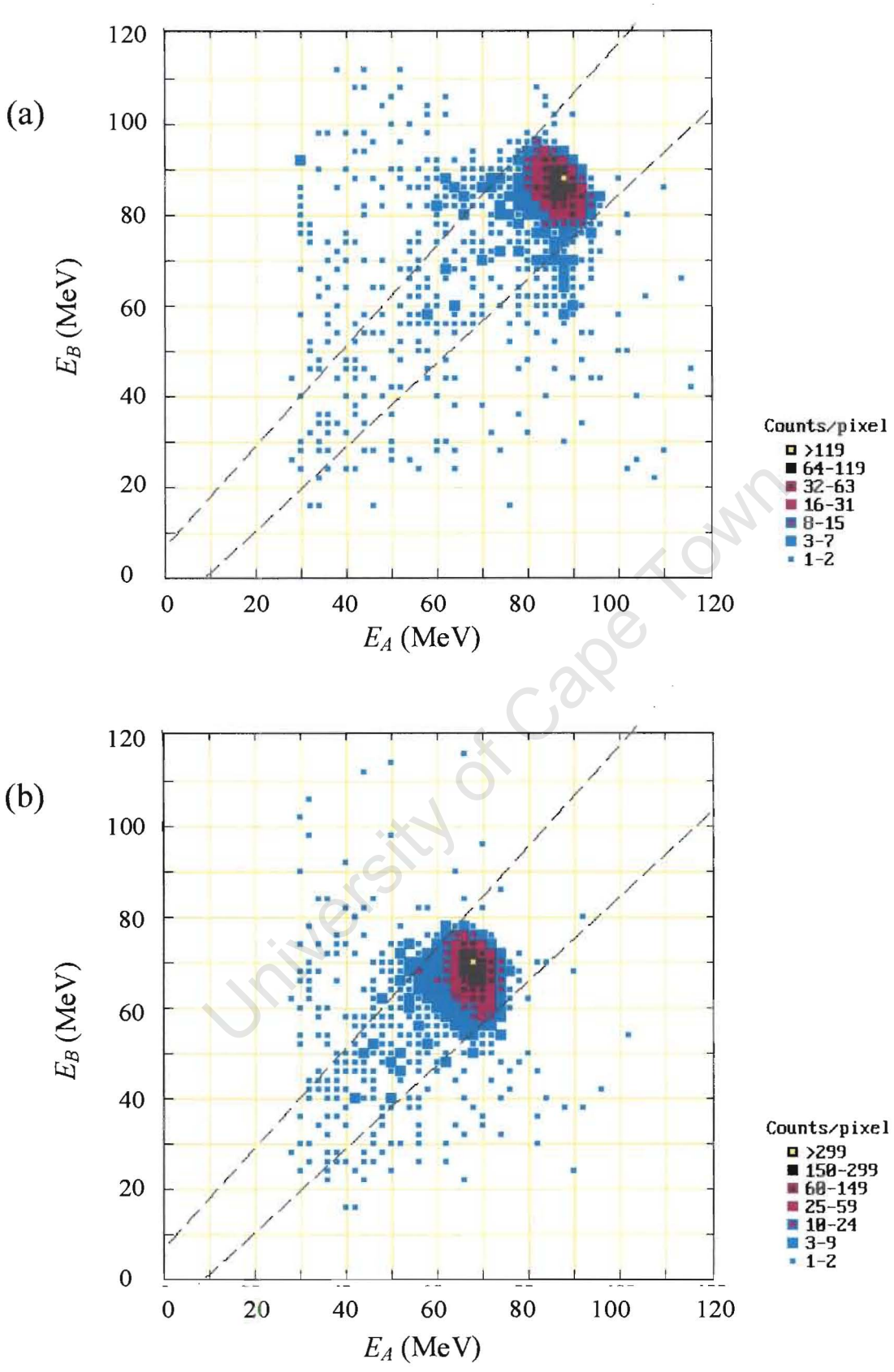

Figure 4.1: *Events per pixel as a function of energies E_A and E_B for proton beams with E_{iso} values of (a) 174.1 (run 373) and (b) 134.6 MeV (run 399). The LS, ΔE–E and T cuts were imposed to select coincidence events. The dashed lines indicate the E_{AB} cut used in the analysis.*

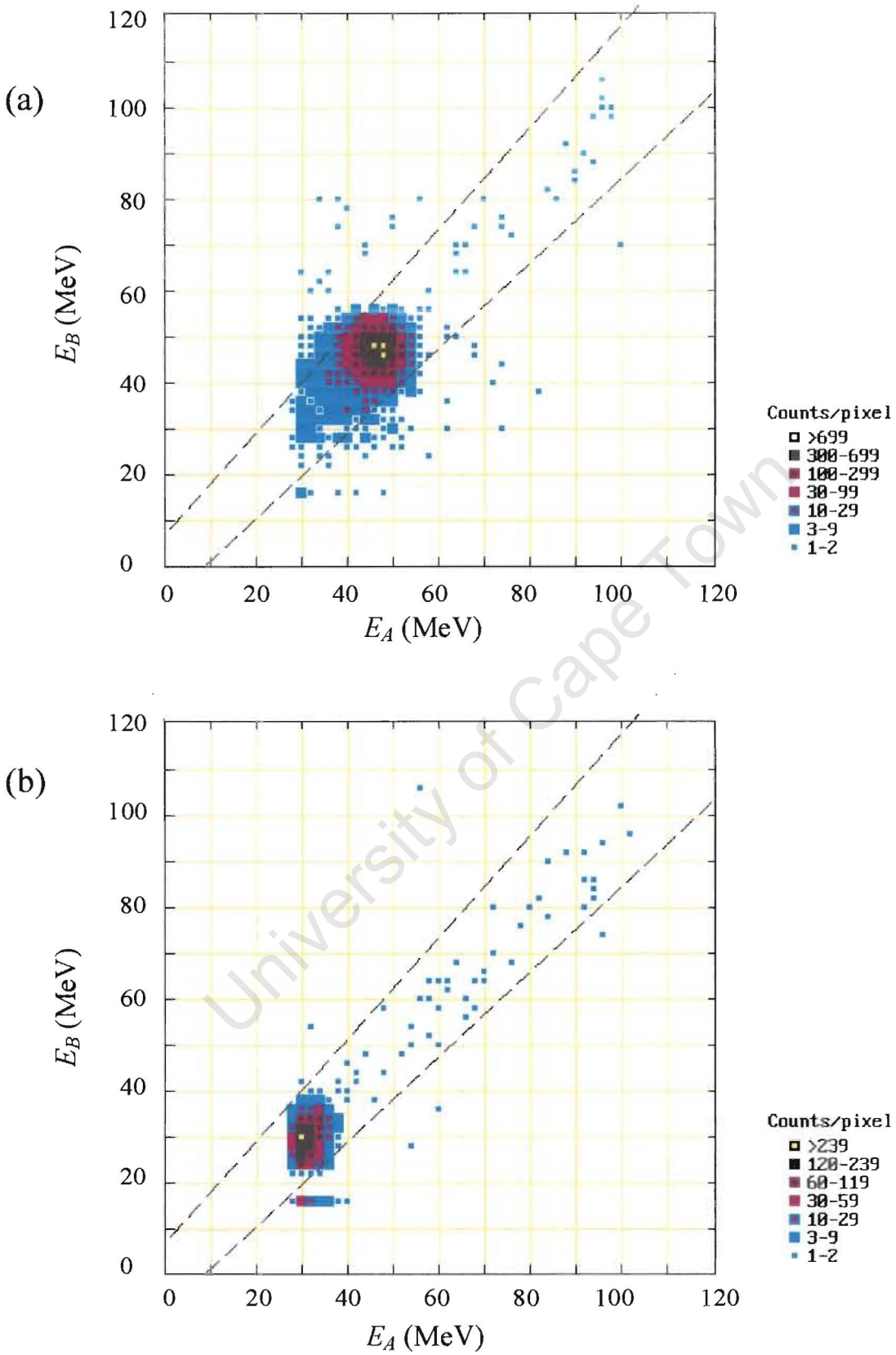

Figure 4.2: *Events per pixel as a function of energies E_A and E_B for proton beams with E_{iso} values of (a) 91.9 (run 366) and (b) 59.3 MeV (run 374). The LS, ΔE–E and T cuts were imposed to select coincidence events. The cut-offs in the events at $E_A \approx 23$ MeV and $E_B \approx 27$ MeV show the energy thresholds of the detector telescopes. The dashed lines indicate the E_{AB} cut used in the analysis.*

concentrated within the $E_A \approx E_B$ window, extending from the dominant peaks corresponding to 91.9 ($E_A \approx E_B \approx 46$ MeV) and 59.3 MeV ($E_A \approx E_B \approx 30$ MeV) proton beams to high energies ($E_A \approx E_B \approx 96$ MeV). This implies that there are protons with energies up to 190.8 MeV entering the radiator along the beam direction even when the graphite wedges (energy degraders) are in position in the beam. This is unexpected because protons in these beams cannot have energies greater than the expected maximum energies if they passed through the graphite degraders. It may be plausible that a very small fraction of the protons could somehow undergo multiple scattering along paths that bypass the graphite degrader and then return to a trajectory within the beam. The computerised feedback system acting on the two steering magnets used to control the beam at the NAC [NA94, Jo94, Sc95] is designed to work with high beam currents used for therapy and relies on the beam monitor that could not be operated at the low that were used in these experiments (section 1.2). The beam may therefore have been unstable in some of the measurements and protons may sometime have scattered on the steering magnets and the iron shielding on the sides of the graphite wedges thereby bypassing the wedges. An alternative possibility is that high-energy neutrons could possibly have been released from nuclear interactions, such as ^{12}C(p,n)^{12}N, occurring in the graphite degraders, followed by the n-p elastic scattering of the forward-emitted neutrons in hydrogenous material between the wedges and the radiator.

The effects of the graphite wedges on the proton energy spectrum are illustrated in figure 4.3 (a), which shows the energy spectra measured when graphite wedges are inserted to degrader the energy of the beam to E_{iso} values of 174.1, 134.6, 91.9 and 59.3 MeV. The energy spectrum of the standard proton therapy beam, that is the 190.8 MeV incident proton beam, is included for reference. Figure 4.3 (a) also shows that there is an increasing fraction of low energy protons (i.e. protons with energies less than the peak energy) in the beam with increasing incident proton beam energy. Figure 4.3 (b) shows a plot of running integrals $P(E)$ over the proton energy spectra $N(E)$ shown in figure 4.3 (a). These integrals over the spectra also show that the 190.8 and 174.1 MeV spectra have slightly larger fractions of low energy protons compared to the 134.6 and 91.9 MeV spectra, as shown by L(E) in table 4.2. L(E) is the percentage of protons in the spectrum, which have energy E_p within the range $E_{th} < E_p < E_{iso} - 10$ MeV. The peak on the proton energy

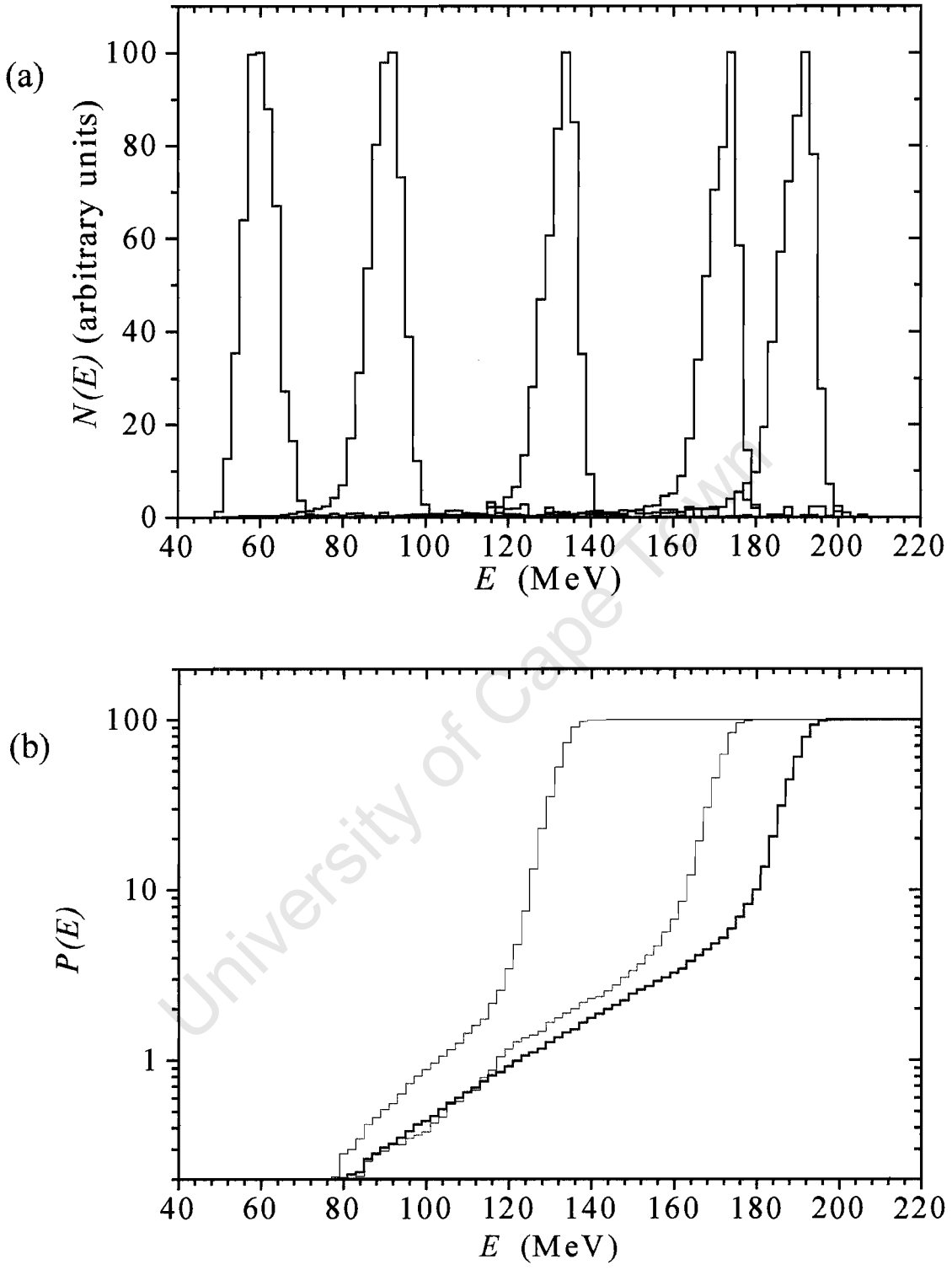

Figure 4.3: *(a) Proton energy spectra N(E) measured for incident protons with E_{iso} values of 190.8, 174.1, 134.6, 91.9 and 59.3 MeV. (b) Integrals P(E) over the proton energy spectra N(E) shown in (a) showing the percentage of protons in the spectrum which have energy E_p within the range $E_{th} < E_p < E$.*

Table 4.2: *Summary of experimental results indicating the effects of energy degraders and collimators on the percentage of low energy protons in the measured proton energy spectra. L(E) are the percentage of protons in each spectrum with energy E_p within the range $E_{th} < E_p < E_{iso} - 10$ MeV.*

Run number	E_{iso} (MeV)	Collimator radius (mm)	L(E)
365	190.8	40	10
373	174.1	40	10
399	134.6	40	8
366	91.9	40	7
387	190.8	5	5
388	190.8	10	5
389	190.8	100	13

spectrum of the 59.3 MeV incident proton beam lies close to the energy threshold (E_{th}) of the detection system (see figure 4.3 (a)).

4.1.2 Modulator propellers

Figure 4.4 shows E_A-E_B plots when the 50 mm (SOBP-50) and 110 mm (SOBP-110) modulator propellers (see section 2.2) were included in the beam modification system (runs 384 and 385). A large fraction of events lie in the diagonal region where $E_A \approx E_B$ as expected, from the E_{iso} down to the energy associated with the thickest blade of each modulator propeller. Figure 4.5 shows the proton energy spectra $N(E)$ and the associated running integrals $P(E)$ over the spectra for a 190.8 MeV proton beam measured without (dotted histogram) and with a 50 mm (solid histogram) and a 110 mm (dashed histogram) modulator propeller in the beam. Figure 4.6 shows the proton energy spectra $N(E)$ of a proton beam with E_{iso} of 91.9 MeV with a 50 mm modulator propeller excluded (dotted histogram) and included (solid histogram) in the beam modification system. The modulator propellers broadened the high-energy components of the spectra as expected, and there is no significant change in the fraction of protons below the (broadened) peak at high energy in the energy spectra measured with modulator propellers in the beam compared to that in the spectrum of the standard proton therapy beam.

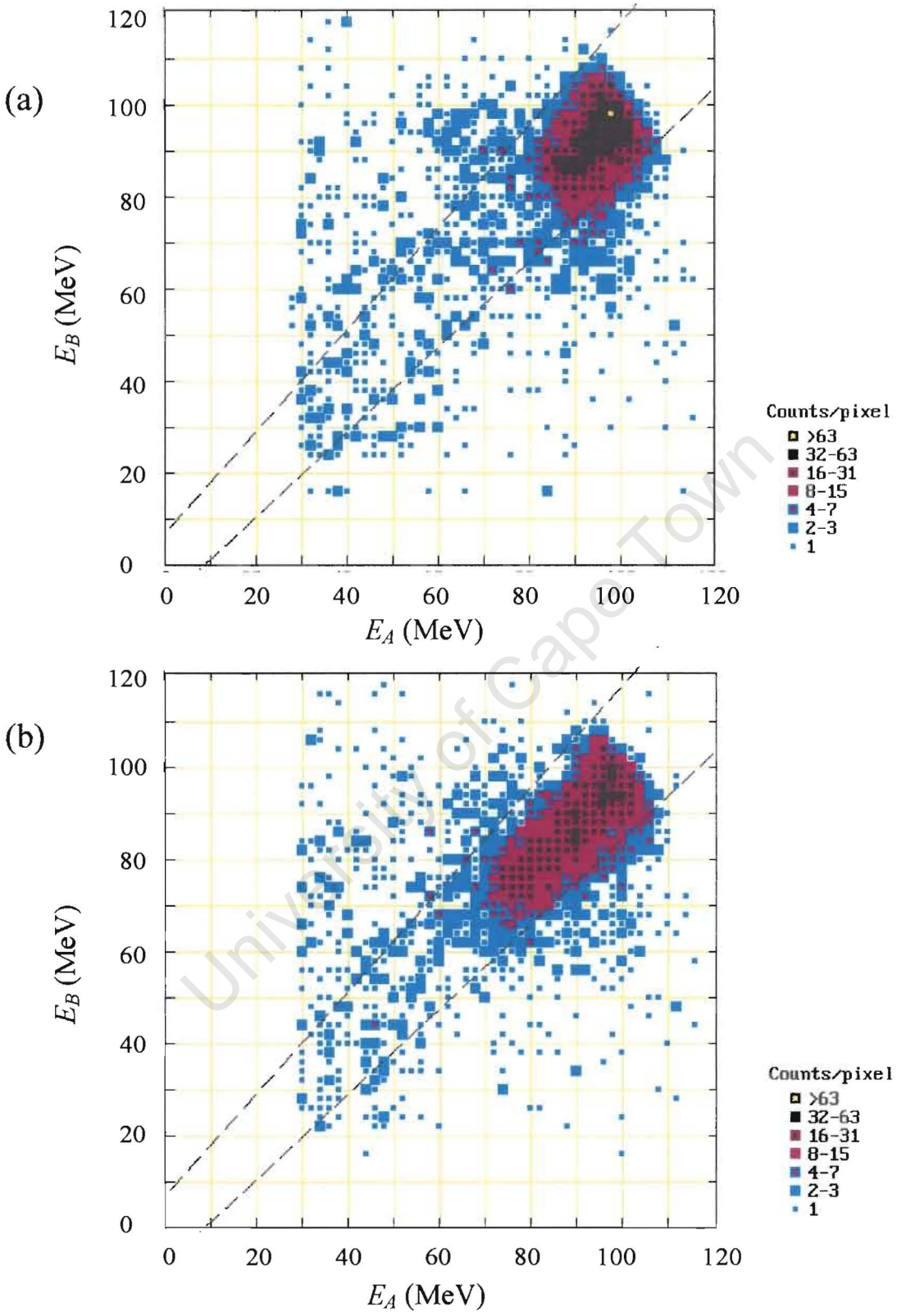

Figure 4.4: *Events per pixel as a function of energies E_A and E_B for an incident proton beam with E_{iso} of energy 190.8 MeV (a) with a 50 mm (SOBP-50) and (b) 110 mm (SOBP-110) modulator propeller included in the beam modification system. See text for details*

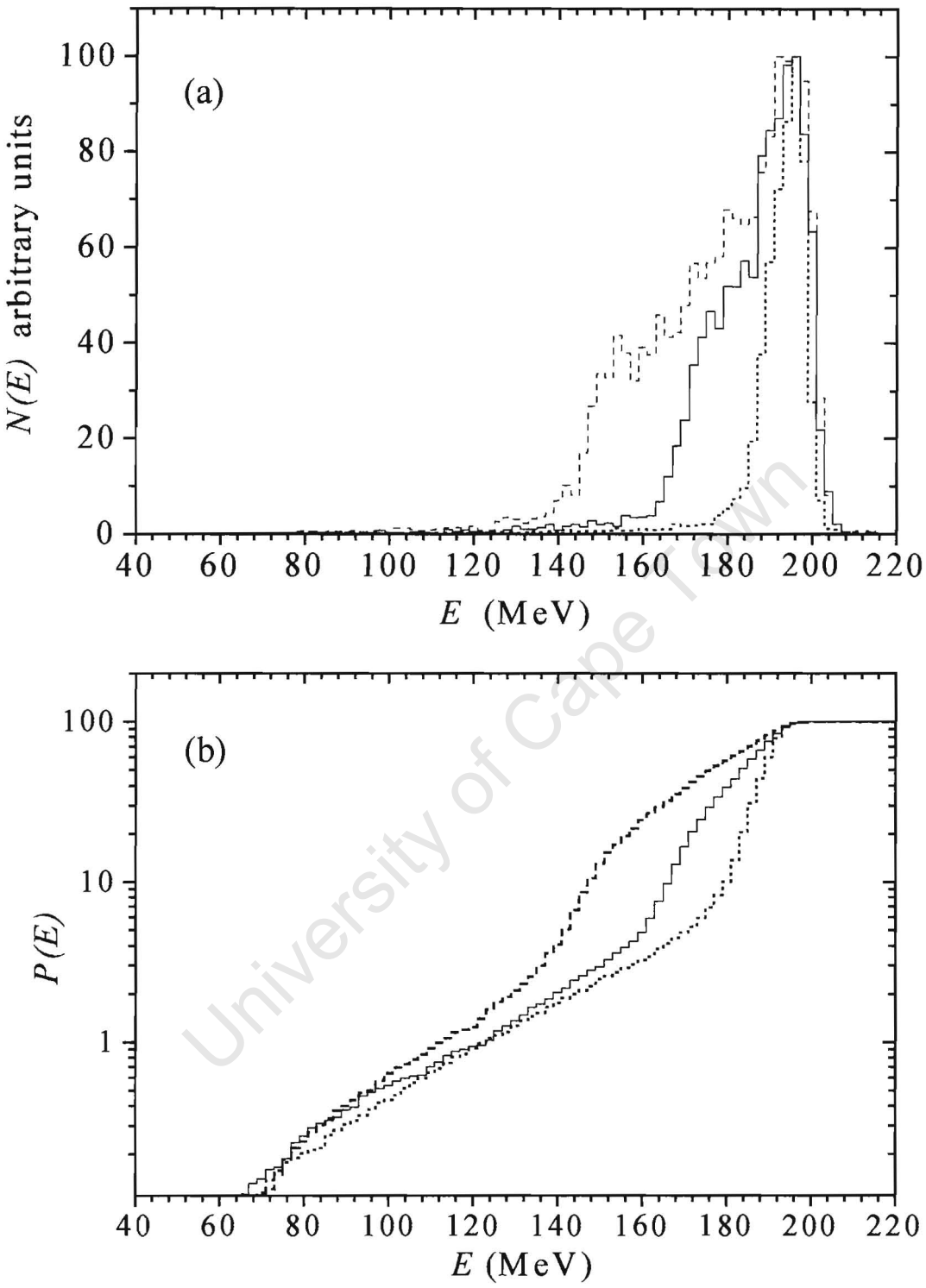

Figure 4.5: *Proton energy spectra N(E) measured for incident protons with E_{iso} of 190.8 MeV, without (dotted histogram), and with a 50 mm (solid histogram) and a 110 mm (dashed histogram) modulator propeller included in the beam modification system. (b) Integrals P(E) over the proton energy spectra N(E) shown in (a) showing the percentage of protons in the spectrum which have energy E_p within the range $E_{th} < E_p < E$.*

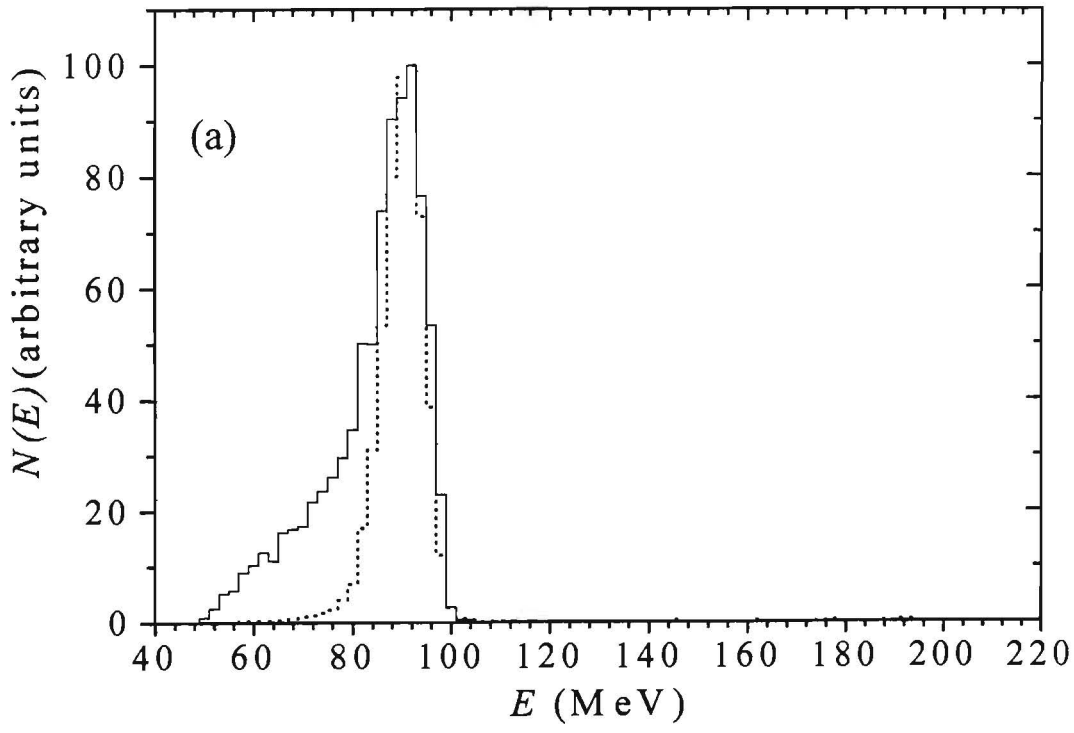

Figure 4.6: *(a) Proton energy spectra $N(E)$ measured for incident protons with E_{iso} of 91.9 MeV without (dotted histogram) and with a 50 mm modulator propeller (solid histogram) included in the beam modification system.*

4.1.3 Collimators

Circular collimators with diameters of 5, 10, 40 and 100 mm were used to investigate the effect of the collimator size on the energy spectrum (runs 387, 388, 365 and 389). Figure 4.7 shows the proton energy spectra $N(E)$ of a 190.8 MeV proton beam measured with collimators of four different diameters, and figure 4.8 shows the running integrals over the energy spectra $P(E)$. The increase in the diameter of the final (patient) collimator could be associated with an increase in the number of low energy protons reaching the treatment isocentre (see figure 4.8 and table 4.2). These results are in contrast to results obtained at the Kernfysich Versneller Instituut (KVI), Groningen, Netherlands using the Monte Carlo code GEANT 3.21 [Lu01]. The Monte Carlo results from KVI indicated that an increase in collimator diameter should yield a smaller fraction of scattered protons. The source of the discrepancy is not clear and must be investigated with more experimental measurements and Monte Carlo simulations.

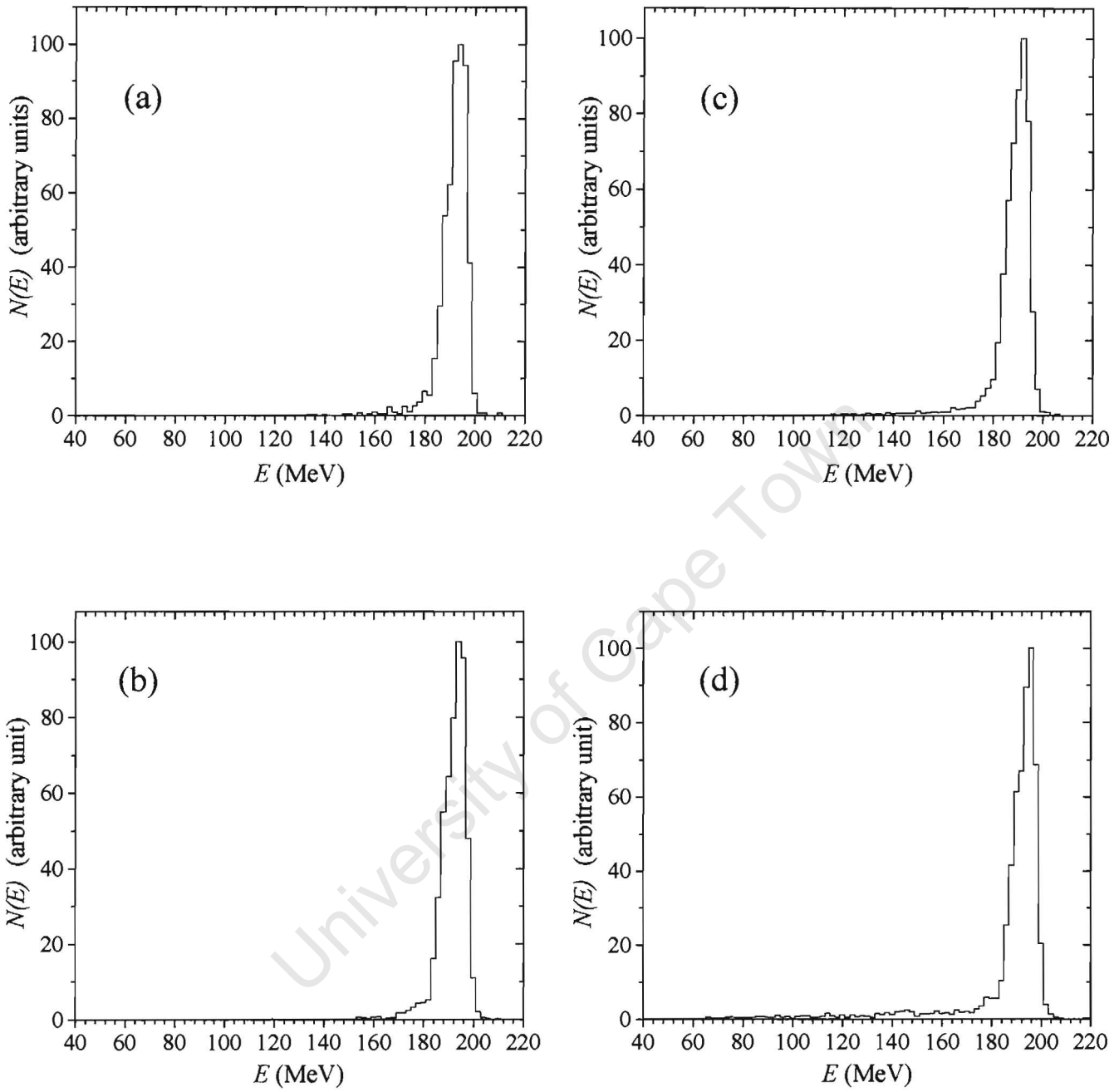

Figure 4.7: *Proton energy spectra N(E) of an incident proton beam with E_{iso} of 190.8 MeV and a final (patient) collimator of (a) 5, (b) 10, (c) 40 and (d) 100 mm radius in place.*

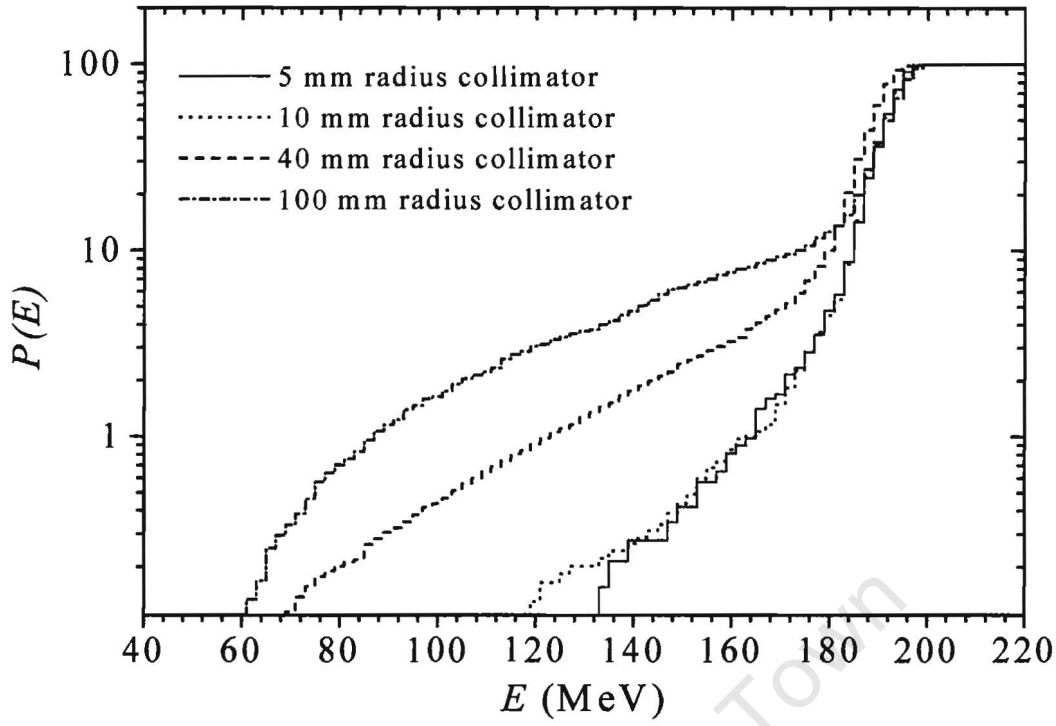

Figure 4.8: *Integrals P(E) over the energy spectra N(E) shown in figure 4.7, showing the percentage of protons with energy E_p within the range $E_{th} < E_p < E$ for a proton with E_{iso} of 190.8 MeV measured with a final collimator diameter of 5, 10, 40 and 100 mm in the beam modification system.*

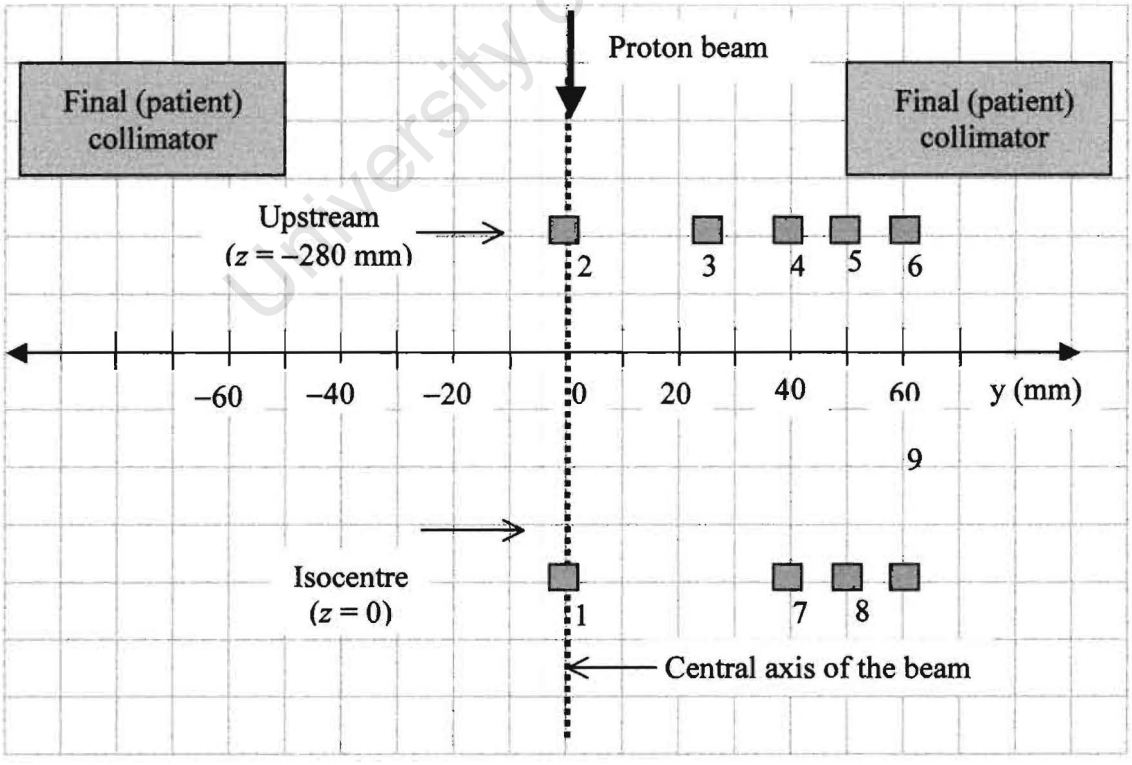

Figure 4.9: *A schematic diagram showing the positions of the centre of the radiator for measurements of the energy spectra at positions displaced from the isocentre. The (y,z) coordinates of the positions (1 to 7) are listed in table 4.3. See text for details.*

Table 4.3: *Summary of experimental results indicating the distribution of protons at positions displaced from the treatment isocentre, perpendicular to (y) and along (z) the central axis. L(E) are the percentage of protons in each spectrum which have energy E_p within the range $E_{th} < E_p < E_{iso}$ - 10 MeV.*

Run number	Collimator radius (mm)	Position of radiator in figure 4.10	Displacement from isocentre		L(E)
			y (mm)	z (mm)	
365	40	1	0	0	10
390	50	2	0	−280	19
391	50	3	25	−280	20
392	50	4	40	−280	20
393	50	5	50	−280	20
396	50	8	50	0	13
397	50	7	40	0	14

4.2 Measurements at positions away from the isocentre

Measurements were made at positions displaced from the isocentre both along and perpendicular to the beam axis (runs 390 to 397). These measurements were made by moving the table, as explained in chapter 3, so as to position the centre of the radiator at positions displaced 40, 50 and 60 mm from the isocentre perpendicular to the central axis, and 0, 25, 40, 50 and 60 mm lateral from the central axis, and on a plane 280 mm upstream of the isocentre (see figure 4.9 and table 4.3). All these measurements were undertaken with the flattening device (double scatter plus occluding rings) and a 100 mm diameter final collimator in place in order to provide a proton beam with a radius of 50 mm at the isocentre. Figure 4.10 shows the proton energy spectra $N(E)$ measured at positions displaced 40 and 50 mm from the isocentre (runs 396 and 397) compared with the standard proton beam spectrum (run 365). The spectra show that the percentage of low energy protons in the beam increases with the increase in displacement from the isocentre lateral to the beam's axis (see figure 4.11 and table 4.3).

Figure 4.12 (a) shows the proton energy spectrum $N(E)$ measured at a position 280 mm upstream of the isocentre along the central axis (solid histogram) compared

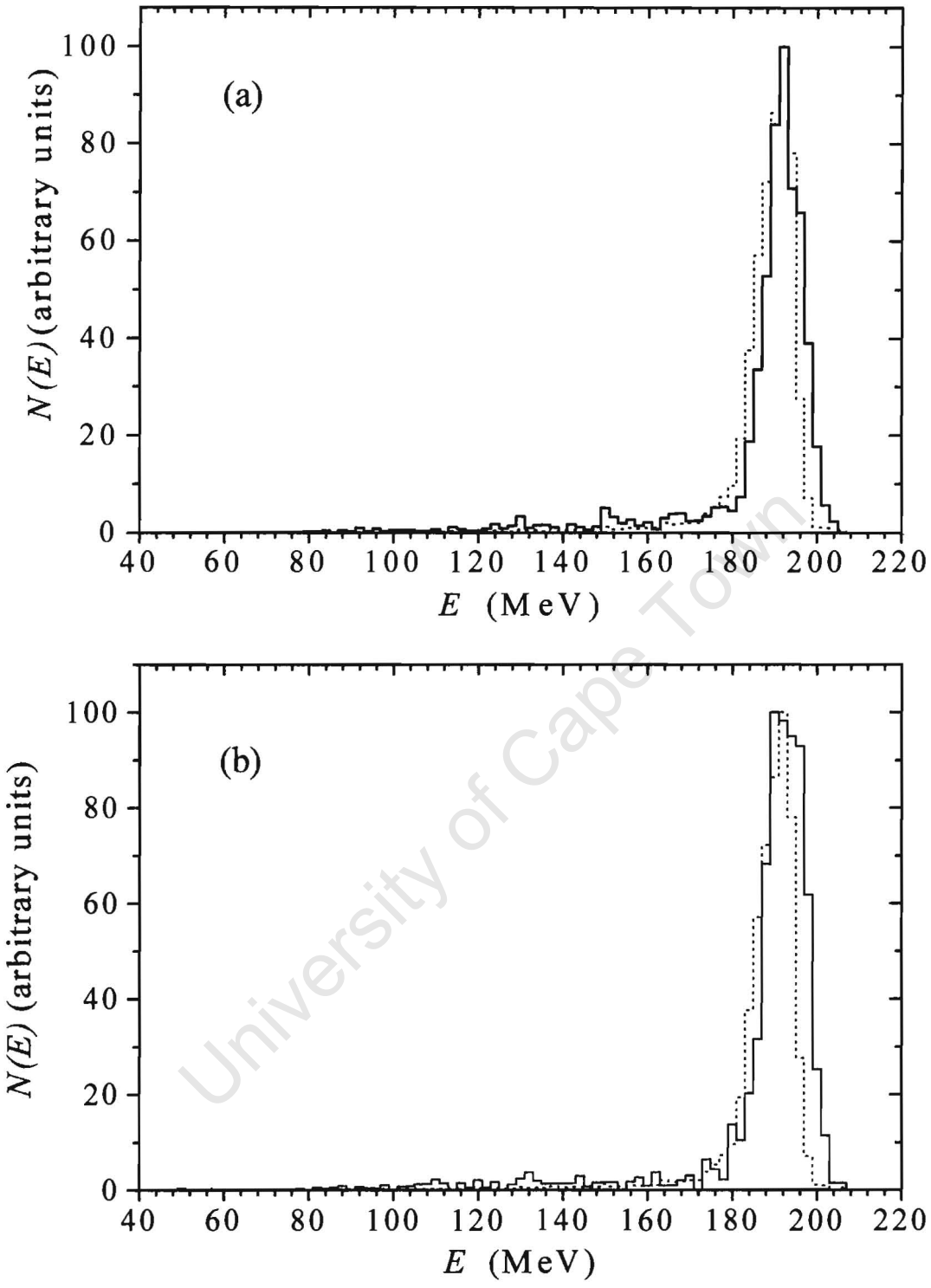

Figure 4.10: *Proton energy spectra measured at positions displaced (a) 40 and (b) 50 mm laterally from the isocentre (solid histograms), compared with the energy spectrum of the standard proton therapy beam (dotted histograms) measured with the radiator mounted at the isocentre.*

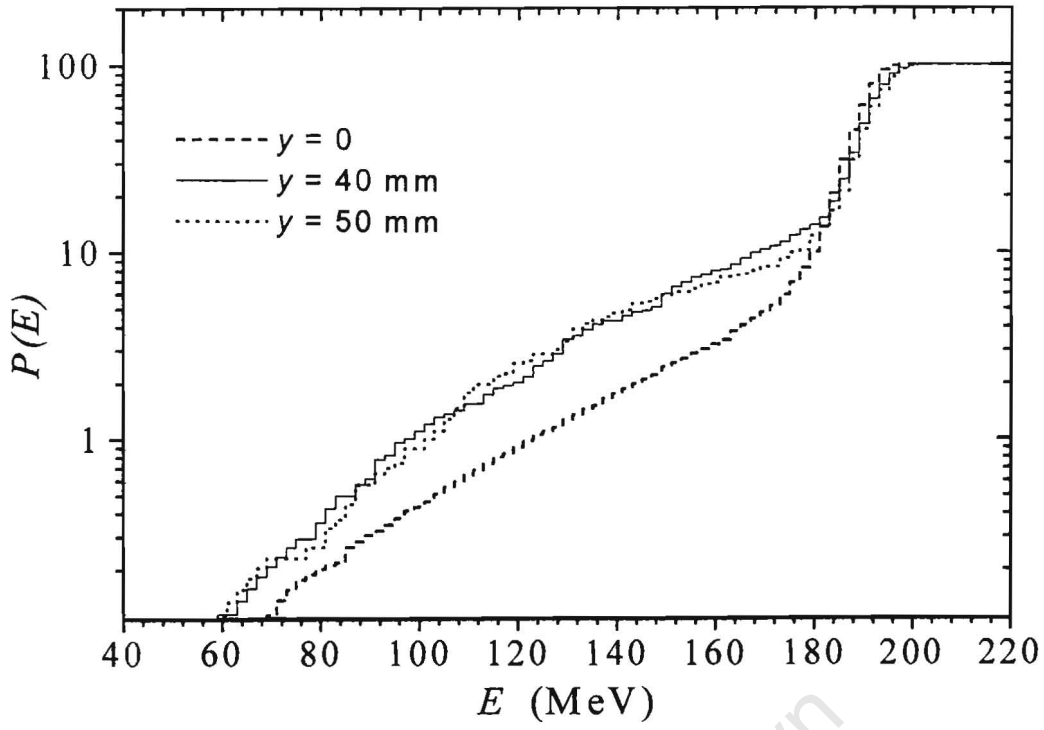

Figure 4.11: *Integrals $P(E)$ over the proton energy spectra $N(E)$ shown in figure 4.9, showing the percentage of protons in the spectrum which have energy E_p within the range $E_{th} < E_p < E$ for an incident proton beam of 190.8 MeV measured at positions displaced 0, 40, and 50 mm from the isocentre lateral to the beam's axis.*

with the spectrum of standard proton therapy beam measured at the isocentre (dotted histogram). The peak in the spectrum measured 280 mm upstream of the treatment isocentre moved to a higher energy by about 2 MeV as expected, due to the reduction in the amount of absorbing material (air) traversed. Furthermore the percentage of low energy protons in the spectra L(E) is higher at a position 280 mm upstream of the isocentre (see figure 4.12(b) and table 4.3). Figure 4.13 (a) shows a E_A-E_B plot for a proton beam with E_{iso} of 190.8 MeV, measured with the centre of the radiator placed 280 mm upstream of the isocentre along the beam axis (position 2 in figure 4.9). The E_A-E_B plot for a proton beam energy with E_{iso} of 190.8 MeV, measured at the isocentre (figure 3.24) is included in figure 4.12 for comparison. The low energy events, that is events lying on the region where $E_A < 80$ MeV and $E_B < 80$ MeV, are distributed evenly across the E_A-E_B plot, without any concentration of events in any region. The increase in the number of low energy protons observed in figure 4.12 and table 4.3 could be attributed to protons scattered by the brass collimator positioned 191 mm upstream of the final collimator. Figure 4.14 shows the integrals over the proton energy spectra measured with the centre of the radiator located at positions displaced by 25, 40 and 50 mm lateral to

the central (beam) axis, 280 mm upstream of the treatment isocentre (positions 3, 4 and 5 in figure 4.9), indicating the percentage of protons in the spectrum which have energy E_p within the range $E_{th} < E_p < E$. The fraction of the low-energy component in the energy spectrum measured with the centre of the radiator placed at positions 3, 4 and 5 in figure 4.9 did not change significantly (see figure 4.14 and table 4.3). This indicates that the fraction of low-energy protons in the beam is constant across the diameter of the beam in the plane 280 mm upstream of the isocentre. The count rate dropped significantly when the radiator was moved from 50 mm to 60 mm from the beam axis both around the isocentre (i.e. from position 5 to 6 in figure 4.9) and at a positions displaced 280 mm upstream of the isocentre (i.e. from position 8 to 9 in figure 4.9), which indicates that the beam had a sharp lateral penumbra. Figure 4.15 shows E_A-E_B plots of proton events measured when the detection system was positioned with the centre of the radiator placed at $z = 0$, $y = 60$ mm (position 6 in figure 4.9) and at $z = -280$ mm, $y = 60$ mm (position 9 in figure 4.9). The few events detected are dispersed randomly on the E_A-E_B plane without any concentration of events in any region. These events may be attributed to accidental coincidences due to protons scattered by the final collimator.

4.3 Background and instrumental effects

4.3.1 Background measurements

The contribution of background radiation and accidental coincidences in the measured energy spectra were investigated by taking measurements with (i) a graphite radiator in place of the polyethylene radiator at the isocentre (run 378), (ii) no radiator in place (run 376) and (iii) the final collimator blocked (run 398). The measurement with a graphite radiator in place of the polyethylene radiator was made to investigate the contribution from the proton interactions with the carbon nuclei in the radiator to the coincidence events. Figure 4.16 shows a E_A-E_B plot for an incident proton beam with E_{iso} of 190.8 MeV, measured (a) with a graphite radiator mounted at the isocentre and (b) with no radiator at the isocentre. The events in figure 4.16 are distributed uniformly across the two-parameter plots and there is no indication of a concentration of events in any region on the plot. Protons detected by the telescopes in run 378 are predominantly from elastic scattering of

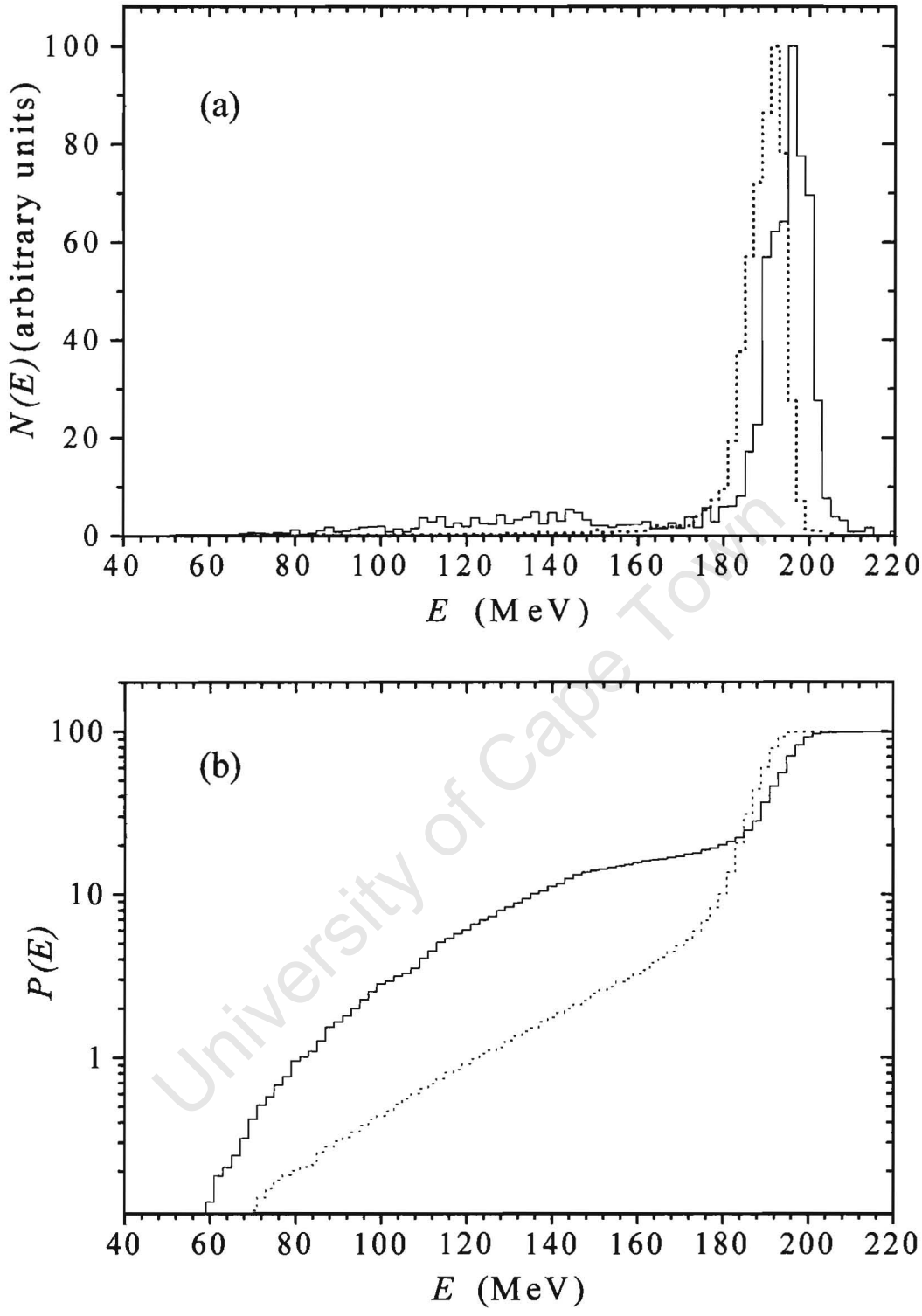

Figure 4.12: *(a) Energy spectra of a proton beam with E_{iso} of 190.8 MeV measured with the polyethylene radiator positioned at the isocentre (dotted histogram) and 280 mm upstream of the isocentre along the central axis (solid histogram). (b) Running integrals over the energy spectra shown in (a) showing percentage of protons in the spectra, which have energy E_p within the range $E_{th} < E_p < E$.*

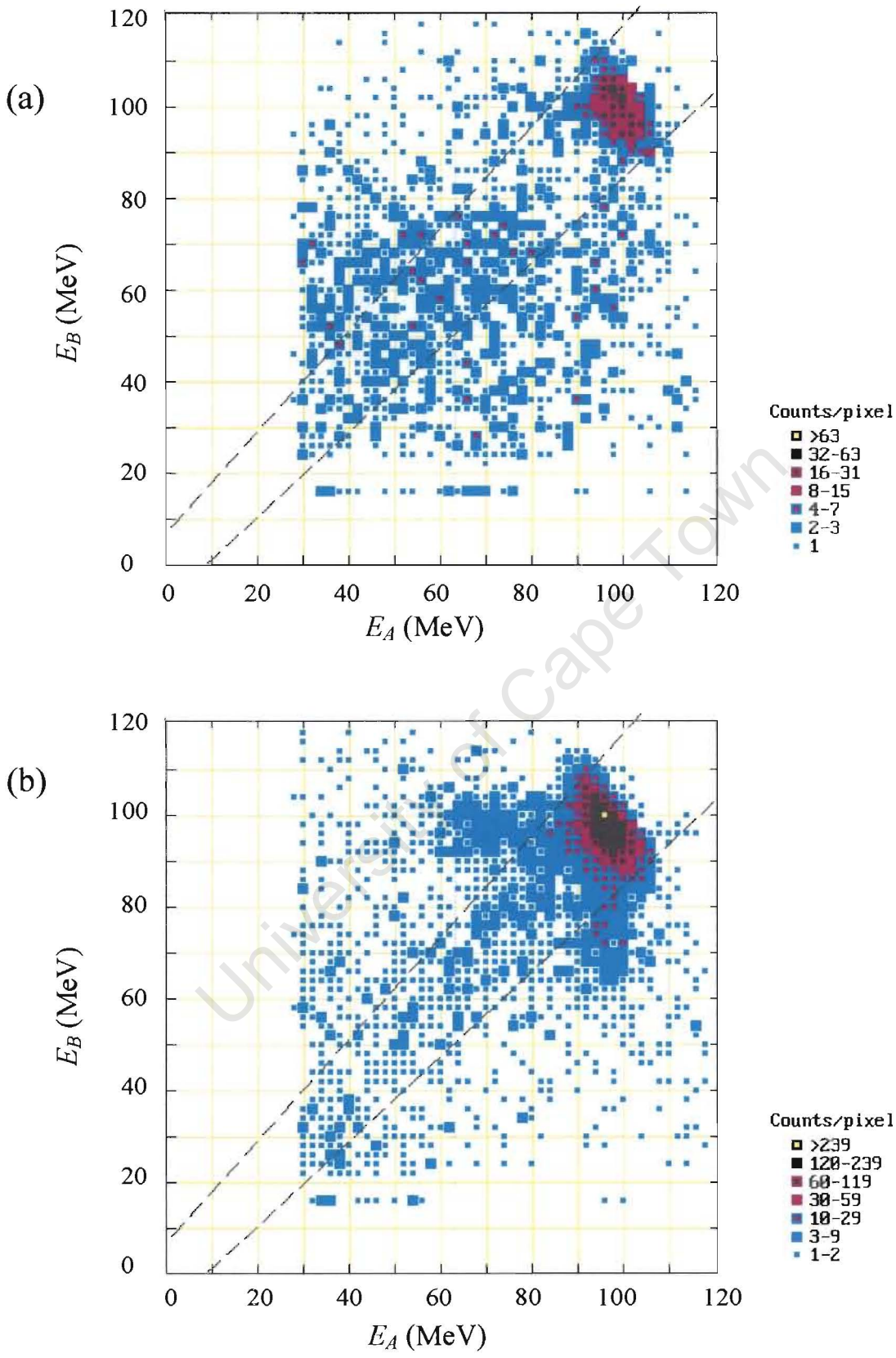

Figure 4.13: *Events per pixel as a function of energies E_A and E_B for incident proton with E_{iso} of 190.8 at the isocentre measured (a) at a position displaced 280 mm upstream of the isocentre along the beam axis (run 390) and (b) at the isocentre (as in figure 3.24 (a)). The dashed lines indicate the E_{AB} cut used to select coincident proton pairs.*

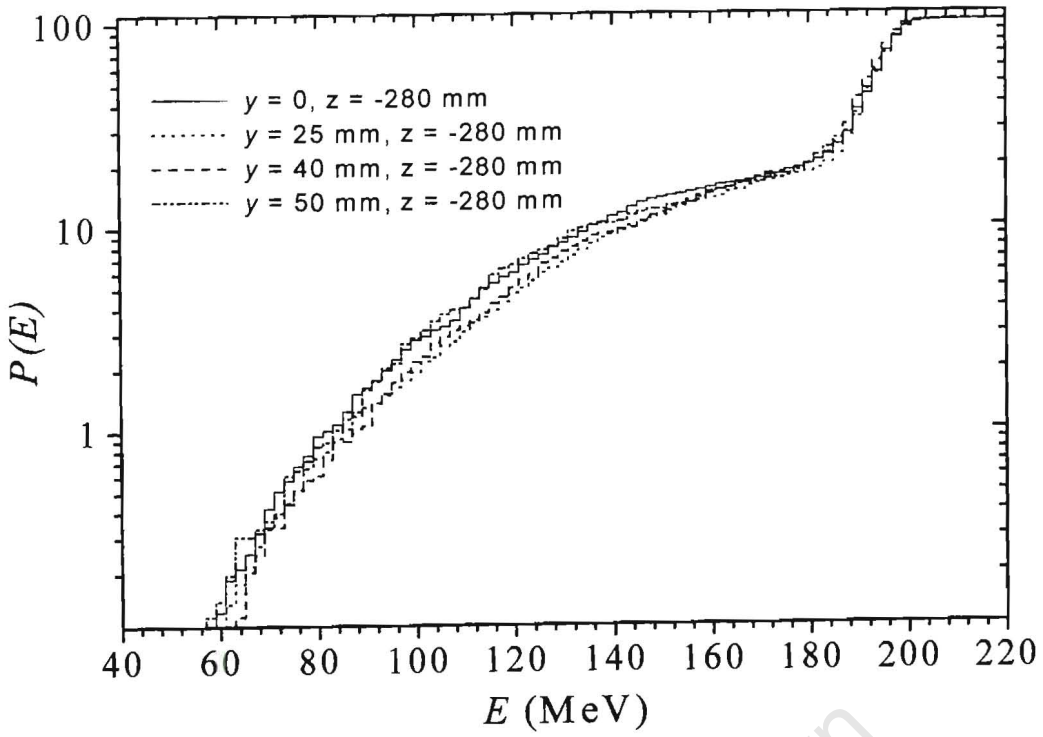

Figure 4.14: *Integrals $P(E)$ over the proton energy spectra showing the percentage of protons in the spectrum which have energy E_p within the range $E_{th} < E_p < E$ measured 280 mm upstream of the treatment isocentre along the beam axis and at positions displaced 25, 40, and 50 mm lateral to the beam's axis.*

incident protons by the carbon nuclei in the graphite radiator. Events detected by the two telescopes in run 376 are attributed to accidental coincidences of protons scattered by the final collimator. Runs 378 and 376 were about 1 hour and 0.5 hour long, respectively and the standard proton therapy beam run (run 365) was about 4 hours long. The beam current, based on the cyclotron operating log, was approximately the same and constant during all of these runs (365, 376 and 378) therefore the runs may all be normalized (approximately) to the same number of protons incident on the radiator by normalizing them to the same run duration, in other words by multiplying counts observed in runs 376 and 378 by factors of 8 and 4 respectively. When this is done the counts/pixel in figure 4.16 (b) (run 376) indicate that the number of events in the measurements made without the radiator will be similar to the number of events in the measurement made with the graphite radiator figure 4.16 (a). This implies that most of the events observed in figure 4.16 (a) are due to the accidental coincidences of protons scattered by the final collimator and not by the accidental coincidences of proton scattered by the carbon nuclei in radiator. Therefore most of the accidental coincidences in the measurements made with the polyethylene radiator placed at the isocentre are due

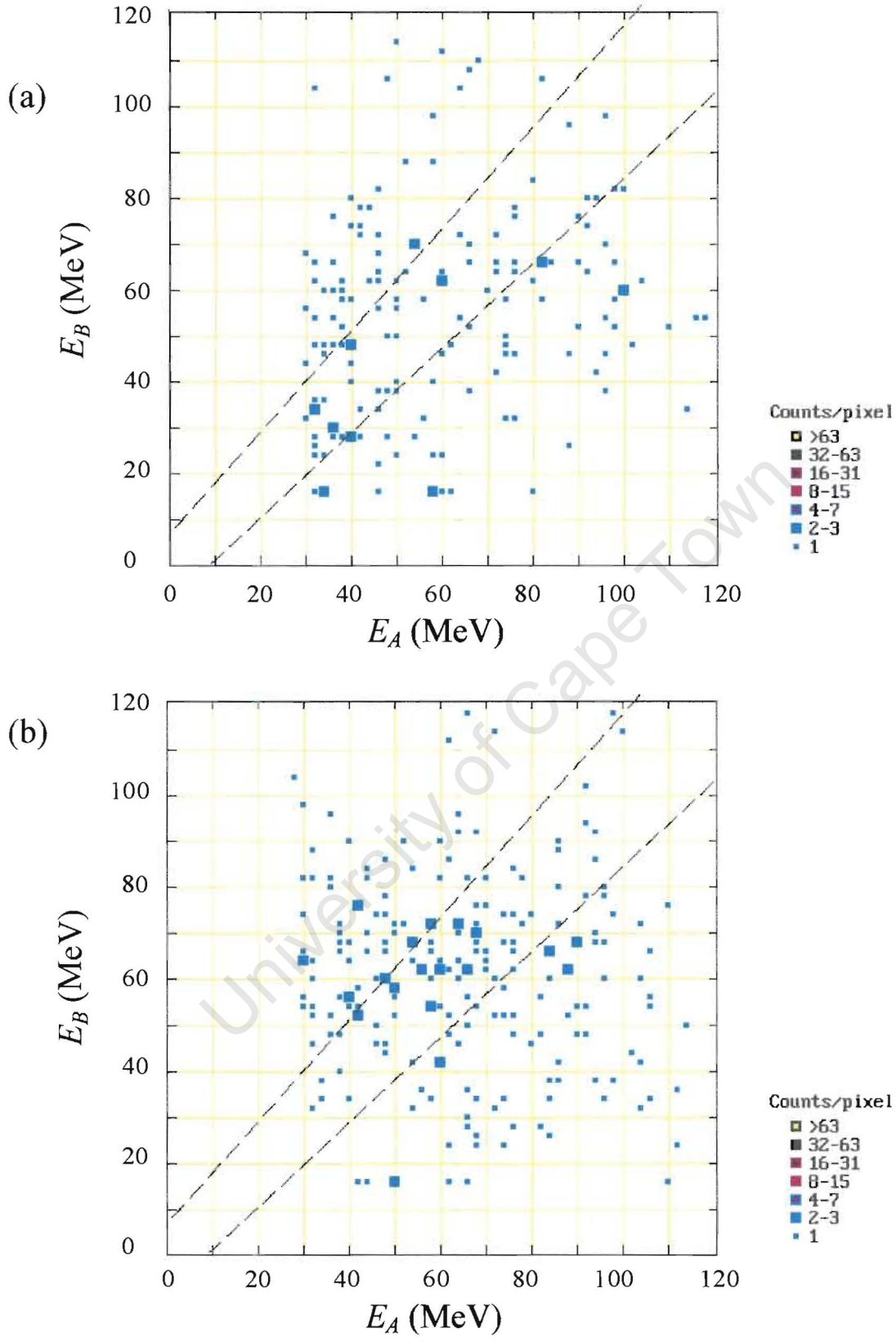

Figure 4.15: *Events per pixel as a function of energies E_A and E_B for measurements made at positions displaced 60 mm from the central beam axis (a) around the isocentre (run 395) and (b) 280 mm upstream of the isocentre along the central axis (run 394).*

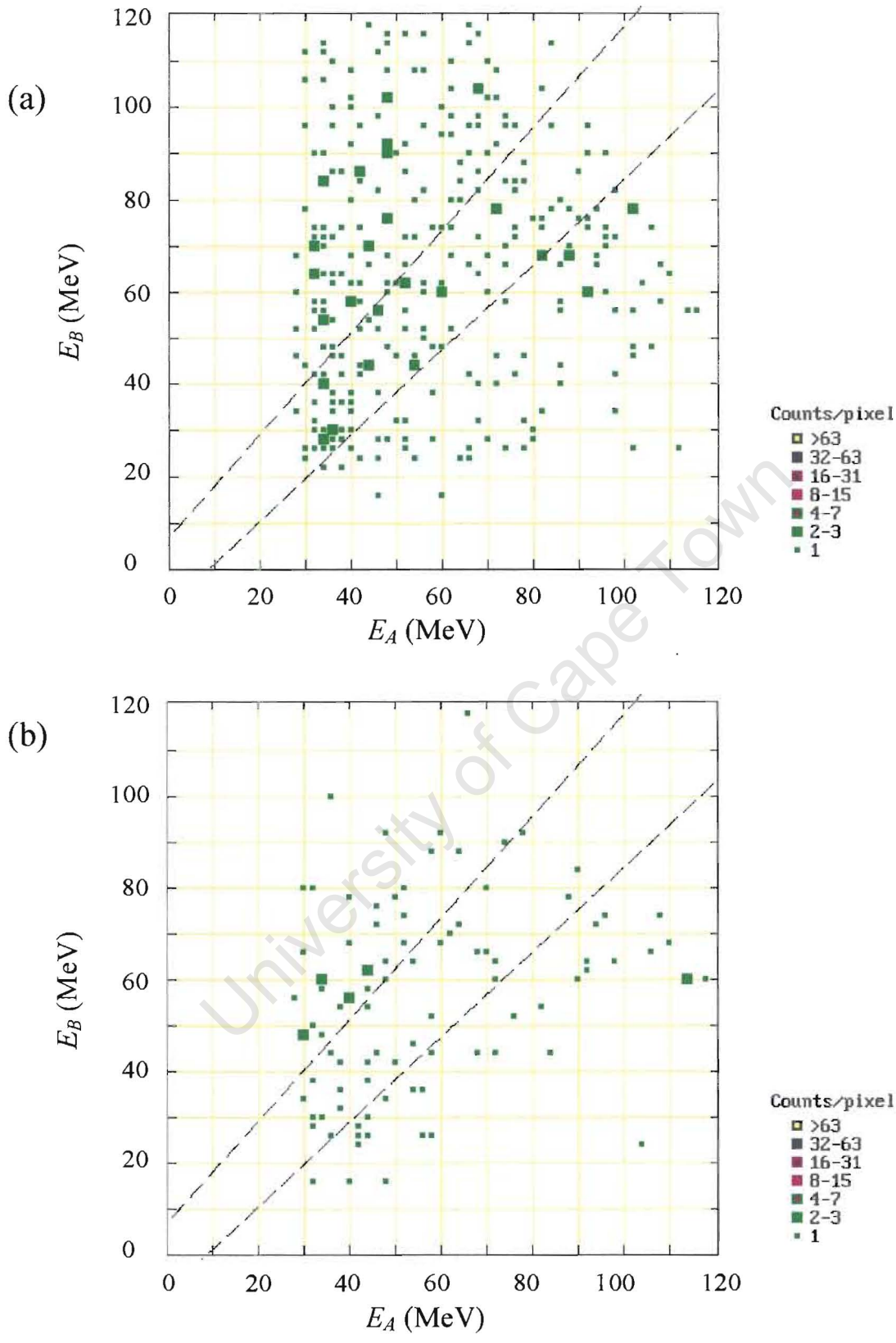

Figure 4.16: *Events per pixel as a function of energies E_A and E_B for a 190.8 MeV proton beam incident at the isocentre with (a) a graphite radiator mounted at the isocentre (run 378) and (b) no radiator mounted at the isocentre (run 376).*

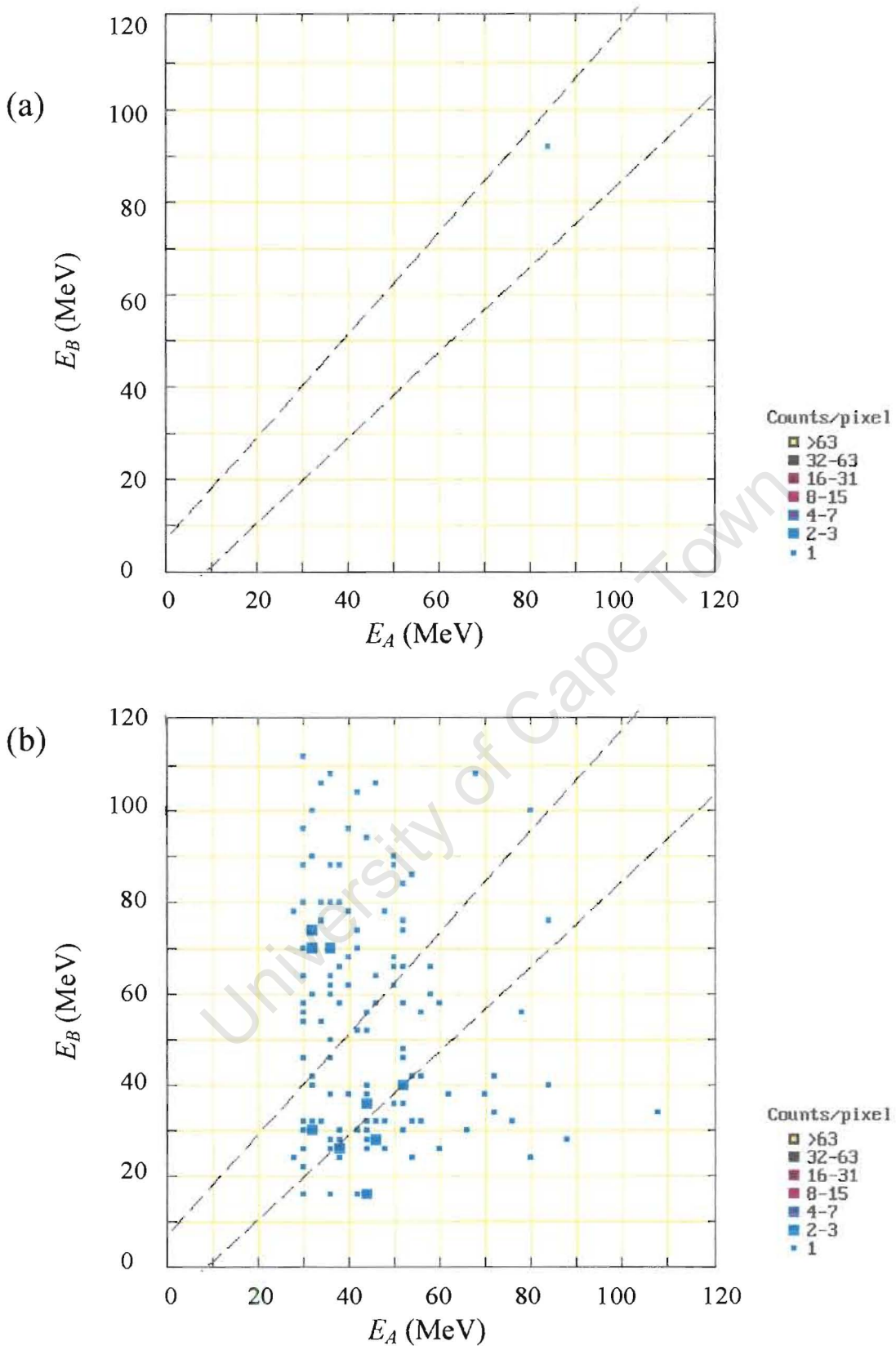

Figure 4.17: *Events per pixel as a function of energies E_A and E_B for a 190.8 MeV proton beam incident at the isocentre with (a) the final collimator blocked (run 398) and (b) T cut set to select the satellite peak at channel number 1200 instead of the prompt coincidence peak at channel number 2000 in figure 3.14 (run 365).*

to protons scattered by the final collimator.

Figure 4.17 shows a E_A-E_B plot for an incident proton beam energy of 190.8 MeV at the isocentre, measured (a) with the final (patient) collimator blocked and (b) with the T cut set to select the satellite peak at channel number 1200 in figure 3.14 instead of the prompt coincidence peak at channel number 2000. The events in figure 4.17 (b) are attributed to the coincidences due to protons from preceding and succeeding cyclotron bursts with protons in the cyclotron burst producing the main coincidence time delay peak in figure 3.14 (b) satisfying the LS and DC cuts (see section 3.2.3). The low number of events in figure 4.17 (b) and the uniform distribution of events on the E_A-E_B plot indicate that the contribution of these accidental coincidences to the proton energy spectrum $N(E)$ is negligible. These measurements indicate that the proton pair spectrometer is successful in selecting coincident proton pairs and discriminating against the background and accidental coincidences. A similar number of these accidental coincidence peaks will also be in the prompt coincidence peak.

4.3.2 Effects of radiator size

Measurements of the energy spectrum of the incident proton beam with E_{iso} values of 190.8 and 91.9 MeV were made with radiators of different dimensions mounted at the isocentre to investigate the effects of the radiator size, if any, on the measured energy spectra (see tables 4.1 and 4.4). Figure 4.18 shows the proton energy spectrum of a proton beam with E_{iso} of 91.9 MeV measured with radiators of dimensions: 10 mm diameter, 3 mm thick (solid histogram); and 10 mm diameter, 1 mm thick (dotted histogram) mounted at the isocentre. Figure 4.18 indicates that the increase in the thickness of the radiator from 1 mm to 3 mm is associated with an increase of about 1 MeV in the FWHM of the high-energy peak in the spectrum. Figure 4.19 shows the energy spectra $N(E)$ and the corresponding running integrals $P(E)$ over the spectra of the 190.8 MeV proton beam measured with radiators of dimensions: 10 mm diameter, 3 mm thick (solid histogram); 10 mm diameter, 1 mm thick (dashed histogram); and 10 mm diameter, 10 mm thick (dotted histogram) mounted at the isocentre. The increase in the thickness of the radiator from 3 mm

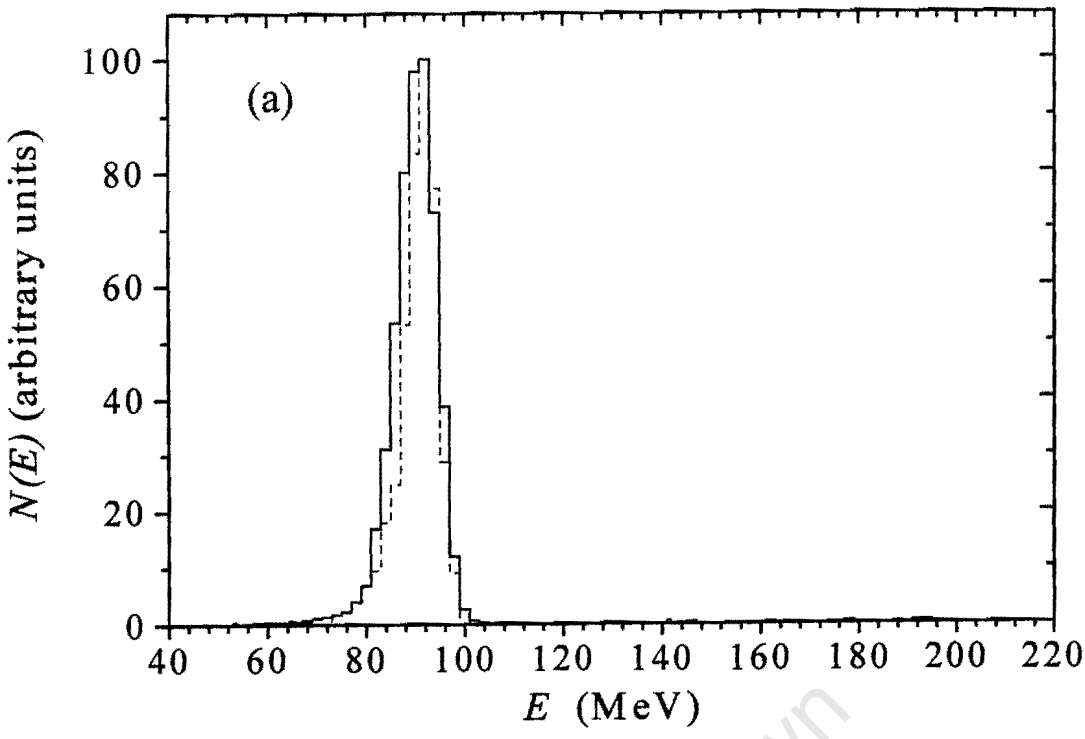

Figure 4.18: *(a) Energy spectra for a 91.9 MeV proton beam measured with radiators of dimensions: 10 mm diameter, 3 mm thick (solid histogram) and a 10 mm diameter, 1 mm thick (dashed histogram), mounted at the treatment isocentre.*

to 10 mm does not seem to significantly affect the fraction of low energy protons in the measured energy spectrum (see figures 4.18 and 4.19, and table 4.4). The energy spectrum measured with a thin radiator (10 mm diameter, 1 mm thick) seems to have a larger fraction of low energy protons (see figure 4.19). The reduction in the thickness of the radiator resulted in a smaller number of proton targets available for p-p elastic scattering in a 1 mm thick radiator compared to number of proton targets available in runs made with a 3 mm thick radiator mounted at the isocentre. The accidental coincidences due to protons scattered from the final collimator will however be the same in all the runs when they are all normalized to the same number of protons incident on the radiator. The signal to accidental coincidences ratio will therefore be low in the measurements made with a thinner (1 mm) radiator compared to that of measurements with thicker radiators (3 and 10 mm) when normalized to the same number of protons incident on the radiator. The energy spectrum measured with a thinner radiator mounted at the isocentre is therefore expected to have a lower signal to accidental coincidences ratio compared to that of the spectra measured with thicker radiators. Due to this low signal to accidental coincidences ratio the energy spectrum measured with a 1 mm radiator appears to have a high proportion of low energy protons (see figure 4.19). The increase in the diameter of the radiator does not seem to affect the fraction of low energy protons in the measured energy spectrum (see figure 4.20 and table 4.4).

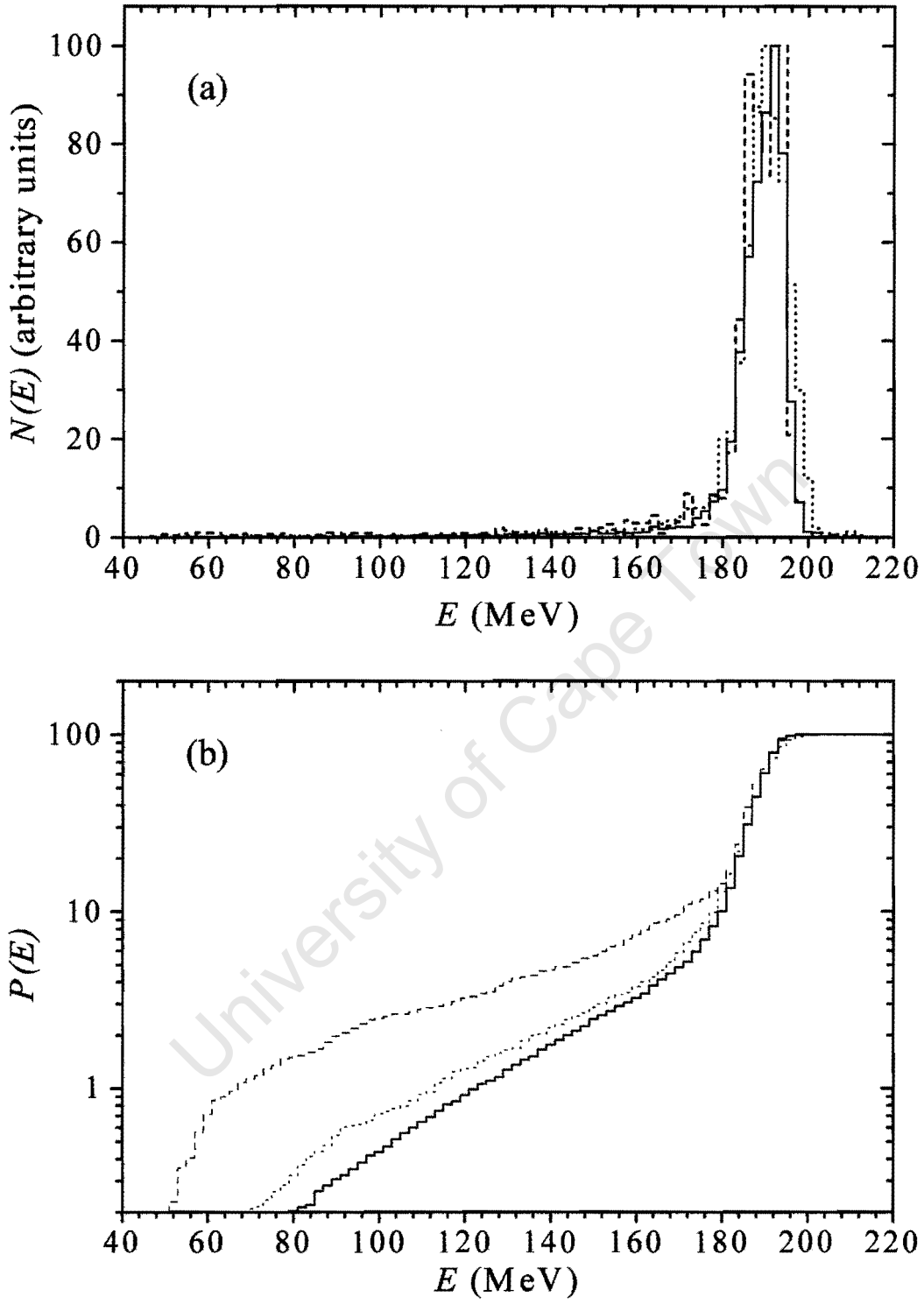

Figure 4.19: *(a) Energy spectra N(E) for a 190.8 MeV proton beam measured with radiators of dimensions: 10 mm diameter, 3 mm thick (solid histogram), 10 mm diameter, 1 mm thick (dashed histogram) and 10 mm diameter, 10 mm thick (dotted histogram), mounted at the treatment isocentre. (b) Integrals P(E) over the energy spectra shown in (a) showing the percentage of protons in the spectrum which have energy E_p within the range $E_{th} < E_p < E$.*

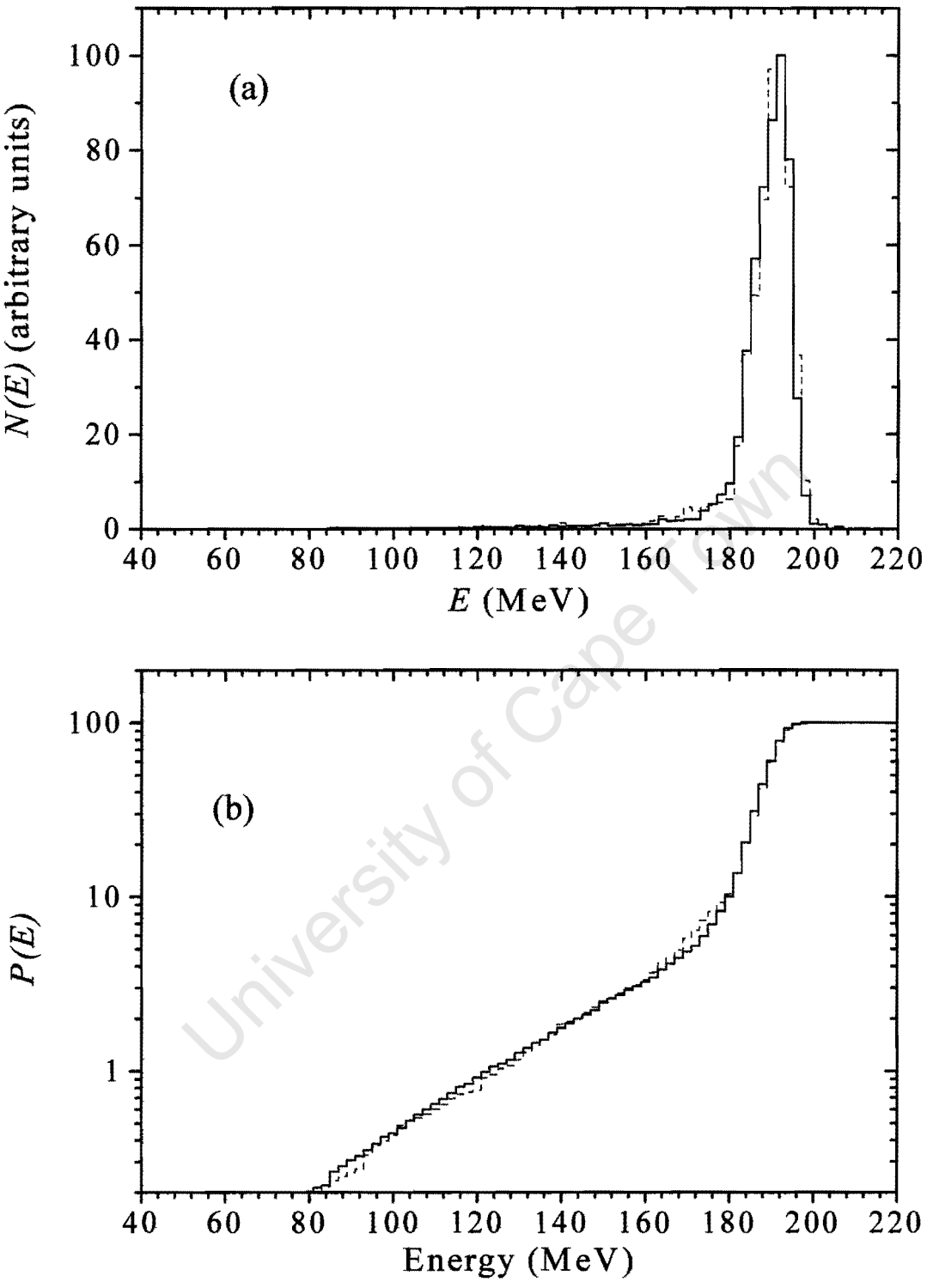

Figure 4.20: *Energy spectra N(E) for a 190.8 MeV proton beam measured with radiators of dimensions: 10 mm diameter, 3 mm thick (solid histogram) and 22 mm diameter, 3 mm thick (dashed histogram), mounted at the treatment isocentre. (b) Integrals P(E) over the energy spectra shown in (a) showing the percentage of protons in the spectrum which have energy E_p within the range $E_{th} < E_p < E$.*

Table 4.4: *Summary of experimental results indicating the effects of radiator size on the percentage of low energy protons in the beam. L(E) are the percentage of protons in each spectra with energy E_p within the range $E_{threshold} < E_p < E_{iso} - 10$ MeV.*

Run number	E_{iso} (MeV)	Radiator size (mm)		L(E)
		Diameter	Thickness	
366	91.9	10	3	7
400	91.9	10	1	7
365	190.8	10	3	10
401	190.8	10	1	13
402	190.8	10	10	13
404	190.8	22	3	14

4.3.3 Energy resolution

The broadening (FWHM) of the peaks in the energy spectra measured by the telescopes of the proton pair spectrometer is affected by the statistical nature of the radiation detection process, instrumental effects such as energy straggling in the radiator and detectors, fluctuations in the photomultiplier tube gain from event to event and gain drifts in the detection system (see figure 3.23), and the energy spread of the proton beam being measured. The energy resolution function of the proton pair spectrometer can be determined by using it to measure a monoenergetic proton spectrum consisting of a single sharp peak which may be considered to approximate to a delta function. Such a spectrum can be provided by removing all beam modification devices from the proton therapy beam (see for example [Br97b] and figure 2.4). Such a measurement was made (run 382) using a 10 mm diameter × 3 mm thick polyethylene radiator mounted at the isocentre. However severe technical problems were experienced in this run, due to beam instability at low currents, and the data obtained were unfortunately unsuitable for analysis. The energy resolution (FWHM) of the spectrometer was therefore estimated in the following way, from the measurement made with for the standard proton therapy beam (run 365), at E_{iso} = 190.8 MeV. The FWHM of the peaks of the measured proton energy spectra was determined from the energy spectra of proton therapy beams with E_{iso} values of 190.8, 174.1, 134.6 and 91.9 MeV (see figure 4.3 (a)). Table 4.5 show the FWHM of the high-energy peaks in the energy spectra shown in figure 4.3 (a) and the energy resolution (FWHM/E_{iso}) of the proton pair

Table 4.5: *FWHM of the peaks in the measured proton energy spectra of proton therapy beams with E_{iso} of 190.8, 174.1, 134.6 and 91.9 MeV (figure 4.3 (a)) and the corresponding energy resolution (FWHM / E_{iso}) values of the proton pair spectrometer at these energies.*

Run Number	E_{iso} (MeV)	FWHM (MeV)	FWHM / E_{iso} (%)
365	190.8	10	5.2
373	174.1	10	5.7
399	134.6	8	5.9
366	91.9	10	10.9

spectrometer as a function of energy. The FWHM of these peaks is attributed to broadening of the incident proton beam due to energy straggling and multiple scattering in the beam line components such as the lead scatterers and occluding ring system, the broadening due to the multiple scattering in the air and the radiator, and the broadening introduced by the detection system. The resolution of the spectrometer is observed to be in the range 5 to 11 %.

Chapter 5

Monte Carlo Calculations

Energy spectra and dose distributions delivered by the proton therapy beams in water at the NAC were computed with the Monte Carlo code MCNPX 2.1.5[1] [Hu97, Wa99]. MCNPX is a merger of the LAHET [Pr89] high energy all particle code and the MCNP [Br97a] code. The MCNP code can be used to track neutrons, electrons and photons of energies ranging up to 20 MeV using nuclear data tables. The LAHET Code System (LCS) is based on the High Energy Transport Code (HETC) [Ar72] developed at the Oak Ridge National Laboratory. MCNPX tracks particles using the physical models from LAHET and the evaluated cross section data in nuclear data tables [Hu97, Wa99], where available. Some of the nuclear models included in the MCNPX 2.1.5 code are: the Bertini [Be69] and ISABEL [Ya79, Ya81] intranuclear cascade (INC) models; FLUKA96 [Fa96] high energy particle generator; the multistage pre-equilibrium exciton model [Pr88]; the evaporation model [Dr81]; the Fermi breakup model [Br81]; nucleon elastic scattering model [Pr95]; the Oak Ridge National Laboratory [Ba81] and the Rutherford Appelton Laboratory [At80] fission models. Energy loss by interaction with electrons of the absorbing material is calculated in MCNPX by using the continuous slowing down approximation (csda), while charged particle Coulomb scattering is treated using a small-angle Coulomb approach based on a Gaussian model developed by Rossi [Ro41]. A prototype Vavilov straggling model [Hu95] that accounts for the Gaussian and Landau limits of the Vavilov model [Va57] is implemented in MCNPX 2.1.5.

[1] A beta version of the MCNPX Monte Carlo code that is currently being developed at the Los Alamos National Laboratory.

MCNPX treats particle interaction by the intranuclear cascade (INC) model (see appendix A) [Be69, Ya79, Ya81] followed by the multistage pre-equilibrium exciton model [Pr88] and finally the evaporation [Dr81] and/or fission models. The interaction process of the proton and the nucleus in the Bertini INC model [Be69] is illustrated in figure 5.1. In the first stage of the interaction, the particle incident on the nucleus interacts with individual nucleons inside the nucleus, initiating a cascade inside the nucleus. The kinematics of the collisions are treated relativistically, and the particle-particle interactions are evaluated using cross sections in a potential which describes the density of the nucleus as a function of the radius (see appendix A) [Pr94, Wa99]. This phase of the interaction is called the intranuclear cascade stage. The high-energy particles and light ions are emitted from the nucleus and are able to interact with other nuclei. The residual nucleus either release neutrons and light ions through the evaporation process, or fission. In the final stage, the excited nucleus decays by gamma emission. The multistage pre-equilibrium exciton model acts as an intermediate stage between the intranuclear cascade stage and the evaporation phase of the nuclear interaction [Br97a, Pr94]. The Fermi breakup model [Br81] is used as a default model in MCNPX in the evaporation phase of the interaction. It treats the de-excitation process as a sequence of simultaneous breakups of the excited nucleus into two or three fragments, which may be stable or unstable nuclei or nucleons. The unstable products may undergo further breakups [Pr94, Wa99]. The MCNPX default cutoff energy of 1 MeV for tracking protons was used in the simulation of the NAC proton therapy beam line.

5.1 Simulation of the NAC proton therapy facility

Figure 5.2 shows a schematic representation of the beam line components included in the geometry used in the Monte Carlo simulation of the proton therapy facility at the South African National Accelerator Centre. In the Monte Carlo simulations, each proton was followed from the source, located upstream of the Havar window, and its history recorded until the proton was either "terminated" by absorption or nuclear interactions, or escaped from the beam through large angle scattering. Any secondary protons generated by the absorption or other interactions of primary

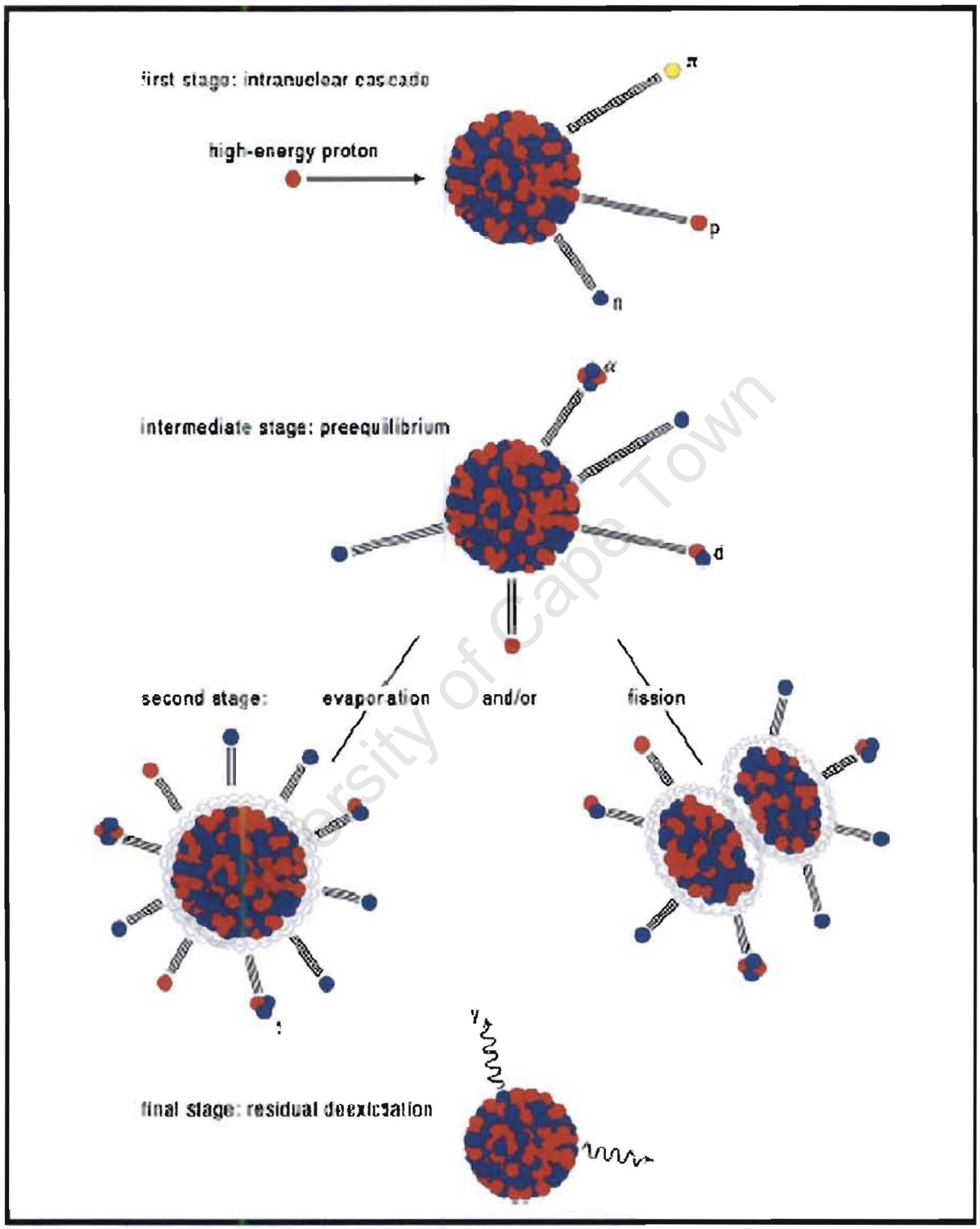

Figure 5.1: *The interaction process of a proton with a nucleus in the Bertini intranuclear cascade model [Be69]. Reproduced from MCNPX Users Manual [Wa99].*

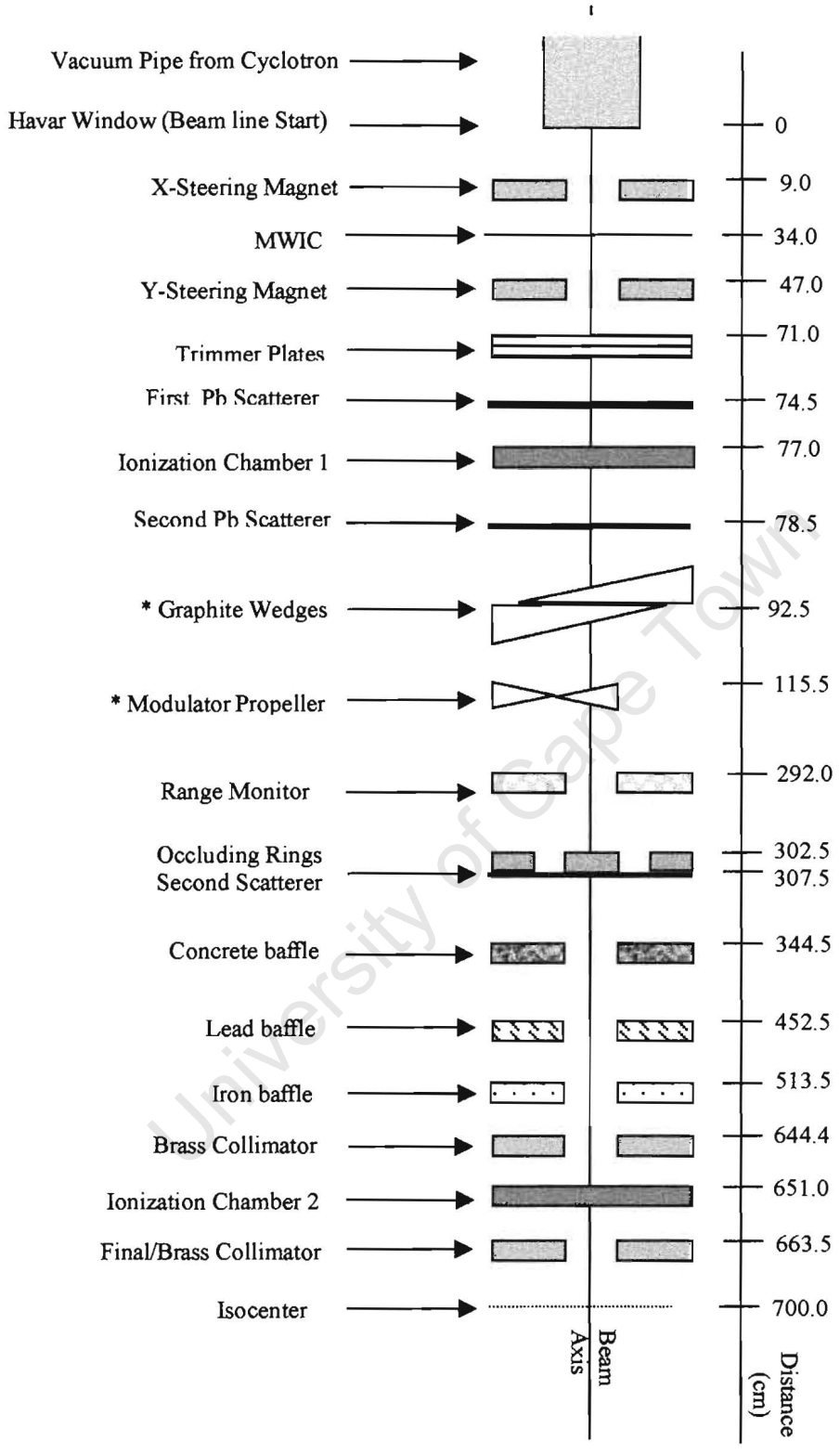

Figure 5.2: *A schematic representation of the beam line components of the proton therapy facility at the National Accelerator Centre as simulated in the MCNPX Monte Carlo code (see also figure 2.1). The proton source was located upstream of the Havar window in the MCNPX calculations. Devices marked with an asterisk are not always in the beam during treatment, and the range monitor is out of the beam during treatment. See table 2.1 for details of the beam line components.*

protons with nuclei were also tracked. The MCNPX input file included information about the material isotopic composition, density, and dimensions of each beam line component (see appendix B). All the calculations were completed using the Bertini model for the intranuclear cascade calculation, the multistep preequilibrium model, and the Fermi breakup model in the evaporation phase. Elastic scattering was allowed for both protons and neutrons. In the simulation of the NAC proton therapy beam line, protons were transported using only physical models as MCNPX 2.1.5 does not have the capability to utilize the proton libraries.

Table 5.1 lists the beam line components and how they were modelled in the MCNPX simulations. The proton source (protons from the cyclotron) was simulated as a parallel beam of protons with a Gaussian energy distribution over a circle of 3 mm radius. The beam energy used in the calculations was chosen as 204 ± 1 MeV, which is the estimated average value for the proton beam exiting the Havar vacuum window. Each collimator was simulated as a sheet of material located perpendicular to the beam axis with a circular aperture whose centre coincided with the beam axis. The aperture in the concrete wall and the steering magnets were also modelled as collimators with rectangular apertures with centres coinciding with the beam axis. The tracking of the particles after the Havar window was done in air i.e. the material between the beam modification elements was included as air in the simulations. Particles scattered beyond a radius of 500 mm from the central axis of the beam and 50 mm downstream of the treatment isocentre were not tracked any further. The calculations were performed on a Linux platform running on an Intel Pentium II 400 MHz with 96 Megabytes of RAM. For fluence calculations up to the isocentre, 10 million particle histories were simulated and a single calculation took about 72 hours.

5.2 Results of the Monte Carlo calculations

The MCNXP Monte Carlo code was tested by calculating the range of protons with E_{iso} of 190.8 MeV in water. In this test, the model of the water phantom was included in the beam line model with the entrance point at the isocentre. The energy deposition in the phantom was calculated in a 1 mm long cylinder with a

Table 5.1: *Beam line components and how they were modelled in the MCNPX simulations. Each collimator was modelled as a sheet of material located perpendicular to the beam axis with a circular aperture whose centre coincided with the beam axis. The concrete wall and the X and Y steering magnet were also modelled as collimators made up of concrete and iron, respectively, with square apertures with centres coinciding with the beam axis.*

Beam line components		MCNPX model
Occluding rings	Lead scatterer	1.0 mm thick plates perpendicular to the beam axis
	Brass scatterer	1.0 mm thick plates perpendicular to the beam axis
	Central stopper	Cylinder of 13.44 mm and 50.0 mm long
	Outer brass ring	Hollow brass cylinder of inner radius 24.18 mm and outer radius of 36.11 mm
Ionization chambers	Multiwire ionisation chamber	A series of tungsten rods (0.1 mm in diameter) spaced at 2 mm intervals in the x and y directions.
	First ionization chamber	0.01 mm layer of mylar in the beam
	Second ionization chamber	A layer of mylar (0.001 mm) followed by layers of aluminium (0.0125 mm) and kapton (0.0070 mm).
Energy Degraders	Trimmer plates	0.05 mm thick plastic sheets perpendicular to the beam axis
	Graphite wedge system	A sheet of carbon perpendicular to the beam axis, the thickness of the sheet was varied to give the following energies at the isocentre: 174.1, 134.6, 91.9 and 59.3 MeV.
	Modulator propellers	Acrylic sheets of different thickness (see table 2.2) placed perpendicular to the beam axis.
Collimators	X and Y steering magnets	200.0 mm sheets of iron placed perpendicular to the beam axis, with rectangular holes of 80.0 and 200.0 mm sides, in the x- and y-axis respectively.
	Concrete wall	190 mm thick sheet of concrete with a square aperture of 200 mm sides.
	Lead	49 mm thick sheet of lead with a 120 mm radius aperture.
	Iron	50 mm thick sheets of iron with a 120 mm radius aperture.
	First brass	50 mm thick sheets of brass with a 100 mm radius aperture.
	Patient (final)	50 mm thick brass sheet with a 50 mm radius aperture.

centre lying along the beam axis and a 10 mm radius, at 1 mm increments along the axis of the beam. The range of the proton beam in water (240 mm) determined from the depth dose calculation is consistent with the range of the proton beam with E_{iso} of 190.8 MeV in water determined from the range calculations using electronic stopping power data [IC49]. Figure 5.3 shows the dose at different depth in the water phantom measured with an air-filled thimble ionization chamber [Sc95] (dotted curve) and calculated with the MCNPX Monte Carlo code (solid histogram). The dose measurements are normalized to a peak intensity of 100 J/kg and the MCNPX computed data is normalised to the same area as the area under the experimental curve. The computed data (solid histogram in figure 5.3) have a higher peak to entrance dose ratio (about 10:2) compared to the measured data (about 10:3) and the peak corresponding to the maximum dose (Bragg peak) in the computed data is narrower compared to that of the measured data. This is because the MCNPX computed data does not include the experimental broadening associated with the resolution of the measuring instrument. The experimental broadening was included in the computed data by convoluting the computed data with the following equation [Ze63].

$$N_c(E) = \int_0^\infty \Phi(E) f(E', E) dE \tag{5.1}$$

where $f(E', E)$ is a Gaussian function. The MCNPX computed depth dose matched the measured depth dose after including experimental broadening, with σ set to be 3 to give the best fit. Figure 5.4 shows the MCNPX computed results of dose as a function of depth in water compared with the results of the measurements made with an air-filled ionization chamber in a water phantom, for a 190.8 MeV proton beam with a 50 mm modulator propeller (SOBP-50) rotating in the beam. The measured dose data is normalized to a peak intensity of 100 J/kg and the MCNPX computed data is normalized to the same area as the area under the experimental curve. The ratio of the entrance dose to maximum dose of the MCNPX computed result is higher than that of the experimental measurements. The nine "peaks" in the dose distribution curve (dashed histogram) are attributed to protons that passed through the different sections of the SOBP-50, that is through the "open" section and the eight blades of the SOBP-50 (see table 2.2 and figure 2.5). The calculation was performed by simulating 1 million histories per acrylic slab of the modulator propeller, and adding the results of the simulation after multiplying by the appropriate weighting factor (see table 2.2).

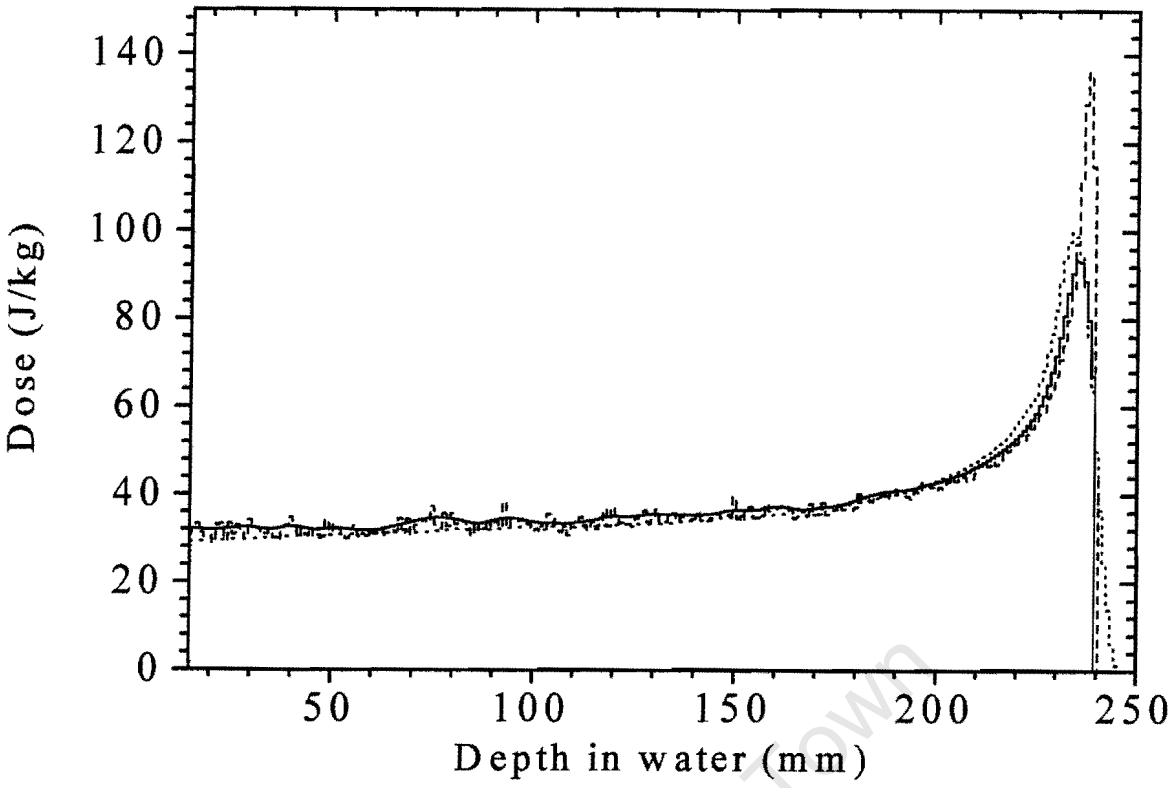

Figure 5.3: *Energy deposited per unit mass (dose) as a function of depth in water for a proton beam with E_{iso} of 190.8 MeV calculated with the MCNPX Monte Carlo code (dashed histogram), calculated with MCNPX and convoluted with a Gaussian function to include experimental broadening (solid curve), and ionization chamber measurements (dotted curve). The experimental measurements are normalized to a peak intensity of 100 J/kg, and the MCNPX data are normalized to the same area as that covered by the measured data.*

Figure 5.5 shows the assumed fluence spectrum corresponding to the proton source, upstream of the Havar window and the changes in the spectrum after the proton beam has passed through the Havar window, X-steering magnets, the multiwire ionizing chamber, the Y-steering magnet and the polyethylene trimmer plates. The X-steering magnet does not have any effect on the spectrum as the radius of the beam at this point is smaller than the aperture in the magnet (see table 5.1). The increase in the low-energy component after the X-steering magnet is attributed to backscattering in the multiwire wire ionization chamber (MWIC). The small reduction in the low-energy component after the Y-steering magnet indicates the collimation effect of the Y-steering magnet on the beam. The multiwire ionizing chamber and the plastic trimmer plates introduce low-energy components in the fluence spectra.

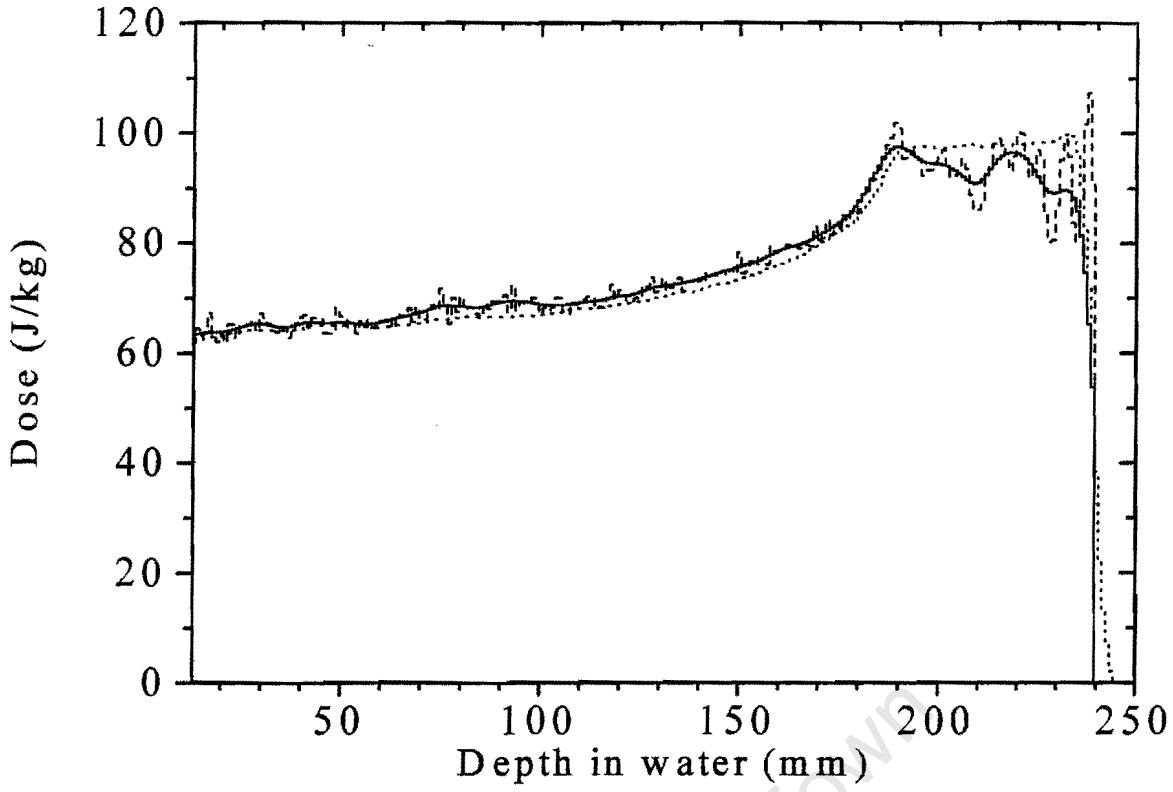

Figure 5.4: *Energy deposited per unit mass (dose) as a function of depth in water for a proton beam with E_{iso} of 190.8 MeV with a 50 mm modulator propeller rotating in the beam calculated with the MCNPX Monte Carlo code (dashed histogram), calculated with MCNPX and convoluted with a Gaussian function to include experimental broadening (solid curve), and ionization chamber measurements (dotted curve). The experimental measurements are normalized to a peak intensity of 100 J/kg, and the MCNPX data are normalized to the same area as that covered by the measured data.*

Figure 5.6 shows the calculated spectra after the first lead scatterer, the first ionization chamber, the second lead scatterer, the range monitor and the occluding rings. The lead scatterers increase the low-energy component significantly while the ionization chamber has a negligible effect on the spectrum. The increase in the low-energy component after the range monitor, which was modelled as a collimator, is due to the backscattering from the brass occluding rings located downstream of the range monitor. The occluding rings further increase the low-energy component and reduces the energy of the beam by about 6 MeV.

Figure 5.7 shows the fluence spectra calculated after the concrete, lead, iron and brass baffles, and the second ionization chamber. The concrete, lead and iron baffles reduced the low-energy component of the spectrum. The slight increase in the low energy component after the brass collimator is attributed to the backscattering of protons from the second ionization chamber. Figure 5.7 also shows the fluence spectrum at the isocentre which has a significantly smaller low-energy component than the spectrum computed after the second ionization chamber. The reduction of low-energy component is due to the smaller diameter of the final (patient)

collimator, which reduces the low energy protons at the edge of the beam.

Figure 5.8 shows (a) the MCNPX computed spectrum (dotted histogram) and (b) the proton energy spectrum $N(E)$ (solid histogram) measured with the proton pair spectrometer shown in figure 3.1, for an incident proton beam with E_{iso} of 190.8 MeV (run 365 in table 3.1). The peak at high energy in the computed spectrum (dotted histogram in figure 5.8) is narrower than the corresponding peak in the measured spectrum (solid histogram in figure 5.8) due to the broadening of the peaks (FWHM) in the measured spectrum attributed to the resolution of the detection system. The broadening (FWHM) of the peaks in the measured proton energy spectra depends on the photoelectron statistics in the photomultiplier tube in the detection process, energy straggling in the components of the detector telescope, the energy distribution of the incident radiation and the stability of the detection system. The effect of straggling can be described by an energy-dependent probability function [Sk67, Bi70, Wi76], such as a Gaussian function. Measurements of the standard proton therapy beam (runs 365, 380 and 403) indicated that there was a gain drift in the detection system (see figure 3.23). Since the peaks in the pulse height spectra (see figures 3.20, 3.21 and 3.23) remained symmetric (Gaussian), the contribution of the gain drifts in the energy resolution (FWHM) was included in the convolution function used to include the experimental broadening in the Monte Carlo simulations. The MCNPX computed energy spectrum $\Phi(E)$ was convoluted with a five-term Gaussian energy spread function $f(E', E)$ to include the experimental broadening due to these effects by equation 5.1 where

$$f(E', E) = \mathrm{A}_1 e^{\frac{(E'-E+x_1)}{2\sigma^2}} + \mathrm{A}_2 e^{\frac{(E'-E+x_2)}{2\sigma^2}} + \mathrm{A}_3 e^{\frac{(E'-E+x_3)}{2\sigma^2}} + \mathrm{A}_4 e^{\frac{(E'-E+x_4)}{2\sigma^2}} + \mathrm{A}_5 e^{\frac{(E'-E+x_5)}{2\sigma^2}}$$

The five terms were included to take into consideration the gain drift during the run and the statistical effect is included through σ. σ was kept constant for all the convolutions and the parameters A_1 to A_5 were adjusted in each convolution to suit the data. The simulated spectrum $N_c(E)$, that is the broadened computed spectrum ((c) in figure 5.8), matched the measured spectra when σ was set to 2.5 MeV and the parameters A_1 to A_5 were set to 0.7, 0.1, 1.3, 0.36 and 0.001, respectively. The simulated proton energy spectrum $N_c(E)$ is shown in figure 5.8 (solid curve) with the measured energy spectrum (solid histogram) of the standard proton therapy beam. The measured spectrum is normalised to a peak value of 100

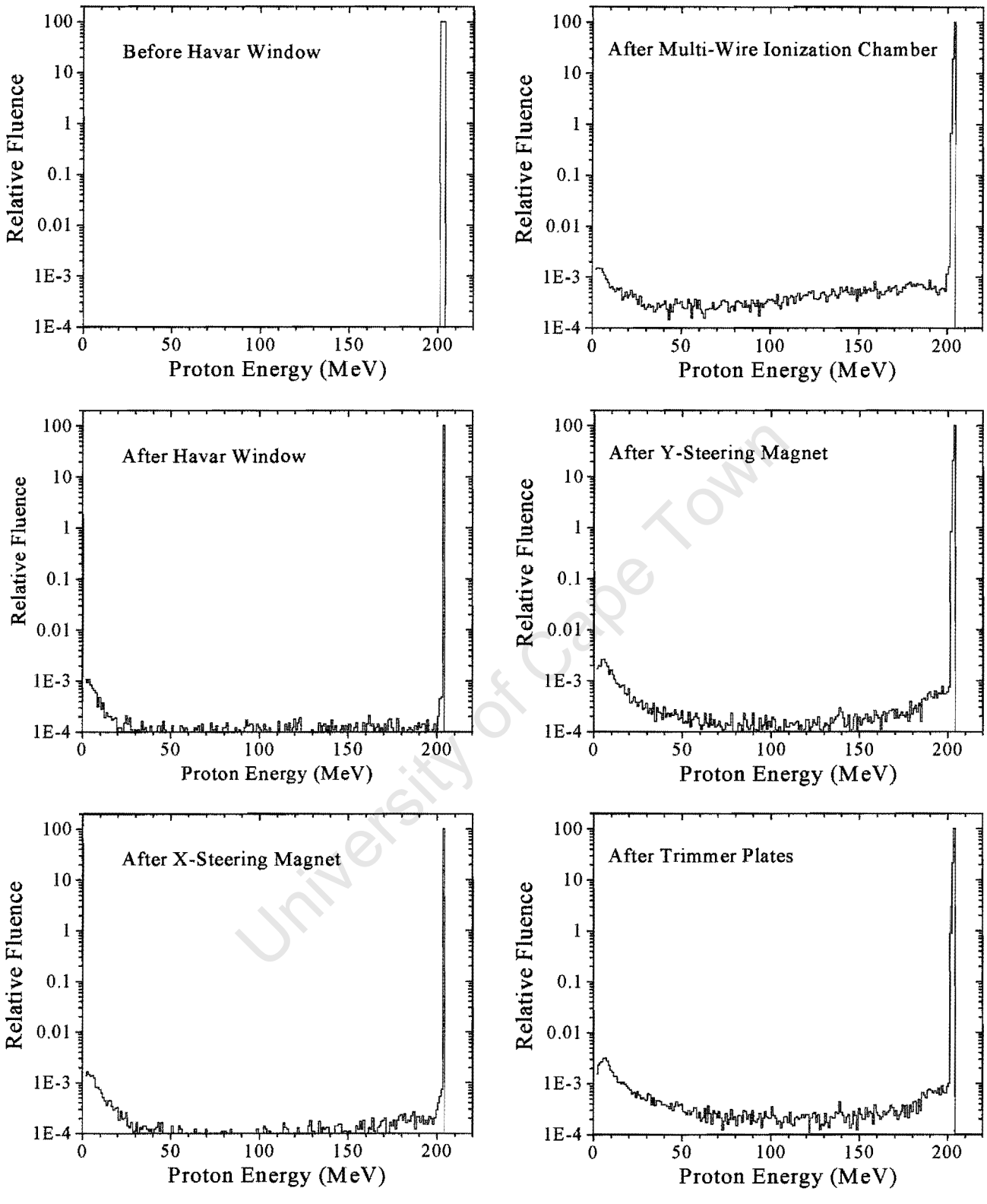

Figure 5.5: *Computed proton fluence spectra for the NAC proton therapy beam line, showing the fluence spectra of the proton source, and the spectra after the protons have passed through the Havar window, X-steering magnets, the multiwire ionizing chamber, the Y-steering magnet and the polyethylene trimmer plates. The changes in the spectra depict the influence of the preceding beam line component.*

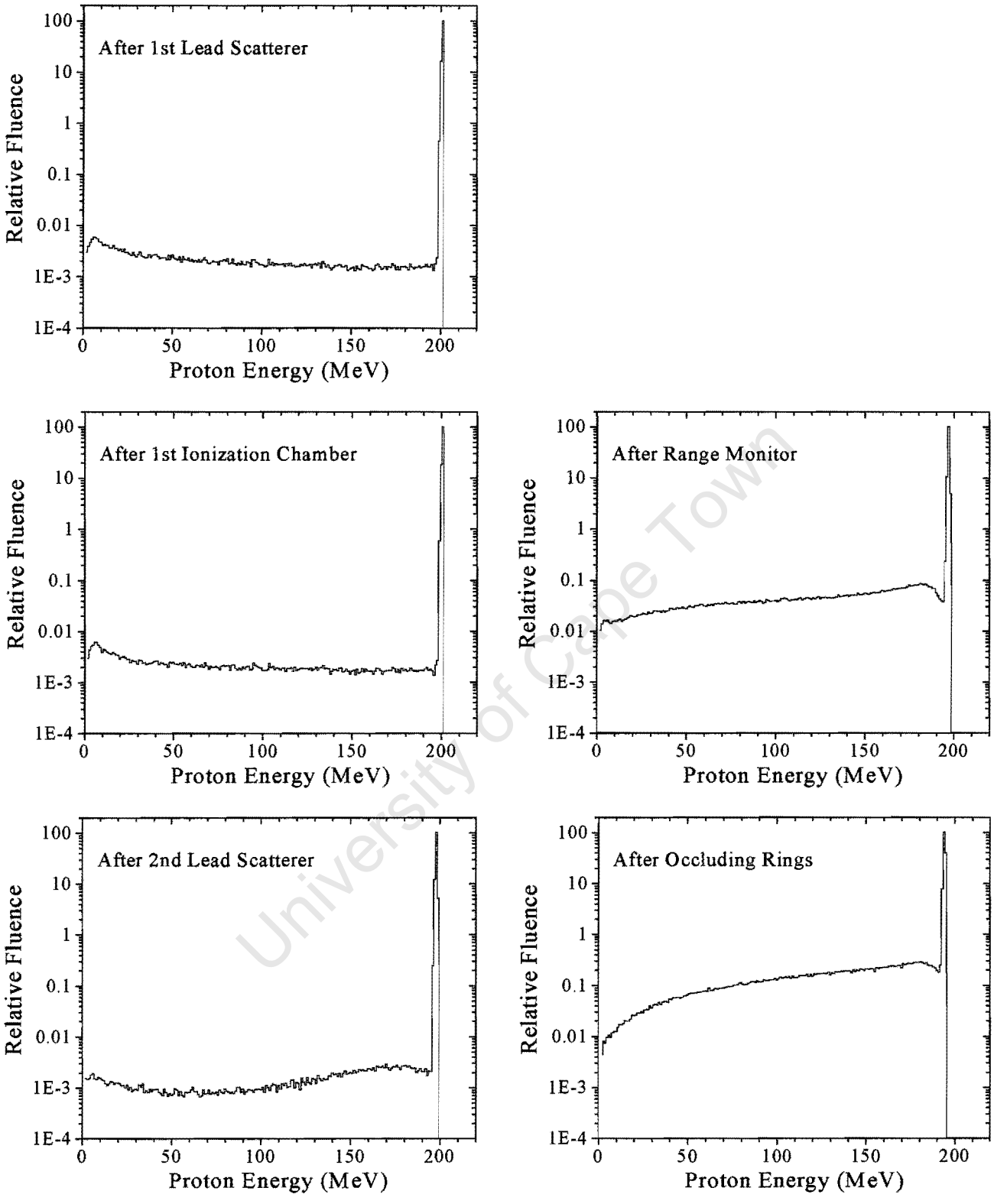

Figure 5.6: *Computed proton fluence spectra of the proton after the beam has passed through the first lead scatterer, the first ionization chamber, the second lead scatterer, the range monitor and occluding rings.*

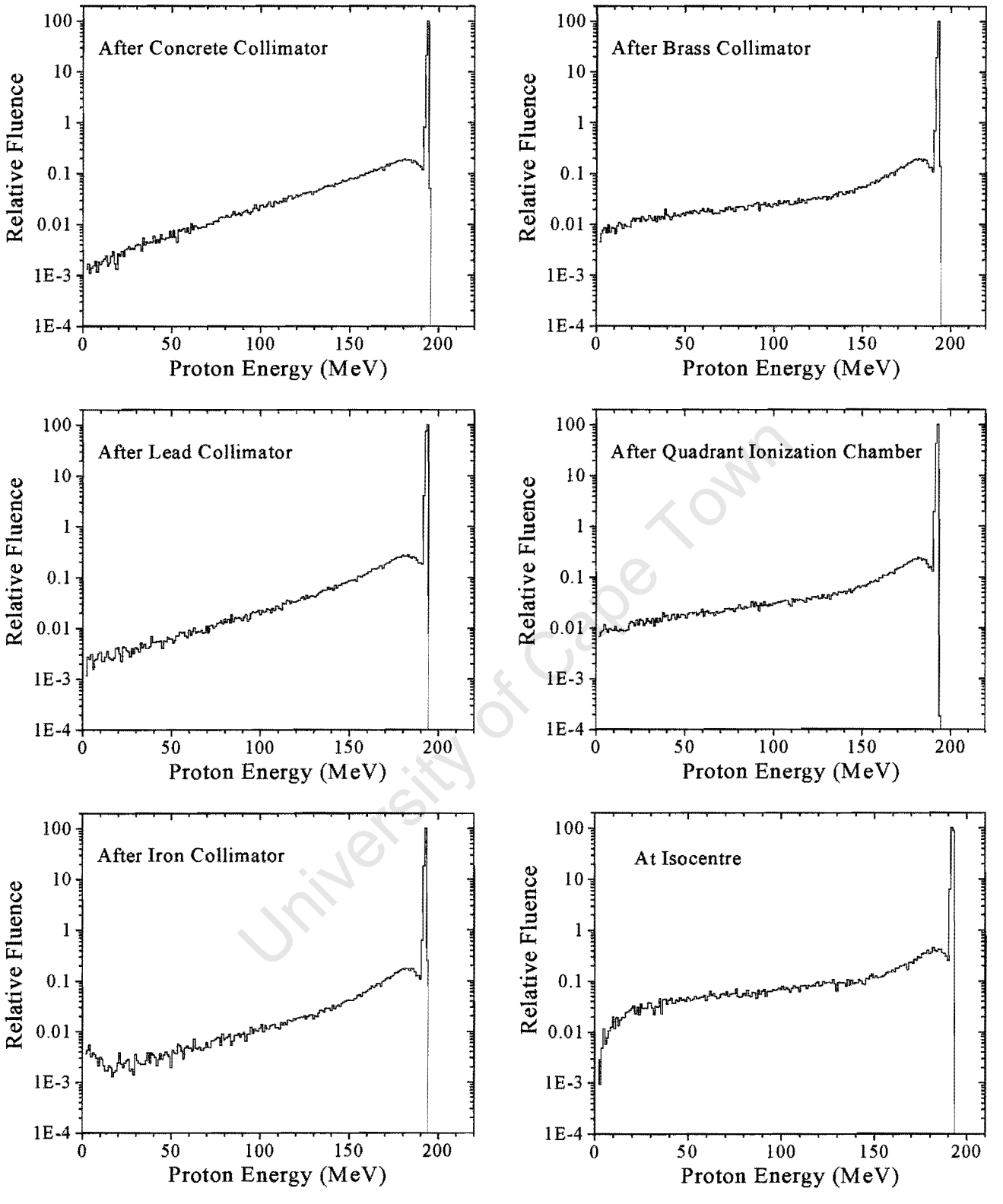

Figure 5.7: *Computed proton fluence spectra after the beam has passed through the concrete, lead, iron and brass collimators, after the quadrant ionization chamber and at the isocentre.*

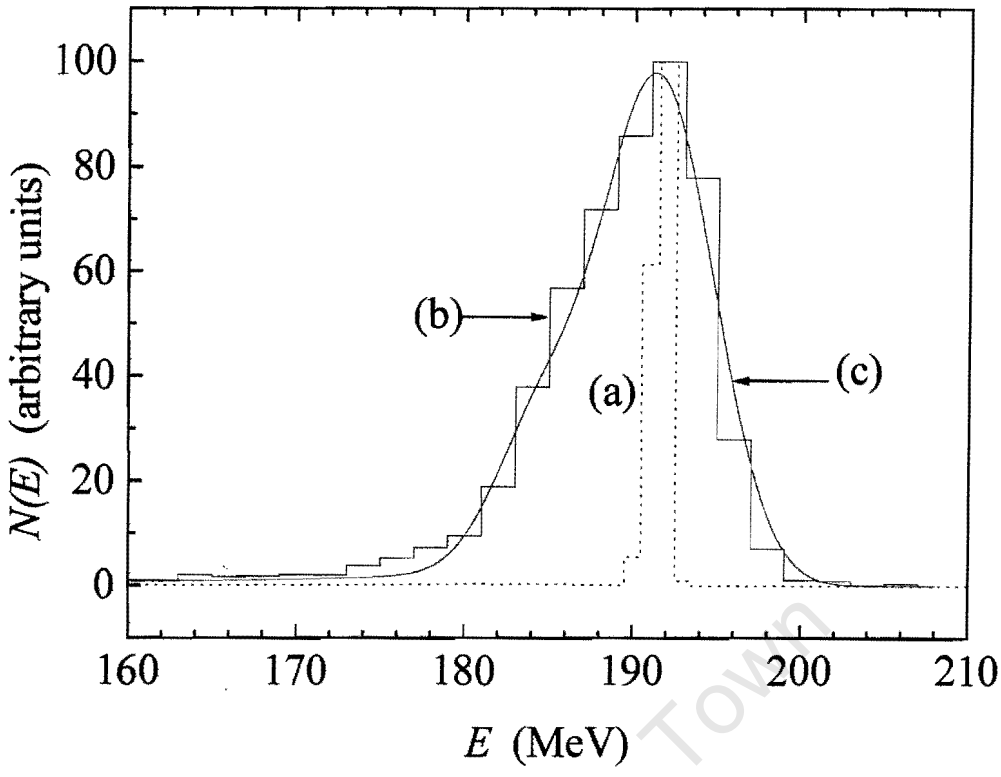

Figure 5.8: *Proton spectrum N(E) of a 190.8 MeV proton therapy beam: (a) measured spectrum (solid histogram); (b) spectrum simulated with MCNPX (dotted histogram); (c) spectrum (b) convoluted with a Gaussian energy spread function of the form shown in equation 5.1 (solid curve).*

counts per bin and the simulated spectrum is normalised to the same total proton count as in the measured spectrum.

The MCNPX Monte Carlo code has been tested with a range calculation problem, and the results are agreement with the experimental results. The code was used to calculate the energy spectrum after every beam line component from the Havar window up to the isocentre. The results showed the expected changes in the spectrum such as the reduction in the number of low energy protons due to collimators in the beam line and other components that have a similar effect on the beam such e.g. range monitor. The spectrum calculated at the isocentre was compared with the energy spectrum of the standard proton therapy beam measured with the proton pair spectrometer at the isocentre. There is a good agreement between the calculated and measured spectra after the calculated spectrum was convoluted with a five term Gaussian energy spread function shown in equation 5.1. More comparisons of the Monte Carlo and experimental results will be presented in chapter 6.

Chapter 6

Discussion and Conclusion

6.1 Comparison between experimental results with Monte Carlo calculations

Figure 6.1 shows the energy spectra which were measured (histograms), together with those computed using MCNPX (curves) for proton beams with E_{iso} of 190.8, 174.1, 134.6 and 91.9 MeV. The simulated spectra have been convoluted with a Gaussian energy spread function (equation 5.1) with parameter σ adjusted to 2.5 and the parameters A_1 to A_2 set to values listed in table 6.1. The measured spectra are normalised to a peak value of 100 counts per bin, and each simulated spectra is normalised to the same integral counts in the corresponding measured spectrum. Figure 6.2 shows the measured proton spectra for a proton beam with E_{iso} of 190.8 MeV with a 50 mm modulator propeller (SOBP-50) included in the beam modification system (solid histogram) and the MCNPX simulated proton energy spectrum (solid curve). The spectrum measured without a propeller (dotted histogram) is included for reference. Figures 6.3 and 6.4 show the integrals $P(E)$ (equation 3.12) over the measured proton energy spectra (solid histograms) and the MCNPX simulated spectra (dotted histograms) for incident proton beams of 190.8, 174.1 and 134.6 MeV. The MCNPX simulated spectra are in reasonable agreement with the measured spectra in all cases, although a slightly larger percentage of low energy protons is evident in the calculated spectra.

As can be seen from figures 6.1 to 6.4, the calculated spectra are in agreement with the measured spectra, suggesting that the MCNPX 2.1.5 code can reproduce the

Table 6.1: *Parameters used in equation~6.1 in the convolution of the MCNPX computed proton energy spectra with Gaussian energy spread functions. The spectra are for proton beams with E_{iso} of 190.8, 174.1, 134.6, and 91.9 MeV and for the proton beam with E_{iso} of 190.8 MeV and a SOBP–50 included in the beam modification system.*

	190.8 MeV	174.1 MeV	134.6 MeV	91.9 MeV	SOBP–50
A_1	0.7	0.15	0.2	0.1	1.2
A_2	0.1	0.05	0.1	0.05	0.005
A_3	1.3	0.35	0.6	0.8	1.8
A_4	0.36	0.001	0.0001	0.001	1.1
A_5	0.0001	0.002	0.0001	0.001	0.4

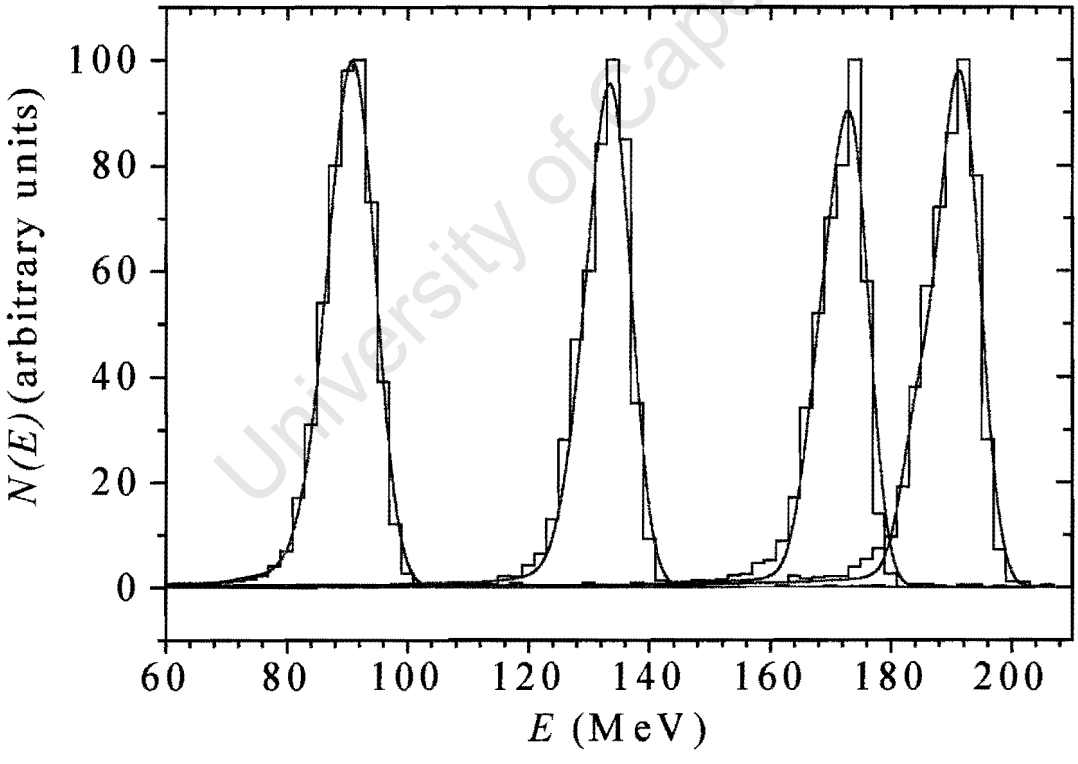

Figure 6.1: *Measured proton spectra N(E) for proton therapy beams with E_{iso} of 190.8, 174.1, 134.6 and 91.9 MeV (solid histograms) and the associated MCNPX simulated spectra, each convoluted with a Gaussian energy spread function of the form shown in equation 5.1 (solid curves).*

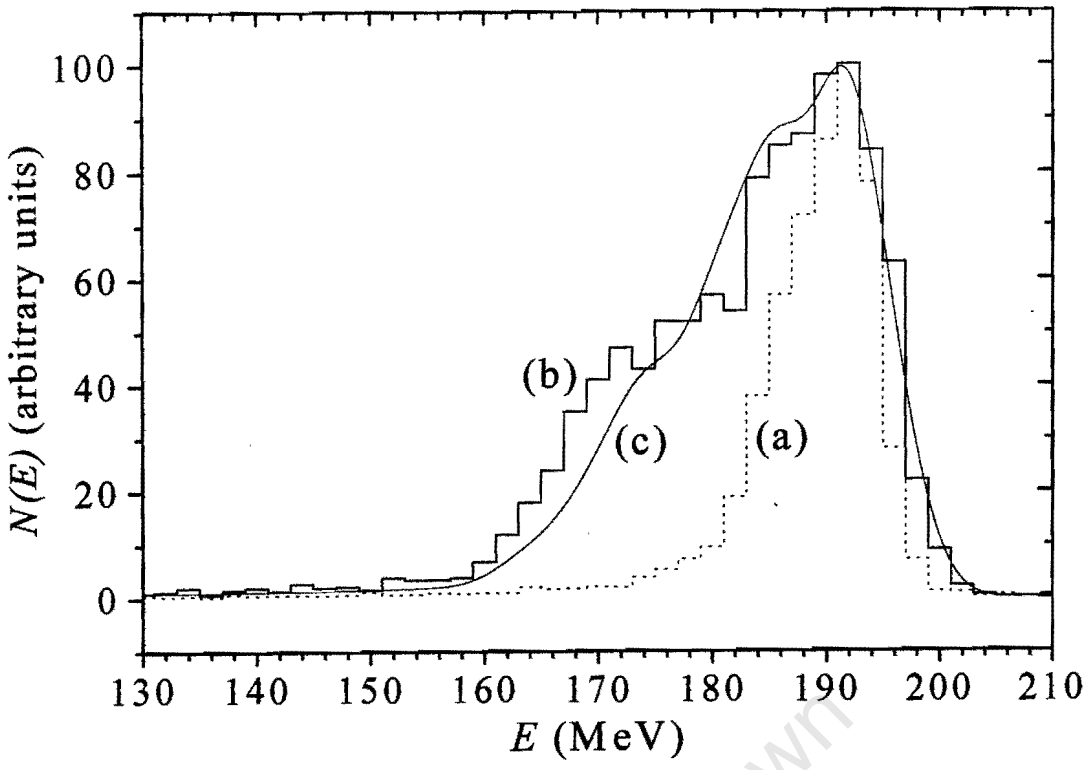

Figure 6.2: *Proton spectrum of a proton beam with E_{iso} of 190.8 MeV measured spectrum (a) without (dashed histogram) and (b) with a SOBP-50 included in the beam modification system. Spectrum (c) (solid curve) was simulated using MCNPX for the proton beam with E_{iso} of 190.8 MeV with a SOBP-50 included in the beam modification system.*

combined effects on the proton energy spectrum of all the beam line components such as graphite wedges and modulator propellers. Plots of the measured and simulated integrals $P(E)$ are shown only for proton beams for which $E_{iso} > 130$ MeV. For the lower energy beams studied, $E_{iso} = 91.9$ and 59.3 MeV, the data obtained for these integrals are of limited value, owing to the proximity of the threshold energy $E_{th} = \sim 55$ MeV, used in the integrals (see equation 3.12). The effect of each individual beam modification element on the energy spectrum can be investigated from the Monte Carlo spectra calculated at positions after each element (see figures 5.5 to 5.7). For example, it can be seen from figure 5.7 that the collimators and beam modification elements which also act as collimators (e.g. range monitor) reduces the proportion of low energy protons in the beam. In figure 5.6, it can be seen that the scatterers increase the proportion of low energy protons. Since the transport of the beam through all the beam modification elements (figures 5.5 to 5.7) appears to be well produced, any future changes to the beam modification system of the NAC proton therapy beam line can therefore be investigated by Monte Carlo alone with confidence.

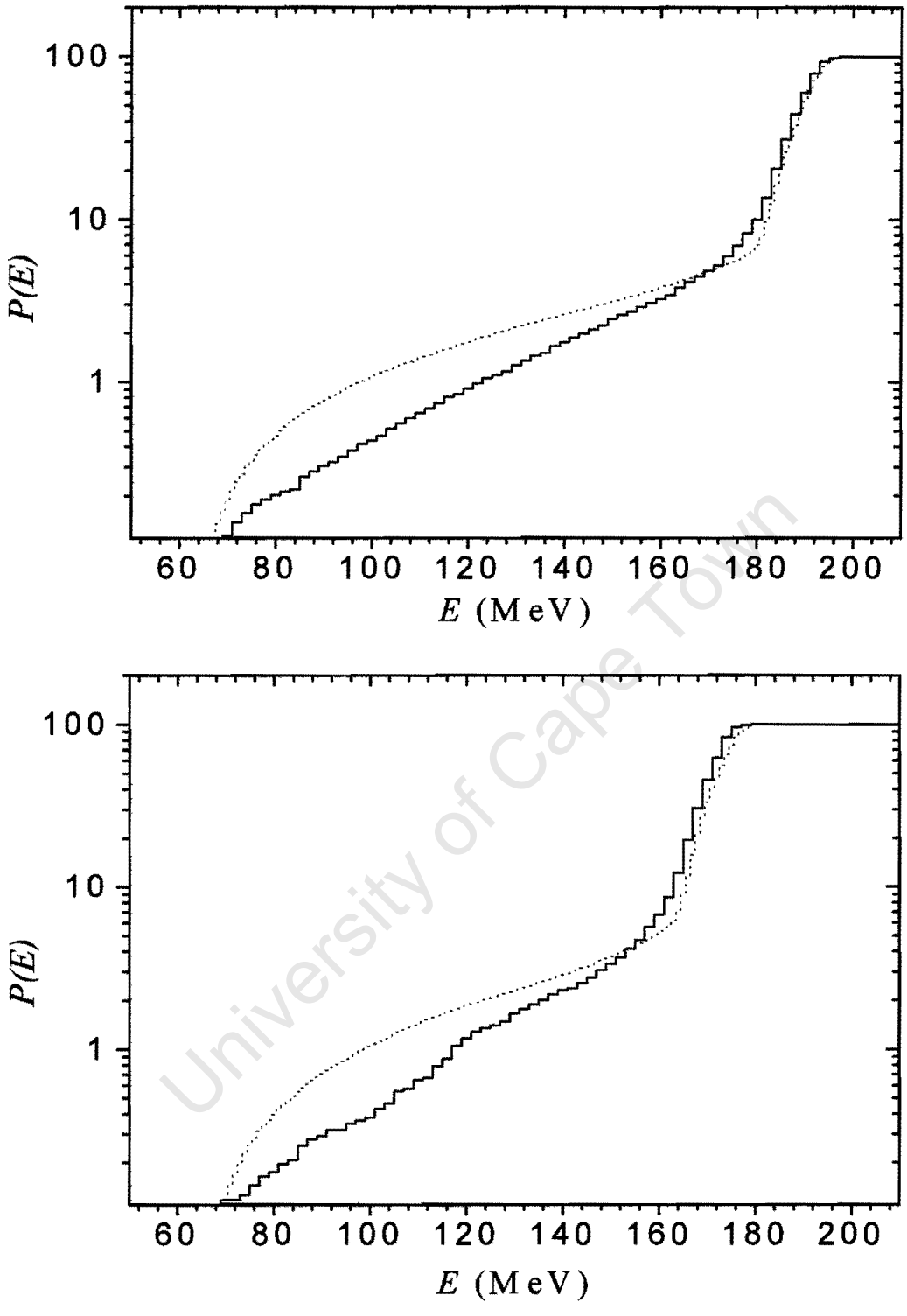

Figure 6.3: *Integrals over the measured (solid histogram) and MCNPX computed (dotted histogram) proton energy spectra shown in figure 6.1 showing the percentage of protons in the spectra which have energy E_p within the range $E_{th} < E_p < E$ for an incident proton beam with E_{iso} of (a) 190.8 MeV and (b) 174.1 MeV.*

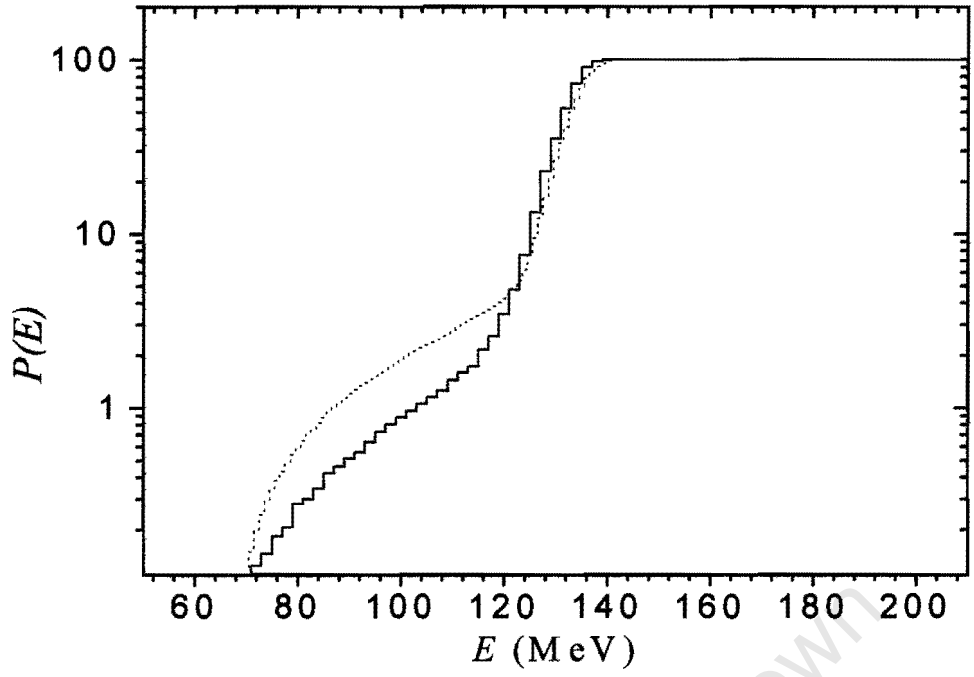

Figure 6.4: *Integrals over the measured (solid histogram) and MCNPX computed (dotted histogram) proton energy spectra shown in figure 6.1 showing the percentage of protons in the spectra which have energy E_p within the range $E_{th} < E_p < E$ for an incident proton beam of 134.6 MeV.*

Table 6.2: *Summary of experimental results, indicating the percentage of low energy protons L(E) in the beam. L(E) are the percentage of protons in each spectrum which have energy E_p within the range $E_{th} < Ep < E_{iso} - 10$ MeV.*

Run number	Aim of run	E_{iso} (MeV)	Collimator diameter (mm)	Displacement from isocentre		L(E)
				y (mm)	z (mm)	
365	Measurements of the standard proton therapy beam	190.8	40	0	0	10
380		190.8	40	0	0	10
403		190.8	40	0	0	10
373	Measurements with energy degrading material in the beam	174.1	40	0	0	10
399		134.6	40	0	0	8
366		91.9	40	0	0	7
387	Measurements made with different final (patient) collimator diameters.	190.8	5	0	0	5
388		190.8	10	0	0	5
389		190.8	100	0	0	13
390	Upstream measurement	190.8	100	0	–280	19
391	Measurements made off the beam axis, upstream of the isocentre.	190.8	100	25	–280	20
392		190.8	100	40	–280	20
393		190.8	100	50	–280	20
396	Measurements made off the beam axis, at the isocentre.	190.8	100	50	0	13
397		190.8	100	40	0	14

6.2 Summary of main results

Table 6.2 presents a summary of the most important measurements completed in this work. These are measurements made with energy degrading material in the beam, with final (patient) collimators of various diameters, and at positions displaced from the isocentre. One of the main interests of the present work was to investigate the component of low energy protons in the various beams. The fraction of low energy protons in each beam was investigated by considering the factor L(E), which is the percentage of protons in the spectrum which have energy E_p within the range $E_{th} < E_p < E_{iso} - 10$ MeV, where E_{th} is the threshold energy (56 MeV).

It was found that the graphite wedge system can be used to reduce E_{iso}, and hence the range of the proton beam in tissue, without introducing a significant fraction of low energy protons in the beam (see table 6.2). The energy spectra of the 190.8 and 174.1 MeV beams have a similar fraction of low energy protons (L(E) =10) compared to the 134.6 and 91.9 MeV spectra, for which L(E) values of 8 and 7 were determined, respectively (see also figures 6.3 and 6.4). The modulator propellers broadened the high-energy components of the spectra without introducing a significant fraction of low energy protons. The modulator propellers are successful in broadening the high-energy components of the spectra (see figures 4.5, 4.6 and 6.2), without introducing a significant low energy component. The modulator propellers can therefore be used to attain a uniform dose distribution over the length of the tumour.

The sharp decline in the yield for measurements made at the edge of the beam (see figure 4.16) indicates that the beam is well collimated has a sharp lateral penumbra. This implies that the proton beam can be focused on the target area (lesion) without significantly irradiating adjacent structures. It was also found that increasing the diameter of the final (patient) collimator resulted in an increase in the fraction of low energy protons reaching the treatment isocentre (see figures 4.8 and table 6.2). However these low energy protons are mainly to be found on the periphery of the beam. Furthermore, the percentage of low energy protons (L(E)) in the beam also increases with position away from the isocentre, perpendicular

to the axis of the beam (see figure 4.12 and table 6.2). The implications of this finding for proton therapy needs to be assessed since it might not be appropriate to irradiate tumours with a large cross sectional area (diameter greater than about 10 mm) with a single broad beam.

The measurements also revealed some unexpected results. For example, the E_A-E_B plots for proton beams with E_{iso} of 91.9 and 59.3 MeV indicate that there were protons with energies up to 190.8 MeV reaching the isocentre when the graphite wedges (energy degraders) were included in the beam modification system (see figure 4.2). On the other hand, the E_A-E_B plots for the proton beam with E_{iso} of 134.6 and 174.1 MeV beams do not show this phenomenon. As only the setting of the graphite wedge system was changed between these runs, it seems that these high-energy protons reach the isocentre only at wedge settings for E_{iso} of 91.9 and 59.3 MeV (see section 4.1.1). This effect may also be due to the problems experienced with tuning the beam at the low currents used during the measurements, which may have increased the scattering of the beam on the magnet used to steer the beam. Although this effect is relatively small ($< 1\%$), it is obviously important to understand the phenomenon in view of possible implications for proton therapy. Further investigations are needed to fully understand the cause of this effect.

6.3 Future work

The measurements in the present run series were performed over a period of about 60 hours, with the average length of the run being about 1.5 hours. In future work, the duration of the runs should be increased to improve the statistical accuracy of the measured spectra, which will enable additional information to be gained from the experiments. For example, previous studies showed that increasing the thickness of the degrading material in the beam increased the broadening (FWHM) of the peaks of the energy spectra [Br97b]. However, this effect was not evident in the present measurements.

After a p-p scattering event in the radiator, each proton lost about 20 MeV

in moving from the event position in the radiator to a position just inside the NE213 scintillator (see section 3.3). Thus a spectrometer of this nature cannot have a detection threshold lower than 40 MeV. The results show that the proton pair spectrometer used in this work had an effective lower "threshold" of about 58 MeV. This implies that each NE213 scintillator had a detection threshold of about 9 MeV. Although there was no information on the component of the measured energy spectra below 56 MeV, Monte Carlo results (see figure 5.7) showed that the yield in the energy spectrum decreased with decreasing proton energy. Future measurements could be extended to lower proton energies by replacing the surface barrier detector and NE213 liquid scintillator detectors with single smaller detectors, such as stilbene crystals. The advantage of using crystals over liquid scintillators is that it is not necessary to put crystals in cylinders with "thick" windows. This will therefore minimize the energy lost in the window of the scintillator (Δ_w in figure 3.15). Pulse shape discrimination could be used to select coincidence proton pairs that stop in these crystals, and veto detectors (liquid or plastic scintillators, for example) could be placed behind the stilbene crystals to reject protons that pass through the crystals.

The present work was particularly affected by three limitations which could and should be avoided if any further experiments of this type are undertaken. These are:

1. a good measurement should be made using a virgin beam, as described in section 4.3.3, in order to ensure that the spectrometer resolution function can be accurately estimated;

2. gain stabilization should be incorporated, for example by means of LED pulsers, as discussed in section 3.1; and

3. a method for estimating and correcting for the small but non-negligible background remaining after making the E_{AB} cut (see figure 3.24 and section 4.3) should be incorporated.

The Monte Carlo code used in this work (MCNPX 2.1.5) does not have the capability to utilize the available proton libraries, hence the calculations were performed by invoking the intranuclear cascade nuclear models (see section 5.1). Future comparisons should be made with calculations using newer versions of

the code, such as MCNPX 2.4, which utilizes evaluated proton cross sections to transport protons with energies up to 150 MeV, and the nuclear models for proton with energies greater than 150 MeV.

6.4 Conclusion

It has been demonstrated that the proton pair spectrometer used in this project, like the predecessor on which it is based [Br97b], enables *in situ* measurements to be made of energy spectra of proton therapy beams from a passive beam delivery system. The use of a coincidence system significantly reduces backgrounds and provides an effective way of discriminating against reaction tail events. The use of NE213 scintillators instead of NaI(tl) scintillators and the application of pulse shape discrimination in the NE213 scintillators reduced the number of accidental coincidences due to background neutron and gamma radiation to improve the selection of coincident proton pairs. The surface barrier detectors further contribute to the selection of p-p coincidences by the ΔE-E method of particle identification.

The results of this work are important as they provide an insight into what needs to be done for future developments in the NAC proton therapy beam line. The results also provide valuable information, which must be taken into account during treatment planning. For example, the results show that the beam incident at the isocentre has a small fraction of low-energy protons, which may lead to an increase in the dose delivered in the region before the lesion. Experimental results have also shown that the increase in the size of the final collimator is associated with an increase in the low-energy component in the energy spectrum. This increase in the low-energy component is attributed to the scattering in the collimator.

The measurements have also shown that the graphite wedges do not introduce a low-energy tail in the proton spectra. The measurements have however shown that there is small percentage of high-energy protons reaching the isocentre when the wedges are in the beam. The Monte Carlo calculations do not show this feature. This could be due in part to the low number of histories (10 million) used in the

simulations compared to the number of protons transported through the beam line in the experiment. The current used during the experiments was about 0.5 nA and the length of the runs simulated with MCNPX were each about 1.5 hours long, except for run 365 which was about 4 hours long. This implies that about 10^{13} protons were transported from the Havar exit window of the beam line, which is far greater than the 10^7 protons transported in the Monte Carlo calculations. An increase in the number of histories in the Monte Carlo simulations may show up this feature. This effect must be carefully studied as it implies that some protons may be bypassing the wedges when the beam current is low or that there are nuclear reactions in the wedges. Future calculations to investigate the effect of the energy degraders must also be done with the latest MCNPX code, which uses proton libraries to transport protons at energies below 150 MeV, instead of MCNPX 2.1.5, which only uses nuclear models.

Measurements made at positions displaced from the isocentre showed that the fraction of low-energy protons (which could be due to scattering in the final collimator) is high for measurements made closer to the collimator. Similar results were also found from Monte Carlo simulations made at the Kernfysich Versneller Instituut, Groningen, Netherlands [Lu01] using the code GEANT 3.21. Integrals over the energy spectra indicate that the low-energy component is higher in MCNPX computed spectra compared with the low-energy component in the measured spectra. This could be due to the sharp threshold of about 60 MeV used in the Monte Carlo calculation as compared to the varying detection threshold (about 55-70 MeV) of the detection system.

The experimental results from this work have been used to validate MCNPX calculations and can be used to validate calculations from other Monte Carlo codes. The agreement between the experimental data and the Monte Carlo calculations indicate that MCNPX can be used to predict the effects of different beam modification elements on the proton energy spectrum.

Appendix A

Intranuclear Cascade Models

The basic assumptions underlying the intranuclear cascade (INC) models were first proposed by Serber [Se47] and later revised by Bertini ([Be63] and [Be69]) and Chen *et al* [Ch71]. Yariv and Fraenken ([Ya79] and [Ya81]) extended the model to include the interaction of incident heavy-ion with nuclei. The statistical calculations based on this approached were first done by Goldberger [Go48], Metropolis *et al* ([Me58a] and [Me58b]), and later by Bertini ([Be63] and [Be69]) and Chen *et al* [Ch68]. A review of the intranuclear cascade model formulated by the above authros is given in the following sections.

The Bertini INC model treats the reaction of high energy ($E > 100$ MeV) nucleons with nuclei as free particle-particle collisions within the nucleus. The nucleus is regarded as a degenerate Fermi gas governed by the Pauli exclusion principle. The process is similar to the high energy scattering between free particles. The collision time between the incident nucleon and the nucleons inside the nucleus is shorter than the time between the collisions of nucleons inside the nucleus. The total cross section for scattering of one nucleon by another is inversely proportional to the energy of the incident nucleon, hence at sufficiently high energies the nucleus becomes transparent to the bombarding particles. The incident nucleon loses only a small fraction of its energy in a single interaction, the momentum transfer is $\sim \frac{\hbar}{a}$ where a is the range of the nuclear force. The reaction of a high energy nucleon and a target nucleus is regarded as a two stage process:

1. The first, fast stage ($\approx 10^{-22} s$), where the incoming nucleon collides with the nucleon inside the nucleus, initiating a cascade in the nucleus.

2. The second, slow stage, where the residual excited nucleus left after the cascade de-excites.

The INC model is applicable in the fast stage and the second stage and can be described by models such as the evaporation model. Depending on the collision site in the nucleus, the incident nucleon can be scattered out of the nucleus after a single (or few) collision(s) if the collision occurs on the edge of the nucleus, or experience several collisions if the collision occurs in the centre of the nucleus. Since the energy transfer in each collision is small, the recoiling nucleons have lower energies and shorter mean free paths and thus can only escape nuclear matter without further collisions if the collision is at the edge of the nucleus. For collisions inside the nucleus, the recoiling nucleons collide with other nucleons inside the nucleus and the energy distributed over the nucleus. Exchange collisions are also possible if the collision is at the edge of the nucleus, a neutron knocking out a proton or vice versa. The interactions in the cascade stage are regarded as being between individual nucleons in the nucleus, including the interactions where the incident nucleon interacts with a nucleon constituting a cluster of nucleons such as deuterons, tritons and alphas. The wavelength of the incoming particle and that of the collision products is smaller than the average internucleon distance ($\approx 10^{-13}$ cm), hence the collision between the incident energy nucleon and the nucleons inside the nucleus can be described with the aid of free particle cross sections.

The collisions between the nucleons are not entirely free, there is interference from other nucleons in the nucleus because of the degeneracy of nuclear matter. The kinematics of the collisions are treated relativistically, and the nucleon-nucleon interactions are evaluated using free particle cross sections, modified by Pauli exclusion principle. Statistical sampling techniques are used in the INC model to determine the location and type of collision, momentum of the recoiling and scattered nucleon, and the scattering angles for each collision. The collision sites are restricted by short-range nuclear correlation effects. The nucleon pair correlation function depends on the interaction potential between two nucleons and the Pauli exclusion principle. The correlation effects restricts the collision sites inside the nucleus in the following way: if an incident nucleon engages in a Pauli allowed collision inside the nucleus at collision site r_1 (where r is the radial distance inside the nucleus), the scattered and recoiling nucleons will experience Pauli allowed collisions at collision sites r_2 and r_3 if and only if r_1, r_2, and r_3 are separated by a distance d, which is determined by the nuclear correlation effects.

The nuclear density is described by a step function, where the nucleus is regarded as being made up of concentric spheres, each having a constant density. The spheres divide the nucleus into regions having different densities. The number of regions and their densities, in particular the central and outer regions, are determined using results from experiments such as the electron scattering experiment. The diffuseness of the outer edge of the nucleus is also taken into consideration in the determination of the outer region's density. The momentum distribution of the nucleons in each region is assumed to be that of a degenerate Fermi gas with the Fermi energy

$$E_{f_i} = \left(\frac{\hbar^2}{2m}\right)\left(3\pi^2\rho_i\right)^{\frac{3}{2}} \tag{A.1}$$

where i is either a proton or a neutron, m is the nucleon mass and ρ_i is the density of the neutron or proton.

The nuclear potential of the neutrons and protons differs in the various regions as a result of the variations in their respective Fermi energies (see equation A.1). The kinetic energies of the nucleons will therefore change as the nucleons move from one region to another in accordance with the principle of energy conservation. The nucleons will also be subjected to refraction and reflection at the boundaries of the regions.

The ISABEL model ([Ya79] and [Ya81]) is a generalization of the Bertini model, it describes the collision process for heavy-ion interactions, in contrast to the Bertini model, which only considers the interaction of a single high energy nucleon with the nucleus. The nuclear density in ISABEL is approximated by up to 16 density levels in contrast to three in the Bertini model. The nuclear density of the incident nucleus is also approximated by a step function, and the momentum distribution of the nucleons is assumed to be that of a degenerate Fermi gas, and the effects of the Pauli exclusion principle are taken into account. The ISABEL model also takes into account the depletion in the nuclear density of the Fermi sea as a result of the cascade [Ya79]. The nucleons in the incident and target nuclei are bound together in their respective nuclei by potential wells which are uniquely determined by nuclear densities for a degenerate Fermi gas. The nucleons of the incident nucleus feel the potential of their nucleus while they are in the nuclear volume and are free outside this volume i.e. they do not feel the potential of the target nucleus even when they are inside the volume of the target nucleus, and the same applies to the potential felt by the target nucleons.

The interactions of the incident and target nuclei are taken as interactions between Fermi sea particles of the incident nucleus and the Fermi sea particles of the target nucleus or as the interactions of the cascade particles and the Fermi sea particles of either the target or incident nuclei. Scattering between two cascading particles is also allowed, on condition that they cannot interact more than once, until one of them have interacted with a third particle, which may be a third cascading particle or a nucleon in the target nucleus [Ya81].

Appendix B

Monte Carlo Input File

```
NAC Proton beamline - Large final collimator (r=0.5)
 C  Cell Cards - Beamline Cells
1 0 +1 :-50 :+20                $ outer edge on everything
2 0 +50 -100 -1                     $ source cell
1700 12 -0.0012 +10 -20 -1          $ between isocentre and outer limit
C Vacuum Window
100 20 -8.3 +100 -110 -1
110 12 -0.0012 +100 -6000 #100 -1 $ air from vacuum window to next component
C X Steering Magnet (Treat as Iron Collimator)
6000 3 -7.88 +6000 -6100 (+6020 :+6040 :-6030 :-6050) $ Rectangular Iron col
6010 12 -0.0012 +6000 -500 #6000 -1 $ air till next component
C NAC MWIC
C Wires Parallel to the X axis
501 14 -19.3 -501 -5999
502 14 -19.3 -502 -5999
503 14 -19.3 -503 -5999
504 14 -19.3 -504 -5999
505 14 -19.3 -505 -5999
506 14 -19.3 -506 -5999
507 14 -19.3 -507 -5999
508 14 -19.3 -508 -5999
509 14 -19.3 -509 -5999
510 14 -19.3 -510 -5999
511 14 -19.3 -511 -5999
512 14 -19.3 -512 -5999
513 14 -19.3 -513 -5999
514 14 -19.3 -514 -5999
515 14 -19.3 -515 -5999
516 14 -19.3 -516 -5999
517 14 -19.3 -517 -5999
518 14 -19.3 -518 -5999
519 14 -19.3 -519 -5999
520 14 -19.3 -520 -5999
521 14 -19.3 -521 -5999
522 14 -19.3 -522 -5999
523 14 -19.3 -523 -5999
524 14 -19.3 -524 -5999
525 14 -19.3 -525 -5999
526 14 -19.3 -526 -5999
527 14 -19.3 -527 -5999
528 14 -19.3 -528 -5999
529 14 -19.3 -529 -5999
530 14 -19.3 -530 -5999
531 14 -19.3 -531 -5999
```

```
532 14 -19.3 -532 -5999
533 14 -19.3 -533 -5999
534 14 -19.3 -534 -5999
535 14 -19.3 -535 -5999
536 14 -19.3 -536 -5999
537 14 -19.3 -537 -5999
538 14 -19.3 -538 -5999
539 14 -19.3 -539 -5999
540 14 -19.3 -540 -5999
541 14 -19.3 -541 -5999
542 14 -19.3 -542 -5999
543 14 -19.3 -543 -5999
544 14 -19.3 -544 -5999
545 14 -19.3 -545 -5999
546 14 -19.3 -546 -5999
547 14 -19.3 -547 -5999
548 14 -19.3 -548 -5999
549 14 -19.3 -549 -5999
C Wires Parallel to the Y axis
551 14 -19.3 -551 -5999
552 14 -19.3 -552 -5999
553 14 -19.3 -553 -5999
554 14 -19.3 -554 -5999
555 14 -19.3 -555 -5999
556 14 -19.3 -556 -5999
557 14 -19.3 -557 -5999
558 14 -19.3 -558 -5999
559 14 -19.3 -559 -5999
560 14 -19.3 -560 -5999
561 14 -19.3 -561 -5999
562 14 -19.3 -562 -5999
563 14 -19.3 -563 -5999
564 14 -19.3 -564 -5999
565 14 -19.3 -565 -5999
566 14 -19.3 -566 -5999
567 14 -19.3 -567 -5999
568 14 -19.3 -568 -5999
569 14 -19.3 -569 -5999
570 14 -19.3 -570 -5999
571 14 -19.3 -571 -5999
572 14 -19.3 -572 -5999
573 14 -19.3 -573 -5999
574 14 -19.3 -574 -5999
575 14 -19.3 -575 -5999
576 14 -19.3 -576 -5999
577 14 -19.3 -577 -5999
578 14 -19.3 -578 -5999
579 14 -19.3 -579 -5999
580 14 -19.3 -580 -5999
581 14 -19.3 -581 -5999
582 14 -19.3 -582 -5999
583 14 -19.3 -583 -5999
584 14 -19.3 -584 -5999
585 14 -19.3 -585 -5999
586 14 -19.3 -586 -5999
587 14 -19.3 -587 -5999
588 14 -19.3 -588 -5999
589 14 -19.3 -589 -5999
590 14 -19.3 -590 -5999
591 14 -19.3 -591 -5999
592 14 -19.3 -592 -5999
593 14 -19.3 -593 -5999
594 14 -19.3 -594 -5999
595 14 -19.3 -595 -5999
```

```
596 14 -19.3 -596 -5999
597 14 -19.3 -597 -5999
598 14 -19.3 -598 -5999
599 14 -19.3 -599 -5999
C Air outside of the X wires
5001 12 -0.0012 +500 -550 -5100 -1
             #501 #502 #503 #504 #505
             #506 #507 #508 #509 #510
5002 12 -0.0012 +500 -550 +5100 -5110 -1
             #511 #512 #513 #514 #515
             #516 #517 #518 #519 #520
             #521 #522 #523 #524 #525
5003 12 -0.0012 +500 -550 +5110 -5120 -1
             #526 #527 #528 #529 #530
             #531 #532 #533 #534 #535
             #536 #537 #538 #539 #540
5004 12 -0.0012 +500 -550 +5120 -1
             #541 #542 #543 #544 #545
             #546 #547 #548 #549
C Air outside of Y wires
5005 12 -0.0012 +550 -5000  -5200 -1
             #551 #552 #553 #554 #555
             #556 #557 #558 #559 #560
5006 12 -0.0012 +550 -5000  +5200 -5210 -1
             #561 #562 #563 #564 #565
             #566 #567 #568 #569 #570
             #571 #572 #573 #574 #575
5007 12 -0.0012 +550 -5000  +5210 -5220 -1
             #576 #577 #578 #579 #580
             #581 #582 #583 #584 #585
             #586 #587 #588 #589 #590
5008 12 -0.0012 +550 -5000  +5220 -1
             #591 #592 #593 #594 #595
             #596 #597 #598 #599
5000 11 -2.69 +5000 -5010 -5999 -1   $ HV foils
5010 18 -1.42 +5010 -5020 -5999 -1   $ kapton windows
5020 12 -0.0012 +5000 -600 -1 #5000 #5010    $ air till next component -600
C Collimator (magnet pole gap) -Y Steering Magnet
600 3 -7.88 +600 -610 (+620 :-630 :+640 :-650) -1 $ material=iron
610 12 -0.0012 +600 -700 #600 -1 $ Air aperture
C Trimmer Plates
700 16 -1.1 +700 -710 -705
710 12 -0.0012 +700 -200 #700 -1             $ air till next component
C First Scatterer
200 1 -11.69 +200 -210 -1          $ For Standard Beam - material=lead
210 12 -0.0012 +210 -300 #200 -1 $ air till next comp
C Ionization Chamber 1
300 5 -1.92 +300 -310 -1
310 12 -0.0012 +310 -1900 #300 -1  $ air till next component
C Second Lead Scatterer
1900 1 -11.69 +1900 -1910 -1          $ For Standard Beam - material=lead
1910 12 -0.0012 +1910 -1800 #1900 -1 $ air till next comp
C Degraders
C Multilayer Faraday Cup
1800 8 -8.52 +1800 -1810 +1820 -1830 -1
1810 12 -0.0012 +1800 -800 #1800 -1       $ Air inside of aperture
C 400 - Modulator Propeller
C Range Monitor (Treated as a Brass Collimator)
800 8 -8.52 +800 -810 +820 -830
810 12 -0.0012 +800 -1000 -1 #800 -1         $ air aperture
C Occluding Rings (Second Scatterer)
1000 8 -8.52 +1000 -1010 -1020               $ Central Plug of Occluder
1010 12 -0.0012 +1000 -1010 +1020 -1030      $ Gap in Occluder
1020 8 -8.52 +1000 -1010 +1030 -1040         $ Outer Occluder
```

```
 1030 12 -0.0012 +1000 -1010 +1040 -1       $ Air outside of Occluder
 1050 8 -8.52 +1010 -1050 -1060               $ Brass second scatterer
 1060 12 -0.0012 +1010 -1100 #1050 -1   $ Air outside of second scatterer
 C Concrete Collimator
 1100 18 -1.42 +1100 -1110 (-1120 :+1125 :-1130 :+1135) -1 $ material=concret
 1110 12 -0.0012 +1100 -1200 #1100 -1 $ Air inside of aperture
 C Lead Collimator
 1200 1 -11.69 +1200 -1210 +1220 -1
 1210 12 -0.0012 +1200 -1300 #1200 -1      $ Air inside of aperture
 C Iron Collimator
 1300 3 -7.88 +1300 -1310 +1320 -1
 1310 12 -0.0012 +1300 -1400 #1300 -1  $ Air inside of aperture
 C Brass Collimator
 1400 8 -8.52 +1400 -1410 +1420 -1
 1410 12 -0.0012 +1400 -1500 #1400 -1       $ Air inside of aperture
 C Ionization Chamber 2
 1500 5 -1.92 +1500 -1510 -1550
 1510 11 -2.69 +1510 -1520 -1550
 1520 18 -1.42 +1520 -1540 -1550
 1540 12 -0.0012 +1500 -1600 -1 #1500 #1510 #1520
 C Final collimator (PATIENT COLLIMATOR)
 1600 8 -8.52 +1600 -1610 +1620 -1630
 1610 12 -0.0012 +1600 -10 -1 #1600       $ Air inside of aperture

C SURFACE_DEFINITIONS
 C Beamline Surfaces
  10  PZ 700                        $ BEAMLINE-STOP (ISOCENTER)
C  10 PZ 672                         $ 28 cm upstream, close to finalcollimator
  1  CZ 50                          $ outer edge on everything
C  2  CZ 20
  2 CZ 10                           $ Scoring CylinderC Final (Patient) Collimator
  20  PZ +705                       $ BEAMLINE-STOP+5
  50  PZ -10
  100  PZ 0                         $ BEAMLINE START
 C Vacuum Window
  110  PZ 0.0025                    $ BEAMLINE_START+VACUUM_WINDOW_THICKNESS
  C X Steering Magnet
  6000 PZ 9.0
  6100 PZ 29.0
  6020 PY +10
  6030 PY -10
  6040 PX +4
  6050 PX -4
  C MWIC
  500 PZ 34.0                       $ BEAMLINE_START+MWIC_DISTANCE
  550 PZ 35.0                       $ MIDPLANE=BEAMLINE_START+MWIC_DISTANCE+1
  C X wires
  C ID     Y    Z    R
  501 C/X -4.8 34.5 0.01  $ 1
  502 C/X -4.6 34.5 0.01
  503 C/X -4.4 34.5 0.01
  504 C/X -4.2 34.5 0.01
  505 C/X -4.0 34.5 0.01
  506 C/X -3.8 34.5 0.01
  507 C/X -3.6 34.5 0.01
  508 C/X -3.4 34.5 0.01
  509 C/X -3.2 34.5 0.01
  510 C/X -3.0 34.5 0.01   $ 10
  511 C/X -2.8 34.5 0.01
  512 C/X -2.6 34.5 0.01
  513 C/X -2.4 34.5 0.01
  514 C/X -2.2 34.5 0.01
  515 C/X -2.0 34.5 0.01
  516 C/X -1.8 34.5 0.01
```

```
517 C/X -1.6 34.5 0.01
518 C/X -1.4 34.5 0.01
519 C/X -1.2 34.5 0.01
520 C/X -1.0 34.5 0.01   $ 20
521 C/X -0.8 34.5 0.01
522 C/X -0.6 34.5 0.01
523 C/X -0.4 34.5 0.01
524 C/X -0.2 34.5 0.01
525 C/X +0.0 34.5 0.01
526 C/X +0.2 34.5 0.01
527 C/X +0.4 34.5 0.01
528 C/X +0.6 34.5 0.01
529 C/X +0.8 34.5 0.01
530 C/X +1.0 34.5 0.01    $ 30
531 C/X +1.2 34.5 0.01
532 C/X +1.4 34.5 0.01
533 C/X +1.6 34.5 0.01
534 C/X +1.8 34.5 0.01
535 C/X +2.0 34.5 0.01
536 C/X +2.2 34.5 0.01
537 C/X +2.4 34.5 0.01
538 C/X +2.6 34.5 0.01
539 C/X +2.8 34.5 0.01
540 C/X +3.0 34.5 0.01    $ 40
541 C/X +3.2 34.5 0.01
542 C/X +3.4 34.5 0.01
543 C/X +3.6 34.5 0.01
544 C/X +3.8 34.5 0.01
545 C/X +4.0 34.5 0.01
546 C/X +4.2 34.5 0.01
547 C/X +4.4 34.5 0.01
548 C/X +4.6 34.5 0.01
549 C/X +4.8 34.5 0.01    $ 49
C Y-wires
C ID      Y     Z     R
551 C/Y -4.8 35.5 0.01    $ 1
552 C/Y -4.6 35.5 0.01
553 C/Y -4.4 35.5 0.01
554 C/Y -4.2 35.5 0.01
555 C/Y -4.0 35.5 0.01
556 C/Y -3.8 35.5 0.01
557 C/Y -3.6 35.5 0.01
558 C/Y -3.4 35.5 0.01
559 C/Y -3.2 35.5 0.01
560 C/Y -3.0 35.5 0.01     $ 10
561 C/Y -2.8 35.5 0.01
562 C/Y -2.6 35.5 0.01
563 C/Y -2.4 35.5 0.01
564 C/Y -2.2 35.5 0.01
565 C/Y -2.0 35.5 0.01
566 C/Y -1.8 35.5 0.01
567 C/Y -1.6 35.5 0.01
568 C/Y -1.4 35.5 0.01
569 C/Y -1.2 35.5 0.01
570 C/Y -1.0 35.5 0.01     $ 20
571 C/Y -0.8 35.5 0.01
572 C/Y -0.6 35.5 0.01
573 C/Y -0.4 35.5 0.01
574 C/Y -0.2 35.5 0.01
575 C/Y +0.0 35.5 0.01
576 C/Y +0.2 35.5 0.01
577 C/Y +0.4 35.5 0.01
578 C/Y +0.6 35.5 0.01
579 C/Y +0.8 35.5 0.01
```

```
 580 C/Y +1.0 35.5 0.01     $ 30
 581 C/Y +1.2 35.5 0.01
 582 C/Y +1.4 35.5 0.01
 583 C/Y +1.6 35.5 0.01
 584 C/Y +1.8 35.5 0.01
 585 C/Y +2.0 35.5 0.01
 586 C/Y +2.2 35.5 0.01
 587 C/Y +2.4 35.5 0.01
 588 C/Y +2.6 35.5 0.01
 589 C/Y +2.8 35.5 0.01
 590 C/Y +3.0 35.5 0.01    $ 40
 591 C/Y +3.2 35.5 0.01
 592 C/Y +3.4 35.5 0.01
 593 C/Y +3.6 35.5 0.01
 594 C/Y +3.8 35.5 0.01
 595 C/Y +4.0 35.5 0.01
 596 C/Y +4.2 35.5 0.01
 597 C/Y +4.4 35.5 0.01
 598 C/Y +4.6 35.5 0.01
 599 C/Y +4.8 35.5 0.01    $ 49
 5000 PZ 36.0   $ BEAMLINE_START+MWIC_DISTANCE+2.0(Aluminum HV plate enter)
 5010 PZ 36.025 $ BEAMLINE_START+MWIC_DISTANCE+2.0+0.025(Al HV plate exit)
 5020 PZ 36.027 $ BEAMLINE_START+MWIC_DISTANCE+2.0+0.025+0.002 Kapton Win
 5100 PY -2.9
 5110 PY +0.1
 5120 PY +3.1
 5200 PX -2.9
 5210 PX +0.1
 5220 PX +3.1
 5999 CZ 5.0   $ outer limit of interest of MWIC
 C Collimator - (Steering Magnet Y)
 600  PZ 47                  $ BEAMLINE_START+47
 610  PZ 67                 $ BEAMLINE_START+47+20
 620  PY +4
 630  PY -4
 640  PX +10
 650  PX -10
 C Trimmer Plates
 700 PZ 71                  $ BEAMLINE_START+(TRIMMER_PLATES_DISTANCE=71)
 710 PZ 71.005                 $ BEAMLINE_START+71+TRIMMER_THICKNESS
 705 CZ 12                   $ Outer useful radius of thiolyte plates
 C First Scatterer
 200  PZ 74.5                  $ BEAMLINE_START+S1_DISTANCE
 210  PZ 74.6          $ BEAMLINE_START+S1_DISTANCE+(S1_THICKNESS=0.1)
 C Ionization Chamber 1
 300  PZ 77.00               $ BEAMLINE_START+IC_1_DISTANCE
 310  PZ 77.01               $ BEAMLINE_START+IC_1_DISTANCE+(NAC_IC1_THICKNE
 C Second Lead Scatterer
 1900  PZ 78.5                 $ BEAMLINE_START+LEAD_S2_DISTANCE
 1910  PZ 78.6          $ BEAMLINE_START+LEAD_S2_DISTANCE+(LEAD_S2_THICKNESS
C Degraders
C Multilayer Faraday Cup (Treat as Brass Collimator)
 1800  PZ 92.5   $ BEAMLINE_START+(MULTILAYER_FC_DISTANCE=99)
 1810  PZ 102.5  $ BEAMLINE_START+MULTILAYER_FC_DISTANCE+(MULTILAYER_FC__THIC
 1820  CZ 3    $ MULTILAYER_FC__RADIUS
 1830  CZ 20
 C 400 Modulator Propeller
 C Range Monitor (Treat as Brass Collimator)
 800 PZ 292                    $ BEAMLINE_START+292
 810 PZ 301                    $ BEAMLINE_START+290+9
 820 CZ 5
 830 CZ 20
C Occluding Rings (Second Scatterer)
 1000 PZ 302.5                  $ BEAMLINE_START+OCCLUDER_DISTANCE
```

```
 1010 PZ 307.5        $ BEAMLINE_START+(OCCLUDER_DISTANCE+OCCLUDER_THICKNESS=5
 1020 CZ 1.344                  $ Central Brass stopper
 1030 CZ 2.418                  $ Inner radius of stopper
 1040 CZ 3.611                  $ Outer radius of stopper
C Second Scatterer (Back of Occluding Rings)
 1050 PZ 307.6                  $ SURFACE=1010+(S2_THICKNESS=0.1cm?)
 1060 CZ 10.0                   $ outer radius of interest
 C Concrete Collimator
 1100 PZ 344.5                  $ BEAMLINE_START+CONCRETE_COL_DISTANCE
 1110 PZ 363.5                  $ SURFACE=1100+(CONCRETE_COL_THICKNESS=19)
 1120 PX -10
 1125 PX +10
 1130 PY -10
 1135 PY +10
C Lead Collimator
 1200 PZ 452.5                  $ BEAMLINE_START+LEAD_COL_DISTANCE
 1210 PZ 457.4        $ BEAMLINE_START+LEAD_COL_DISTANCE+(LEAD_COL_THICKNESS=4
 1220 CZ 12                     $ LEAD_COL_RADIUS
C Iron Collimator
 1300  PZ 513.5                 $ BEAMLINE_START+IRON_COL_DISTANCE
 1310  PZ 518.7          $ BEAMLINE_START+IRON_COL_DISTANCE+(IRON_COL_THICKNESS=
 1320  CZ 12             $ IRON_COL_RADIUS
C Brass Collimator
 1400  PZ 644.4    $ BEAMLINE_START+BRASS_COL_DISTANCE
 1410  PZ 649.4  $ BEAMLINE_START+BRASS_COL_DISTANCE+(BRASS_COL_THICKNESS=5cm
 1420  CZ 10       $ BRASS_COL_RADIUS
C Ionization Chamber 2
 1500 PZ 651
 1510 PZ 651.001
 1520 PZ 651.0135
 1540 PZ 651.0205
 1550 CZ 12.0
C Final Collimator (patient Collimator)
 1600 PZ 663.5     $ BEAMLINE_START+PATIENT_COL_DISTANCE
 1610 PZ 668.5     $ BEAMLINE_START+PATIENT_COL_DISTANCE+(PATIENT_COL_THICKNES
 1620 CZ 2       $ PATIENT_COL_RADIUS (FINAL_COLLIMATOR)
 1630 CZ 30

mode h
C Beamline Importances
imp:h 0 1 1
C Vacuum window
      1 1
C X Steering Magnet
      1 1
C MWIC
C X Wires
      1 1 1 1 1 1 1 1 1 1 1 1 1 1 1
      1 1 1 1 1 1 1 1 1 1 1 1 1 1 1
      1 1 1 1 1 1 1 1 1 1 1 1 1 1 1
      1 1 1 1
C Y Wires
        1 1 1 1 1 1 1 1 1 1 1 1 1 1 1
        1 1 1 1 1 1 1 1 1 1 1 1 1 1 1
        1 1 1 1 1 1 1 1 1 1 1 1 1 1 1
        1 1 1 1
C Air between the X wires
      1 1 1 1
C Air between the Y wires
      1 1 1 1
C Al, Kapton, air
      1 1 1
C Y Steering Magnet
      1 1
```

```
C Trimmer Plates
     1 1
C First Scatterer
     1 1
C Ioninzation Chamber 1
     1 1
C Second Lead Scatterer
     1 1
C Degraders
C Multilayer Faraday Cup
     1 1
C Modulator Poropeller
C Range Monitor
     1 1
C Occluding Rings
     1 1 1 1 1 1
C Concrete Collimator
     1 1
C Lead Collimator
     1 1
C Iron Collimator
     1 1
C Brass Collimator
     1 1
C Ionization Chamber 2
     1 1 1 1
C Final (Patient) Collimator
     1 1
C Source Definition
SDEF DIR=1 VEC=0 0 1 X=D1 Y=D2 Z=-1 ERG=204 TR=1
SP1 -41 1.17741 0
SP2 -41 1.17741 0
TR1 0 0 0 0 1 0 -1 0 0 0 0 1
C SI3 201.1 201.2 201.3 201.375 201.45 201.5 201.55 201.625 201.7 &
C 201.8 201.9 202 202.1 202.175 202.25 202.3 202.35 202.425 202.5 &
C 202.6 202.7
C SP3 0 0.0013 0.0228 0.0668 0.1587 0.2119 0.2743 0.3446 0.4013 0.4602 &
C 0.5 0.5398 0.5987 0.6554 0.7257 0.7881 0.8413 0.9332 0.9772 0.9987 1
C Physics Cards
C LCA 2 0 0
LCA 0 0 0
C Material Definition
m1 82207 1                                  $ Lead
m3 26053 1                                   $ Iron changed from 26052 to 26053
m5 1001 -0.041959 6012 -0.625017 8016 -0.333025  $ Mylar
m8 29063 -0.62 30064 -0.38                   $ Brass 30065 changed to 30064
m11 13027 1                                  $ Aluminum
m12 6012 -0.000124 7014 -0.755267 8016 -0.231781 18040 -0.012827  $ Air
m14 74184 1                                  $ Tungsten
m16 1001 -0.143711 6012 -0.856289            $ Polyethylene
m18 1001 -0.026362 6012 -0.691133 8016 -0.209235 7014 -0.073270  $ Kapton for
m20 27059 -0.1 24052 -0.1 12024 -0.1 42096 -0.1 28059 -0.1 74184 -0.1 26055 &
-0.4    $ Havar
C Energy Cutoffs
PHYS:H 205 0 0
C Tallies
C F1:H 100 6000 500 600 700 200 300 1900 1800 800 1000 1100 1200 1300 &
C 1400 1500 1600 10
F1:H 10
FS1 -2
C F101 10
C FS101 -2
E0 0 1 2 3 4 5 6 7 8 9 10 11 12 13 14 15 16 17 18 19 20 21 22 23 24 25 26 27 &
28 29 30 31 32 33 34 35 36 37 38 39  40 41 42 43 44 45 46 47 48 49 50 51 52 &
```

```
53 54 55 56 57 58 59 60 61 62 63 64 65 66 67 68 69 70 71 72 73 74 75 76 77 &
78 79 80 81 82 83 84 85 86 87 88 89 90 91 92 93 94 95 96 97 98 99 100 &
101 102 103 104 105 106 107 108 109 110 111 112 113 114 115 116 117 118 119 &
120 121 122 123 124 125 126 127 128 129 130 131 132 133 134 135 136 137 138 &
139 140 141 142 143 144 145 146 147 148 149 150 151 152 153 154 155 156 157 &
158 159 160 161 162 163 164 165 166 167 168 169 170 171 172 173 174 175 176 &
177 178 179 180 181 182 183 184 185 186 187 188 189 190 191 192 193 194 195 &
196 197 198 199 200 201 202 203 204 205 206 207 208 209 210
C FT1 GEB 6 2 0
C Problem Cutoff (no. of histories)
nps 100000000
PRDMP j j 1 2
c end
```

Bibliography

[Ad78] J.M. Adams and G. White, "A versatile pulse shape discriminator for charged particle separation and its application to fast neutron time-of-flight spectroscopy". Nucl. Instr. Meth. **156**, 459-476 (1978).

[Ar96] G. Arduini, R. Cambria, C. Canzi, F. Gerardi, B. Gottschalk, R. Leone, L. Sangaletti, and M. Silari, "Physical specifications of clinical proton beams from a synchroton". Med. Phys. **23**, 939-951 (1996)

[Ar72] T.W. Armstrong and K.C. Chandler, "HETC, A high-energy transport code". Nucli. Sci. Eng., **49** (1972).

[At80] F. Atchison, "Spallation and fission in heavy metal nuclei under medium energy proton bombardment", in *Targets for Neutron Spallation Sources*, Jul-Conf–34, Kernforchun-sanlage Julich GmbH (January 1980).

[Ba69] C.A. Baker, B.E. Bonner, I.M. Blair, F.P. Brady, J.A. Edginton and V.J. Howard, "A measurement of nuclear interactions in plastic scintillators". Nucl. Instr. Meth. **71**, 117-120 (1969).

[Ba81] J. Barish, T.A. Gabriel, F.S. Alsmiller and R.G. Alsmiller, Jr., "HETFIS high-energy nucleon meson transport code with fission", report ORNL-TM-7882, Oak Ridge National Laboratory (July 1981).

[Be93] M.J. Berger, "Proton Monte Carlo program PTRAN". *Report NISTIR 5113*, National Institute for Standards and Technology, Gaithersburg MD, 1993.

[Be63] H.W. Bertini, "Low-energy intranuclear cascade calculation." Phys. Rev. **131**, 1801-1821 (1963).

[Be69] H.W. Bertini, "Intranuclear-cascade calculation of the secondary nucleon spectra from nucleon-nucleus interactions in the energy range 340 to 2900

MeV and comparisons with experiment." Phys. Rev. **188**, 1711-1730 (1969).

[Be53a] H.A. Bethe, "Molière's theory of multiple scattering". Phys. Rev. **89** 1256-1266 (1953).

[Be53b] H.A. Bethe and J. Ashkin in *Experimental Nuclear Physics* Vol. 1, Edited by E. Segre, Wiley, New York, (1953) p.282.

[Bi70] H. Bichsel, "Straggling and particle identification in silicon detectors". Nucl. Instr. Meth. **78**, 277-284 (1970).

[Bi82] H. Bichel, "Lateral displacement in small angle multiple scattering". Phys. Med. Biol. **27**, 959-961 (1982).

[Bi89] H. Bichsel and T. Hiraoka, "Energy spectra and depth-dose curves for 70 MeV protons". Int. J. Quant. Chem. **23**, 565-574 (1989).

[Bl83] "Fundamentals of Cancer Management 1. Radiation Therapy Planning", edited by N.M Bleehen, E. Gladstein and J.L. Haybittle. Marcel Dekker, inc. New York.

[Bo99] T.D. Bohm, P.M. DeLuca Jr., L.J. Cox, R.L. Maughan, D.T.L. Jones and A. Lennox, "Monte Carlo calculations to characterize the source for neutron therapy facilities." Med. Phys. **25**, 783-792 (1999).

[Bo93] D.E. Bonnett, "Current developments in proton therapy: areview". Phys. Med. Biol. **38**, 1371-1392 (1993).

[Bo96] T. Bortfeld and W. Schlegel, "An analytical approximation of depth-dose distributions for therapeutic proton beams". Phys. Med. Biol. **41**, 1331-1339 (1996).

[Br62] E. Brannen and G.L. Olde, "The response of organic scintillators to electron energy deposited in them". Radiat. Res. **16**, 1-6 (1962).

[Br81] D.J. Brenner, R.E. Prael, J.F. Dicello and M. Zaider, "Improved calculations of energy deposition from fast neutrons", in *Proceedings of Fourth Symposium on Neutron Dosimetry*, EUR-7448, Munich-Neuherberg (1981).

[Br97a] J.F. Briemeister, editor, "MCNP^{TM} - A general Monte Carlo N-Particle Transport Code", report LA-12625-M, Los Alamos National Laboratory (March 1997).

[Br79] F.D. Brooks, "Development of organic scintillators". Nucl. Instr. Meth. **162**, 477-505 (1979).

[Br88] F.D. Brooks, W.A. Cilliers, B.R.S. Simpson, F.D. Smit, M.S. Allie, D.T.L. Jones, W.R. McMurray and J.V. Pilcher, "Deuterated anthracene spectrometer for 5-30 MeV neutrons". Nucl. Instr. Meth. **A270**, 149-156 (1988).

[Br95] F.D. Brooks, D.T.L. Jones, C.C. Bowley, A. Buffler, M.S. Allie and J.E. Symons "Assesment of spectral changes in a high- energy proton therapy beam." 1st Research Co-ordinating Meeting of IAEA Program on Application of Heavy Charged Particles in Cancer Radiotherapy, Vienna, (1995).

[Br97b] F.D. Brooks, D.T.L. Jones, C.C. Bowley, J.E. Symons, A. Buffler and M.S. Allie, "Energy spectra in the NAC proton therapy beam." Radiat. Prot. Dosim. **70**, 477-480 (1997).

[Br01] F.D. Brooks, private communication.

[Bu86] W.E. Burcham, *Elements of Nuclear Physics*, Longman Scientific and Technical, 1986.

[Bu59] E.J. Burge, "The total proton reaction cross section of carbon from 10-68 MeV by a new method". Nucl. Phys. **13**, 511-515 (1959).

[Bu70] G.W. Butler, A.M. Poskanzer and D.A. Landis, "Identification of nuclear fragments by a combined time-of-flight, ΔE- E technique". Nucl. Instr. Meth. **89**, 189-198 (1970).

[Ca73] J. Carlsonn and K. Rosander, "Effects of multiple scattering on proton beams in radiotherapy". Phys. Med. Biol. **18**, 633-640 (1973).

[Ca97] A.K. Carlsson, P. Andreo and A. Brahme, "Monte Carlo and analytic calculation of proton pencil beams for computerized treatment plan optimization". Phys. Med. Biol. **42**, 1033-1053 (1997).

[Ch99] M.B. Chadwick, D.T.L. Jones, G.J. Arendse, A.A. Cowley, W.A. Richter, J.J. Lawrie, R.T. Newman, J.V. Pilcher, F.D. Smit, G.F. Steyn, J.W. Koen and J.A. Stander, "Nuclear interaction cross sections for proton radiotherapy". Nucl. Phys. **A654**, 1051c-1057c (1999).

[Ch68] K. Chen, Z. Fraenkel, G. Friedlander, J.R. Grover, J.M. Miller and Y. Shimamoto, Vegas: A Monte Carlo simulation of intranuclear cascades." Phys. Rev. **166**, 949-967 (1968).

[Ch71] K. Chen, G. Friedlander, G.D. Harp and J.M. Miller, "Effects of nucleon-pair correlations on Monte Carlo intranuclear cascade simulations." Phys. Rev. **C4**, 2234-2240 (1971).

[Ch93] W.T. Chu, B.A. Ludewigt and T.R. Renner, "Instrumentation for treatment of cancer using protons and light-ion beams". Rev. Sci. Instrum. **64** 2055-2122 (1993).

[Co71] B.L. Cohen, Concepts of Nuclear Physics, McGraw Hill Book Company, 1971.

[Co92] J.L. Conradie, "Improved proton beam quality and intensity from a 200 MeV cyclotron system". PhD Thesis, Unpublished (1992).

[Cr70] R.L. Craun and D.L. Smith, "Analysis of response data for several organic scintillators". Nucl. Instr. Meth. **80**, 239-244 (1970).

[De98] J.J. DeMarco, T.D. Solberg and J.B. Smathers. "A CT-based Monte Carlo simulation tool for dosimetry planning and analysis." Med. Phys. **25**, 1-11(1998).

[Dr81] L. Dresner, "EVAP - A Fortran program for calculating the evaporation model of various particles from excited compound nuclei", report ORNL-TM-7882, Oak Ridge National Laboratory (July 1981).

[Ei63] R. Eisberg, S. Mayo and W. Schimmerling, "Nuclear interaction correction for deuteron scintillation counting". Nucl. Instr. Meth. **21**, 232-234 (1963).

[Ev55] R.D. Evans, The Atomic Nucleus, McGraw Hill Book, 1955.

[Fa63] H. Faissner, F. Ferrero, A. Ghani and M. Reinharz, "Performance of large liquid scintillation counters". Nucl. Instr. Meth. **20**, 289-293 (1963).

[Fa96] A. Fasso, A. Ferrari, J. Ranft, and P.R. Sala, *Proceedings of the 2nd Workshop on Simulating Accelerator Radiation Environment (SARE-2)*, CERN, Geneva, October 9-11, 1995 (1996).

[Fe95] M.I. Ferrero, R. Ragona, V. Rolando, G.L. Sannazzari and A. Solano, "Monte Carlo simulation of a proton therapy system for calculation of the dose distribution in a patient". Report TERA 95/4 TRA 14, Fondazione per Adroterapie Oncologica, Novara, Italy, 1995.

[Gi64] R.A. Giles and E.J. Burge, "The measurement of the total proton reaction cross-section of carbon in the energy region up to 50 MeV". Nucl. Phys. **50**, 327-336 (1964).

[Go48] M.L. Goldberger, "The interaction of high energy neutrons and heavy nuclei." Phys. Rev. **74**, 1269-1277 (1948).

[Go59] T.J. Gooding, "Proton total reaction cross section at 34 MeV". Nucl. Phys. **12**, 241-248 (1959).

[Go60] T.J. Gooding and H.G. Pugh, "The response of scintillators to high energy particles". Nucl. Instr. Meth. **7**, 189-192 (1960).

[Go90] B. Gottschalk, "Proton nozzle design program NEU". Internal Report, Harvard University Cyclotron Laboratory, 1990.

[Go93] B. Gottschalk, A.M. Kohler, R.J. Schneider, J.M. Sisterson, and M.S. Wagner, "Multiple Coulomb scattering of 160 MeV protons". Nucl. Instr. Meth. **B74**, 467-490 (1993).

[Go99a] B. Gottschalk, "Physical parameters of small proton beams". PTCOG XXXI, Bloomington, IN, October 11-13 (1999).

[Go99b] B. Gottschalk, R Platais and H.Paganetti, "Nuclear interactions of 160 MeV protons stopping in copper: A test for Monte Carlo models". Med. Phys. **26**, 2597-2601 (1999).

[Go64] F.S. Goulding, D.A. Landis, J. Cerny and R.H. Pehl, "A new particle identifier technique for $Z = 1$ and $Z = 2$ particles in the energy range $>$ 10 MeV". Nucl. Instr. Meth. **31**, 1-12 (1964).

[Go75] F.S. Goulding and B.G. Harvey, "Identification of nuclear particles". Ann. Rev. Nucl. Sci. **25**, 167-240 (1975).

[Gu97] J.Gueulette, L. Böhm, B. De Coster, S Vynkier, M. Octave-Prignot, A.N. Schreuder, J.E. Symons, D.T.L. Jones, A. Wambersie and P. Scalliet, " RBE variation as a function of depth in the 200 MeV proton beam produced at the National Accelerator Centre in Faure (South Africa)". Radiother. Oncol. **42**, 303-309 (1997).

[Ha95a] C.L.Hartman Siantar, W.P. Chandler, J.A. Rathkopf, M.M. Svatos and R.M. White, "PEREGRINE: An all particle Monte Carlo code radiation therapy." *Proceedings of the International Conference on Mathematics and Computaions, Reactor Physics and Environmental Analyses*, American Nuclear Society, LaGrange Park, 1995, pp.857-865.

[Ha95b] C.L.Hartman Siantar, W.P. Chandler,M.B. Chadwick, H.M. Blann, L.J. Cox, D.A. Resler J.A. Rathkopf, T.R. Mackie, J.V. Siebers, M.A. Ross, P.M. DeLuca Jr., K.A. Weaver and R.M White, "Dose distribution calculated with the PEREGRINE all particle Monte Carlo code." Med. Phys. **22**, 994 (1995).

[Ha98] C.L.Hartman Siantar and E. I. Moses. " The PEREGRINE^{TM} program: using physics and computer simulation to improve radiation therapy for cancer." Eur. J. Phys. **19**, 513-521 (1998).

[Hi75] V.L. Highland, "Some practical remarks on multiple scattering". Nucl. Instr. Meth. **129**, 497-499 (1975).

[Hi79] V.L. Highlands, "Erratum; Some practical remarks on multiple scattering". Nucl. Instr. Meth. **129**, 497-499 (1975)". Nucl. Instr. Meth. **161**, 171 (1979).

[Ho96] L. Hong, M. Goiten, M. Bucciolini, R. Comiskey, B, Gottschalk, S. Rosenthal, C. Serago, and M. Urie, "A pencil beam algorith for proton dose calculations." Phys. Med. Biol. **41**, 1305-1330 (1996).

[Hu97] H. G. Hughes, R.E. Prael and R.C. Little, "MCNPX - The LAHET/MCNP code merger", X-Division research note XTM-RN(U)97-012, LA-UR-97-4891, Los Alamos National Laboratory (April 1997).

[Hu95] H.G. Hughes and L.S. Waters, "Energy straggling module prototype", Los Alamos National Laboratory memorandum XTM:95-305 (U) (November 1995).

[IC49] ICRU report 49, Stopping powers and ranges for protons and alpha particles. International Commision on Radiation Units and Measurements, Bethesda, MD, 1993.

[ICRU59] ICRU report 59, Clinical proton dosimetry part 1: Beam production, beam delivery and measurement of absorbed dose. International Commision on Radiation Units and Measurements, 1998.

[IC63] ICRU report 63, Nuclear data for neutron and proton radiotherapy and for radiation protection. International Commision on Radiation Units and Measurements, Bethesda, MD, 2000.

[Ja82] J.F. Janni, "Proton range-energy tables". Atomic data and nuclear data tables, Vol 27 1982.

[Jo58] L.H. Johnston and D.A. Swenson, "Proton-proton scattering at 40 MeV". Phys. Rev. **111**, 212-218 (1958).

[Jo94] D.T.L. Jones, A.N. Schreuder J.E. Symons and M. Yudelev, "The NAC particle therapy facilities". Hadrontherapy in Oncology, edited by U. Amaldi and B. Larson. Amsterdam: Elsevier Science Publishers BV, 307-328, 1994.

[Jo95a] D.T.L. Jones, "The only particle therapy facility in the Southern Hemisphere". Ion Beams in Tumor Therapy, edited by U. Linz. Weinheim, Germany: Chapman and Hall, 350-359, 1995.

[Jo95b] D.T.L. Jones, A.N. Schreuder and J.E. Symons, "Particle therapy at the NAC: physical aspects. *Proceedings of the 14th international Conference on Cyclotrons and their Applications*, Edited by J.C. Cornell. Singapore: World Scientific, 491-498, 1995.

[Jo99] D.T.L Jones, A.N. Schreuder, J.E. Symons, E.A. de Kock, F.J.A. Vernimmen, C.E. Stannard, J. Wilson and G. Schmitt, "Status report of the NAC particles therapy programme". Strahlenther. Onkol. **175: Suppl II**, 30-32 (1999).

[Jo01b] D.T.L Jones and A.N. Schreuder, "Magnetically scanned proton therapy beams: rationales and principles". Rad. Phys. Chem. **61**, 615-618 (2001).

[Jo01c] D.T.L. Jones, A.N. Schreuder, E.A. de Kock, J.E. Symons and A. Tourovsky, "The proton therapy quality assurance program at NAC". PTCOG XXXV, Tsukuba, Japan, 14-16 November (2001).

[Ka83] T. Kanai, K. Kawach and H. Matsuzawa, "Three-dimensional beam scanning for proton therapy". Nucl. Instr. Meth. **214**, 491-496 (1983).

[Kh98] V.S. Khoroshkov and E.I. Minakova, "Proton beams in radiotherapy". Eur. J. Phys. **19**, 523-536 (1998).

[Kn89] G.F. Knoll, Radiation Detection and measurement, Second Edition, John Wiley and Sons, 1989.

[Ko75] A.M. Koehler, R.J. Schneider, and J.M. Sisterson, "Range modulators for protons and heavy ions". Nucl. Instr. Meth. **131**, 437-440 (1975).

[Ko77] A.M. Koehler, R.J. Schneider, and J.M. Sisterson, "Flattening of proton dose distributions for large-field radiotherapy". Med. Phys. **4**, 297-301 (1977).

[Ko72] A.M. Koehler and W.M. Preston, "Protons in radiation therapy". Radiology **104**, 191-195 (1972).

[Ko97] H.D. Kogelnik, "Hadrontherapy - do we need it?" Advances in Hadrontherapy, edited by U. Amaldi, B.Larsson and Y. Lemoigne. Excerpta Media. International Congress Series 1144, 1997 pp13-28.

[Ko68] J.J. Kolata, T.M. Moss and H. Bichsel, "Energy loss straggling of protons in silicon". Phys. Rev. **176**, 484-489 (1968).

[Ku66] P. Kuijper, C.J. Tiesinga and C.C. Jonker, "Light attenuation in scintillation counters." Nucl. Instr. Meth. **42**, 56-6- (1966).

[Le87] W.R. Leo, Techniques for Nuclear and Particle Physics Experiments, Springer-Verlag, 1987.

[Le93] M. Lee, A.E. Nahum and S. Webb, "An emperical method to build up a model of proton dose distribution fro a radiotherapy treatment planning package." Phys. Med. Biol. **38**, 989-998 (1993).

[Lu01] P. van Luijk, A.A. van't Veld, H.D. Zelle and J.M. Schippers, Phys. Med. Biol. **46**, 653-670 (2001).

[Ma97] C.M. Ma, B.A. Faddegon, D.W.O. Rogers and T.R. Mackie. "Accurate characterization of Monte Carlo calculated electron beams for radiotherapy." Med. Phys. **24**, 401-416 (1997).

[Ma68a] H.D. Maccabee, M.R. Raju and C.A. Tobias, "Fluctuations of energy loss by heavy charged particles in thin absorbers". Phys. Rev **165**, 469-474 (1968).

[Ma68] M.Q. Makino, C.N. Waddell and R.M. Eisberg, "The nuclear reaction efficiency correction for silicon and germanium detectors". Nucl. Instr. Meth. **60**, 109-112 (1968).

[Ma69] P. Marmier and E. Sheldon, *Physics of Nuclei and Particles*, Volume 1, Academic Press Inc. 1969.

[Me65] D.F. Measday, "Loss of protons by nuclear interactions in sodium iodide crystals". Nucl. Instr. Meth. 34, 353-355 (1965).

[Me66] D.F. Measday and R.J. Schneider, "Loss of charged particles by nuclear interactions in scintillators". Nucl. Instr. Meth. **42**, 26-28 (1966).

[Me69] D.F. Measday and C. Richard-Serre, "The loss of protons by nuclear inelastic interactions in various materials". Nucl. Instr. Meth. **76**, 45-54 (1969).

[Me97] J. Medin and P. Andreo, "Monte Carlo calculated stopping power ratios, water/air, for clinical proton dosimetry". Phys. Med. Biol. **42**, 89-105 (1997).

[Me58a] N. Metropolis, R. Bivins, M.Storm, A. Turkevich, J.M. Millar and G. Friedlander, " Monte Carlo calculations on intranuclear cascades. II. High energy studies and pion processes." Phys. Rev. **110**, 185-203 (1958).

[Me58b] N. Metropolis, R. Bivins, M.Storm, J.M. Millar, G. Friedlander and A. Turkevich, " Monte Carlo calculations on intranuclear cascades. II. High energy studies and pion processes." Phys. Rev. **110**, 204-219 (1958).

[Me67] W.E. Meyerhof, Elements of Nuclear Physics, McGraw Hill Book Company, 1967 Company,1955.

[Mo81] R.F. Mould, "Medical Physics Handbooks 7. Radiotherapy Treatment Planning". Adam Hilger Ltd, Bristol.

[Mi97] R. Miralbell, "Treatmet precision with proton beams: clinical experience and new indications." Advances in Hadrontherapy, edited by U. Amaldi, B.Larsson and Y. Lemoigne. Excerpta Media. International Congress Series 1144, 1997 pp120-138.

[NA94] Annual Report NAC/AR/95-01, National Accelerator Centre, South Africa (1995) p85.

[NA98] Annual Report NAC/AR/98-01, National Accelerator Centre, South Africa (1998).

[Ok95] P. Okunieff, D. Morgan, A. Niemierko and H.D. Suit, "Radiation dose-response of human tumors". Int. J. Radiat. Oncol., Biol., Phys. **32**, 1227-1237 (1995).

[Pa96] H. Paganetti and Th Schmitz, "The influence of the beam modulation technique on dose and RBE in proton radiation therapy". Phys. Med. Biol. **41**, 1649-1663 (1996).

[Pa98] H. Paganetti, "Monte Carlo method to study the proton fluence for treatment planning." Med. Phys. **25**, 2370-2375 (1998).

[Pa2000] H. Paganetti and M. Goitein, "Radiobiological significance of beamline dependent proton energy distributions in a spread-out Bragg peak". Med. Phys. **27**, 1119-1126 (2000).

[Pa69] J.N. Palmieri and J. Wolfe, "Loss of protons by nuclear interactions in sodium iodide crystals". Nucl. Instr. Meth. **76**, 55-58 (1969).

[Pe95] E. Pedroni, H. Blattmann, T. Bohringer, A. Coray, A. Lomax, S. Lin, G. Munkel, S. Scheib, U. Schneider and A. Tourovsky, "The 200- MeV proton therapy project at the Paul Scherrer Institute: Conceptual design and practical realization". Med. Phys. **22**,37-53 (1995).

[Pe79] L.J. Perkins and M.C. Scott, "The application of pulse shape discrimination in NE213 to neutron spectrometry". Nucl. Instr. Meth. **166**, 451-464 (1979).

[Pe76] D.G. Perry and L.P. Remsberg, "Particle identification with very thin transmission detectors". Nucl. Instr. Meth. **135**, 103-109 (1976).

[Pe90] P.L. Petti, J.T. Lyman, T.R. RennerJ.R. Castro, J.M. Collier, I.K. Daftari and B.A. Ludewigt, "Design of beam-modulating devices for charged-particle therapy." Med. Phys. **18**, 513-519 (1990).

[Pe92] P.L. Petti, "Differential pencil beam dose calculations for charged particles." Med. Phys. **19**, 137-149 (1992).

[Pe94] P.L. Petti and A.J. Lennox, "Hadronic radiotherapy." Ann. Rev. Nucl. Part. Sci. **44**, 155-197 (1994).

[Pe96] P.L. Petti, "Evaluation of a pencil-beam dose calculation technique for charged particle radiotherapy." Int. J. Radiat. Oncol., Biol., Phys. **35**, 1049-1057 (1996).

[Pr89] R.E. Prael and H. Lichtenstein, "User guide to LCS: The LAHET Code System", report LA-UR-89-3014, Los Alamos National Laboratory (September 1989).

[Pr88] R.E. Prael and M. Bozoian, "Adaptation of the Multistage Preequilibrium Model for the Monte Carlo Method (I)", report LA-UR-88-3238, Los Alamos National Laboratory (September 1988).

[Pr95] R.E. Prael and D.G. Madland, "LAHET Code System modifications for LHAET2.8", report LA-UR-95-3605 Los Alamos National Laboratory (September 1995).

[Pr93] R.E. Prael, "LAHET calculations for accelerator neutron production". *American Nuclear Society Transactions, 69*, San Francisco Nov. 14 to Nov. 18, 1993, p.426.

[Pr94] R.E. Prael, "A review of physics models in the LAHET code". Intermediate Energy Nuclear Data: Models and Codes, Proceedings of a specialists' meeting, Issyles-Moulineaux (France), May 30 to June, 1 1994, p.145.

[Pr98] R.E. Prael, "Upgrading physics packages for LAHET/MCNPX". *Proceedings of the 2nd International Topical Meeting on Nuclear Applications of Accelerator Technology*, Gatlinburg, TN, Sept 20-23, 1998. American Nuclear Society, p.276 (1998).

[Ra97] R. Ragona, V. Rolando and A. Solano. "Treatment planning of proton beams using the GEANT Monte Carlo." Advances in Hadrontherapy, edited by U. Amaldi, B.Larsson and Y. Lemoigne. Excerpta Media. International Congress Series 1144, 1997 pp706-711.

[Ra95] M.R. Raju, "Proton radiology, radiosurgery and radiotherapy." Int. J. Radiat. Biol., **67**, 237-259 (1995).

[Re72] P.U. Renberg, D.F. Measday, B. Favier, C. Richard-Serre, M. Pepin and P. Schwaller, "Loss of protons in thin absorbers". Nucl. Instr. Meth. **104**, 157-152 (1972).

[Ro41] B. Rossi and K. Greisen, Rev. Mod. Phys. **13**, 240 (1941).

[Ru95] K.R. Russel, E. Grusell and A. Montelius, "Dose calculations in proton beams: range straggling corrections and energy scaling." Phys. Med. Biol. **40**, 1031-1043 (1995).

[Sa66] M.W. Sachs, C. Chasman and D.A. Bromley, "Heavy ion reaction product identification by measurements of dE/dx and E". Nucl. Instr. Meth. **41**, 213-225 (1966).

[SA97] G.A. Sandisson C-C Lee, X. Lu and L.S. Papiez, "Extension of a numerical algorithm to proton dose calculations. I. Comparisons with Monte Carlo simulations". Med. Phys. **24**, 841-849 (1997).

[Sc95] A.N. Schreuder, D.T.L. Jones, J.E. Symons, T. Fulcher and A. Kiefer, "The NAC proton therapy beam delivery system". *Proceedings of the 14th international Conference on Cyclotrons and their Applications*, Edited by J.C. Cornell. Singapore: World Scientific, 523-526, 1995.

[Sc95] A.N. Schreuder, D.T.L. Jones, and A. Kiefer, "A small ionization chamber for dose distribution measurements in a clinical proton beam". Advances in Hadrontherapy, edited by U. Amaldi, B.Larsson and Y.

Lemoigne. Excerpta Media. International Congress Series 1144, 1997 pp284-289.

[Se77] A.G. Seamster, R.E.L. Green and R.G. Korteling, "Silicon detector ΔE, E particle identification: A theoretically based analysis algorithm and remarks on the fundamental limits to the resolution of particle type by ΔE, E measurements". Nucl. Instr. Meth. **145**, 583-591 (1977).

[Se47] R. Serber, "Nuclear reactions at high energies." Phys. Rev. **72**, 1114-1115 (1947).

[Sh79] W.U. Shipley, J.. Tepper, G.R. Prout, L.J. Verhy, O.A. Mendiondo, M.G. Goiten, A.M. Koehler and H.D. Suit, "Proton radiation as boost therapy for localised prostatic carcinoma". J. Am. Med. Assoc. **241**, 1912-1915 (1979).

[Si97] J.V. Siebers and M.M. Traynor, "Modelling of proton treatment nozzles with LAHET Monte Carlo code." J. Brachytherapy Int. **13**, 95-99 (1997).

[Si95] J.M. Sisterson, "Proton radiation therapy: a summary of the world wide experience". Nucl. Instr. Meth. **B99**, 827-829 (1995).

[Sk67] D.J. Skyrme, "The passage of charged particles through silicon". Nucl. Instr. Meth. **57**, 61-73 (1967).

[Sm86] F.D. Smit, Ph.D. Thesis, University of Cape Town, 1986 (unpublished).

[Sm87] F.D. Smit and F.D. Brooks, "Angular distribution of neutrons from ^{2}H(γ,n)^{1}H at $E_\gamma = 2.75$ MeV". Nucl. Phys. **A465**, 429-444 (1987).

[Sm68] D.L. Smith, R.G. Polk and T.G. Miller, "Measurement of the response of several organic scintillators to electrons, protons and deuterons". Nucl. Instr. Meth. **64**, 157-166 (1968).

[Su75] H.D. Suit, M. Goiten, J.Tepper, A.M. Koehler, R.A. Schmidt and R. Schneider, " Exploratory study of proton radiation therapy using large field techniques and fractionated dose schedules". Cancer **35**, 1646-1657 (1975).

[Su77] H.D. Suit, M. Goiten, J.E. Tepper, L. Verhy, A.M. Koehler, Schneider and E. Gragoudas, "Clinical experience and expectaion with protons and heay ions". Int. J. Radiat. Oncol., Biol., Phys. **3**, 115-125 (1977).

[Su80] H.D. Suit, M. Goiten, J.E. Munzenrider, L. Verhy, E. Gragoudas, A.M. Koehler, M. Urano, W.U. Shipley, R.M. Linggood, C. Friedberg and M. Wagner, "Clinical Experience with proton beam radiation therapy". Jour. Canadian Assoc. Radiol. 31, 35-39 (1980).

[Su92] H.D. Suit and M. Urie, "Proton beams in radiation therapy". Jour. Natl. Canc. Inst. 84, 155-163 (1992).

[Su90] H.D. Suit, M. Goiten, J.E. Munzenrider, L. Verhy, M. Urie, E. Gragoudas, A. Koehler, B. Gottschalk, H. Tatsuzaki and R. Miralbell, "Increased efficacy of radiation therapy by use of proton beam". Strahlenther. Onkol. **166**, 40-44 (1990).

[Su97] H.D. Suit and M. Krengli, "Basis for interest in proton beam radiation therapy". Advances in Hadrontherapy, edited by U. Amaldi, B.Larsson and Y. Lemoigne. Excerpta Media. International Congress Series 1144, 1997 pp29-37.

[Su92a] H.D. Suit, "Local control and patient survival". Int. J. Radiat. Oncol., Biol., Phys. **23**, 653-660 (1992).

[Su74] H.D. Suit and M. Goiten, "Cose-limiting tissues in relation to types and location of tumors: implications for efforts to improve radiation dose distributions". Europ. J. Cancer **10**, 217-224 (1974).

[Ts68a] T.S. Tschalär, "Straggling distributions of large energy losses". Nucl. Instr. Meth. **61**, 141-156 (1968).

[Ts68b] T.S. Tschalär, "Straggling distributions of extremely large energy losses". Nucl. Instr. Meth. **64**, 237-243 (1968).

[Ur86] M.M. Urie, J.M. Sisterson, A.M. Koehler, M. Goiten, and J. Zoesman, "Proton beam penumbra: Effects of separation between patient and beam modifying devices". Med. Phys. **13**, 734-741 (1986).

[Va57] P.V. Vavilov, "Ionization losses of high-energy heavy particles" *Soviet Physics JETP5*, No. 5 (1957) 749.

[Ve79] L.J. Verhy, A.M. Koehler, J.C. McDonald, M. Goiten, I-Chang Ma, R.J. Schneider and M. Wagner, "The determination of absorbed dose in a

proton beam for purposes of charged-particle radiation therapy". Radiat. Res. **79**, 34-54 (1979).

[Ve82] L.J. Verhy and J.E. Munzenrider, "Proton beam therapy". Ann. Rev. Biophys. Bioeng. **11**, 331-357 (1982).

[Wa82] M.S. Wagner, "Automated range compensation for proton therapy". Med. Phys. **9**, 749-752 (1982).

[Wa99] L.S. Waters, editor, "MCNPX^{TM} users manual", report TPO-E83-G-UG-X-00001, Los Alamos National Laboratory (November 1999).

[Wa99] A. Wambersie, T. Auberger, R.A. Gahbauer, D.T.L. Jones and R. Pötter, "A challenge for high precision radaition therapy: The case for hadrons." Strahlenther. Onkol. **175**, Suppl II:122-128 (1999).

[Wa98] (1998). L. Wang, C.S. Chui and M. Lovelock. "A patient-specific Monte Carlo dose-calculation method for proton beams." Med. Phys. **25**, 867-878 (1998).

[Wi76] B. Wilken and T.A. Fritz, "Energy distribution functions of low energy ions in silicon absorbers measured for large relative energy losses". Nucl. Instr. Meth. **138**, 331-343 (1976).

[Wi46] R.R Wilson, "Radiological use of fast protons." Radiology **47**, 487-491 (1946).

[XSYS] XSYS, IUCF Data acquisition software, IUCF Internal Report, Indiana University Cyclotron Facility, Bloomington, Indiana.

[Ya79] Y. Yariv and Z. Fraenkel, "Intranuclear cascade calculation of high energy heavy-ion interactions." Phys. Rev. **C20**, 2227-2243 (1979).

[Ya81] Y. Yariv and Z. Fraenkel, "Intranuclear cascade calculation of high energy heavy-ion interactions: Effects of interactions between cascade particles." Phys. Rev. **C24**, 488-494 (1981).

[Ze63] C.D. Zerby, "Response of gamma-ray scintillation counters"in Methods in computational physics, Advances in research and applications Vol.1 Statistical Physics, edited by B. Alder. academic Press, New York (1963).